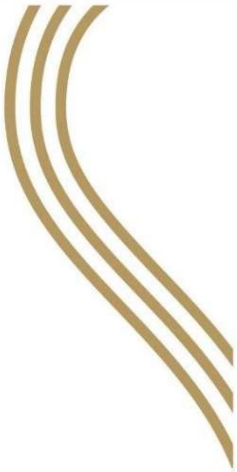

Mathematical pore-scale modelling of kinematic and geometric properties of fibrous porous media

by
Esmari Maré

Dissertation presented for the degree of Doctor of Philosophy in the Faculty of Science at Stellenbosch University

Supervisor: Prof. Sonia Fidder

December 2023

Declaration

By submitting this dissertation electronically, I declare that the entirety of the work contained therein is my own, original work, that I am the sole author thereof (save to the extent explicitly otherwise stated), that reproduction and publication thereof by Stellenbosch University will not infringe any third party rights and that I have not previously in its entirety or in part submitted it for obtaining any qualification.

December 2023

Abstract

This study involves the mathematical modelling of permeability (of both the Darcy and Forchheimer flow regimes) and specific surface area of fibre-type and foamlike porous media using geometric models. Several existing models for predicting these properties have been studied in the literature, with the Representative Unit Cell (RUC) model being of particular interest due to its simple rectangular geometry and good performance compared to other models and experimental data from the literature. This study includes a comparative analysis of the permeability and specific surface area prediction of different versions of the RUC model for fibrous media involving the 2D RUC models for in-plane and through plane flow, the 3D RUC model, the two-strut RUC models for in-plane and through plane flow, and the three-strut RUC model. It furthermore incorporates novel contributions such as the adaptation of the three-strut (or foam) RUC model by adding solid material to account for the observed lump at the intersection of struts in actual metal and ceramic foams. The RUC models are also adapted analytically to take secondary effects such as compression or variable rectangular geometry into account. Additionally, the models are adapted to include changes in the predictions of the permeability due to the Klinkenberg effect, an effect that accounts for the increase in the permeability of gas flow as opposed to that of a liquid. The novelty of this study lies in the incorporation of these effects into the model predictions, which extends the range of applicability of the proposed models beyond those available in the literature. In order to ensure the user-friendliness of the analytical models provided, the predictive equations are expressed in terms of measurable macroscopic parameters. Furthermore, the models are evaluated through comparison with other models from the literature as well as available experimental and numerical data, which yield results that are satisfactory. The findings contribute positively towards industrial applications such as filtration and heat transfer processes, facilitating their effective operation by means of analytical modelling and analysis of the physical flow processes involved.

Uittreksel

Hierdie studie behels die wiskundige modellering van permeabiliteit (van beide die Darcy- en Forchheimer-vloeigebiede) en spesifieke oppervlakarea van vesel-tipe en harde spons poreuse media deur geometriese modelle te gebruik. Verskeie bestaande modelle vir die voorspelling van hierdie eienskappe vanuit die literatuur is bestudeer, met die verteenwoordigende eenheidsel (VES) model wat van besondere belang is as gevolg van sy eenvoudige reghoekige geometrie en goeie prestasie in vergelyking met ander modelle en eksperimentele data vanuit die literatuur. Hierdie studie sluit 'n vergelykende ontleding van die permeabiliteit en spesifieke oppervlakarea voorspelling van verskillende weergawes van die VES-model vir veselagtige media bestaande uit die 2D VES-modelle vir in-vlak en deur vlak vloei, die 3D VES model, die twee-been VES modelle vir in-vlak en deur vlak vloei, en die drie-been VES model. Dit inkorporeer verder nuwe bydraes soos die aanpassing van die drie-been (of spons) VES-model deur soliede materiaal by te voeg om rekening te hou met die waargenome opeenhoping van materiaal by die kruising van die bene van die spons in werklike metaal- en keramieksponse. Die VES-modelle is ook analities aangepas om sekondêre effekte soos samepersing en reghoekige geometrie in ag te neem. Daarbenewens is die modelle aangepas om veranderinge in die voorspellings van die permeabiliteit in te sluit as gevolg van die Klinkenberg-effek, 'n effek wat verantwoordelik is vir die toename in die gaspermeabiliteit in vergelyking met die vloeistofpermeabiliteit. Die nuutheid van hierdie studie lê in die inkorporering van hierdie uitwerkings in die modelvoorspellings, wat die toepassingsgebied van die voorgestelde modelle verder uitbrei as dié wat in die literatuur beskikbaar is. Om die gebruikersvriendelikheid van die analitiese modelle wat verskaf is te verseker, word die voorspellende vergelykings uitgedruk in terme van meetbare makroskopiese parameters. Verder word die modelle geëvalueer deur vergelyking met ander modelle uit die literatuur asook beskikbare eksperimentele en numeriese data, wat bevredigende resultate lewer. Die bevindinge dra positief by tot industriële toepassings soos filtrasie- en hitte-oordragprosesse, wat die effektiewe werking daarvan vergemaklik deur middel van analitiese modellering en ontleding van die betrokke fisiese vloeiprosesse.

Acknowledgements

The author wishes to acknowledge the following people for their various contributions towards the completion of this study:

- God, who gave me life, who saved me and sent His Son to die for me that I might know Him and His love for me. May I never cease to be amazed and grateful for the precious gift He has given me. Thank You for pursuing me, for leading and guiding me in life and for making life beautiful and full of purpose.
- Professor Sonia Fidder-Woudberg who went above and beyond to help me navigate the landscape of research, thesis writing and mathematical modelling and who invested so much in me and my future. Thank you.
- My parents, Liesl and Siegfried Maré, who carried me in prayer and encouraged me to the end.
- My grandparents, Lisa and Salie de Swardt, who gave so freely and opened their homes for me as safe havens whenever I needed it. Dankie Oupa vir Oupa se liefde, ondersteuning en trots, ek sal dit altyd onthou en koester.
- My siblings, Abigail, Siegfried and Stephanie, who loved me, laughed with me and reminded me of the important things in life.
- Hlubi Hadebe, who loved, encouraged and supported me in this journey through prayer, songs, acts of service, words and lots of food. Who never stopped believing in me.
- Tannie Louise, my mentor in life and its various trials.
- Marilie, my partner and sister in Christ.
- Marlise, my dear friend.
- Jason George, my big brother in Christ.
- The rest of my family, Oom Stephan, Tannie Daphne, Oom Hennie and Tannie Sanna who helped when I needed it and shared with me some keys to life.
- My friends, housemates and smallgroup who supported me with many prayers.
- Jakoba, Jonleif, Buhle, Muofhe, Timna, Abby, Minnie, Bonnie, Ashley, Marizan, Briance, Claudia, Tosca, Karien, Monique, Annare, Karla, Carien, Nadia, Tenita, Elsje, Martin, Dirkie, James, Adriaan, Elijah and all the rest who gave me precious nuggets of support in this time.

- Wilhelm Frank for the prestigious scholarship.
- Prof Hale for the many references and whole-hearted support.
- Dr. Diedericks for all the opportunities and the open door to come ask questions at any time.
- Stellenbosch University for the opportunity to undertake this research.
- Shofar Christian Church, a major part of my community who helped me keep my focus on Jesus and encouraged me to run the race of life with endurance.

'When I look at your heavens, the work of your fingers, the moon and the stars, which you have set in place, what is man that you are mindful of him, and the son of man that you care for him?' Psalm 8:3,4

Table of Contents

Nomenclature

Standard characters

A	[m^2]	base area of container enclosing porous medium
A_{add}	[m^2]	area added to "fat" dodecahedron model
A_{fr}	[m^2]	frontal area subject to recirculation
A_o	[m^2]	RUC base area
A_p	[m^2]	constant cross-sectional flow area
$A_{p_\parallel}$	[m^2]	streamwise cross-sectional flow area
$A_{p_\perp}$	[m^2]	transverse cross-sectional flow area
a	[m]	fibre/strut radius
B	[m]	linear dimension
b	[m]	fibre diameter
C	[-]	empirical coefficient
$C_{D,f}$	[-]	form drag coefficient for high Reynolds number flow
$C_{D,v}$	[-]	friction coefficient for low Reynolds number flow
C_E	[-]	Forchheimer coefficient
c_d	[-]	interstitial form drag coefficient
D_h	[m]	hydraulic diameter
D_p	[m]	face diameter
d	[m]	RUC face diameter
d^*	[m]	NARUC face diameter
d_c	[m]	cell diameter
d_p	[m]	RUC pore diameter
d_p^*	[m]	NARUC pore diameter
d_s	[m]	RUC strut diameter
d_s^*	[m]	NARUC strut diameter
e	[-]	compression ratio
f	[-]	shear factor
f_f	[-]	drag force for low Reynolds number flow
f_v	[-]	drag force for high Reynolds number flow
h	[m]	filter thickness
K	[m^2]	permeability coefficient of Darcy regime
$K_\parallel$	[m^2]	permeability coefficient of Darcy regime of 1D RUC model for parallel flow
$K_\perp$	[m^2]	permeability coefficient of Darcy regime of 1D RUC model for transverse flow

K_F	[m^{-1}]	permeability coefficient of Forchheimer regime
$K_{F_\parallel}$	[m^{-1}]	permeability coefficient of Forchheimer regime of 1D RUC model for parallel flow
$K_{F_\perp}$	[m^{-1}]	permeability coefficient of Forchheimer regime of 1D RUC model for transverse flow
K_g	[m^2]	gas permeability
K_l	[m^2]	liquid permeability
Kn	[-]	Knudsen number
k	[-]	node number
L	[m]	linear dimension
l_s	[m]	strut length
$\underline{n}$	[-]	unit vector perpendicular to fluid-solid surface
$\underline{\hat{n}}$	[-]	macroscopic direction of flow
p	[Pa]	pressure
$p_{\bar{a}\bar{v}g}$	[Pa]	average of inlet and outlet pressures
q	[$m.s^{-1}$]	magnitude of superficial velocity
R	[-]	RUC node ratio
r_1	[-]	node ratio
r_2	[-]	node ratio
r_{cf}	[-]	ratio of linear dimensions of dodecahedron model with cylindrical "fat" struts
r_{cs}	[-]	ratio of linear dimensions of dodecahedron model with cylindrical "slim" struts
r_{tf}	[-]	ratio of linear dimensions of dodecahedron model with triangular "fat" struts
r_{ts}	[-]	ratio of linear dimensions of dodecahedron model with triangular "slim" struts
S	[m^2]	surface area
S_{add}	[m^2]	specific surface area added to "fat" dodecahedron model
S_{face}	[m^2]	RUC solid cross-sectional area facing upstream
S_{fs}	[m^2]	fluid-solid surface area
S_v	[m^{-1}]	specific surface area
$S_\parallel$	[m^2]	RUC solid surface parallel to streamwise direction
$S_\perp$	[m^2]	RUC solid surface perpendicular to streamwise direction
s_{D_h}	[m]	standard deviation of hydraulic diameter measurements
t	[m]	triangular strut edge width
U	[m^3]	compressed RUC cell volume
U_f	[m^3]	RUC fluid volume
U_o	[m^3]	uncompressed RUC cell volume
U_s	[m^3]	RUC solid volume
$U_{s_{\text{node}}}$	[m^3]	RUC node solid volume
U_s^*	[m^3]	NARUC solid volume
U_t	[m^3]	RUC transfer volume
$U_\parallel$	[m^3]	RUC streamwise fluid volume
$U_\perp$	[m^3]	RUC transverse fluid volume
V_f	[m^3]	fluid volume
V_o	[m^3]	volume of fibrous porous medium
V_s	[m^3]	volume of struts

$\underline{v}$	[m.s^{-1}]	velocity
v_{avg}	[m.s^{-1}]	magnitude of average velocity
v_p	[m.s^{-1}]	magnitude of average pore velocity
v_∞	[m.s^{-1}]	magnitude of approaching velocity
w	[m]	linear dimension
$w_\parallel$	[m.s^{-1}]	magnitude of streamwise average duct velocity
$w_\perp$	[m.s^{-1}]	magnitude of transverse average duct velocity
x	[m]	linear dimension

Greek symbols

α	[-]	constant
β	[-]	RUC coefficient
δ	[-]	node accumulation constant
ϵ	[-]	porosity
ϵ_o	[-]	porosity of uncompressed state
ϵ_p	[-]	percolation threshold
λ	[m]	molecular mean free path
μ	[N.s.m^{-2}]	dynamic viscosity
ξ	[-]	RUC coefficient
ρ	[kg.m^{-3}]	fluid density
ρ_g	[kg.m^{-3}]	foam apparent density
ρ_s	[kg.m^{-3}]	strut density
σ	[-]	tangential momentum accommodation coefficient
$\underline{\underline{\tau}}$	[N.m^{-2}]	shear stress
$\bar{\tau}_w$	[N.m^{-2}]	magnitude of average wall shear stress
$\tau_{w_\parallel}$	[N.m^{-2}]	magnitude of streamwise average wall shear stress
$\tau_{w_\perp}$	[N.m^{-2}]	magnitude of transverse average wall shear stress
ϕ	[-]	golden ratio
$\phi_\parallel$	[-]	weight constant assigned with $K_\parallel$
$\phi_\perp$	[-]	weight constant assigned with $K_\perp$
χ	[-]	tortuosity
ψ	[-]	RUC geometric factor
ψ_o	[-]	RUC geometric factor of uncompressed state

Abbreviations

CT	Computer Tomography
CUC	Cubic Unit Cell
MCL	Modified Cubic Lattice
MRI	Magnetic Resonance Imaging
NARUC	Node Adjusted Representative Unit Cell
PPI	Pores Per linear Inch
RUC	Representative Unit Cell

TMAC	Tangential Momentum Accommodation Coefficient

Subscripts

$_b$	pore boundary
exp	experimental values
$_o$	uncompressed dimension
$\parallel$	parallel to streamwise direction
$\perp$	perpendicular to streamwise direction
$_x$	direction with respect to streamwise flow direction

Operators

Δ	change in streamwise property
∇	gradient
$\langle\,\rangle$	phase average
$\langle\,\rangle_f$	intrinsic phase average

List of Figures

List of Tables

CHAPTER 1

Introduction

1.1 Fibrous porous media

Fibres and foamlike media are both classified as fibrous porous media (e.g., Tadrist et al. [27]). There are numerous applications for fibres in industry that make use of filtration processes, transport in biological systems, acoustic properties, compact heat exchangers, technology in fuel cells, paper production, fibrous beds for manufacturing processes and many other mechanical, biological and chemical systems (Soltani et al. [28], Stylianopoulos et al. [29], Tahir and Tafreshi [30]). An example is coalescing filters which make use of fibres, such as glass fibres, as a filter medium and remove droplets from liquid aerosols and other air streams and include applications in dehumidification, filtration of cabin air, automotive engine crank case ventilation and metal working (Manzo et al. [23]). The popularity of fibres in such systems are accredited to their mechanical strength, flexible structure, large specific surface area, low weight, high heat transfer coefficients and high permeability, as well as their high porosities (Tahir and Tafreshi [30], Tamayo and Bahrami [31]). The study of transport properties and morphological parameters of fibres is therefore an important and necessary contribution towards the effective operation of fibres in all these various fields of application. Figure 1.1 shows fibres with arbitrary orientations under magnification.

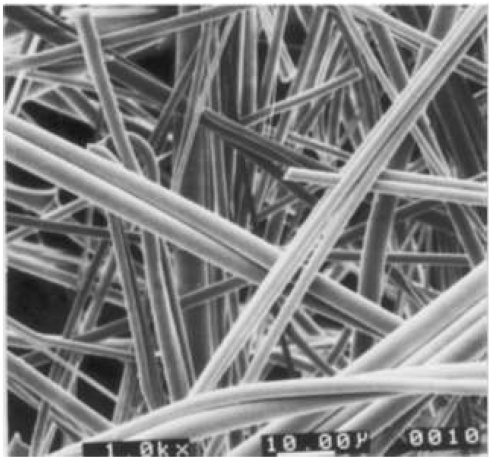

FIGURE 1.1: *Fibres with arbitrary orientations (Source: Woudberg and Du Plessis [14])*

Foamlike media, referring to ceramic and metal foams, also cover a wide range of applica-

tions in industry. A few examples include uses in compact heat sinks for power electronics, catalytic beds, air cooled condensers, multi-functional heat exchangers, cryogenics, combustion chambers and other applications requiring effective heat transfer characteristics (Mancin et al. [21]). Foams have similar properties to fibres that make them attractive to use in gas filters, heat exchangers, porous burners and catalyst supports, namely their mechanical strength, large specific surface areas and high porosities which lead to good chemical resistance, enhanced heat and mass transfer properties and low pressure drops (Inayat et al. [32]). Edouard et al. [15] noted that the specific surface area, denoted by S_v, is important for many industrial systems because it is responsible for the high performance and successful design of reactors. They stated that $S_v > 2000\,\mathrm{m}^{-1}$ for foam matrices, even at very low densities, and that compact heat exchangers generally require that $S_v > 700\,\mathrm{m}^{-1}$. Figure 1.2(a) and (b) show images of metal- and ceramic-based foams, respectively.

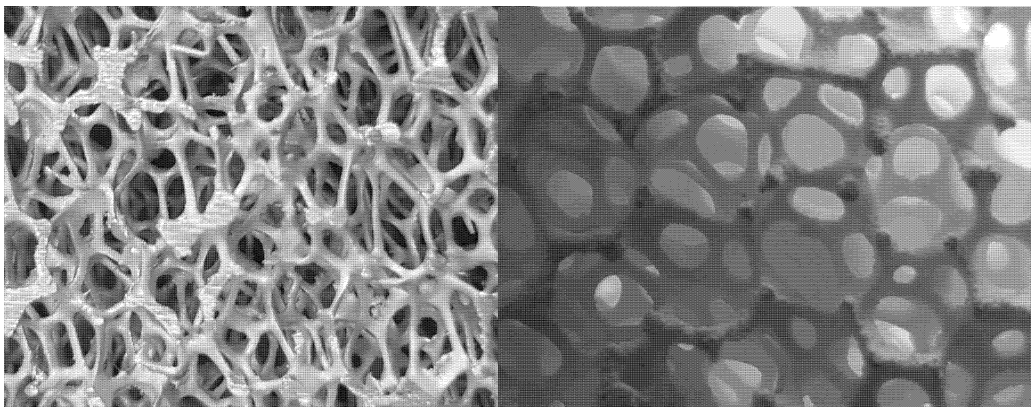

(a) *Metal foam* (b) *Ceramic foam*

FIGURE 1.2: *Examples of open-celled foams*

Some of the key parameters used to describe fibrous porous media throughout this study will be identified in the subsections that follow. These parameters include the permeability of both the Darcy and Forchheimer flow regimes, the specific surface area, porosity and strut, fibre, pore, face and cell diameters.

1.1.1 Permeability

In this study both the permeability coefficients of the Darcy and Forchheimer flow regimes, denoted by K and K_F, respectively, will be considered. The Darcy permeability (with unit m^2) is the measure of ease with which a fluid flows through a porous medium (Speight [33]) and can be determined by making use of Darcy's law (Dukhan [34]) where low Reynolds number flow is considered. The Forchheimer permeability (with unit m), also known as the passability (e.g. Gerbaux et al. [35], Woudberg [36]), or the reciprocal of the inertial coefficient, is calculated when higher laminar Reynolds number flow is considered. The most frequently used correlation between the permeability and the average pore-scale parameters of a porous medium is the Ergun equation (Ergun [37]). This equation is based on flow through granular media, although some authors in the literature have proposed different versions of the Ergun equation for other types of porous media, e.g. foams, as briefly summarized by Moreira and Coury [38]. Most of these versions, however, involve an empirical adjustment to the coefficients in the Ergun equation, as done by e.g. Dietrich

et al. [20].

Experimental studies of the permeability of porous media are most often performed by measuring the pressure drop of a fluid flowing through a porous medium and using the Darcy-Forchheimer equation to determine the permeability values, given by

$$\frac{\Delta p}{L} = \frac{\mu}{K} q + \frac{\rho}{K_F} q^2 , \tag{1.1}$$

where $\Delta p/L$ is the pressure gradient, μ is the dynamic viscosity of the fluid, ρ is the fluid density and q is the magnitude of the superficial velocity. In order to obtain the experimental data of K and K_F, using equation (1.1) and measured pressure drop data, some authors (e.g. Bhattacharya et al. [3] and Dietrich et al. [20]) perform a least squares fit directly on equation (1.1), as a parabolic function, in order to determine the coefficients of q and q^2. Other authors (e.g. Hunt and Tien [39]) first divide both sides of equation (1.1) by q and then perform a least squares fit on the resulting linear function to obtain the required coefficients. Antohe et al. [40] argued that the method of using a parabolic fit relies on extrapolation and therefore results in a higher error in the final results, whereas Bhattacharya et al. [3] stated that they found the difference in the results between the linear and quadratic fits to be negligible and preferred the parabolic method because of its convenience. For either method, the permeability coefficients are then obtained by setting the coefficient terms given in equation (1.1) equal to the corresponding coefficients of the linear or quadratic equations.

1.1.2 Specific surface area

The specific surface area is a measure of the total surface area of the fibrous medium per unit volume (m^{-1}) (Schaschke [41]). In other words, it is the fluid-dynamically relevant outer surface areas of the fibres or struts related to the volume of the fibrous medium, as stated by Grosse et al. [42], and can be presented as:

$$S_v = \frac{S_{fs}}{V_o} , \tag{1.2}$$

where S_{fs} is the total surface area of the fibrous medium presented to the flow and V_o is the total volume of the medium. In order to obtain experimental measurements of the specific surface area image analysis, also known as X-ray Computer Tomography (CT), and Magnetic Resonance Imaging (MRI) are used (Grosse et al. [42]). CT is where thin slices of each foam type are cut and analysed under magnification. In Figure 1.3 the set-up of how a foam can be analysed is shown, i.e. by placing it under a microscope that is connected to a computer. The measurements can then be performed with the aid of software.

1.1.3 Porosity

The porosity ϵ is the ratio between the volume available for fluid flow through the porous structure V_f and the total volume of the medium, thus it may be expressed as (Bird et al. [43]),

$$\epsilon = \frac{V_f}{V_o} , \tag{1.3}$$

FIGURE 1.3: *Foam analysis under magnification*

and since $V_o = V_f + V_s$, where V_s denotes the solid volume of the porous medium, the porosity can furthermore be written in the following form:

$$\epsilon = 1 - \frac{\rho_g}{\rho_s} \ , \tag{1.4}$$

where ρ_g is the apparent density and ρ_s is the strut density. Equation (1.4) is generally used in the literature for calculating the porosity, as stated by Edouard et al. [15], since the apparent density and strut density can be determined experimentally. The apparent density can be derived by using the weight and the volume of the fibrous medium, as discussed by Buciuman and Kraushaar-Czarnetzki [44] and Richardson et al. [45]. The strut density can be measured as done by Richardson et al. [45] using a Helium (He) multipycnometer, i.e. an instrument that uses He-displacement to measure the volume of solid materials. CT is also used to acquire measurements for porosity (Grosse et al. [42]), but another way is through mercury porosimetry in which a non-wetting fluid, such as mercury, is used to fill the porous medium and the porosity is determined from the measured mercury intrusion into the pores (Garrido et al. [19]).

1.1.4 Other measurable parameters

Other measurable parameters relevant to this study include the strut, fibre, pore, face and cell diameters, respectively. The strut diameter, denoted by d_s, (also known as the ligament diameter, as done by Mancin et al. [46]) is defined as the thickness in the middle of the strut. This is usually the thinnest part between the nodes of foams (Grosse et al. [42]). The strut diameter of a metal foam is indicated in Figure 1.4. For fibre-type materials the fibre diameter will be denoted by b. The pore diameter, denoted by d_p (or window or inner diameter) is the distance between two struts (Grosse et al. [42]), as shown in Figure 1.4 for a foam. The sizes of the pores of a foam vary significantly, therefore the pore diameter given is usually a statistically determined average obtained from a Guassian normal distribution of experimentally measured values (Garrido et al. [19]). There exist some studies regarding the definition and calculation of the pore diameters of

fibre-type materials (e.g. Mickel et al. [47], Huang et al. [48]). The average diameters of fibres tend to be constant with increase in the number of fibres, whereas the definition of pore diameters of fibre-type media in the literature is not consistent and is consequently difficult to measure (Huang et al. [48]). Due to the complexity of determining and defining the pore diameter of fibre-type materials, equations in this study will rather be provided in terms of the fibre diameter for models that represent this type of porous medium. The equations that will be proposed for the foam model will, however, generally be provided in terms of the pore diameter, due to experimental data in the literature being more readily available for the pore diameter of foam samples than the strut diameter. This generalization of the equations related to models that represent fibre-type and foamlike media loses its applicability when models with more complex geometries due to anisotropic adjustments are considered. Where equations predicting the properties of models with anisotropic adjustments are considered, more than one pore-scale dimension is required to calculate the required prediction. The face diameter, denoted by D_p, is defined as the sum of the average pore diameter and strut (or fibre) diameter, i.e. the average distance between opposite struts that form the boundaries of a pore, and can thus be represented by the following equation (Garrido et al. [19]):

$$D_p = d_p + d_s \ . \tag{1.5}$$

The cell diameter, denoted by d_c, is defined as the diameter of a foam cell, such that if the cell was represented by a sphere, the cell diameter would be equal to the sphere diameter.

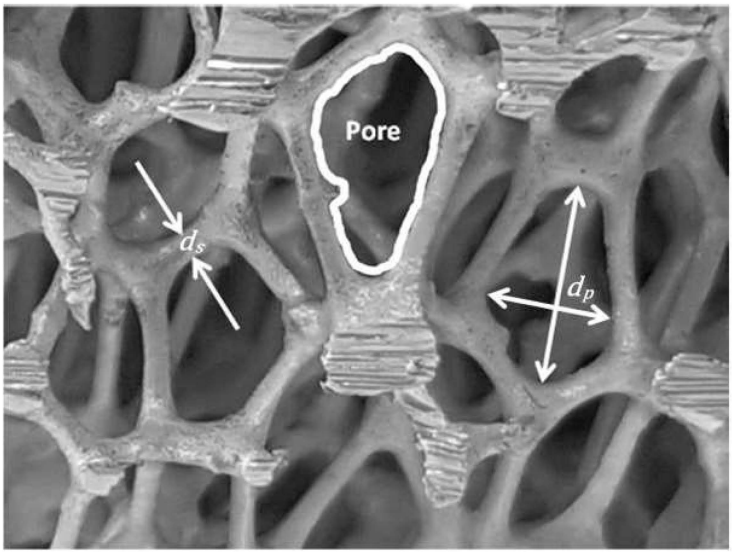

FIGURE 1.4: *Strut and pore diameters of a metal foam*

Experimental measurements of the pore and strut diameters discussed in the literature are mostly performed by CT, where the lengths of, for example, over a 100 of the windows and struts are measured under a microscope and then statistically evaluated. For the pore diameters, two orthogonal lengths are usually measured for each pore (as shown on the right-hand side in Figure 1.4) of which the average is calculated, as previously mentioned. Another technique used to acquire images to measure the dimensions of porous media is serial sectioning-imaging, where images of two dimensional cross-sections of the medium are combined to form a three-dimensional image. In Jaganathan et al. [10] a digital volumetric imaging instrument was used to measure dimensions by serial sectioning-imaging.

In the remainder of this study, the average strut, average fibre and average pore diameters obtained through experimental measurements will merely be referred to as the strut, fibre and pore diameters, respectively.

1.2 Representative Unit Cell modelling

The Representative Unit Cell (RUC) modelling approach was first presented by Du Plessis and Masliyah [49] for foamlike media and was further developed to account for granular and fibre porous media by Du Plessis and Masliyah [50], Du Plessis [51], Du Plessis and Van der Westhuizen [52], and Du Plessis [53]. In the RUC modelling approach, a Representative Elementary Volume (REV) of the porous medium is used, from which the average geometric characteristics of a porous medium are determined and incorporated into a rectangular RUC. That is, the rectangular solid struts or fibres represent the average solid geometry of the fibrous porous medium under consideration. The notation for some of the parameters will therefore differ slightly to those already mentioned and will be introduced for this model in this section. The geometric models obtained from this modelling approach will be the main focus of this study due to its simple rectangular geometry that can be adapted to accommodate changes to its morphological structure, such as compression, as well as its reported success in providing accurate model predictions for various porous media parameters.

Tamayol and Bahrami [54] identified three main categories of fibre-like media: fibres with one-dimensional (1D), two-dimensional (2D) and three-dimensional (3D) fibre arrangements. For unidirectional fibrous porous media, the 1D fibre arrangement is divided into flow parallel and perpendicular to the axes of the fibres. For fibres randomly distributed in a plane, the 2D layered fibre arrangement is divided into in-plane and through plane flow and the 3D arrangement describes fibres that are randomly distributed in space. Woudberg [55] presented 1D, 2D and 3D RUC models to represent fibre-like media accordingly. The three-strut (or foam) RUC model was furthermore developed by Crosnier et al. [56] and Woudberg and Du Plessis [14] and a two-strut RUC model was proposed by Van Heyningen [57]. The 2D and two-strut RUC models, as well as the 3D and three-strut RUC models, respectively resemble one another in structure, but different modelling approaches have been used to obtain the permeability coefficient predictions of these models. The two-strut and three-strut RUC model permeability coefficients were obtained by assuming double piece-wise parallel plate flow through the two and three duct sections of these models respectively, whereas the 2D and 3D RUC permeability coefficients were obtained by applying weights to the permeability expressions obtained from the 1D RUC model for transverse flow and the 1D RUC model for parallel flow. A schematic representation of all the RUC models mentioned above is shown in Figure 1.5.

In Figure 1.5(a) the 1D RUC model is shown and the direction of flow through the structure for transverse flow and parallel flow are both indicated. Transverse flow is regarded as flow perpendicular to the fibre axis and parallel flow is parallel to the fibre axis. The 2D (or two-strut) RUC model and its flow directions are shown in Figure 1.5(b), where in-plane flow is parallel to the plane formed by the two rectangular struts and through plane flow is perpendicular to this plane. Figure 1.5(c) shows the 3D (or three-strut) RUC model and consists of three rectangular struts that are mutually perpendicular. The struts represent the average geometry of the randomly distributed fibres in the case

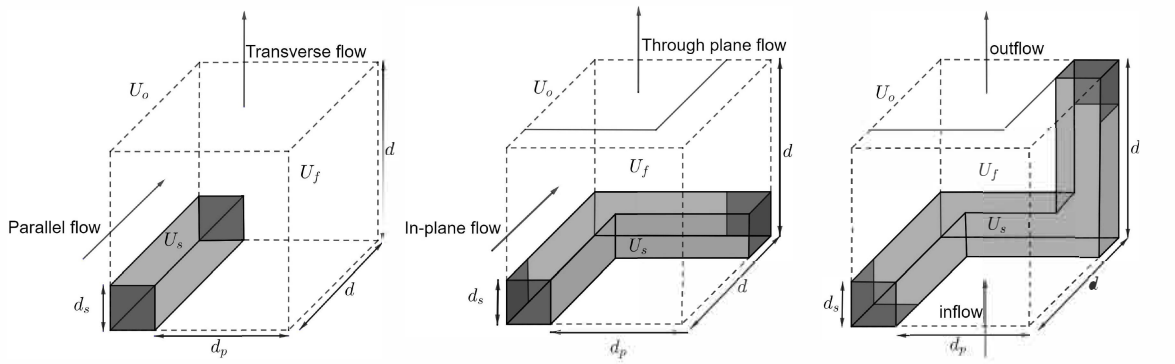

(a) *1D RUC model* (b) *2D (or two-strut) RUC model* (c) *3D (or three-strut) RUC model*

FIGURE 1.5: *RUC models*

of fibre materials and the average strut geometry of foam matrices in the case of foamlike media. Inflow through this RUC model is indicated in Figure 1.5(c), from where the flow will consecutively be directed into the two transverse directions after which it will flow outwards as indicated. The darker shaded areas on the struts in Figure 1.5 indicate where supposed 'latch areas' between struts of consecutive pores would be, i.e. areas that are not exposed to the fluid flow through the fibrous porous medium. In Figure 1.5 the parameters U_o, U_s and U_f represent the total volume, solid volume and fluid (or void) volume in RUC model notation, respectively. The face diameter of the RUC model is denoted by d, d_p once again denotes the pore diameter and the strut diameter d_s is defined such that $d_s^2 = \frac{\pi}{4}b^2$ for the 1D, 2D, two-strut and 3D RUC models, and $d_s^2 = b^2$ for the three-strut RUC model. The strut diameter is calculated in this manner due to the 1D, 2D, two-strut and 3D RUC models being used to geometrically represent fibre materials. In the literature fibres are usually approximated to be cylindrical in shape and the fibre diameter is therefore defined as the diameter of a circle. This is implemented as done by Woudberg [55] for the 2D and 3D RUC models, where the cross-sectional area of a rectangular strut, as shown in Figure 1.5, is set equal to the cross-sectional area of a cylindrical strut (i.e. the area of a square is set equal to the area of a circle with diameter b). The three-strut RUC model is generally used to represent foam materials, where strut diameters vary in shape and are not necessarily regarded as cylindrical. As a result of this b is therefore defined as the side-length of the square strut as represented in Figure 1.5(c) by d_s. The three-strut RUC model will, however, also be used in this study in a comparison involving fibre-type media in order to compare its performance with the 3D RUC model, but the same definition of the strut (or fibre) diameter will be maintained.

In RUC notation, the porosity is given by

$$\epsilon = \frac{U_f}{U_o}\,, \tag{1.6}$$

and another parameter used frequently, known as the geometric factor and denoted by ψ, is defined as

$$\psi = \frac{U_f}{U_{||} + U_t}\,, \tag{1.7}$$

where $U_{||}$ is the total streamwise fluid volume, i.e. the fluid volume that is parallel to the direction of the superficial velocity, and U_t is known as the transfer volume and represents the fluid volumes that are not bordered by solid surfaces (Woudberg and Du Plessis [14]).

In the RUC models where no stagnant fluid volumes are present, the geometric factor is equal to the geometric tortuosity of the model. The geometric tortuosity is generally defined as the winding path length available within the porous medium for flow under a constant cross-section to the macroscopic streamwise length scale of the porous medium structure (Ahmed et al. [7]).

The manner in which the pressure drop for the Darcy and Forchheimer regimes of the 1D, two- and three-strut RUC type models are determined will be shown next. The 1D RUC model will form the basis of the 2D and 3D RUC models. The pressure drop is required in order to determine expressions for the permeability coefficients of these models. The pressure drop equations are given by Woudberg and Du Plessis [14], who provided the derivation of a theoretical Ergun-type equation for the three-strut RUC model. The onset of determining such an equation for all the RUC models under consideration is the streamwise pressure gradient obtained by applying closure modelling to the volume averaged continuity and Navier-Stokes equations, which yields (Woudberg [36])

$$-\nabla\langle p\rangle = \frac{1}{U_o}\iint_{S_{fs}} (\underline{n}p - \underline{n}\cdot\underline{\underline{\tau}})\mathrm{d}S\,, \tag{1.8}$$

where $\langle p\rangle$ is the phase averaged pressure, S_{fs} is the total fluid-solid surface areas in the RUC, $\underline{n}$ is the unit vector that is directed inwardly and perpendicular to the fluid-solid surfaces and $\underline{\underline{\tau}}$ is the shear stress tensor. Considering the limit of low Reynolds number flow, as well as a uniform porosity, Woudberg [36] showed that from equation (1.8), the pressure gradient may be written as:

$$-\nabla\langle p\rangle_f = \frac{S_\parallel + \beta\xi S_\perp}{\epsilon U_o}\tau_{w_\parallel}\psi\underline{\hat{n}}\,, \tag{1.9}$$

where $\langle p\rangle_f$ denotes the intrinsic phase averaged pressure, $S_\parallel$ and $S_\perp$ are the solid surfaces parallel and perpendicular to the streamwise direction, respectively, $\tau_{w_\parallel}$ is the magnitude of the streamwise average wall shear stress and $\underline{\hat{n}}$ is the macroscopic direction of flow. The coefficient β is furthermore defined such that $\beta = w_\perp/w_\parallel = A_{p_\parallel}/A_{p_\perp}$ and the coefficient ξ is introduced to account for the reduced area of transverse surfaces subject to shear stresses in a fully staggered array containing volumes where flow is perpendicular to the streamwise direction. The average channel velocities in the transverse and streamwise directions are denoted by $w_\perp$ and $w_\parallel$, respectively. The cross-sectional flow area in the streamwise direction is furthermore represented by $A_{p_\parallel}$ and $A_{p_\perp}$ denotes the cross-sectional flow area in the transverse direction. The coefficient ξ is defined by Woudberg [36] for different transverse flux divisions and the values for $\beta\xi$ for the foam (or three-strut) and fibre (or 1D) RUC models were also provided. In this study the assumption that the RUC models are transversely isotropic will be adopted and a mathematical average will be calculated for the models that cannot be regarded as transversely isotropic (such as the 1D RUC models). The transversely isotropic RUC models will be referred to as 'isotropic' in the remainder of the study. The values assumed for the ξ coefficient depend on the assumption of staggeredness. The magnitude of the pressure drop can be determined from equation (1.9) and can also be written in the following form (Woudberg [36]):

$$\Delta p = \frac{S_\parallel\tau_{w_\parallel} + \xi S_\perp\tau_{w_\perp}}{A_{p_\parallel}}\,, \tag{1.10}$$

where $\tau_{w_\perp}$ is the magnitude of the transverse average wall shear stress. Equation (1.10) can be used to obtain the low Reynolds pressure drop number term of the type of porous

medium under consideration by applying the equation to the relevant RUC model. The average wall shear stress τ_w can be determined using the following formula:

$$\tau_w = \frac{12\mu v_{\text{avg}}}{D_h}\,, \tag{1.11}$$

where v_{avg} is the average channel velocity and D_h is the hydraulic diameter. The hydraulic diameter is equal to four times the cross-sectional area through which the fluid flows divided by the wetted perimeter (Bird et al. [43]). Plane Poiseuille flow is assumed for the RUC models and for most of the models, the distance between the parallel plates can easily be deduced from the schematic representations of the model. The hydraulic diameter is equal to two times the distance between the parallel plates for these RUC models and the formula for the wall shear stress for flow between parallel plates is consequently given by

$$\tau_w = \frac{6\mu v_{\text{avg}}}{B}\,, \tag{1.12}$$

where B is the distance between the parallel plates. The exception is the 1D RUC model for parallel flow, since the visualisation of the distance between the parallel plates is not as readily deduced. Equation (1.11) is therefore utilized for the calculation of the average wall shear stress for this model. For the RUC models the average channel velocity in the streamwise channels, $w_{\parallel}$, is determined using the following expression (Woudberg [36]):

$$w_{\parallel} = \frac{A_o}{A_{p_{\parallel}}}\, q\,, \tag{1.13}$$

and due to conservation of mass,

$$A_{p_{\parallel}} w_{\parallel} = A_{p_{\perp}} w_{\perp}\,, \tag{1.14}$$

from which the average channel velocity in the transverse direction, $w_{\perp}$, can be determined. In equation (1.13) A_o represents the total cross-sectional area in the streamwise direction and for the isotropic or cubic RUC models, $A_o = d^2$. Consequently, the permeability coefficient of the Darcy regime can be obtained for the relevant RUC model by utilizing equations (1.10) and (1.12) (or 1.11) and comparing the resulting pressure drop expression to the Darcy term in equation (1.1).

In the case where the higher Reynolds number limit is considered, that is for the steady laminar limit of the inertial flow regime, form drag predominates over viscous drag, such that the shear stress term is negligible. Thus equation (1.8) simplifies to (Woudberg [36])

$$-\nabla\langle p\rangle = \frac{1}{U_o}\iint_{S_{fs}} \underline{n} p \,\mathrm{d}S\,. \tag{1.15}$$

Equation (1.15) can then be simplified further by splitting the surface integral into surface integrals for upstream and downstream transverse surfaces and by furthermore assuming that the pressure is uniform on these surfaces. Consequently, equation (1.15) can then be expressed as

$$-\nabla\langle p\rangle = \frac{S_{\text{face}}}{U_o}\Delta p\, \underline{\hat{n}}\,, \tag{1.16}$$

where S_{face} is the cross-sectional solid area that faces upstream. The pressure drop Δp can be obtained by dividing the total drag force on a single submerged solid by the projected cross-sectional area of the solid, i.e. (Woudberg [36])

$$\Delta p = c_d \frac{\rho\, v_{\infty}^2}{2}\,, \tag{1.17}$$

where v_∞ is the approaching velocity from upstream, and c_d is the interstitial form drag coefficient with a value of $c_d = 2$ (Woudberg and Du Plessis [14]), which corresponds to that for flow past a single square rod and is thus used for the RUC models. Substitution of equation (1.17) into equation (1.16), along with the assumption that the approaching velocity is equal to the streamwise average channel velocity (Woudberg [36]), leads to

$$-\nabla\langle p\rangle = \frac{S_{\text{face}}}{U_o}\,\rho\, w_\parallel^2\,\underline{\hat{n}}\,, \tag{1.18}$$

and in terms of the intrinsic phase average pressure

$$-\nabla\langle p\rangle_f = \frac{S_{\text{face}}}{\epsilon U_o}\,\rho\, w_\parallel^2\,\underline{\hat{n}}\,. \tag{1.19}$$

Equation (1.19) may be used to determine the expression for the Forchheimer permeability coefficient of the relevant RUC model after comparing the resulting pressure drop expression to the Forchheimer term in equation (1.1).

Finally,

$$S_v = \frac{S_{fs}}{U_o}\,, \tag{1.20}$$

which is the specific surface area equation in RUC notation. Two approaches for determining the specific surface area of the RUC models will be considered in this study: the geometric approach and the combined kinetic-geometric approach. The geometric approach requires equation (1.20) and the geometry of the RUC model under consideration. The specific surface area is then determined as a function of the porosity and a geometric linear dimension such as the strut or pore diameter (or more than one pore-scale dimension in the case of the anisotropically adjusted models). The combined approach entails incorporating the permeability expression (in terms of, for example, the porosity and a geometric linear dimension such as the strut diameter) with the expression obtained for the specific surface area using the geometric approach in order to determine an equation for the specific surface area in terms of the porosity and a permeability coefficient (either Darcy or Forchheimer).

1.3 Models and data from the literature

In this section different empirical and analytical models representing fibrous porous media will be discussed, along with experimental and numerical data acquired from fibre- and foam like materials, obtained from the literature. These models and data sets will be used in this study for comparison and evaluation purposes of the RUC models. It should be noted that although most of the analytical models obtained from the literature that are used in this study are discussed in this section, some models obtained from the literature with special adjustments will be added throughout the study in later chapters. In line with this, not all the data sets utilized in this study are provided in this section.

1.3.1 Fibre models

There are numerous models that predict the Darcy permeability of fibre structures and a few authors have also compared some of these models to one another and experimental

data (e.g. Jackson and James [8], Tamayol and Bahrami [58] and Zhang et al. [59]). As already mentioned, Tamayol and Bahrami [54] identified three main categories of fibre-like media: fibres with 1D, 2D and 3D fibre arrangements, respectively. A few of these models, primarily for 2D and 3D flow, available in the literature will be utilised in this study for comparative analysis.

Tomadakis and Robertson [60] determined an expression for predicting the Darcy permeability of 2D and 3D fibre media by employing electrical conduction principles. The dimensionless Darcy is given by

$$\frac{K}{a^2} = \frac{\epsilon}{8\ln\epsilon^2}\frac{(\epsilon-\epsilon_p)^{\alpha+2}}{(1-\epsilon_p)^{\alpha}\left[(\alpha+1)\epsilon-\epsilon_p\right]^2}, \tag{1.21}$$

where a denotes the fibre radius, ϵ_p denotes the percolation porosity threshold and α a constant. For 2D in-plane flow, $\epsilon_p = 0.11$ and $\alpha = 0.521$, for 2D through plane flow, $\epsilon_p = 0.11$ and $\alpha = 0.785$ and for 3D flow $\epsilon_p = 0.037$ and $\alpha = 0.661$. Van Doormal and Pharoah [61] presented simulated correlations for 2D in-plane and through plane Darcy permeabilities of fibre-type media, given by

$$\frac{K}{a^2} = 0.26\frac{\epsilon^{3.6}}{1-\epsilon}, \tag{1.22}$$

and

$$\frac{K}{a^2} = 0.28\frac{\epsilon^{4.3}}{1-\epsilon}, \tag{1.23}$$

respectively in dimensionless form. Tamayol and Bahrami [54] studied the transverse Darcy permeability of fibre-type media, both theoretically and experimentally, providing equations for unidirectional aligned fibres for different arrays, 2D mats and cubic structures (i.e. 1D, 2D and 3D fibre arrangements, respectively). The expression for the dimensionless Darcy permeability of the 2D fibre media is given by

$$\frac{K}{b^2} = 0.008\sqrt{\epsilon}\left[\left(\frac{\pi}{4(1-\epsilon)}\right)^2 - 2\frac{\pi}{4(1-\epsilon)} + 1\right], \tag{1.24}$$

and the expression for the 3D fibre media is

$$\frac{K}{b^2} = 0.08\frac{(H-b)^4}{H^2 b^2 \epsilon^{0.3}}, \tag{1.25}$$

where the ratio of H and b can be calculated from

$$\epsilon = 1 - \frac{3\pi}{4}\frac{b^2}{H^2} + \sqrt{2}\frac{b^3}{H^3}, \tag{1.26}$$

with b denoting the fibre diameter of the fibre-type media considered, as with the RUC models, such that $b = 2a$. In all the equations provided by Tamayol and Bahrami [54], they used the solid volume fraction instead of porosity. In equations (1.24) to (1.26) the solid volume fractions are replaced with $1-\epsilon$ for consistency purposes in this study. Very few studies on the Forchheimer permeability coefficient for fibre-type media were found in the literature. Tamayol et al. [62] presented numerical correlations for different fibre arrangements for flow within the Forchheimer flow regime but provided these correlations in terms of only numerically obtained constants and the porosity. Due to the correlations

not being provided in terms of the fibre radius or diameter, it could therefore not be used for comparison purposes in this study. Reference to the specific surface area of fibres together with experimental measurements thereof are provided by Sullivan [63]. No equations for predicting the specific surface area of fibre-type media could however be found in the literature.

1.3.2 Foam models

Equations for predicting the permeability of foamlike materials are available in the literature and such equations, acquired from Dietrich et al. [20] and Giani et al. [64], will specifically be used for comparison purposes in this study. Dietrich et al. [20] provided experimental results for the pressure drop of different ceramic foams and furthermore used the results to obtain coefficients for an Ergun-type equation. They provided correlations between the permeability coefficients and the hydraulic diameter. Dietrich et al. [20] furthermore presented the specific surface area in terms of the hydraulic diameter and provided an expression for the specific surface area proposed by Buciuman and Kraushaar-Czarnetzki [44]. From all the information provided, the permeability coefficients could be determined in this study in terms of the porosity. The resulting permeability coefficients, dimensionalized with the pore diameter, are given by

$$\frac{K}{d_p^2} = 0.018\frac{\epsilon^3}{\sqrt{1-\epsilon}}\left(1-\sqrt{\frac{1-\epsilon}{2.59}}\right)^{-2}, \tag{1.27}$$

and

$$\frac{K_F}{d_p} = 0.96\frac{\epsilon^3}{(1-\epsilon)^{0.25}}\left(1-\sqrt{\frac{1-\epsilon}{2.59}}\right)^{-1}. \tag{1.28}$$

Giani et al. [64] investigated the pressure drop and mass-transfer properties of metallic foams. They determined an expression for the pressure drop in terms of the porosity and pore diameter, for both the Darcy and Forchheimer flow regimes. Only the Forchheimer permeability coefficient will be given in this study and utilised due to the Darcy permeability coefficient yielding predictions that are different in trend than most other predictions for the Darcy permeability. The dimensionless Forchheimer permeability coefficient is given by

$$\frac{K_F}{d_p} = 2.30\left(1-\sqrt{\frac{4}{3\pi}(1-\epsilon)}\right)^4. \tag{1.29}$$

A few authors in the literature have provided expressions for the prediction of the specific surface area of foamlike porous media. The visual representation of the foam models used are shown in Figure 1.6. A summary of the expressions for the specific surface area obtained using these foam models will be given (as also provided by Maré [65]).

A cubic lattice in staggered alignment representing the foam structure was first proposed by Gibson and Ashby [66]. The cubic unit cell model, shown in Figure 1.6(a), was proposed by Lu et al. [67], who investigated the use of open-celled foams in heat transfer applications. Giani et al. [64] also used the cubic unit cell (CUC) model to study the mass-transfer properties of open-celled foams. They presented expressions for the specific surface area in terms of the pore diameter d_p and the strut diameter d_s, based on the

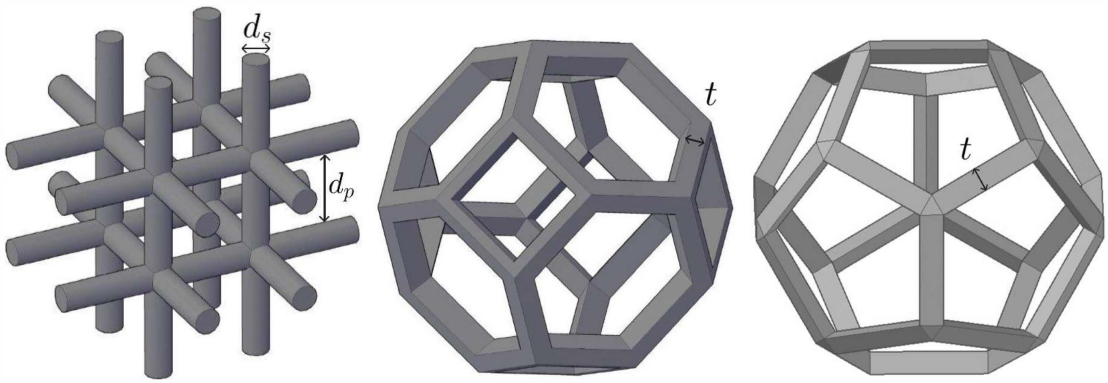

(a) *Cubic unit cell model* (b) *Tetrakaidecahedron model* (c) *Dodecahedron model*

FIGURE 1.6: *Isotropic geometric models for foamlike porous media*

CUC model geometry. The latter two linear dimensions are indicated in Figure 1.6(a). The resulting expressions are given by

$$S_v = \frac{2}{d_p}\sqrt{3\pi(1-\epsilon)}\,, \tag{1.30}$$

and

$$S_v = \frac{4}{d_s}(1-\epsilon)\,. \tag{1.31}$$

Lacroix et al. [68] conducted a study to obtain the pressure drop for SiC foams by also utilising the CUC geometry. They investigated the pressure drop predictions using an Ergun-type equation and merely made use of the model geometry to determine the specific surface area in order to find correlations (among other parameters) necessary for the pressure drop predictions. Lacroix et al. [68] also presented equation (1.31) to predict the specific surface area using the CUC. Based on work done by Lacroix et al. [68], an approach for determining the specific surface area in terms of the pore diameter is considered, where the total volume of a unit cell is given by $(d_p + d_s)^3$, as opposed to the approach based on the work of Gaini et al. [64], who defined the total volume as d_p^3. The resulting expression obtained is:

$$S_v = \frac{2}{d_p}\left[\sqrt{3\pi(1-\epsilon)} - 2(1-\epsilon)\right]\,. \tag{1.32}$$

A schematic representation of the tetrakaidecahedron model is shown in Figure 1.6(b). A packing of tetrakaidecahedra structure was first described by Lord Kelvin (Thomas [69]) and was then used to describe the morphology of foams because of the similarity between the Kelvin cell and the cells of actual foams (Grosse et al. [42]). This model resembles a truncated octahedron, having eight hexagonal faces and six square faces (Buciuman and Kraushaar-Czarnetzki [44]). The struts are furthermore triangular prisms with the edge width of the strut being t, as indicated in Figure 1.6(b), and not cylinders as in the case of the cubic unit cell model. Gibson and Ashby [66] considered different polyhedra in which the structures of foams could be modelled and concluded that the tetrakaidecahedron yielded the most consistent agreement with observed properties. Some geometric relationships were furthermore derived by Gibson and Ashby [66] for the tetrakaidecahedron unit cell. These results were also used by Richardson et al. [45], who studied and

measured the pressure drop of flow through ceramic foams and derived a specific surface area equation from the tetrakaidecahedron model. The expression they determined for the specific surface area in terms of the pore diameter is given by

$$S_v = \frac{12.979}{d_p}\sqrt{1-\epsilon}\left(1 - 0.971\sqrt{1-\epsilon}\right) . \tag{1.33}$$

It was however noted by Maré [65] that the coefficient in equation (1.33) i.e., 12.979, should be 5.621 and that it is possible that there was a mistake made in the calculation of the coefficient in the expression of Richardson et al. [45]. Buciuman and Kraushaar-Czarnetzki [44] also made use of the tetrakaidecahedron model. They presented the expressions for the specific surface area in terms of the face diameter, which is the sum of the strut and pore diameters. Using the geometry of the unit cell of the tetrakaidecahedron model, as defined by Buciuman and Kraushaar-Czarnetzki [44], an expression for the specific surface area in terms of the pore diameter was determined by Maré [65] and is given by

$$S_v = \frac{4.82\sqrt{1-\epsilon} - 2.99(1-\epsilon)}{d_p} . \tag{1.34}$$

Inayat et al. [32] investigated specific surface area predictions based on various model geometries and compared it to experimental data. The model geometries which they considered were the CUC model, the dodecahedron model and the tetrakaidecahedron model. They determined that the tetrakaidecahedron geometry was the most suitable model for describing foam structures and also made adjustments to the strut geometry of the model in order to accommodate the changes in strut morphologies at different porosities. Huu et al. [5] modelled solid foams using a geometric approach involving the pentagonal dodecahedron due to the dodecahedron structure having such a close resemblance to a foam cell. Huu et al. [5] differentiated between the dodecahedron model with triangular struts for high porosities ($\epsilon > 0.9$) and the dodecahedron model with cylindrical struts for lower porosities ($\epsilon < 0.9$). They furthermore made a distinction between "slim" and "fat" struts, where "slim" struts have triangular nodes (where the struts connect) and "fat" struts are more rounded at the edges of the nodes. In Figure 1.6(c), a schematic representation of the dodecahedron model with triangular "slim" strut geometry is shown, where t is the triangular edge width, similar to that of the tetrakaidecahedron model. For the dodecahedron with cylindrical struts, d_s denotes the diameter of the cylinders. Huu et al. [5] furthermore provided expressions for the specific surface area from which predictions in terms of the pore diameter could be deduced. Only the equations for the "slim" dodecahedron model will be shown in this section since the "fat" dodecahedron model is classified in this study as a foam model with adjusted nodes to accommodate the solid volumes present at strut intersections in some foams. The "fat" dodecahedron model will therefore be discussed in a subsequent chapter. The expression for the specific surface area of the dodecahedron model with triangular "slim" struts is given by

$$S_v = \frac{60\, r_{ts}}{\sqrt{5}\,\phi^3\sqrt{3-\phi}\, d_p}\left(1 - \frac{1}{2}\sqrt{\frac{2}{3}}\, r_{ts}\right)^2 , \tag{1.35}$$

where r_{ts}, with 'ts' referring to triangular "slim" struts, can be determined from the following expression:

$$-\frac{\sqrt{10}}{3\phi^4} r_{ts}^3 + \frac{\sqrt{15}}{\phi^4} r_{ts}^2 - (1-\epsilon) = 0 . \tag{1.36}$$

Similarly, the specific surface area of the dodecahedron model with cylindrical "slim" struts can be expressed as

$$S_v = \frac{20\pi\, r_{cs}}{\sqrt{5}\,\phi^3\sqrt{3-\phi}\,d_p}\left(1-\frac{1}{2}\sqrt{\frac{2}{3}}\,r_{cs}\right)^2, \tag{1.37}$$

where r_{cs} can be determined from the following expression:

$$\left(\frac{\sqrt{10}}{6\phi^4}-\frac{\sqrt{5}\pi}{2\phi^4}\sqrt{\frac{2}{3}}\right)r_{cs}^3+\frac{\sqrt{5}\pi}{\phi^4}r_{cs}^2-(1-\epsilon)=0\,, \tag{1.38}$$

with 'cs' referring to cylindrical "slim" struts. In equations (1.35) to (1.38) ϕ denotes the golden ratio, equal to the value of $\left(1+\sqrt{5}\right)/2$.

Another model available in the literature, introduced by Phelan et al. [70], is known as the Weaire-Phelan structure. The unit cell of this structure consists of a combination of six tetrakaidecahedra and two dodecahedra with pentagonal and hexagonal faces chosen in such a way as to fit together. Grosse et al. [42] provided an expression for the specific surface area using the Weaire-Phelan structure. The results of their evaluation of the model, however, revealed that the model over-predicted their measured data and the other models represented by cubic lattice or tetrakaidecahedra structures. They consequently provided an empirically adjusted equation for the specific surface area, based on the expression obtained using the Weaire-Phelan structure. Due to the complexity and non-uniformity of this model, as well as the unsatisfactory performance, this model is not included in this study.

1.3.3 Experimental data

This section gives experimental data obtained from the literature, that will be used for validation purposes in this study. Data sets containing the values for the porosity, Darcy and Forchheimer permeability, specific surface area and fibre or pore diameter (for fibre-type media or foam-type media, respectively) are required altogether for the validation purposes of this study, since most of the model equations will be given in terms of these parameters. In some cases where no other means were available, the pores per linear inch (PPI) number was used to obtain the pore diameter in order to complete the data set.

Kim et al. [16]:

The impact that metal fin, which is a piece of metal foam used to increase the heat transfer area, has on the pressure drop of heat exchangers was investigated by Kim et al. [16].

TABLE 1.1: *Experimental data obtained from Kim et al. [16] for metal fin*

ϵ	$d_p\,[\mu\text{m}]$	$K \times 10^9\,[\text{m}^2]$	$S_v\,[\text{m}^{-1}]$
0.89	1270	89.6	2020
0.92	2540	236	790
0.92	1270	107	1720
0.92	635	71.5	2740
0.94	1270	130	1510
0.96	1270	116	1240

The measured values acquired from the experimental data provided by Kim et al. [16] is listed in Table 1.1.

Bhattacharya et al. [3]:

Bhattacharya et al. [3] conducted a study on the thermophysical properties of metal foams, i.e. the thermal conductivity, Darcy permeability and inertia coefficient. From their pressure drop measurements, they provided experimental data from which the Darcy and Forchheimer permeability coefficients could be obtained and are presented in Table 1.2.

TABLE 1.2: *Experimental data obtained from Bhattacharya et al. [3] for metal foams*

ϵ	$d_p\,[\mu\text{m}]$	$K \times 10^9\,[\text{m}^2]$	$K_F \times 10^3\,[\text{m}]$
0.8991	3200	94	4.51
0.9005	2580	90	3.41
0.905	3800	174	5.35
0.906	2600	85.4	3.44
0.909	2960	111	4.06
0.9118	3800	180	4.99
0.9132	1800	53	2.74
0.9138	3280	110	4.74
0.9245	2900	110	3.19
0.9272	2020	61	2.78
0.937	2000	56.8	2.65
0.946	3900	217	4.71
0.9486	3130	120	3.57
0.949	3100	149	3.90
0.949	2700	118.5	3.44
0.952	1980	56.2	2.43
0.9546	2700	130	3.88
0.9659	1900	55	2.32
0.971	4000	252	5.23
0.972	1800	52	2.43
0.9726	4020	270	5.36
0.978	2800	142	4.33

Bhattacharya et al. [3] also noted that the metal foam samples they used had accumulation of solid present at the strut intersections.

Gostick et al. [17]:

Gostick et al. [17] measured the Darcy permeability of gas flow through common gas diffusion layer (GDL) materials at different porosities. They conducted the measurements in three perpendicular directions to investigate anisotropic properties and tabulated the Darcy permeability values obtained for through plane flow. Porosity values and fibre diameters for all the samples were furthermore provided. The data obtained from Gostick et al. [17] is listed in Table 1.3.

TABLE 1.3: *Experimental data obtained from Gostick et al. [17] for GDL materials*

ϵ	$b\,[\mu\text{m}]$	$K \times 10^9\,[\text{m}^2]$
0.78	9.9	0.0694
0.80	9.2	0.00899
0.81	8.0	0.0145
0.84	7.6	0.0163
0.85	7.4	0.00570
0.88	9.2	0.0374

Only the through plane Darcy permeability data was tabulated by Gostick et al. [17] and therefore the data in Table 1.3 can only be used in this study for evaluation purposes of through plane flow through fibres.

Topin et al. [18]:

Topin et al. [18] conducted an experimental analysis on metal foams. They provided experimental values for the porosity, pore diameter, Darcy permeability and specific surface area. The air inertia coefficient for allied nickel foams and one for copper foams were also provided. All the corresponding data values utilized in this study are presented in Table 1.4.

TABLE 1.4: *Experimental data obtained from Topin et al. [18] for metal foams*

ϵ	$d_p\,[\mu\text{m}]$	$K \times 10^9\,[\text{m}^2]$	$K_F \times 10^3\,[\text{m}]$	$S_v\,[\text{m}^{-1}]$
0.87	569	2.13	0.7519	5303
0.88	1840	28.1	2.04	1658
0.89	2452	60.2	2.62	1295
0.91	831	4.44	0.9302	3614
0.92	4055	81.7	4.98	758

The inertia coefficient is the reciprocal of the Forchheimer permeability coefficient, as previously mentioned. The values of the inertia coefficient could therefore be used to obtain the Forchheimer permeability data in Table 1.4.

Dukhan [9]:

Dukhan [9] investigated different correlations of the pressure drop for flow through aluminium foam samples in which they considered both their own experimental data and predictions obtained elsewhere in the literature.

TABLE 1.5: *Experimental data obtained from Dukhan [9] for aluminium foams*

ϵ	d_p [μm]	$K \times 10^9$ [m^2]	$K_F \times 10^3$ [m]	S_v [m^{-1}]
0.915	2540	80	37000	0.00081
0.919	2540	100	48000	0.00079
0.919	1270	63	34000	0.0013
0.923	635	47	26000	0.0018
0.924	1270	54	36000	0.0012

All the experimental data of Dukhan [9] relevant to this study are listed in Table 1.5.

Garrido et al. [19]:

Garrido et al. [19] investigated mass transfer and pressure drop properties of open-cell foams. They made use of specific surface area predictions obtained from both the CUC and the tetrakaidecahedron models in order to determine mass transfer coefficients and obtained experimental specific surface area values to furthermore compare it to the model predictions. The experimental specific surface area data was obtained using MRI. Darcy and Forchheimer permeability data for different porosity values, along with the pore diameter values, were also provided by Garrido et al. [19] for ceramic foams. The porosity values were acquired using mercury porosimetry and the pore diameters were obtained through image analysis. All the relevant data gathered from Garrido et al. [19] is listed in Table 1.6.

TABLE 1.6: *Experimental data obtained from Garrido et al. [19] for ceramic-based foams*

ϵ	d_p [μm]	$K \times 10^9$ [m^2]	$K_F \times 10^3$ [m]	S_v [m^{-1}]
0.777	1069	6.74	1.36	1290.3
0.804	1192	9.17	1.67	1187.0
0.813	666	6.23	1.49	1884.3
0.816	871	7.23	1.45	1437.8
0.818	1933	28.59	3.13	675.4
0.848	687	9.95	1.83	1816.3
0.852	2252	39.5	5.94	629.3
0.852	861	11.07	1.89	1422.4
0.858	1131	14.66	1.98	1109.1

The data in Table 1.6 consists of all the required parameters needed for evaluation purposes of foamlike materials in this study.

Dietrich et al. [20]:

Dietrich et al. [20] presented experimental results of pressure drop measurements for various porosity and pore sizes of ceramic-type foams, as previously mentioned in Section 1.3.2, which they used to obtain coefficients for an Ergun-type equation. Both the Darcy and Forchheimer permeability coefficients were therefore provided. Dietrich et al. [20] used the weight and density of the foams to determine the porosities, light microscopy to determine the window diameters, which is synonym to the pore diameter, and MRI measurements to determine the specific surface area values.

TABLE 1.7: *Experimental data obtained from Dietrich et al. [20] for ceramic-based foams*

Foam sample	ϵ	d_p [μm]	$K \times 10^9$ [m^2]	$K_F \times 10^3$ [m]	S_v [m^{-1}]
Alumina	0.754	1529	130	0.88	1090
	0.808	2253	77	1.87	664
	0.802	1091	54	1.14	1204
	0.806	884	32	0.98	1402
	0.809	625	20	0.76	1884
	0.854	1464	144	1.80	1109
Mullite	78.9	1405	88	1.22	1291
	0.793	1127	45	1.02	1395
	0.797	685	29	0.66	2126

They performed these measurements on three types of ceramic foams, i.e. Alumina, Mullite and OBSiC, of which only the former two samples had a complete data set and of which the values are given in Table 1.7.

Mancin et al. [21]:

Mancin et al. [21] investigated six different aluminium open-cell foam samples by experimentally measuring the pressure drop of air flow through the foams.

TABLE 1.8: *Experimental data obtained from Mancin et al. [21] for aluminium foams*

ϵ	d_p [μm]	$K \times 10^9$ [m^2]	$K_F \times 10^3$ [m]
0.903	2540	190	5.88
0.921	5080	236	4.88
0.930	635	63.4	2.92
0.932	1270	82.4	4.42
0.934	2540	187	5.26
0.956	2540	182	4.17

Table 1.8 lists the porosity, pore diameter and permeability data obtained from Mancin et al. [21].

Mancin et al. [22]:

Copper foams and their heat transfer and pressure drop properties were the focus of the study of Mancin et al. [22]. They provided values for the specific surface area which they obtained from the manufacturers of the copper foams, as well as the Darcy permeability coefficient and drag coefficient (again defined as the inertia coefficient in this study) measurements, obtained from their own pressure drop experiments.

TABLE 1.9: *Experimental data obtained from Mancin et al. [22] for copper foams*

ϵ	d_p [μm]	$K \times 10^9$ [m^2]	$K_F \times 10^3$ [m]	S_v [m^{-1}]
0.905	2540	121	6.21	831
0.933	5080	97	6.10	299
0.933	2540	209	5.03	698
0.933	1270	41	5.18	1148
0.934	635	44	3.50	1635

The permeability and specific surface area data for given porosity and pore diameter values acquired from the data given by Mancin et al. [22], is consequently presented in Table 1.9.

Kumar et al. [71]:

Kumar et al. [71] also studied the thermophysical properties of metal foams, but more specifically, metal foams casted as Kelvin cells, i.e. a periodic and isotropic mesh of tetrakaidecahedron cells. They furthermore provided measured morphological data for the specific surface area, as listed in Table 1.10.

TABLE 1.10: *Experimental data obtained from Kumar et al. [16] for open-cell Kelvin metal foam*

ϵ	d_p [μm]	S_v [m^{-1}]
0.825	6800	370.9
0.84	6800	357.4
0.845	9900	263.9
0.85	10200	252.2

Kumar et al. [71] also noted and studied the effect of the change in strut shape and solid accumulation at the strut intersections of the foam samples.

Manzo et al. [23]:

Manzo et al. [23] compared the properties of stainless steel fibres with those of glass fibres, as well as the coalescence performance of the fibre-type media, and provided the porosity and Darcy permeability data, amongst other measurements.

TABLE 1.11: *Experimental data obtained from Manzo et al. [23] for stainless steel and glass fibres*

fibre-type	ϵ	$b\,[\mu\text{m}]$	$K \times 10^9\,[\text{m}^2]$
Stainless steel fibres	0.986	6.5	2.76
	0.988	2	0.282
Glass fibres	0.963	6	0.323
	0.965	2	0.102

Table 1.11 lists the data of Manzo et al. [23] that will be utilized in this study.

Théron et al. [24]:

Woudberg et al. [72] utilized data for the Darcy permeability obtained from cotton and polyester fibre materials, as well as stainless steel fibres, of which the experimental characterization of the former two fibre materials is detailed by Théron et al. [24]. Woudberg et al. [72] provided the fibre diameters of the media, which was obtained by picture treatment of scanning electron microscopy observations, and the mean porosity which was obtained using mercury porosimetry. They furthermore provided the experimental Darcy permeability data obtained from pressure drop measurements, with the aid of permeametry. The data acquired is presented in Table 1.12.

TABLE 1.12: *Experimental data obtained from Théron et al. [24] for cotton and polyester fibres*

ϵ	$b\,[\mu\text{m}]$	$K \times 10^9\,[\text{m}^2]$
0.85	24.0	0.823
0.92	13.8	2.02

Woudberg et al. [72] provided the data of three fibre samples where only the cotton and polyester fibre sample data will be considered, and is presented in Table 1.12, due to the other stainless steel sample being obtained from Manzo et al. [23], which was already discussed and given in this section.

1.3.4 Numerical data

Similar to the previous section, numerical data obtained from the literature is presented in this section for the use of the validation of models considered in this study that represent fibrous porous media. The manner in which the numerical data sets will be presented is similar to that of Section 1.3.3.

Higdon and Ford [25]:

Higdon and Ford [25] analysed viscous flow through 3D models of fibre-type media. They computed and presented numerical solutions for the resistance force and permeability of fibre-type media, based on cubic lattice models. They provided data for the tangential and normal force per unit length for different solid volume fraction values, as well as an

expression for the correlation between the dimensionless Darcy permeability and these force values. The expression relating the force and permeability is given as follows:

$$\text{Dimensionless force} = \frac{\pi}{1-\epsilon}\left(\frac{a^2}{K}\right) . \tag{1.39}$$

The dimensionless Darcy permeability for parallel and transverse flow can therefore be determined using the resistance force per unit length data and equation (1.39). The permeability acquired from the tangential force is the permeability parallel to the fibre orientation and the permeability acquired from the normal force is the permeability perpendicular to the fibre orientation, similarly as the parallel and transverse flow introduced for the 1D RUC model. The numerical data obtained from Higdon and Ford [25] was therefore utilized in the same manner as done by Woudberg [55], who applied the unweighted resistivity mixing rule in order to obtain the permeability for 2D in-plane and through plane flow, as well as for the 3D fibre arrangement.

TABLE 1.13: *Numerical data obtained from Higdon and Ford [25] for cylindrical fibres*

ϵ	K/b^2 []		
	2D In-plane	2D Through plane	3D
0.2500	2.8242×10^{-4}	1.7803×10^{-4}	2.3625×10^{-4}
0.3000	6.0806×10^{-4}	4.0505×10^{-4}	5.2102×10^{-4}
0.4000	0.0020	0.0015	0.0018
0.5000	0.0056	0.0041	0.0050
0.6000	0.0142	0.0106	0.0127
0.7000	0.0361	0.0270	0.0325
0.8000	0.1024	0.0769	0.0922
0.9000	0.4167	0.3125	0.3750
0.9500	1.3307	0.9980	1.1976
0.9900	13.0313	9.7735	11.7282
0.9990	225.4947	169.1211	202.9453
0.9999	3.2136×10^{3}	2.4099×10^{3}	2.8921×10^{3}

The data acquired from the study of Higdon and Ford is listed in Table 1.13. Only the data provided for the hexagonal lattice was considered in this study due to the assumption that the hexagonal array is similar to the fully staggered array of the RUC model (as was assumed in the study of Woudberg [55]).

Fotovati et al. [26]:

Fotovati et al. [26] studied the effects of dust loading on the pressure drop of pleated filters. They used expressions for the in-plane and through plane Darcy permeability, along with an expression used to obtain the Darcy permeability of a 3D fibre structure, all proposed by Spielman and Goren [73]. The information obtained from these expressions was used to simulate the pressure drop across the pleated media under investigation.

TABLE 1.14: *Numerical data obtained from Fotovati et al. [26] for pleated filters*

ϵ	$b\,[\mu\text{m}]$	$K \times 10^9\,[\text{m}^2]$		
		2D In-plane	2D Through plane	3D
0.9	6	0.0278	0.0151	0.0225
0.925	10	0.122	0.0710	0.101
0.96	15	0.692	0.440	0.588

They provided permeability coefficients for in-plane, through plane and isotropic fibre-type arrangements and the relevant data is listed in Table 1.14.

1.4 Objectives and proposed contributions

The first objective of this study is to summarize the work done in Maré [65] in the respective and relevant chapters as introduction to continue the investigation of the RUC models. This includes summaries of the two- and three-strut RUC models and adjustments made to account for compression as well as for the Klinkenberg effect, specifically to the predictive equations for the permeability and specific surface area. Some of the results obtained from Maré [65] is furthermore included as simplified or case specific scenarios of the RUC models presented in this study. Another objective of this study is to investigate the fibre RUC models available in the literature. Firstly, a comparison between the 2D, 3D, two-strut and three-strut RUC models is conducted, and an evaluation of which models would suit fibre-like media and which would suit foam-like media is also included with regards to permeability and specific surface area predictions. The 2D and 3D RUC models were specifically introduced in order to represent layered fibre arrangements and fibres distributed randomly in space, respectively, as previously mentioned, and the three-strut RUC model was introduced to represent foams. The two-strut RUC model was also applied to fibres by Van Heyningen [57].

The study of the fibre and foam RUC models will be continued by adapting the models to account for the effect of anisotropy introduced by compression and the Klinkenberg effect and resulting predictions will also be compared to experimental data, where available. Incorporating the Klinkenberg effect entails the analytical relation of the permeabilities for gas flow to the permeability for liquid flow and results in the additional expression of the permeabilities in terms of the Knudsen number and a parameter that accounts for the reduction in the momentum of gas molecules colliding with the pore wall. The subject matter of the streamwise compression of soft fibrous media was addressed in Maré [65], specifically for the three-strut and two-strut through plane flow RUC models, and will be continued in this study by adjusting the two-strut RUC model for in-plane flow accordingly. The study of compression of the three-strut and two-strut RUC models will furthermore be extended to provide equations that incorporate both streamwise and transverse compression on either fibrous material with hard (uncompressible) or with soft (compressible) struts, which are all novel contributions. A special case will also be included where the predictions of the RUC models account for media that resemble a rectangular-type geometry rather than cubic or isotropic geometry. The objective is therefore to adapt the RUC geometry and adjust the mathematical modelling procedure accordingly in order to portray the correct relationship between the porosity and pore-scale linear

dimensions as a result of compression or presence of rectangular geometry. The RUC models adapted to account for these structure transformations will also be included in models accounting for the Klinkenberg effect, along with the uncompressed RUC models. Models of fibrous media accounting for both compression and the Klinkenberg effect is another novel contribution of this study.

There are extensive studies on permeability predictions of fibre-type porous media, but less studies on the specific surface area predictions. As previously mentioned, no models predicting the specific surface area of fibre media could be found in the literature other than the specific surface area prediction of the two-strut RUC model for through plane flow presented by Maré [65]. There are, however, literature sources that contain experimental data and reference to the use of the specific surface area of fibres (e.g. Sullivan [63], Huang et al. [48], Nava et al. [74], Zeng et al. [75]), even though the data sets are not sufficient for comparison purposes in this study. Therefore, such models predicting the specific surface area of fibre media will also be introduced in this study using the RUC modelling approach in order to fill this gap. The predictions of the 2D RUC model for both through plane and in-plane flow, the 3D RUC model and the two-strut RUC model for in-plane flow are all novel contributions. It is furthermore noticed that specific surface area predictions often depend on parameters such as the strut and pore diameters. Dietrich et al. [20] presented an Ergun-type equation for foams in terms of the hydraulic diameter in order to provide a simple method for determining hydraulic diameters for foams from pressure drop measurements, even with unknown geometric parameters, such as the strut and pore diameters. In a similar manner, the specific surface area will be related to permeability values in this study in order to provide a method of determining the specific surface area of fibrous media from pressure drop measurements with unknown strut and pore diameter values. A comparison between two different approaches in obtaining the specific surface area of the RUC models will therefore be conducted where the one approach makes use of the pore-scale parameters, such as pore and strut diameters, and the other makes use of permeability predictions obtained from either the Darcy or the Forchheimer flow regimes. These are the geometric and combined approaches, respectively, mentioned in Section 1.2.

The combined approach involving the three-strut model, presented in Maré and Woudberg [76], and the combined approach involving the two-strut model for through plane flow have already been addressed in Maré [65]. The aforementioned model approaches are developed further and expanded upon in this study by including effects of compression and the Klinkenberg effect and is published in Woudberg et al. [77]. The permeability coefficients, obtained for both the Darcy and Forchheimer flow regimes, of each of the RUC models considered in this study will be provided. All the permeability coefficients obtained from flow in the Darcy regime for these models are available elsewhere in the literature, with the exception of the two-strut RUC model for in-plane flow, but the Forchheimer permeability coefficients of the 2D, 3D and two-strut RUC models (for both in-plane and through plane flow) will be newly proposed equations and adds novelty to this study. The two-strut RUC model for in-plane flow is a new model proposed in this study and has not been provided elsewhere in the literature. Therefore, any predicting equations obtained from this model are novel contributions. Another objective is to propose a weighted average method for determining the Forchheimer permeability coefficients of the 2D and 3D RUC models from the Forchheimer permeability coefficients predicted by the 1D RUC model. Comparison of the permeability predictions of all the proposed RUC models with one another, as well as with data obtained from the literature for the permeability,

furthermore adds to the objective of determining the most suitable and accurate RUC model predictions for the different media types. Since there is a lack of models and data for the specific surface area of fibre materials this (i.e. proposing the most suitable model) will only be possible by using the 3D and three-strut RUC models, together with data for foamlike media, when predicting the specific surface area. Experimental data for the specific surface area for fibre materials were found in the literature, but other corresponding parameters such as the permeability and pore or fibre diameters were not provided and therefore the data could not be used for validation purposes of the models under consideration. A detailed comparative analysis of the 2D and 3D RUC modelling approaches to that of the two-strut and three-strut approaches provides further novelty to this study. The predictive equations for the permeability and specific surface area of the RUC models, along with the accompanying comparative analysis and resulting findings, were furthermore published by Maré and Woudberg [78].

Garrido et al. [19] observed an overestimation of the specific surface area predicted by the CUC and tetrakaidecahedron models, and also mentioned that the overestimation could be due to the assumption of constant thickness of struts in the geometric models, whereas ceramic foams tend to have accumulation of solid material around the nodes. With regards to the foam RUC model (i.e. the three-strut RUC model), an investigation will be conducted in order to introduce a change in the geometry of the model to account for these solid lumps that are often found in foamlike materials at the intersection of struts. The objective is to discuss different foam models in the literature that account for the additional solid material and propose a few options of adjusting the three-strut RUC model. The results of the adjusted RUC model will be compared to the models obtained from the literature, along with experimental data for the permeability and specific surface area. The objective of this part of the study is to create and identify an adjusted three-strut RUC model that provides the most accurate prediction for the permeability and specific surface area and thus proves to be an improvement to the performance of the foam RUC model. This will be the final novel contribution by the author.

1.5 Overview

In this section the overview of this dissertation is presented per chapter.

Chapter 1: (*Current chapter.*) In this chapter an overview is given of fibrous porous media characteristics, models and data, as well as its usefulness and importance, in general. This includes a review of existing models and experimental and numerical data obtained from the literature. A brief history of the RUC model, which is a main focus in the present study, and the modelling process of the model is provided. Both the history of the RUC model and the summary of available models of fibrous porous media in the literature, in this chapter, are published as an introduction in Maré and Woudberg [78]. These sections of the chapter have the purpose of providing a background to this study and will be referred to throughout the dissertation. The objectives and contributions by the author forms part of this chapter, along with publications that resulted from it.

Chapter 2: The topic of uncompressed RUC models that represent fibre-type and foamlike media are addressed in this chapter. The RUC models in this chapter have no geometrical or modelling adjustments included and most of the models have already been presented in the literature, the only addition to the RUC modelling theory being the

two-strut RUC model for in-plane flow. The RUC models presented are the 1D RUC model (for parallel and transverse flow), the 2D RUC model (for in-plane and through plane flow), the 3D RUC model, the two-strut RUC model (for in-plane and through plane flow) and the three-strut RUC model. A description of the difference between the low and high porosity three-strut RUC models is also provided. For each of the RUC models, the permeability coefficients for both the Darcy and Forchheimer regime and the specific surface area are provided. Some of these calculations are present elsewhere in the literature, where-as those that are novel are clearly identified. The permeability and specific surface area predictions of the models are, respectively, compared to one another, as well as to the models obtained from the literature and data provided in Chapter 1. The equations for the permeability and specific surface area of the RUC models and concluding results in this chapter were published in Maré and Woudberg [78].

Chapter 3: In this chapter the effect of additional solid lumps at the strut intersections of foams, otherwise known as the nodes of the foams, on the permeability and specific surface area are investigated. Models in the literature that represent foams and have solid lumps at nodes incorporated are discussed and specific surface area and/or permeability predictions of these models are presented, where not already provided by the literature sources. Two options of three-strut RUC models, adjusted to account for the additional lumps, are also presented. Ratios relating the pore and node dimensions are necessary for the model calculations and different model combinations in order to obtain these relations, are explored. The results of the various node adjusted RUC models and ratio combinations are compared to the models discussed in this chapter, as well as to experimental data provided in Chapter 1. The preferred node adjusted RUC model, based on performance from the comparison, is identified. Work presented in this chapter was submitted to an international journal with reference Maré and Woudberg [79].

Chapter 4: The fibre and foam RUC models are adapted to account for compression or any square to rectangular transformation. The models are furthermore adjusted in such a manner that either compression in the streamwise direction or compression perpendicular to the streamwise direction can be applied to the models. The method of adjusting the model geometries is presented and implemented on all the two-strut and three-strut RUC models considered in Chapter 2. Relationships between the pore-scale dimensions and porosity, as well as expressions for the Darcy permeability coefficient, Forchheimer permeability coefficient and specific surface area (obtained using both the geometric and combined approach), of the compression adjusted RUC models are also presented in this chapter. A section is dedicated to explaining the manner in which the models can be applied to different compression scenarios, i.e. whether streamwise or transverse compression is applied, whether the medium has hard or soft struts and whether the medium is allowed to expand laterally or not during compression. In order to account for soft fibrous media that deform under compression, the strut diameter of the soft struts undergoes compression with compression of the porous medium. Where the struts do not deform in such a manner, it is referred to as being hard. There is also a section in this chapter addressing the calculation of the compression factor-porosity relationship. The resulting permeability and specific surface area expressions of the compression (or rectangular) adjusted RUC models are compared to available experimental data provided in this chapter. A special scenario of the streamwise two-strut RUC model for through plane flow and three-strut RUC model is furthermore included which is published in Woudberg et al. [77]. The compression adjusted three-strut RUC model presented in this chapter

and its application and comparison to the data acquired from Dukhan [9] was presented at the 12th International Conference on Porous Metals and Metallic Foams in Dresden, Germany, from 5 - 7 July 2023. A peer reviewed paper is yet to be published in the conference proceedings with reference Maré and Woudberg [80].

Chapter 5: This chapter deals with the incorporation of the Klinkenberg effect into the RUC modelling process. The conditions under which the Klinkenberg effect becomes relevant are discussed. The equations for predicting the Darcy permeability of all the 2D, 3D, two-strut and three-strut RUC models obtained from Chapters 2 to 4 are consequently adjusted to account for the gas slippage effect, where applicable. Some resulting predictions of the RUC models in which the Klinkenberg effect is incorporated are compared to experimental data provided in this chapter.

Chapter 6: This chapter provides the concluding remarks to this study.

Figure 1.7 shows a visual diagram of the RUC models and model adaptations addressed in each chapter.

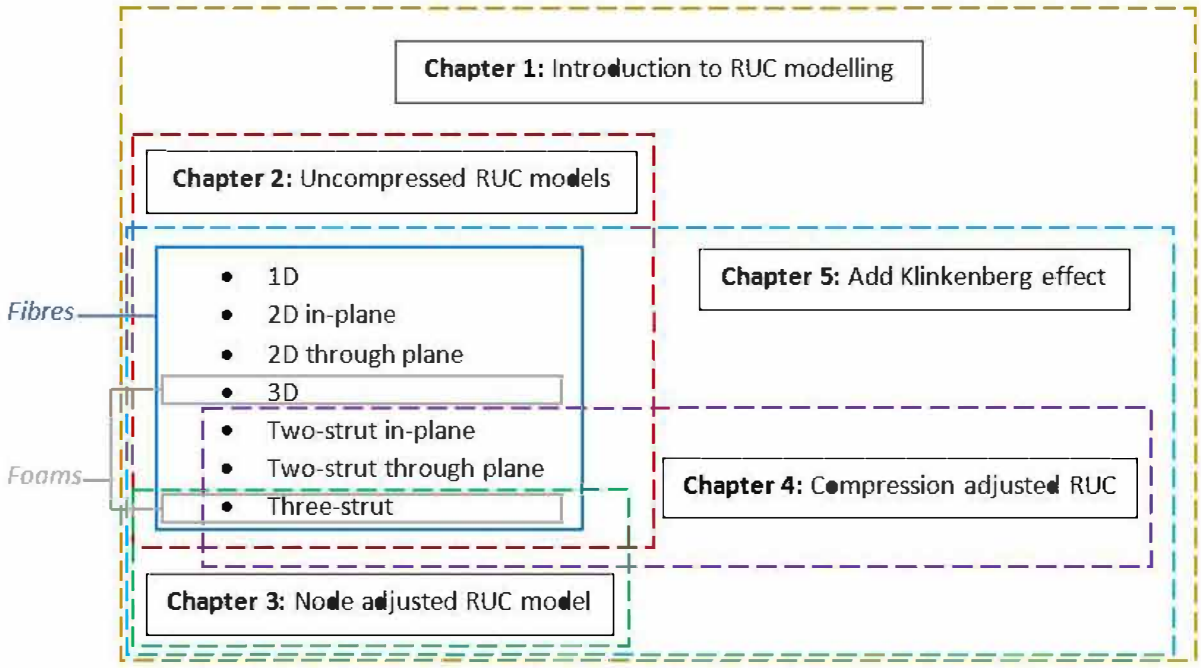

FIGURE 1.7: *Overview of RUC models and model adaptations used in this study to predict the permeability and specific surface area of fibrous porous media*

The type of RUC models adapted in each of the chapters are included in the respective blocks in Figure 1.7, e.g. Chapter 3 contains only the three-strut RUC model and adjustments made to this type of RUC model. The type of media each of the RUC models present, i.e. fibres or foams, are also indicated. Fibres are therefore presented using all the RUC model types addressed in this study, whereas foams are only represented by the 3D and three-strut RUC models.

1.6 Outputs

Some of the results of Chapters 4 and 5 have been published in the international Powder Technology journal in collaboration with the group of Laurence le Coq at IMT Atlantique in Nantes, France, with reference:

> Woudberg, S., **Maré, E.**, Van Heyningen, M.C., Theron, F. and Le Coq, L. (2021), Predicting the permeability and specific surface area of compressed and uncompressed fibrous media including the Klinkenberg effect, *Powder Technology*, vol. 377, pp. 488-505. (Impact factor: 5.64.)

Some of the results of Chapter 2 have been published in the international Transport in Porous Media journal, with reference:

> **Maré, E.**, Woudberg, S. (2023), A Comparative Study of Geometric Models for Predicting Permeability Coefficients and Specific Surface Areas of Fibrous Porous Media, *Transport in Porous Media*, vol. 148, no. 2, pp. 383-416. (Impact factor: 3.61.)

Results obtained in Chapter 3 have been submitted to an international journal, with reference:

> **Maré, E.**, Woudberg, S. (2023), Geometric models for incorporating solid accumulation at the nodes of open-cell foams, (submitted to international journal).

The results obtained for the adjusted three-strut RUC model presented in Chapter 4 was presented at the 12th International Conference on Porous Metals and Metallic Foams and is under review to be published in the conference proceedings, with reference:

> **Maré, E.**, Woudberg, S. (2023), Analytical determination of the geometrical properties of metal foams under compression, *Proceedings of the 12th International Conference on Porous Metals and Metallic Foams*, Metfoam 2023, Dresden Radebeul, Germany, 7-9 July 2023, (submitted/under publication).

CHAPTER 2

Uncompressed fibre and foam RUC models

This chapter deals with the RUC models available in the literature that represent fibre-type and foamlike materials. These include the 1D, 2D, 3D, two-strut and three-strut RUC models. The aim is to present equations for predicting the permeability and specific surface area obtained from each of the RUC models considered, for all the respective flow directions discussed in Section 1.2. All the equations are given in terms of the porosity and one other fibrous media parameter. The relations between the RUC model dimensions for each of the RUC models are also provided which allows for the easy conversion of dimension parameter used in the equations presented. In general, the models representing fibre-type media are given in terms of b and the models representing foamlike media are given in terms of d_p. The method in which the Ergun-type equation for each of the RUC models are determined from equations (1.10) and (1.19) will be included, which then leads to the determining of the permeability coefficients of the Darcy and Forchheimer flow regimes, as mentioned in Section 1.2. Geometric and combined approaches are furthermore used and shown to calculate the expressions for the specific surface area of each RUC model, where the former utilizes equation (1.20) and the latter combines the equations obtained for the specific surface area based on the geometric approach and permeability to acquire the specific surface area in terms of the permeability coefficient, as explained in Section 1.2. Finally, the models obtained in the literature for fibrous porous media, along with the experimental and numerical data for the media under consideration, provided in Section 1.3, will be compared to one another and to the relevant RUC models. Only the 2D, 3D, two-strut and three-strut RUC models will be considered for evaluation purposes due to these RUC models resembling actual fibrous media more closely than the 1D models. The 2D, 3D, two-strut and three-strut RUC models will be considered for the representation of fibre-type media and the 3D and three-strut RUC models will be considered for the representation of foamlike media. The RUC models are evaluated against one another in order to determine the models that perform most accurately for each type of fibrous porous media, when compared to the models and data considered in this study that are given in Section 1.3. The model equations and evaluations of the 2D, 3D, two-strut and three-strut RUC models provided in this chapter are furthermore published in Maré and Woudberg [78].

2.1 1D RUC model

It was already mentioned in Chapter 1 that the basis of the 2D and 3D RUC models is the 1D RUC model. The permeability coefficients for the 2D and 3D RUC models are determined from the "mixing rule", which results from a combination of the 1D RUC models for transverse and parallel flow. This is the reason for including the 1D RUC model in this chapter. For the sake of completeness, the specific surface area equations will be included in this section, but will not be evaluated in a subsequent section. A visual representation of the 1D RUC model is shown in Figure 1.5(a), where both the transverse (i.e. perpendicular to strut orientation) and parallel flow directions are indicated. The 1D RUC models with the different flow directions are once again shown in Figure 2.1 for easy reference. (It is noted that in Figure 2.1, and in the figures throughout the rest of the study, the "flow direction" indicated in the figure refers to the macroscopic streamwise flow direction.)

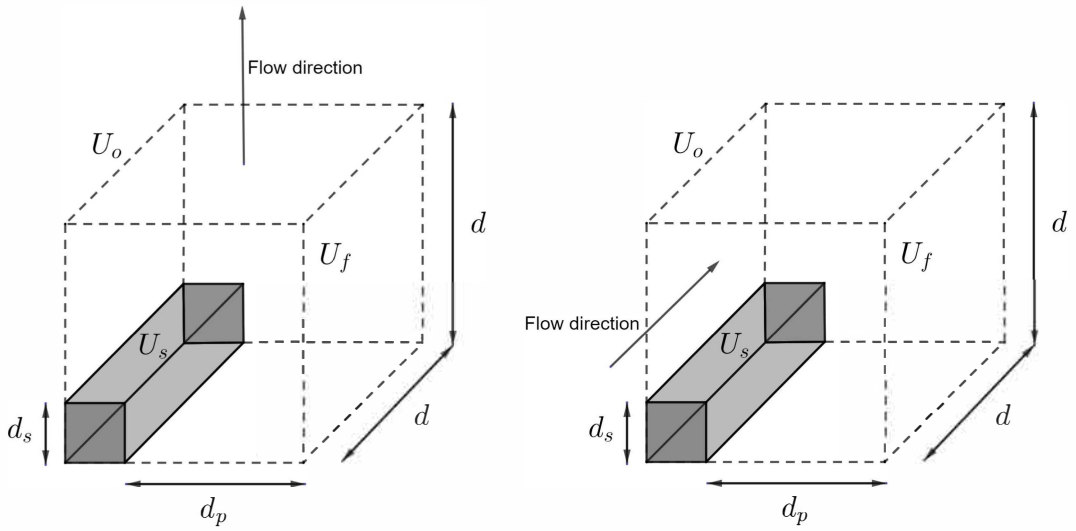

(a) *Transverse flow* (b) *Parallel flow*

FIGURE 2.1: *1D RUC models*

The direction of flow influences the resulting pressure drop equations obtained. The calculation of the permeability and specific surface area will be discussed in the next subsection.

2.1.1 Model dimension relations

The porosity of the 1D RUC model can be calculated using equation (1.6) and Figure 1.5(a) (or Figure 2.1), which produces the following expression:

$$\epsilon = \frac{U_o - U_s}{U_o} = 1 - \frac{d_s^2}{d^2}. \tag{2.1}$$

From equation (2.1) the relation between the strut and face diameters can be determined, resulting in

$$d_s = \sqrt{1-\epsilon}\, d. \tag{2.2}$$

The relations between the strut and pore diameters as well as between the face and pore diameters are as follows:

$$d_s = \frac{\sqrt{1-\epsilon}}{1-\sqrt{1-\epsilon}}\, d_p\,, \tag{2.3}$$

and

$$d = \frac{1}{1-\sqrt{1-\epsilon}}\, d_p\,. \tag{2.4}$$

Furthermore, recall from Chapter 1 that $d_s^2 = \frac{\pi}{4} b^2$ for the 1D, 2D and 3D RUC models. The relations between the fibre diameter b and the face and pore diameters are therefore given by:

$$b = \frac{2}{\sqrt{\pi}}\sqrt{1-\epsilon}\, d \qquad \text{and} \qquad b = \frac{2}{\sqrt{\pi}}\frac{\sqrt{1-\epsilon}}{1-\sqrt{1-\epsilon}}\, d_p\,. \tag{2.5}$$

Due to the dependency of the permeability of the 2D and 3D RUC models on the 1D RUC model, the relations between the dimensions of all these models are the same, i.e. equations (2.2) to (2.5) apply to the 1D RUC model and to the permeability equations of the 2D and 3D RUC models. Similar equations to equations (2.2) to (2.4) can be found in Woudberg [36] and equation (2.2) can also be found in Woudberg [55]. It is noted that the 1D RUC model provided in Woudberg [55] is different when compared to the 1D RUC model shown in this chapter in that the dimension L is made equal to d in the current study. The 1D RUC is therefore cubic whereas in Woudberg [55] it is a rectangular prism.

2.1.2 Permeability prediction

The Ergun-type equation for the 1D RUC models, for both transverse and parallel flow, will be calculated in this section from which the Darcy and Forchheimer permeability coefficients will be determined. The section representing Darcy flow leading up to the calculation of the Darcy permeability coefficient is also found in Woudberg [55]. The 1D RUC model is considered as a representation of fibre-type media and the final equations will therefore be presented in terms of b.

1D RUC model: Transverse flow

The 1D RUC model for transverse flow will be investigated first. It is important to reiterate the assumption of transverse isotropy of RUC models in this study. The 1D RUC is not transversely isotropic and therefore a mathematical average will be calculated between the fully staggered array and the regular array for this model. Extensive descriptions of the different arrays of the RUC models are beyond the scope of this study but can be sourced in Woudberg [36]. The fully staggered and regular arrays are characterized by the $\beta\xi$ coefficient. For the fully staggered array $\beta\xi = 1/4$ ($\beta = 1/2$ and $\xi = 1/2$) and for the regular array $\beta\xi = 0$ ($\beta = 0$ and $\xi = 0$ because $U_\perp = 0$). In the low Reynolds number flow regime, equation (1.10) will be utilised to obtain the pressure drop in the Darcy regime of the 1D RUC model for transverse flow. The streamwise and transverse surface areas of the 1D RUC model for transverse flow are shown in Figure 2.2.

Although the surface areas can be determined from Figure 1.5(a), the reason for including Figure 2.2 is to illustrate the manner in which the surface areas will be displayed throughout the study making it convenient for when the surface partitioning of the RUC

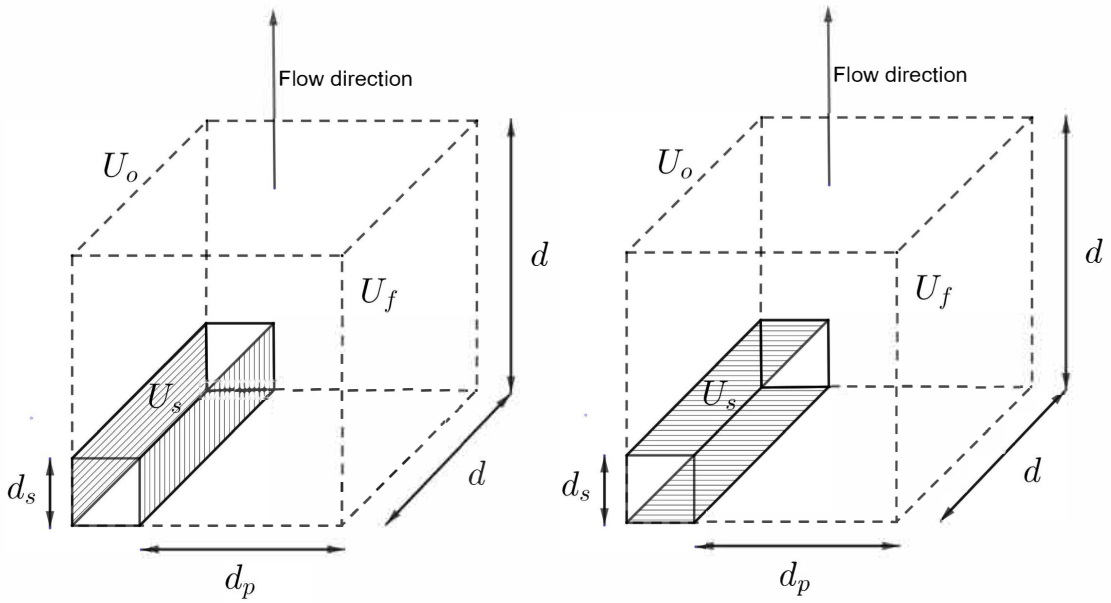

(a) $S_{\parallel}$ (b) $S_{\perp}$

FIGURE 2.2: *Solid surfaces of 1D RUC model for transverse flow*

models become more intricate. The areas of the strut that are not included in either Figure 2.2(a) or (b) are once again the representation of the 'latch areas', as defined for Figure 1.5 in Section 1.2. The $S_{\parallel}$ and $S_{\perp}$ surface areas can consequently be determined using Figure 2.2 and results in the following expressions:

$$S_{\parallel} = S_{\perp} = 2d_s d\,. \tag{2.6}$$

The streamwise cross-sectional flow area is furthermore given by

$$A_{p_{\parallel}} = d_p d\,, \tag{2.7}$$

and utilizing equations (1.12) and (1.13) leads to

$$\tau_{w_{\parallel}} = \frac{6d}{d_p^2}\mu q\,, \tag{2.8}$$

with $v_{\text{avg}} = w_{\parallel}$ and $B = d_p$ (the distance between the parallel plates formed by the streamwise surfaces of solid fibres of two adjacent RUCs). The pressure gradient for the fully staggered array model can consequently be determined by substituting equations (2.6) to (2.8) into equation (1.10), where $\tau_{w_{\perp}} = \beta\tau_{w_{\parallel}}$ and the values for β and ξ are the values provided for the 1D fully staggered array RUC model, yielding:

$$\frac{\Delta p}{d} = \frac{15d_s}{d_p^3}\mu q\,. \tag{2.9}$$

In the case of the regular array, the coefficient of 15 in equation (2.9) is replaced by 12 when the same calculations are performed as in the case of the fully staggered array, except that the relevant β and ξ values for the regular array are used, resulting in

$$\frac{\Delta p}{d} = \frac{12d_s}{d_p^3}\mu q\,. \tag{2.10}$$

Consequently, for the implementation of the transversely isotropic assumption, the average of equations (2.9) and (2.10) are utilized in this study, leading to:

$$\frac{\Delta p}{d} = \frac{13.5 d_s}{d_p^3}\,\mu q\,. \tag{2.11}$$

Equation (2.11) can furthermore be expressed in terms of b by using the relevant relations for the linear dimensions provided in Section 2.1.1, yielding

$$\frac{\Delta p}{d} = \frac{4(13.5)(1-\epsilon)^{3/2}}{\pi b^2\left(1-\sqrt{1-\epsilon}\right)^3}\,\mu q\,. \tag{2.12}$$

Next, the pressure gradient of the Forchheimer flow regime can be determined by utilizing equation (1.19). For all the uncompressed RUC models U_o is given by d^3 and the manner in which $w_{\parallel}$ is determined was discussed in Section 1.2 (resulting in $w_{\parallel} = (d/d_p)\,q$). The cross-sectional solid area facing upstream can be determined from Figure 1.5(a), and results in

$$S_{\text{face}} = d_s d\,. \tag{2.13}$$

Therefore, the pressure gradient of the Forchheimer flow regime, in terms of b, leads to

$$-\nabla\langle p\rangle_f = \frac{2(1-\epsilon)}{\sqrt{\pi} b\epsilon\left(1-\sqrt{1-\epsilon}\right)^2}\,\rho q^2 \underline{\hat{n}}\,. \tag{2.14}$$

Combining equations (2.12) and (2.14), the Ergun-type equation for the 1D RUC model for transverse flow is given by

$$\frac{\Delta p}{d} = \frac{4(13.5)(1-\epsilon)^{3/2}}{\pi b^2\left(1-\sqrt{1-\epsilon}\right)^3}\,\mu q + \frac{2(1-\epsilon)}{\sqrt{\pi} b\epsilon\left(1-\sqrt{1-\epsilon}\right)^2}\,\rho q^2\,, \tag{2.15}$$

from which the following permeability coefficients can be deduced when setting equation (2.15) equal to equation (1.1) with $d = L$:

$$K = b^2\,\frac{\pi\left(1-\sqrt{1-\epsilon}\right)^3}{4(13.5)(1-\epsilon)^{3/2}}\,, \tag{2.16}$$

and

$$K_F = b\,\frac{\sqrt{\pi}\epsilon\left(1-\sqrt{1-\epsilon}\right)^2}{2(1-\epsilon)}\,. \tag{2.17}$$

The Ergun-type equation, and consequently the permeability coefficients, for the 1D RUC model for parallel flow will be investigated next.

1D RUC model: Parallel flow

In the case of the 1D RUC model for parallel flow, there are no distinctive arrays and furthermore, $U_{\perp} = 0$. Consequently, $\xi = 0$. There is thus no transverse flow, which furthermore results in $S_{\perp} = 0$. The only classified non-zero surface area is therefore $S_{\parallel}$ and is shown in Figure 2.3.

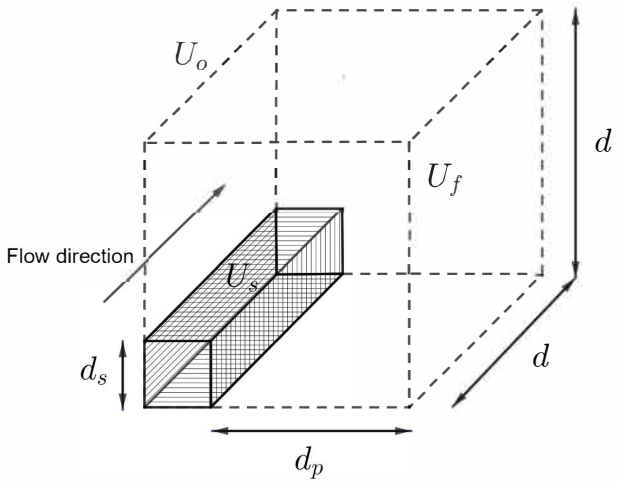

FIGURE 2.3: *Solid surfaces of 1D RUC model for parallel flow*

Utilizing Figure 2.3, $S_{\parallel}$ is determined, yielding

$$S_{\parallel} = 4d_s d\,, \tag{2.18}$$

and it is furthermore deduced that

$$A_{p_{\parallel}} = d^2 - d_s^2\,. \tag{2.19}$$

For the 1D RUC model for parallel flow, equation (1.11) will be utilized to obtain the average wall shear stress. The hydraulic diameter is determined by applying its definition to the 1D RUC model for parallel flow as follows:

$$D_h = \frac{4A_{p_{\parallel}}}{\text{wetted perimeter}} = \frac{4\left(d^2 - d_s^2\right)}{4d_s} = \frac{d^2 - d_s^2}{d_s}\,. \tag{2.20}$$

The result obtained in equation (2.20) is the same as in Woudberg [55]. The average streamwise velocity is also determined by substituting equation (2.19) into equation (1.13) and consequently, substituting the result along with equation (2.20) into equation (1.11) (with $v_{\text{avg}} = w_{\parallel}$), which leads to the streamwise average wall shear stress:

$$\tau_{w_{\parallel}} = \frac{12d_s d^2}{\left(d^2 - d_s^2\right)^2}\,\mu q\,. \tag{2.21}$$

The pressure gradient for flow in the Darcy regime predicted by the 1D RUC model for parallel flow can thereupon be determined in terms of b by substituting equations (2.18), (2.19) and (2.21), along with the relevant relations between the linear dimensions provided in Section 2.1.1 and $S_{\perp} = 0$, into equation (1.10), which yields

$$\frac{\Delta p}{d} = \frac{192(1-\epsilon)^2}{\pi b^2 \epsilon^3}\mu q\,. \tag{2.22}$$

The pressure drop for the Forchhiemer regime of the 1D RUC model for parallel flow is regarded as non-existent since in this regime inertial drag effects dominate which specifically requires flow past an obstacle. There is no obstruction in the flow for flow parallel to the strut in the 1D RUC model and therefore no local flow recirculation will occur on the

lee side of the solid strut at higher average flow velocities. The Ergun-type equation for the 1D RUC model for parallel flow is therefore also given by equation (2.22), the Darcy permeability coefficient is thus given by the following equation:

$$K = b^2 \frac{\pi \epsilon^3}{192(1-\epsilon)^2}\,, \tag{2.23}$$

and no expression for K_F for this model is consequently provided.

The specific surface area obtained using a geometric approach will be shown next for the 1D RUC model.

2.1.3 Specific surface area prediction: Geometric approach

The specific surface area determined using a geometric approach is not dependent on the direction of flow and therefore the resulting expression obtained applies to both the 1D RUC model for transverse and parallel flow. The total surface area is given by the sum of $S_{\parallel}$ and $S_{\perp}$ (as given by equation (2.6)) for the 1D RUC model for transverse flow and the sum of equation (2.18) and $S_{\perp} = 0$ for the 1D RUC model for parallel flow. The total surface area is consequently given by

$$S_{fs} = 4 d_s d\,. \tag{2.24}$$

Substituting equation (2.24), along with $U_o = d^3$, into equation (1.20) and utilizing the relevant relations for the linear dimensions provided in Section 2.1.1, the specific surface area can be expressed as follows:

$$S_v = \frac{8(1-\epsilon)}{\sqrt{\pi} b}\,. \tag{2.25}$$

The specific surface area determined using a combined approach, by utilizing the equations obtained in Sections 2.1.2 and 2.1.3, is addressed in the next subsection.

2.1.4 Specific surface area prediction: Combined approach

The implementation of the combined approach for determining the specific surface area requires the respective permeability and specific surface area expressions, in terms of the same dimension (e.g. b), of the model under consideration. The aim of the combined approach is to determine expressions for the specific surface area in terms of the respective permeability coefficients. Due to the different expressions obtained for the permeability coefficients for the different flow directions, the expression for the specific surface area will differ for the 1D RUC model for transverse and parallel flow and will therefore be discussed separately.

1D RUC model: Transverse flow

In order to determine the specific surface area using a combined approach for the 1D RUC model for transverse flow, the specific surface area obtained in equation (2.25) will first be rewritten as follows:

$$b = \frac{8(1-\epsilon)}{\sqrt{\pi} S_v}\,, \tag{2.26}$$

which is an expression for b in terms of S_v. In order to determine the specific surface area in terms of the Darcy permeability coefficient, equation (2.26) can be substituted into equation (2.16), resulting in

$$K = \left[\frac{8(1-\epsilon)}{\sqrt{\pi}S_v}\right]^2 \frac{\pi\left(1-\sqrt{1-\epsilon}\right)^3}{4(13.5)(1-\epsilon)^{3/2}}. \tag{2.27}$$

Rearranging equation (2.27) to express S_v in terms of K leads to

$$S_v = 4\sqrt{\frac{\sqrt{1-\epsilon}\left(1-\sqrt{1-\epsilon}\right)^3}{13.5K}}, \tag{2.28}$$

which is the expression required. Similarly, the specific surface area in terms of the Forchheimer permeability coefficient is determined by substituting equation (2.26) into equation (2.17), i.e.

$$K_F = \left[\frac{8(1-\epsilon)}{\sqrt{\pi}S_v}\right] \frac{\sqrt{\pi}\epsilon\left(1-\sqrt{1-\epsilon}\right)^2}{2(1-\epsilon)}, \tag{2.29}$$

and rearranging equation (2.29) then leads to

$$S_v = \frac{4\epsilon}{K_F}\left(1-\sqrt{1-\epsilon}\right)^2. \tag{2.30}$$

The calculation of the specific surface area equation based on the combined approach will be shown next for the 1D RUC model for parallel flow.

1D RUC model: Parallel flow

In the case of the 1D RUC model for parallel flow, the only permeability coefficient expression available is the one for the Darcy permeability. Therefore, only the specific surface area in terms of the Darcy permeability is determined. The expression for the fibre diameter in terms of the specific surface area, given by equation (2.26), is also applicable to the 1D RUC model for parallel flow since equation (2.25) applies to both 1D RUC models. Equation (2.26) is therefore substituted into equation (2.23) to obtain

$$S_v = \sqrt{\frac{\epsilon^3}{3K}}, \tag{2.31}$$

which is the specific surface area of the 1D RUC model for parallel flow in terms of the Darcy permeability coefficient.

The 2D RUC model will be investigated in the following section.

2.2 2D RUC model

A visual representation of the 2D RUC model is shown in Figure 1.5(b). The kinematic properties and some of the geometric properties are based on that of the 1D RUC model (Figure 1.5(a)), as mentioned previously. The dimensions of the 2D model are consequently the same as those provided in Section 2.1.1 for the 1D RUC model where the

permeability calculations are considered. The 2D RUC model is furthermore presented for two types of flow: in-plane flow and through plane flow, where both flow directions through the model are indicated in Figure 1.5(b) and the two models are furthermore shown in Figure 2.4 for the sake of completeness.

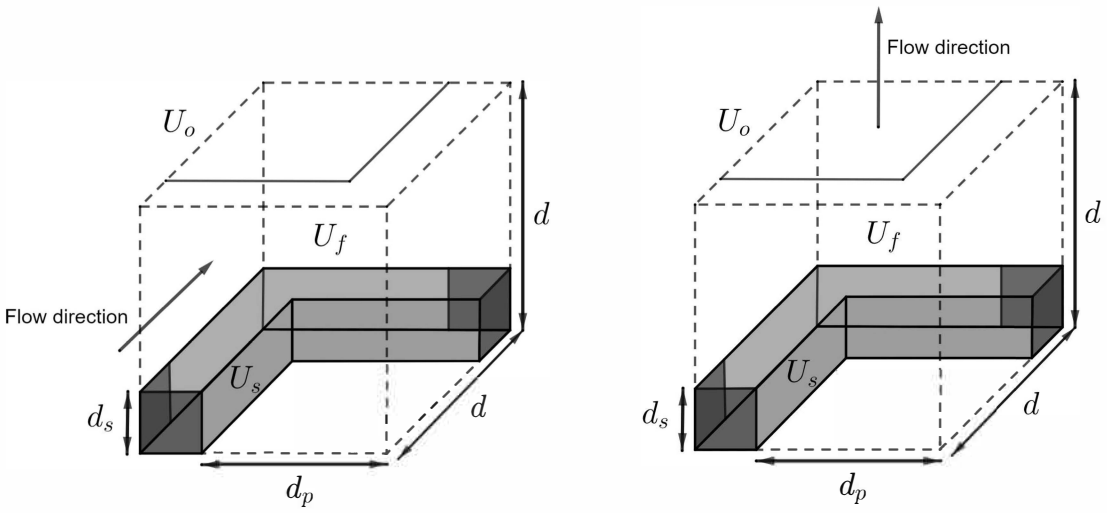

(a) *In-plane flow* (b) *Through plane flow*

FIGURE 2.4: *2D (or two-strut) RUC models*

The darker shaded areas in Figure 1.5(b) (or Figure 2.4) are the areas that do not form part of the outer surface area of the 2D RUC model, similar to the areas that were not shaded in Figures 2.2 and 2.3. These are the 'latching areas' discussed in Section 1.2. Due to the dependence on the 1D RUC model, the calculation of the expressions for the permeability coefficients will make use of the permeability coefficient expressions obtained for the 1D RUC model and the "mixing rule". Along with the calculations of the expressions for the permeability coefficients and the specific surface area equations determined using the geometric and combined approaches based on the 2D RUC model, a brief explanation of the "mixing rule" and the implementation thereof will be discussed in this section. The 2D RUC model will furthermore only be evaluated where fibre-type media are considered, and more specifically, fibre-type media arranged in planes.

2.2.1 Model dimension relations

Another important parameter that will be utilized in the calculations of the 2D RUC model, besides the dimension relations provided for the 1D RUC model in Section 2.1.1, is the geometric factor which is defined in Chapter 1, equation (1.7). The relations obtained in this section for the geometric factor are furthermore also valid for the two-strut RUC model, since it is only dependant on the geometry of the model, as shown in Figure 2.4. The point of departure of finding an expression for the geometric factor is determining an expression for the porosity. The porosity expression obtained for the 2D (or two-strut) RUC model, based on equation (1.6), is given by

$$\epsilon = \frac{U_o - U_s}{U_o} = \frac{d^3 - (2d_s^2 d - d_s^3)}{d^3} = 1 - 2\left(\frac{d_s}{d}\right)^2 + \left(\frac{d_s}{d}\right)^3 . \tag{2.32}$$

The $U_{\parallel}$, $U_{\perp}$ and U_t volumes will be calculated next using Figure 2.4 as reference. In the case of the 2D RUC model for in-plane flow, the volumes where flow parallel and perpendicular to the streamwise flow direction occur are given by

$$U_{\parallel} = d_s d_p \left(2d - d_s\right) , \tag{2.33}$$

and

$$U_{\perp} = d_s d_p^2 . \tag{2.34}$$

The total fluid volume is the sum of the streamwise, transverse and transfer volumes and consequently the transfer fluid volume is given by

$$U_t = d_p^3 . \tag{2.35}$$

Similarly, the volumes for the 2D RUC model for through plane flow can be calculated and are given by

$$U_{\parallel} = d_s d_p^2 , \tag{2.36}$$

$$U_{\perp} = d_s d_p^2 , \tag{2.37}$$

and

$$U_t = d_p^3 + d_s d_p d . \tag{2.38}$$

The following expression relating the porosity and the geometric factor can there-upon be deduced from equations (1.6) and (1.7), yielding

$$\frac{\epsilon}{\psi} = \frac{U_f/U_o}{U_f/\left(U_{\parallel} + U_t\right)} = \frac{U_{\parallel} + U_t}{U_o} . \tag{2.39}$$

It is furthermore noted that $U_{\parallel} + U_t$ of both the 2D RUC model for in-plane and through plane flow produces the same result, i.e.

$$U_{\parallel} + U_t = d^2 \left(d - d_s\right) , \tag{2.40}$$

where $U_{\parallel}$ and U_t can either be obtained from equations (2.33) and (2.35), respectively, or from equations (2.36) and (2.38), respectively. The geometric factor-porosity relationship for both 2D RUC models are therefore the same. Substituting equation (2.40) into equation (2.39) then leads to

$$\frac{\epsilon}{\psi} = \frac{d^2 \left(d - d_s\right)}{d^3} . \tag{2.41}$$

Rearranging equation (2.41) yields

$$\frac{d_s}{d} = 1 - \frac{\epsilon}{\psi} , \tag{2.42}$$

which, when substituted into equation (2.32), leads to the following polynomial:

$$\psi^3 - \psi^2 - \epsilon\psi + \epsilon^2 = 0 . \tag{2.43}$$

Equation (2.43) can then be solved using the Cardanic method (described in Appendix A). The geometric factor in terms of the porosity for the 2D (and two-strut) RUC model is consequently given by

$$\psi = \frac{1}{3} + \frac{2}{3}\sqrt{3\epsilon + 1}\cos\left[\frac{1}{3}\cos^{-1}\left(\frac{9\epsilon - 27\epsilon^2 + 2}{2\sqrt{27\epsilon^3 - 27\epsilon^2 + 9\epsilon + 1}}\right)\right] . \tag{2.44}$$

The geometric factor can be used to relate the different dimension parameters for the geometric 2D (or two-strut) RUC model. The strut diameter in terms of the face diameter is determined using equation (2.42), and is given by

$$d_s = \frac{d}{\psi}(\psi - \epsilon)\,. \tag{2.45}$$

Since $d = d_p + d_s$, the relation between the strut and pore diameter can furthermore be deduced from equation (2.45), i.e.

$$d_s = \frac{d_p}{\epsilon}(\psi - \epsilon)\,, \tag{2.46}$$

and hence, the relation between the face and pore diameters follows:

$$d = \frac{\psi d_p}{\epsilon}\,. \tag{2.47}$$

Due to the 2D and two-strut RUC models mainly representing fibre-type media, the fibre diameter is also defined such that $d_s^2 = \frac{\pi}{4}b^2$. The relations between the fibre diameter and the face and pore diameters can therefore respectively be deduced from equations (2.45) and (2.46) and yields

$$b = \frac{2d}{\sqrt{\pi}\,\psi}\,(\psi - \epsilon) \qquad \text{and} \qquad b = \frac{2d_p}{\sqrt{\pi}\,\epsilon}\,(\psi - \epsilon)\,. \tag{2.48}$$

The geometric factor in all of equations (2.45) to (2.48) is determined from equation (2.44).

It should be noted that although the expression for the geometric factor given by equation (2.44) is valid for the 2D RUC model, the relations for the dimensions given in this section will not be utilized further except for the geometric approach of determining the specific surface area. Only the dimension relations given in Section 2.1.1 will be used otherwise, i.e. where the permeability expressions are concerned. The dimension relations involving the geometric factor, such as equation (2.42), will further be utilized in the case of the two-strut RUC model. The reasoning behind this discretion is that the geometrically determined specific surface area of the 2D and two-strut RUC models are the same due to the similar geometry, but not the kinematic properties or methods of determining the permeability.

2.2.2 Permeability prediction

The permeability coefficients of the Darcy flow regime of the 2D RUC models, for in-plane and through plane flow, are determined by applying weights to the Darcy permeability coefficient of the 1D RUC model for transverse and parallel flow. The Darcy permeability coefficients for the 2D in-plane and 2D through plane models are given by Woudberg [55]. The weighting method that was used for the Darcy permeability coefficient was based on the "mixing rules" proposed by Mattern and Deen [81], called the "unweighted resistivity" and is given by

$$\frac{1}{K} = \frac{\phi_\parallel}{K_\parallel} + \frac{\phi_\perp}{K_\perp}\,, \tag{2.49}$$

where $\phi_{\parallel}$ and $\phi_{\perp}$ are the weights expressed as fractions and $K_{\parallel}$ and $K_{\perp}$ are the Darcy permeability coefficients obtained from the 1D RUC model for parallel and transverse flow, given by equations (2.23) and (2.16), respectively. A transversely isotropic 2D RUC model for through plane flow was also proposed by Woudberg [55], and assumed in this study (as previously mentioned), and therefore the average of the coefficients for one fully staggered array and one regular array was taken. The coefficient of 13.5 in equation (2.16) is therefore applicable to the implementation of the "mixing rule" to the 2D RUC model, where necessary, i.e. the latter value will be used in this study in the $K_{\perp}$ equation for calculations of the 2D (and later the 3D) RUC models.

Woudberg [55] only provided Darcy permeability coefficients for the 2D RUC models and not Forchheimer permeability coefficients. In this study it is therefore proposed that the Forchheimer permeability coefficient of the 2D (and later the 3D) RUC models be determined in a similar way as the Darcy permeability coefficients, in that weights are applied using the following weighting rule:

$$\frac{1}{K_F} = \frac{\phi_{\parallel}}{K_{F\parallel}} + \frac{\phi_{\perp}}{K_{F\perp}}, \tag{2.50}$$

where $K_{F\parallel}$ and $K_{F\perp}$ are the Forchheimer permeability coefficients obtained from the 1D RUC model for parallel and transverse flow, respectively. The Forchheimer permeability coefficient obtained from the 1D RUC model for parallel flow is excluded from the mixing rule, due to there not being an obstruction in the flow in this case, and consequently the $K_{F_{\parallel}}$ term is omitted from equation (2.50), leaving K_F only to dependent on the $K_{F_{\perp}}$-term. Equation (2.50) therefore becomes:

$$K_F = \frac{K_{F_{\perp}}}{\phi_{\perp}}. \tag{2.51}$$

Equation (2.17), along with equation (2.51), are therefore used to determine the Forchheimer permeability coefficients for the 2D (and later the 3D) RUC models, with the weights defined similarly as in the case of the Darcy permeability coefficient. This method of determining the Forchheimer permeability coefficient is unique to this study. Predictions for the Forchheimer permeability based on the 2D and 3D RUC models are furthermore not available elsewhere in the literature, except as published in Maré and Woudberg [78].

2D RUC model: In-plane flow

The expression for the Darcy permeability coefficient of the 2D RUC model for in-plane flow can therefore be determined directly using equation (2.49), and the Forchheimer permeability coefficient expression from equation (2.51). In Figure 2.4(a) it can be seen that there is one strut parallel to the flow and one strut perpendicular to the flow. Therefore, the assigned weights for the "mixing rule" to the 2D RUC model for in-plane flow are $\phi_{\parallel} = 1/2$ and $\phi_{\perp} = 1/2$. Applying these weights to equation (2.49), along with equations (2.23) and (2.16) representing $K_{\parallel}$ and $K_{\perp}$, respectively, the following expression for the Darcy permeability coefficient for the 2D RUC model for in-plane flow is obtained:

$$K = b^2 \frac{\pi}{4} \left[\frac{1}{2} \left[\frac{48(1-\epsilon)^2}{\epsilon^3} \right] + \frac{1}{2} \left[\frac{13.5(1-\epsilon)^{3/2}}{\left(1-\sqrt{1-\epsilon}\right)^3} \right] \right]^{-1}. \tag{2.52}$$

In order to obtain the expression for the Forchheimer permeability coefficient for the 2D model for in-plane flow, $\phi_\perp = 1/2$ and equation (2.17) is substituted into equation (2.51), yielding

$$K_F = b\,\frac{\sqrt{\pi}\,\epsilon\left(1-\sqrt{1-\epsilon}\right)^2}{1-\epsilon}\,. \tag{2.53}$$

Substituting equations (2.52) and (2.53) into equation (1.1), with $L = d$, furthermore yields

$$\frac{\Delta p}{d} = \frac{4}{\pi b^2}\left[\frac{1}{2}\left[\frac{48(1-\epsilon)^2}{\epsilon^3}\right] + \frac{1}{2}\left[\frac{13.5(1-\epsilon)^{3/2}}{\left(1-\sqrt{1-\epsilon}\right)^3}\right]\right]\mu q + \frac{1-\epsilon}{\sqrt{\pi}\,b\epsilon\left(1-\sqrt{1-\epsilon}\right)^2}\rho q^2\,, \tag{2.54}$$

which is the Ergun-type equation for the 2D RUC model for in-plane flow.

2D RUC model: Through plane flow

The permeability coefficients of the 2D RUC model for through plane flow can be determined similarly to that of the model for in-plane flow, the only difference being the values of the weights for the "mixing rule" assigned to this model. There are two struts positioned perpendicular to one another and to the flow (see Figure 2.4(b)). Therefore, $\phi_\parallel = 0/2$ and $\phi_\perp = 2/2$. Substituting these weights, along with equations (2.16) and (2.23), into equation (2.49) leads to the following expression for the Darcy permeability coefficient for the 2D RUC model for through plane flow:

$$K = b^2\,\frac{\pi\left(1-\sqrt{1-\epsilon}\right)^3}{54(1-\epsilon)^{3/2}}\,. \tag{2.55}$$

Substituting the relevant weight value and equation (2.17) into equation (2.51) furthermore leads to the Forchheimer permeability expression, i.e.

$$K_F = b\,\frac{\sqrt{\pi}\epsilon\left(1-\sqrt{1-\epsilon}\right)^2}{2(1-\epsilon)}\,, \tag{2.56}$$

and consequently, substituting equations (2.55) and (2.56) into equation (1.1), with $L = d$, results in the Ergun-type equation for the 2D RUC model for through plane flow:

$$\frac{\Delta p}{d} = \frac{54(1-\epsilon)^{3/2}}{\pi b^2\left(1-\sqrt{1-\epsilon}\right)^3}\mu q + \frac{2(1-\epsilon)}{\sqrt{\pi}b\epsilon\left(1-\sqrt{1-\epsilon}\right)^2}\rho q^2\,. \tag{2.57}$$

The manner in which the specific surface area of the 2D RUC model is determined using a geometric approach, will be investigated next.

2.2.3 Specific surface area prediction: Geometric approach

The geometric approach for determining the predictive equation for the specific surface area of both the 2D and two-strut RUC models are the same, because the differences between the two models are restricted to calculations involving the permeability. The expression for the specific surface area in terms of b for the 2D (and two-strut) RUC

model can therefore be determined from the geometry of the model, as shown in Figure 1.5(b) (or either of the models shown in Figure 2.4). Equation (1.20) is utilized to perform this task and therefore requires the total surface area and the total volume. From Figure 2.4 the total surface area of the struts can be calculated, excluding the darker shaded areas, and yields:

$$S_{fs} = 8d_s d_p + 2d_s^2\,, \tag{2.58}$$

which, when substituted into equation (1.20) along with $U_o = d^3$, leads to the following expression for the specific surface area:

$$S_v = \frac{8d_s d_p + 2d_s^2}{d^3} = \frac{8}{d}\frac{d-d_s}{d}\frac{d_s}{d} + \frac{2}{d}\left(\frac{d_s}{d}\right)^2. \tag{2.59}$$

Substitution of the dimension relation given by equation (2.42) into equation (2.59), along with the relevant relation between the strut and fibre diameters for fibre-type media, leads to the specific surface area in terms of the fibre diameter:

$$S_v = \frac{4}{\sqrt{\pi}\, b\psi^3}\left(\psi-\epsilon\right)^2\left(\psi+3\epsilon\right), \tag{2.60}$$

where ψ can be solved using equation (2.44). It is once again stated that the dimension relations obtained in Section 2.2.1, other than the expression for the geometric factor, is used only for the determination of the geometric specific surface area for the 2D RUC model case. In order to obtain the geometric specific surface area in terms of d or d_p for the 2D RUC model, dimension relations deduced from the geometric model shown in Figure 2.4 and the expressions provided in Section 2.2.1 must be substituted into equation (2.60).

2.2.4 Specific surface area prediction: Combined approach

Determining the expression for the specific surface area using a combined approach for the 2D RUC model is done similarly to that of the 1D RUC model in Section 2.1.4: the relevant specific surface area and permeability expressions of the 2D RUC model are combined to obtain the specific surface area in terms of the Darcy and Forchheimer permeability coefficients, respectively.

2D RUC model: In-plane flow

For the 2D RUC model for in-plane flow, the equation for the specific surface area, i.e. equation (2.60), is combined with equation (2.52) for the Darcy permeability coefficient, yielding

$$S_v = \frac{2(\psi-\epsilon)^2(\psi+3\epsilon)}{\psi^3}\sqrt{\frac{2\epsilon^3\left(1-\sqrt{1-\epsilon}\right)^3}{K\left[48(1-\epsilon)^2\left(1-\sqrt{1-\epsilon}\right)^3+13.5\epsilon^3(1-\epsilon)^{3/2}\right]}}\,, \tag{2.61}$$

which is the specific surface area in terms of the Darcy permeability. Equation (2.60) is combined with equation (2.53) to obtain the specific surface area in terms of the Forchheimer permeability, i.e.

$$S_v = \frac{4\epsilon(\psi-\epsilon)^2(\psi+3\epsilon)\left(1-\sqrt{1-\epsilon}\right)^2}{K_F\psi^3(1-\epsilon)}\,. \tag{2.62}$$

In both equations (2.61) and (2.62), ψ is determined from equation (2.44).

2D RUC model: Through plane flow

Similarly, the predicting equations for the specific surface area of the 2D RUC model for through plane flow are determined by combining equation (2.60) with equation (2.55) and equation (2.56) to respectively obtain

$$S_v = \frac{2(\psi-\epsilon)^2(\psi+3\epsilon)}{3\psi^3}\sqrt{\frac{2\left(1-\sqrt{1-\epsilon}\right)^3}{3K(1-\epsilon)^{3/2}}}, \tag{2.63}$$

for the specific surface area in terms of the Darcy permeability and

$$S_v = \frac{2\epsilon(\psi-\epsilon)^2(\psi+3\epsilon)\left(1-\sqrt{1-\epsilon}\right)^2}{K_F\psi^3(1-\epsilon)}, \tag{2.64}$$

for the specific surface area in terms of the Forchheimer permeability. Once more ψ is determined from equation (2.44).

Next the 3D RUC model will be investigated.

2.3 3D RUC model

The 3D RUC model is based on the 1D RUC model, similar to the 2D RUC model, as mentioned earlier in this study. Therefore, the kinematic properties are deduced from the 1D RUC model expressions by utilizing the "mixing rule" once again and the model dimension relations provided in Section 2.1.1 are also valid for the permeability calculations of the 3D RUC model. A visual representation of the model is shown in Figure 1.5(c) and Figure 2.5, the latter for convenience. The darker shaded areas in both the figures once more represents the areas not included in the outer surface area. The 3D RUC model will be evaluated in the representation of randomly orientated fibre-type media, as well as foamlike media. In this section of study, the unique model dimension relations of the 3D RUC model, along with the calculation of the predicting equations for the permeability coefficients and specific surface area obtained using both geometric and combined approaches will be discussed.

2.3.1 Model dimension relations

Aside from the model dimensions provided in Section 2.1.1, an expression for the geometric factor in terms of the porosity can be determined for the 3D RUC model in a similar way as that of the 2D RUC model. Furthermore, the expressions and dimension relations ob-

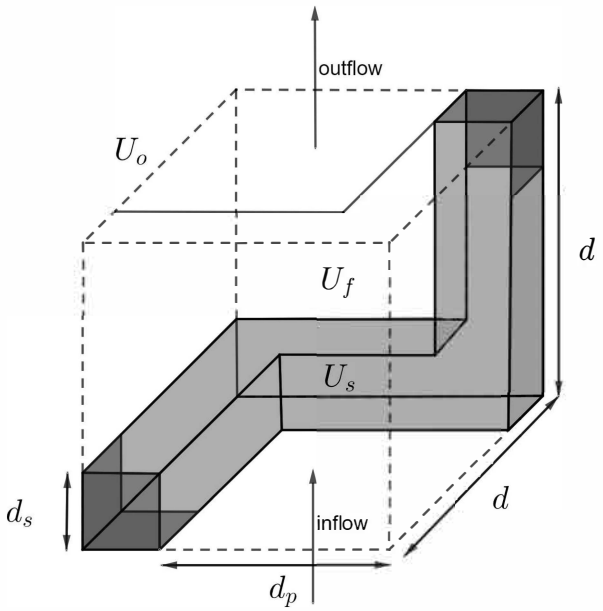

FIGURE 2.5: *3D (or three-strut) RUC model*

tained in this section are also valid for the three-strut RUC model, since it depends on the geometry of the model as given in Figure 2.5. The expression for the porosity, given by equation (1.6), and consequently the required expressions for the respective volumetric parameters, is determined for the 3D RUC model using Figure 2.5 and yields:

$$\epsilon = \frac{U_o - U_s}{U_o} = \frac{d^3 - (3d_s^2 d_p + d_s^3)}{d^3} = 1 - 3\left(\frac{d_s}{d}\right)^2 + 2\left(\frac{d_s}{d}\right)^3 , \tag{2.65}$$

noting that $d_p = d - d_s$. The fluid volumes, $U_{\parallel}$, $U_{\perp}$ and U_t, can be determined with the aid of Figure 2.5. Dividing the volumes as shown in the high porosity model is visually challenging and it is recommended to rather obtain the volumes by making use of the invertible ability of the three-strut RUC model with respect to the solid and fluid volumes, i.e. use the low porosity model. (A visual representation of the low porosity model is provided in a subsequent section in this chapter where the three-strut RUC model is addressed.) Consequently, the fluid volumes are given as follows:

$$U_{\parallel} = d_s d_p^2 , \tag{2.66}$$

$$U_{\perp} = 2 d_s d_p^2 , \tag{2.67}$$

and

$$U_t = d_p^3 , \tag{2.68}$$

where the latter volume can once more be obtained by subtracting the streamwise and transverse volumes from the total fluid volume. Substituting equations (2.66) and (2.68), along with U_f (which is the sum of equations (2.66) to (2.68)), into equation (1.7) leads to the following expression for the geometric factor:

$$\psi = 1 + 2\frac{d_s}{d} , \tag{2.69}$$

which yields

$$\frac{d_s}{d} = \frac{\psi - 1}{2} . \tag{2.70}$$

A polynomial for the geometric factor is then obtained by substituting equation (2.70) into equation (2.65), i.e.

$$\psi^3 - 6\psi^2 + 9\psi - 4\epsilon = 0\,. \tag{2.71}$$

Using the Cardanic method once again, as discussed in Appendix A, the polynomial given by equation (2.71) is used to obtain the following expression for the geometric factor in terms of the porosity:

$$\psi = 2 + 2\cos\left[\frac{4\pi}{3} + \frac{1}{3}\cos^{-1}(2\epsilon - 1)\right]\,. \tag{2.72}$$

Some other relations can be deduced for the geometric 3D (or three-strut) RUC model, using equation (2.70). The strut diameter in terms of the face diameter is determined to be

$$d_s = d\frac{\psi - 1}{2}\,, \tag{2.73}$$

and using $d = d_p + d_s$, it can furthermore be shown that

$$d_s = d_p\frac{\psi - 1}{3 - \psi}\,, \tag{2.74}$$

and

$$d = \frac{2d_p}{3 - \psi}\,. \tag{2.75}$$

Another dimension relation that will prove to be useful is the following:

$$\frac{\epsilon}{\psi} = \frac{d_p^2}{d^2}\,. \tag{2.76}$$

In order to obtain the expression for the fibre diameter, $d_s^2 = \frac{\pi}{4}b^2$ is once again used and leads to

$$b = \frac{d}{\sqrt{\pi}}\,(\psi - 1) \qquad \text{and} \qquad b = \frac{2d_p}{\sqrt{\pi}}\,\frac{\psi - 1}{3 - \psi}\,. \tag{2.77}$$

The relations obtained in this section will once again only be utilized to obtain the specific surface area using a geometric approach. The dimension relations given by equations (2.69), (2.70) and (2.73) to (2.76) will further only be used with the three-strut RUC model. The dimension relations utilized in the calculations involving the permeability of the 3D RUC model is given in Section 2.1.1.

2.3.2 Permeability prediction

In order to determine the equations for the permeability coefficient of the 3D RUC model the "mixing rule" (as described in Section 2.2.2) for both the Darcy and Forchheimer permeability coefficients will be utilized, given by equations (2.49) and (2.51), respectively. There are three struts in the 3D RUC model, one parallel to the streamwise direction and two perpendicular to the streamwise direction. Therefore, the weights assigned to the 3D RUC model are $\phi_{\parallel} = 1/3$ and $\phi_{\perp} = 2/3$. Substituting equations (2.23) and (2.16) into equation (2.49) with these weights, leads to

$$K = b^2\,\frac{\pi}{4}\left[\frac{1}{3}\left[\frac{48(1-\epsilon)^2}{\epsilon^3}\right] + \frac{2}{3}\left[\frac{13.5(1-\epsilon)^{3/2}}{\left(1-\sqrt{1-\epsilon}\right)^3}\right]\right]^{-1}\,, \tag{2.78}$$

which is the expression for the Darcy permeability coefficient. Similarly, substituting equation (2.17) into equation (2.51) together with $\phi_\perp$ of the 3D RUC model, yields

$$K_F = b\frac{3\sqrt{\pi}\,\epsilon\left(1-\sqrt{1-\epsilon}\right)^2}{4(1-\epsilon)}\,, \tag{2.79}$$

which is the expression for the Forchheimer permeability coefficient. Substituting equations (2.78) and (2.79) into equation (1.1), with $L = d$, the Ergun-type equation for the 3D RUC model is deduced, given by

$$\frac{\Delta p}{d} = \frac{4}{\pi b^2}\left[\frac{1}{3}\left[\frac{48(1-\epsilon)^2}{\epsilon^3}\right] + \frac{2}{3}\left[\frac{13.5(1-\epsilon)^{3/2}}{\left(1-\sqrt{1-\epsilon}\right)^3}\right]\right]\mu q + \frac{4(1-\epsilon)}{3\sqrt{\pi}\,b\epsilon\left(1-\sqrt{1-\epsilon}\right)^2}\rho q^2\,. \tag{2.80}$$

The 3D RUC model will be evaluated for both fibre-type and foamlike media and consequently, the permeability coefficients in terms of d_p will also be provided, which is determined by substituting equation (2.5) into equations (2.78) and (2.79), yielding

$$K = d_p^2\frac{1-\epsilon}{\left(1-\sqrt{1-\epsilon}\right)^2}\left[\frac{1}{3}\left[\frac{48(1-\epsilon)^2}{\epsilon^3}\right] + \frac{2}{3}\left[\frac{13.5(1-\epsilon)^{3/2}}{\left(1-\sqrt{1-\epsilon}\right)^3}\right]\right]^{-1}\,, \tag{2.81}$$

and

$$K_F = d_p\frac{3\epsilon\left(1-\sqrt{1-\epsilon}\right)}{2\sqrt{1-\epsilon}}\,, \tag{2.82}$$

for the Darcy and Forchheimer permeability coefficients, respectively.

The specific surface area expression for the 3D RUC model, determined using a geometric approach, will be discussed next.

2.3.3 Specific surface area prediction: Geometric approach

Due to the geometric approach of determining the specific surface area only being dependant on the geometry of the model, as given in Figure 2.5, the 3D and three-strut RUC models have the same resulting specific surface area equation obtained using this approach. In order to obtain the specific surface area equation using a geometric approach, equation (1.20) is used. The total surface area can be determined from Figure 2.5 and is given by

$$S_{fs} = 12 d_s d_p\,. \tag{2.83}$$

Substituting equation (2.83) into equation (1.20) and furthermore utilizing the expressions that are valid for all the RUC models (i.e. $U_o = d^3$ and $d_p = d - d_s$) and equation (2.70), the following specific surface area equation in terms of d_s is obtained:

$$S_v = \frac{3}{2d_s}(3-\psi)(\psi-1)^2\,. \tag{2.84}$$

The equation for the specific surface area of the 3D RUC model in terms of b can consequently be determined by substituting $d_s = \frac{\sqrt{\pi}}{2}b$ into equation (2.84), yielding

$$S_v = \frac{3}{\sqrt{\pi}\,b}(3-\psi)(\psi-1)^2\,, \tag{2.85}$$

where ψ is calculated using equation (2.72). Equation (2.85) will be utilized when 3D arrangements of fibre-type media are considered. In order to obtain the specific surface area in terms of d_p, the dimension relations provided in Section 2.3.1 are utilized which results in the following expression:

$$S_v = \frac{3}{2d_p}(3-\psi)^2(\psi-1)\,. \tag{2.86}$$

Equation (2.86) will consequently be used where foamlike media are concerned.

2.3.4 Specific surface area prediction: Combined approach

The combined approach for determining the specific surface area once again entails combining the specific surface area equation obtained using a geometric approach and the respective expressions for the permeability coefficient in order to obtain the specific surface area in terms of the permeability. The expression for the specific surface area in terms of the Darcy permeability of the 3D RUC model is hence determined by combining equation (2.85) with equation (2.78) and yields:

$$S_v = \frac{3(3-\psi)(\psi-1)^2}{2}\sqrt{\frac{\epsilon^3\left(1-\sqrt{1-\epsilon}\right)^3}{K\left[16(1-\epsilon)^2\left(1-\sqrt{1-\epsilon}\right)^3+9\epsilon^3(1-\epsilon)^{3/2}\right]}}\,. \tag{2.87}$$

In order to obtain the expression for the specific surface area in terms of the Forchheimer permeability, equations (2.85) and (2.79) are combined and leads to

$$S_v = \frac{9\epsilon(3-\psi)(\psi-1)^2\left(1-\sqrt{1-\epsilon}\right)^2}{4K_F(1-\epsilon)}\,. \tag{2.88}$$

In both equations (2.87) and (2.88) ψ is determined using equation (2.72). It is important to note that equation (2.86) cannot be used in the combined approach of the 3D RUC model because the dimension relations of the geometric approach and the permeability calculations are not the same. The former is based on the geometry of the model as given in Figure 2.5 and the latter is based on the 1D RUC model.

In the following section the investigation will continue with the two-strut RUC model.

2.4 Two-strut RUC model

The two-strut RUC model, although similar to the 2D RUC model in representation, depends on the geometry of the model, as shown in Figures 1.5(b) and 2.4, in order to determine its kinematic and geometric properties. The equations and methods provided in Section 1.2 for determining the pressure drop of the Darcy and Forchheimer regimes are therefore valid once more. Two types of flow are investigated for the two-strut RUC model, i.e. in-plane and through plane flow. The in-plane two-strut RUC model is furthermore unique to this study as it has not been presented elsewhere in the literature. The two-strut RUC model will only be evaluated where fibre-type media arranged in planes are considered. The model dimension relations given in Section 2.2.1 are all applicable to the two-strut RUC model and will therefore also be utilized in this section. The derivation of the Ergun-type equation, permeability coefficients and specific surface area expressions will be presented.

2.4.1 Permeability prediction

The Ergun-type equation, and consequently the expressions for the Darcy and Forchheimer permeability coefficients, for the two-strut RUC model are determined in this section. The coefficient ξ has a value of 1 for both the two-strut RUC models for in-plane and through plane flow. Due to the assumption of plane Poiseuille flow for the two-strut RUC model, equation (1.12) will be utilized in order to determine the expressions of the average wall shear stress in this section. The calculations regarding the two-strut RUC model for in-plane flow will be presented first.

Two-strut RUC model: In-plane flow

The pressure drop for the Darcy flow regime is determined from equation (1.10). The streamwise and transverse surfaces of the two-strut RUC model for in-plane flow are shown in Figure 2.6.

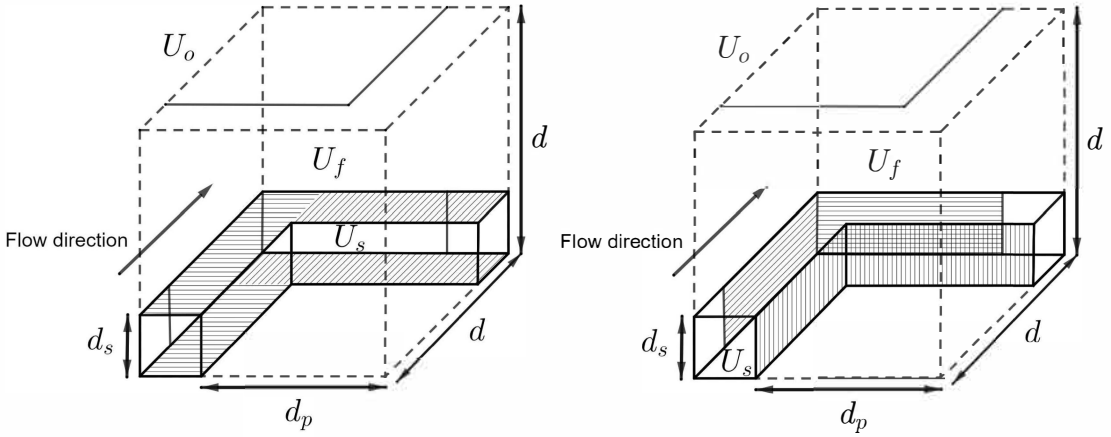

(a) $S_{\parallel}$ (b) $S_{\perp}$

FIGURE 2.6: *Solid surfaces of two-strut RUC model for in-plane flow*

Consequently, the surface areas determined from Figure 2.6 are given by

$$S_{\parallel} = 4d_s d_p + 2d_s^2 \qquad \text{and} \qquad S_{\perp} = 4d_s d_p \,, \tag{2.89}$$

and the streamwise and transverse cross-sectional flow areas by

$$A_{p_{\parallel}} = d_p d \,, \tag{2.90}$$

and

$$A_{p_{\perp}} = d_p^2 \,, \tag{2.91}$$

respectively. Substituting equation (2.90) into equation (1.13) furthermore leads to the average streamwise channel velocity, i.e.

$$w_{\parallel} = \frac{qd}{d_p} \,, \tag{2.92}$$

and utilizing equation (1.14), along with equations (2.90) to (2.92), the average transverse channel velocity is given by

$$w_{\perp} = \frac{A_{p_{\parallel}}}{A_{\perp}} w_{\parallel} = \frac{d_p d}{d_p^2} \frac{qd}{d_p} = \frac{qd^2}{d_p^2} \,. \tag{2.93}$$

In order to determine the average streamwise and transverse wall shear stresses, equations (2.92) and (2.93) are, respectively, substituted into equation (1.12), where B for both two-strut RUC models is equal to d_p. This then yields

$$\tau_{w_\parallel} = \frac{6d}{d_p^2}\mu q \qquad \text{and} \qquad \tau_{w_\perp} = \frac{6d^2}{d_p^3}\mu q\,. \tag{2.94}$$

Utilizing equations (1.10), (2.89), (2.90) and (2.94), along with the relations between the dimensions of the two-strut RUC model given in Section 2.2.1, the pressure gradient for the Darcy term can be determined, resulting in

$$\frac{\Delta p}{d} = \frac{48(\psi-\epsilon)^3(3\psi+\epsilon)}{\pi b^2\epsilon^3\psi}\mu q\,. \tag{2.95}$$

The Forchheimer flow term is determined from equation (1.19), where S_{face} can be determined using Figure 2.4(a) and is given by

$$S_{\text{face}} = d_s d_p\,, \tag{2.96}$$

for the two-strut RUC model for in-plane flow and with U_o remaining the same for all the RUC models, thus yielding

$$-\nabla\langle p\rangle_f = \frac{2(\psi-\epsilon)^2}{\sqrt{\pi}\,b\epsilon^2\psi}\rho q^2\,\underline{\hat{n}}\,. \tag{2.97}$$

The analytical Ergun-type equation for the two-strut RUC model for in-plane flow is therefore given by

$$\frac{\Delta p}{d} = \frac{48(\psi-\epsilon)^3(3\psi+\epsilon)}{\pi b^2\epsilon^3\psi}\mu q + \frac{2(\psi-\epsilon)^2}{\sqrt{\pi}\,b\epsilon^2\psi}\rho q^2\,. \tag{2.98}$$

The permeability coefficients of the two-strut RUC model for in-plane flow is consequently deduced by substituting equation (2.98) into equation (1.1), with $L = d$, resulting in

$$K = b^2\,\frac{\pi\epsilon^3\psi}{48(\psi-\epsilon)^3(3\psi+\epsilon)}\,, \tag{2.99}$$

and

$$K_F = b\,\frac{\sqrt{\pi}\,\epsilon^2\psi}{2(\psi-\epsilon)^2}\,, \tag{2.100}$$

for the Darcy and Forchheimer permeability coefficients, respectively, where ψ is determined from equation (2.44). The complete determination of the permeability coefficients and Ergun-type equation of the two-strut RUC model in this section was published in Maré and Woudberg [78].

Two-strut RUC model: Through plane flow

The solid surface areas of the two-strut RUC model for through plane flow are shown in Figure 2.7. It is evident from Figures 2.6 and 2.7, that $S_\parallel$ and $S_\perp$ are simply inverted.

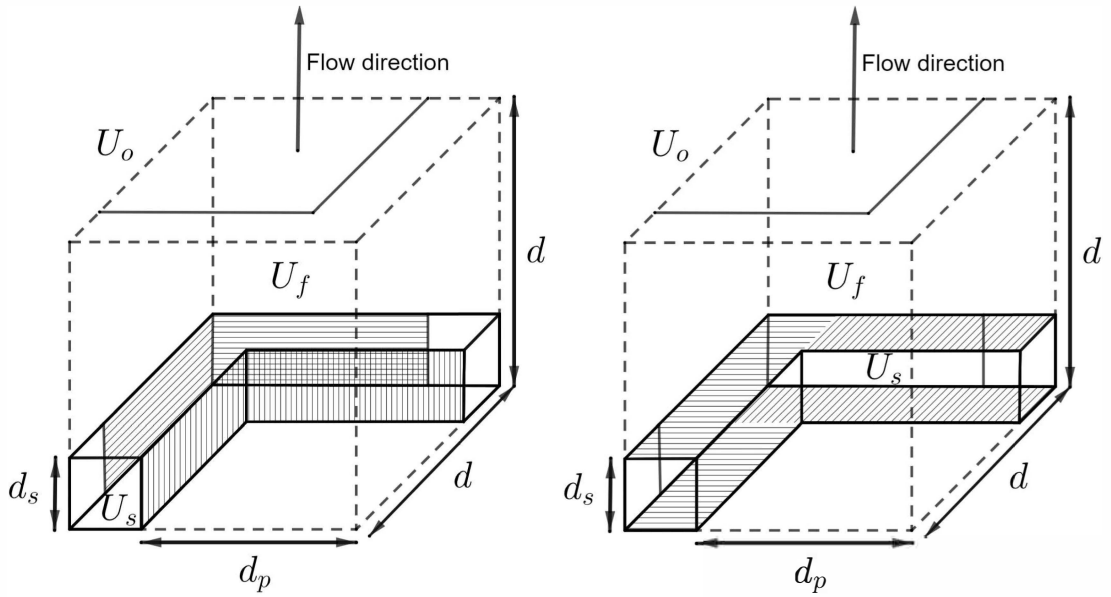

(a) $S_{\parallel}$ (b) $S_{\perp}$

FIGURE 2.7: *Solid surfaces of two-strut RUC model for through plane flow*

Consequently,

$$S_{\parallel} = 4d_s d_p \qquad \text{and} \qquad S_{\perp} = 4d_s d_p + 2d_s^2 \,. \tag{2.101}$$

The streamwise and transverse cross-sectional flow areas of the two-strut RUC model for through plane flow, and furthermore the average channel velocities and average wall shear stresses, are also the opposite from that of the in-plane flow model and are therefore given by

$$A_{p_{\parallel}} = d_p^2 \qquad \text{and} \qquad A_{p_{\perp}} = d_p d \,, \tag{2.102}$$

$$w_{\parallel} = \frac{qd^2}{d_p^2} \qquad \text{and} \qquad w_{\perp} = \frac{qd}{d_p} \,, \tag{2.103}$$

$$\tau_{w_{\parallel}} = \frac{6d^2}{d_p^3}\mu q \qquad \text{and} \qquad \tau_{w_{\perp}} = \frac{6d}{d_p^2}\mu q \,, \tag{2.104}$$

respectively. Substituting equations (2.102) to (2.104) into equation (1.10) then leads to the pressure gradient for the two-strut RUC model for through plane flow in question, i.e.

$$\frac{\Delta p}{d} = \frac{12 d_s (4d - d_s)}{d_p^4}\mu q \,, \tag{2.105}$$

and utilizing the dimension relations provided in Section 2.2.1, the following pressure gradient for Darcy flow in terms of b is determined:

$$\frac{\Delta p}{d} = \frac{48(\psi - \epsilon)^3(3\psi + \epsilon)}{\pi b^2 \epsilon^4}\mu q \,. \tag{2.106}$$

The cross-sectional solid area facing upstream, as determined from Figure 2.4(b), is given by

$$S_{\text{face}} = 2d_s d_p + d_s^2 \,. \tag{2.107}$$

Substituting equation (2.107), along with equation (2.103), $U_o = d^3$ and the relevant dimension relations given in Section 2.2.1 into equation (1.19), results in the expression for the Forchheimer term in terms of b:

$$-\nabla\langle p\rangle_f = \frac{2\psi(\psi-\epsilon)^2(\psi+\epsilon)}{\sqrt{\pi}\, b\epsilon^5}\rho q^2\,\underline{\hat{n}}\,. \tag{2.108}$$

The Ergun-type equation for the two-strut RUC model for through plane flow can finally be expressed as a superposition of equations (2.106) and (2.108) i.e.

$$\frac{\Delta p}{d} = \frac{48(\psi-\epsilon)^3(3\psi+\epsilon)}{\pi b^2\epsilon^4}\mu q + \frac{2\psi(\psi-\epsilon)^2(\psi+\epsilon)}{\sqrt{\pi}\, b\epsilon^5}\rho q^2\,. \tag{2.109}$$

from which it follows that

$$K = b^2\,\frac{\pi\epsilon^4}{48(\psi-\epsilon)^3(3\psi+\epsilon)}\,, \tag{2.110}$$

and

$$K_F = b\,\frac{\sqrt{\pi}\epsilon^5}{2\psi(\psi-\epsilon)^2(\psi+\epsilon)}\,, \tag{2.111}$$

where ψ is given by equation (2.44).

2.4.2 Specific surface area prediction: Geometric approach

The geometric approach for determining the specific surface area of the two-strut RUC model is the same as given in Section 2.2.3 for the 2D RUC model and the resulting expression is furthermore given by equation (2.60). This expression furthermore remains the same for the models for in-plane and through plane flow. In order to find the specific surface area of the two-strut RUC model in terms of d or d_p, the dimension relations provided in Section 2.2.1 can be utilized.

2.4.3 Specific surface area prediction: Combined approach

In order to obtain the specific surface area in terms of the permeability coefficients, the relevant combination of specific surface area and permeability equations need to be applied. Due to the difference in permeability equations for the two different directions of flow, there is once again a distinction between the two-strut RUC models for in-plane and through plane flow.

Two-strut RUC model: In-plane flow

The specific surface area equations of the two-strut RUC model based on the combined approach is determined by combining equations (2.60) and (2.99), for the specific surface area in terms of the Darcy permeability coefficient and equations (2.60) and (2.100) for the specific surface area in terms of the Forchheimer permeability coefficient. These combinations therefore result in the following expressions:

$$S_v = (\psi+3\epsilon)\sqrt{\frac{\epsilon^3(\psi-\epsilon)}{3K\psi^5(3\psi+\epsilon)}}\,, \tag{2.112}$$

and

$$S_v = \frac{2\epsilon^2(\psi + 3\epsilon)}{K_F \psi^2}, \tag{2.113}$$

where ψ in both equations (2.112) and (2.113) are determined from equation (2.44).

Two-strut RUC model: Through plane flow

The expressions for the specific surface area of the two-strut RUC model for through plane flow in terms of the permeability coefficients are similarly determined by combining equations (2.60) and (2.110), resulting in

$$S_v = \frac{\epsilon^2(\psi + 3\epsilon)}{\psi^3} \sqrt{\frac{\psi - \epsilon}{3K(3\psi + \epsilon)}}, \tag{2.114}$$

for the specific surface area in terms of the Darcy permeability coefficient, and combining equations (2.60) and (2.111), resulting in

$$S_v = \frac{2\epsilon^5(\psi + 3\epsilon)}{K_F \psi^4(\psi + \epsilon)}, \tag{2.115}$$

for the specific surface area in terms of the Forchheimer permeability coefficient. In equations (2.114) and (2.115) ψ is once again given by equation (2.44).

The final RUC model, i.e. the three-strut RUC model, will be discussed in the following section.

2.5 Three-strut RUC model

The three-strut RUC model is also based on the geometry of the model, similarly as the two-strut RUC model, and is shown in Figure 2.5. Due to the similar geometry between the 3D and three-strut RUC model, the dimension relations obtained in Section 2.3.1 also applies to the three-strut RUC model, with the exception of the relations involving b since $b = d_s$ for the three-strut RUC model. The three-strut RUC model will be applied to randomly orientated fibre-type and foamlike media. The three-strut RUC model for low porosity fibrous porous media and high porosity fibrous porous media are furthermore respectively shown in Figure 2.8(a) and (b). As mentioned earlier, the two porosity type models are invertible and this will also be shown in this section. The low porosity three-strut RUC model, shown in Figure 2.8(a), is a simpler model to use to determine parameters regarding the geometry related properties of the model. The results are also the same as those obtained from the high porosity model, which makes it a convenient model to work with. The high porosity model is, however, the more accurate representation of the high porosity fibrous porous media considered in this study due to its closer physical resemblance. Reference to only the high porosity model will be made in this study for calculation purposes. The low porosity model is, however, provided as a convenient way to determine the same calculations and can prove to be especially convenient when adjustments, such as compression in Chapter 4, are performed to the model geometry. The low porosity model will not be utilized beyond this section, but the way in which it can be utilized for the adjustments addressed in the subsequent chapters

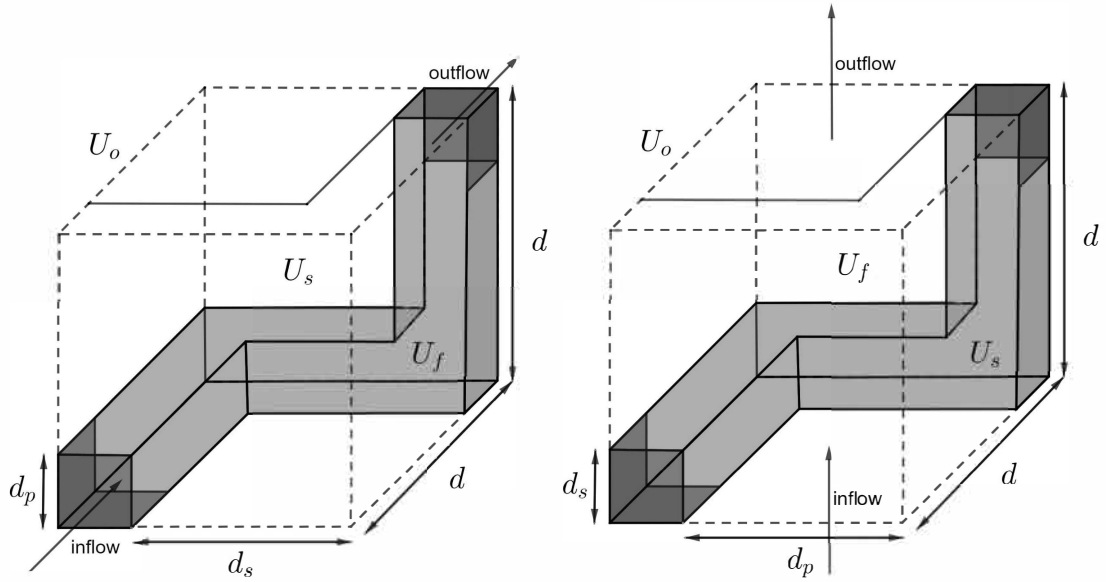

(a) *Low porosity model* (b) *High porosity*

FIGURE 2.8: *Three-strut RUC models*

of this study is similar to the demonstration provided in this chapter. In this section, the permeability coefficients and specific surface area derivations and expressions for the three-strut RUC model are included.

2.5.1 Permeability prediction

Equation (1.10) will once again be used to determine the pressure gradient for the Darcy flow regime and equation (1.19) for the Forchheimer flow regime. For the three-strut RUC model, $\xi = 1$, and the average wall shear stresses can furthermore be determined using equation (1.12) due to the assumption of plane Poiseuille flow. The solid surface areas of the three-strut RUC models are shown in Figures 2.9 and 2.10, for the low and high porosity models, respectively. It is noted that the surface perpendicular to the streamwise flow is divided into two types due to the two perpendicular flow directions present in the three-strut RUC model. The solid surface areas calculated from Figure 2.10 are thus given by

$$S_{\parallel} = S_{\perp_1} = S_{\perp_2} = 4 d_s d_p \,. \tag{2.116}$$

It is also evident that

$$A_{p_{\parallel}} = d_p^2 \,, \tag{2.117}$$

and substituting equation (2.117) into equation (1.13) leads to

$$w_{\parallel} = \frac{q d^2}{d_p^2} \,. \tag{2.118}$$

It furthermore follows that $A_{p_{\parallel}} = A_{p_{\perp}}$, and therefore $w_{\parallel} = w_{\perp}$, due to conservation of mass (equation (1.14)). Consequently,

$$\tau_{w_{\parallel}} = \tau_{w_{\perp_1}} = \tau_{w_{\perp_2}} = \frac{6 d^2}{d_p^3} \mu q \,. \tag{2.119}$$

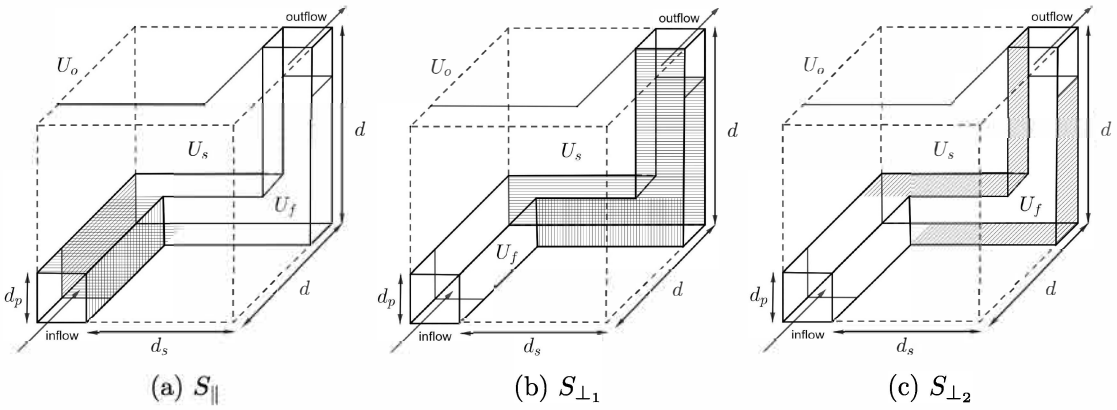

(a) $S_{\parallel}$ (b) $S_{\perp_1}$ (c) $S_{\perp_2}$

FIGURE 2.9: *Solid surfaces of low porosity three-strut RUC model*

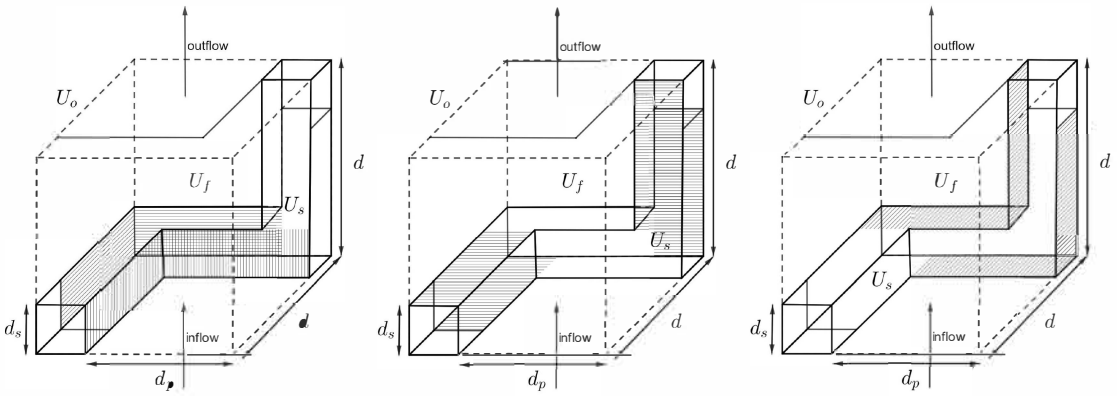

(a) $S_{\parallel}$ (b) $S_{\perp_1}$ (c) $S_{\perp_2}$

FIGURE 2.10: *Solid surfaces of high porosity three-strut RUC model*

Utilizing equation (1.10), along with equations (2.116) to (2.119), and recalling that $b = d_s$ for the three-strut RUC model, the pressure gradient for the Darcy flow regime can therefore be determined as follows:

$$\frac{\Delta p}{d} = \frac{S_{\parallel}\tau_{w_{\parallel}} + S_{\perp_1}\tau_{w_{\perp_1}} + S_{\perp_2}\tau_{w_{\perp_2}}}{A_{p_{\parallel}}} = \frac{72 d_s d}{d_p^4}\mu q = \frac{9\psi^2(\psi-1)^3}{b^2\epsilon^2}\mu q\,. \tag{2.120}$$

The cross-sectional area of solid that faces upstream is furthermore given by

$$S_{\text{face}} = 2 d_s d_p\,. \tag{2.121}$$

Substituting equation (2.121), along with equation (2.118), into equation (1.19) leads to

$$-\nabla\langle p\rangle_f = \frac{\psi^2(\psi-1)^2(3-\psi)}{4b\epsilon^3}\rho q^2\,\underline{\hat{n}}\,, \tag{2.122}$$

which is the pressure gradient for the Forchheimer flow regime. The Ergun-type equation for the three-strut RUC model can therefore be expressed as:

$$\frac{\Delta p}{d} = \frac{9\psi^2(\psi-1)^3}{b^2\epsilon^2}\,\mu q + \frac{\psi^2(\psi-1)^2(3-\psi)}{4b\epsilon^3}\,\rho q^2\,, \tag{2.123}$$

in terms of b and

$$\frac{\Delta p}{d} = \frac{9\psi^2(\psi-1)(3-\psi)^2}{d_p^2\epsilon^2}\mu q + \frac{\psi^2(\psi-1)(3-\psi)^2}{4d_p\epsilon^3}\rho q^2\,, \tag{2.124}$$

in terms of d_p. Substituting equations (2.123) and (2.124) into equation (1.1), with $L = d$, the permeability coefficients in terms of b and d_p are deduced, i.e.

$$K = b^2\frac{\epsilon^2}{9\psi^2(\psi-1)^3}\,, \tag{2.125}$$

and

$$K_F = b\frac{4\epsilon^3}{\psi^2(\psi-1)^2(3-\psi)}\,, \tag{2.126}$$

are the Darcy and Forchheimer permeability coefficients in terms of b and

$$K = d_p^2\frac{\epsilon^2}{9\psi^2(\psi-1)(3-\psi)^2}\,, \tag{2.127}$$

and

$$K_F = d_p\frac{4\epsilon^3}{\psi^2(\psi-1)(3-\psi)^2}\,, \tag{2.128}$$

are the Darcy and Forchheimer permeability coefficients in terms of d_p, respectively, where ψ is given by equation (2.72).

2.5.2 Specific surface area prediction: Geometric approach

The specific surface area determined using a geometric approach is the same as described in the case of the 3D RUC model since the specific surface area obtained in this manner is only based on the geometry of the model. Equations (2.84) to (2.86) will consequently also be utilized to predict the specific surface area obtained using a geometric approach of the three-strut RUC model.

2.5.3 Specific surface area prediction: Combined approach

The combined approach for determining the specific surface area is performed by combining equations (2.86) and (2.127) in order to obtain the specific surface area in terms of the Darcy permeability coefficient, i.e.

$$S_v = \frac{\epsilon(3-\psi)}{2\psi}\sqrt{\frac{\psi-1}{K}}\,, \tag{2.129}$$

and by combining equations equations (2.86) and (2.128) in order to obtain the specific surface area in terms of the Forchheimer permeability coefficient, i.e.

$$S_v = \frac{6\epsilon^3}{K_F\psi^2}\,, \tag{2.130}$$

where ψ is given by equation (2.72).

In the following section, the models obtained from the literature provided in Chapter 1 will be evaluated against data obtained from the literature, also provided in Chapter 1.

2.6 Comparison of literature models

In Section 1.3 of Chapter 1 different analytical models representing fibrous porous media obtained from the literature were provided and summarized, along with experimental and numerical data, for the prediction of the permeability and specific surface area of fibrous media. In this section, these models will be evaluated against the data in order to have a reference of performance to compare that of the RUC models against in the following section, along with some of the RUC model adaptations in future chapters. The manner in which the models are evaluated include tables that give the relative percentage error between the model predictions and data, of the permeability and specific surface area where available, and figures that show the comparison between the model predictions and data. The relative percentage error between the model predictions and data is calculated using the following formula:

$$\text{Rel. \% error} = \frac{|\text{Model prediction} - \text{Data value}|}{\text{Data value}} \times 100\,. \tag{2.131}$$

For a data set, the relative percentages calculated using equation (2.131) of each of the data points in the set are summed and then divided by the number of data points in order to obtain the relative percentage error of the model predictions with respect to the data set. The evaluations are divided into the permeability and specific surface area prediction, which are then subdivided into medium type categories, i.e. fibre and foamlike media.

2.6.1 Permeability predictions

The permeability predictions are made dimensionless using the fibre diameter for the fibre-type media models and data and the pore diameter for the foamlike media models and data. In the case of the fibre-type media, only the Darcy permeability coefficient predictions and data are compared, as no Forchheimer permeability coefficient information could be found in the literature by the author for comparison purposes, as explained in Chapter 1. In the case of foamlike media, both the Darcy and Forchheimer permeability coefficients can be evaluated due to sufficient information provided in the literature.

Fibre-type media

The dimensionless Darcy permeability predictions of the models for fibre-type media and data obtained from the literature are compared in Table 2.1 and Figures 2.11 to 2.13. The relative percentage errors listed in Table 2.1 reveal that the Van Doormal [61] model has an average better performance than the other two models obtained from the literature in the case where 2D in-plane and through plane flow are considered. In the case where 3D fibre arrangement predictions are compared, the Tomadakis and Robertson [60] model performs better than the Tamayol and Bahrami [54] model against the data provided in this study. It is also noted that the relative percentage errors of the comparisons involving the numerical data of Higdon and Ford [25] are significantly higher, in most cases, than the other errors shown. When Figures 2.11 to 2.13 are considered, the Higdon and Ford [25] data seem to give good approximations to the model predictions provided, however, and upon investigation it is noted that these large percentage errors are caused by the last data points where $\epsilon > 0.9$. Due to the tendency of the models and data at such high

TABLE 2.1: *Relative percentage error of fibre models from the literature compared to K/b^2 data of Chapter 1*

Fibre orientation	Data (Sections 1.3.3 and 1.3.4)	Literature models (Section 1.3.1)		
		Tomadakis and Robertson [60]	Van Doormal [61]	Tamayol and Bahrami [54]
2D in-plane	Higdon and Ford [25] (num.)	3789 %	68 %	-
	Fotovati et al. [26] (num.)	65 %	48 %	-
2D through plane	Gostick et al. [17] (exp.)	50 %	53 %	57 %
	Higdon and Ford [25] (num.)	3565 %	55 %	2005 %
	Fotovati et al. [26] (num.)	93 %	12 %	19 %
3D	Manzo et al. [23] (exp.)	27 %	-	167 %
	Theron et al. [24] (exp.)	83 %	-	717 %
	Higdon and Ford [25] (num.)	3728 %	-	7915 %
	Fotovati et al. [26] (num.)	75 %	-	2768 %

porosity values towards infinity, the percentage error increase is understood. When the last two data points of the Higdon and Ford [25] numerical data are removed from the calculation, most of the percentage errors drop to below 200 %. High relative percentage errors, as observed in Table 2.1, are not uncommon where permeability data of porous media are compared to model predictions. Uncertainties in experimental data, especially of porosity measurements, furthermore have a significant effect on percentage error results for higher porosity values due to the steep increase in permeability at high porosities.

Figure 2.11 shows the dimensionless Darcy permeability predictions of the models and data obtained from the literature for 2D in-plane flow of fibre-type media. It can be seen

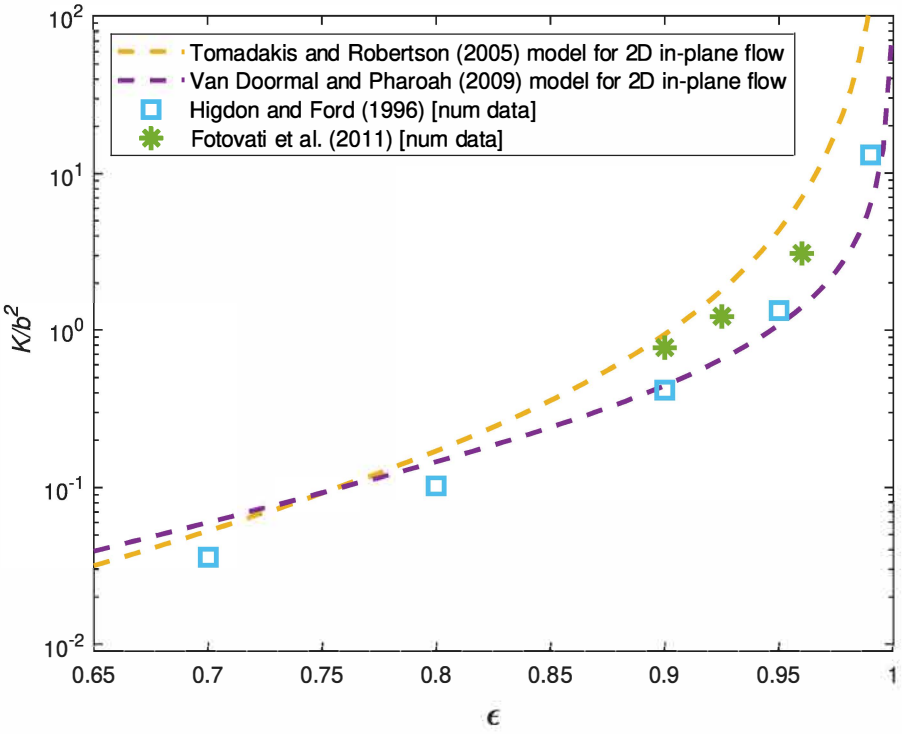

FIGURE 2.11: *Dimensionless Darcy permeability prediction versus porosity of 2D fibre models and data from the literature for in-plane flow*

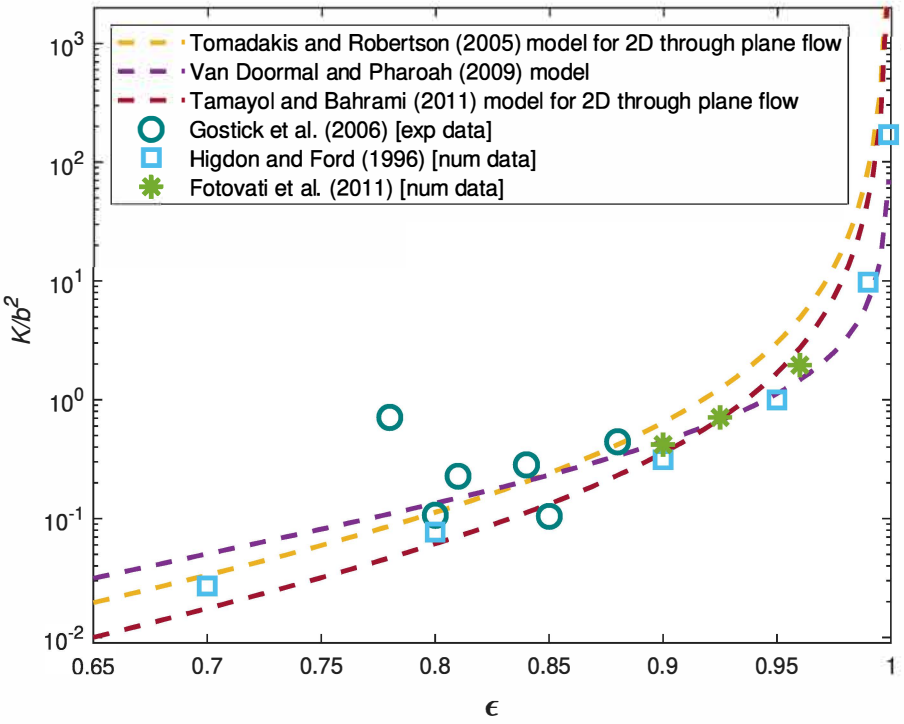

FIGURE 2.12: *Dimensionless Darcy permeability prediction versus porosity of 2D fibre models and data from the literature for through plane flow*

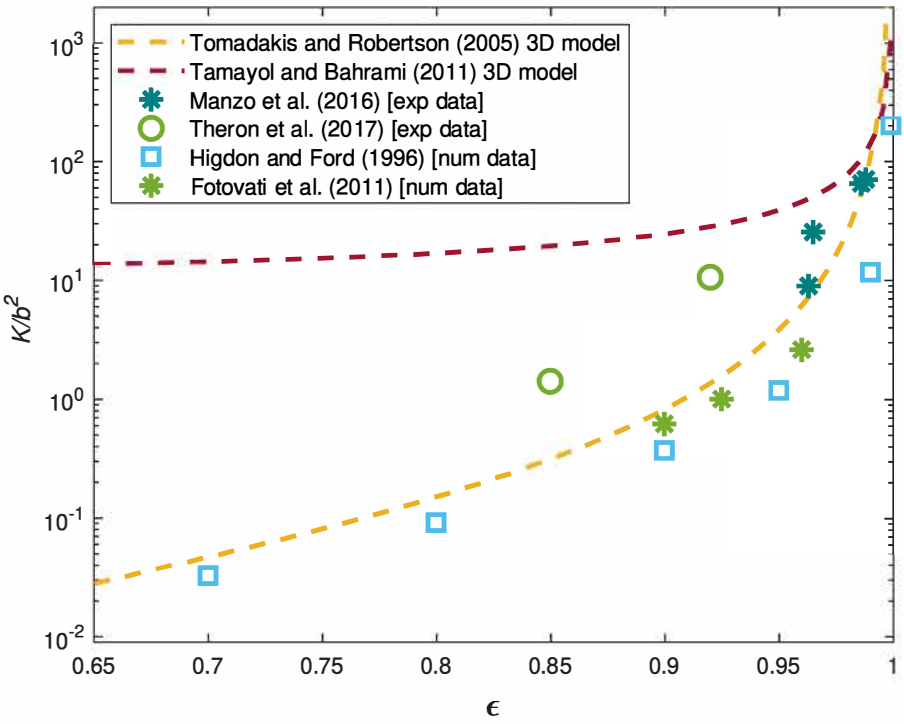

FIGURE 2.13: *Dimensionless Darcy permeability prediction versus porosity of 3D fibre models and data from the literature*

that for high porosity values, the two models enclose the two sets of numerical data. For lower porosity values, both models perform equally well. In Figure 2.12 the dimensionless Darcy permeability predictions of the literature models and data for 2D through plane flow of fibre-type media are shown and also reveals the relatively close correspondence of the models and data. The dimensionless Darcy permeability predictions of the 3D fibre-type media models and data are shown in Figure 2.13. It is evident that the Tomadakis and Robertson [60] model provides closer correspondence to the data than the Tamayol and Bahrami [54] model and that the latter model gives poor correspondence with the data considered. It is furthermore noted that Tomadakis and Robertson [60] have reported excellent correspondence with numerous experimental data samples and other authors in the literature also confirm good agreement of this model with their numerical simulations, such as Soltani et al. [28].

The comparison of the models and data of foamlike media obtained from the literature will be shown next.

Foamlike media

There are not an abundance of literature models for the prediction of the permeability of foamlike media and therefore for the Forchheimer permeability only two models from two different sources are evaluated and in the case of the Darcy permeability prediction, only one model. The relative percentage errors obtained from the comparison of the models and data under consideration are presented in Table 2.2.

TABLE 2.2: *Relative percentage error of foam models from the literature compared to K/d_p^2 and K_F/d_p data of Chapter 1*

Permeability coefficient (dimensionless)	**Experimental data (Section 1.3.3)**	**Literature models (Section 1.3.2)**	
		Dietrich et al. [20]	Giani et al. [64]
K/d_p^2	Kim et al. [16]	38 %	-
	Bhattacharya et al. [3]	520 %	-
	Topin et al. [18]	832 %	-
	Dukhan [9]	174 %	-
	Garrido et al. [19]	365 %	-
	Dietrich et al. [20]	37 %	-
	Mancin et al. [21]	227 %	-
	Mancin et al. [22]	535 %	-
	Average	341 %	-
K_F/d_p	Bhattacharya et al. [3]	46 %	17 %
	Topin et al. [18]	31 %	23 %
	Dukhan [9]	39 %	56 %
	Garrido et al. [19]	39 %	65 %
	Dietrich et al. [20]	14 %	38 %
	Mancin et al. [21]	43 %	47 %
	Mancin et al. [22]	43 %	54 %
	Average	36 %	43 %

In Table 2.2 it can be noticed that the percentage errors concerning the Darcy permeability predictions are much higher than those of the Forchheimer permeability predictions. It is important to note that the Darcy permeability is made dimensionless by dividing by the pore diameter squared and therefore significantly increasing any experimental error that might have been present in the measurement of the pore diameter, whereas the Forchheimer permeability coefficient with division by the pore diameter does

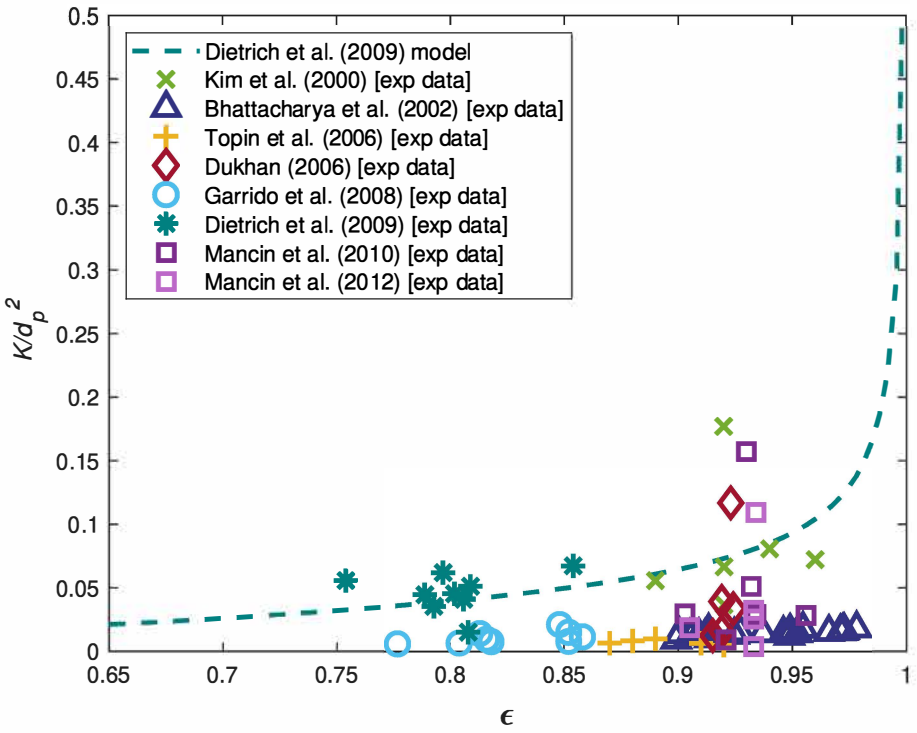

FIGURE 2.14: *Dimensionless Darcy permeability prediction versus porosity of foam models and data from the literature*

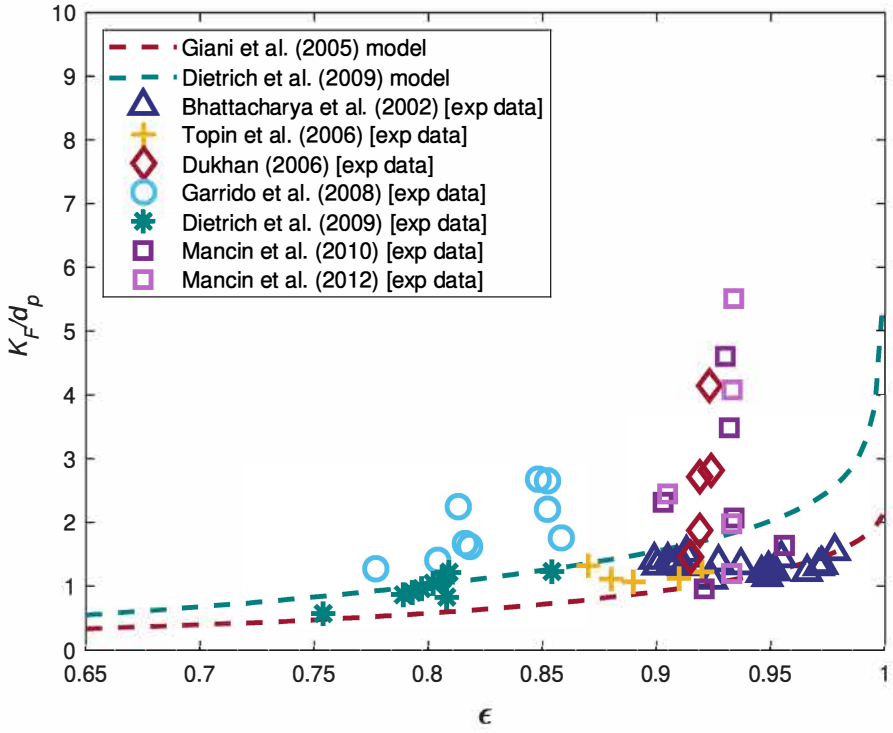

FIGURE 2.15: *Dimensionless Forchheimer permeability prediction versus porosity of foam models and data from the literature*

not involve taking the square of any experimentally obtained value. In the case of the comparisons involving the Forchheimer permeability prediction, the Dietrich et al. [20] model provided on average more accurate predictions than the Giani et al. [64] model. The Dietrich et al. [20] model also compares favourably with the data provided by Dietrich et al. [20] due to this data being incorporated into the model prediction. Figures 2.14 and 2.15 show the model permeability predictions and experimental data for graphical comparison purposes.

In Figure 2.14 it is noted that the majority of the experimental data are lower than the model predictions. The model of Dietrich et al. [20] therefore yields a general over prediction when compared to the experimental data considered. In Figure 2.15 the contrary is however observed with the models under-predicting the majority of the data.

In the following section, the specific surface area predictions and data acquired from the literature will be considered.

2.6.2 Specific surface area predictions

Only the foamlike media models and data are evaluated in this section due to the lack of predictive equations and data for the specific surface area of fibre-type media in the literature. The dimensionless specific surface area is evaluated and is made dimensionless by multiplying the specific surface area with the pore diameter.

Foamlike media

The relative percentage errors between the literature models for the dimensionless specific surface area predictions and experimental data provided in Chapter 1 are presented in Table 2.3. The experimental data values were obtained by multiplying the specific surface area and pore diameter data given in Section 1.3.3. In Table 2.3, the models obtained from the literature are furthermore listed by the geometry type of the model, i.e. cubic unit cell (CUC) model, tetrakaidecahedron model and dodecahedron model. The model obtained from Huu et al. [5], i.e. the dodecahedron model, was divided into the model with triangular (tri.) struts and the model with cylindrical (cyl.) struts, as explained in Chapter 1. The column listing the percentage errors in Table 2.3 for the dodecahedron model with triangular struts are based on data where the porosity was greater than 0.9, whereas the column showing the percentage errors for the dodecahedron model with cylindrical struts are based on data where the porosity was less than 0.9. In general, the model of Richardson et al. [45] (involving the corrected version) and the model of Lacroix et al. [68], performed the best when compared to the experimental data considered. The Buciuman and Kraushaar-Czarnetzki model also performed well, and it is noted that the best performing model in general of all the literature models considered in this section is credited to the tetrakaidecahedron model.

In Figure 2.16 the dimensionless specific surface area of the models and data obtained from the literature are shown. The comparison of the models and the data, as shown in Figure 2.16, reveals that the data that give most of the performance credit to the tetrakaidecahedron model are the sets obtained from Garrido et al. [19] and Dietrich et al. [20]. The other data sets at medium to higher porosity values correspond better to the specific surface area predicted by the model of Giani et al. [64]. For high porosity

TABLE 2.3: *Relative percentage error of foam models from the literature compared to $S_v d_p$ data of Chapter 1*

Experimental data (Section 1.3.3)	**Literature models (Section 1.3.2)**					
	CUC		Tetrakaidecahedron		Dodecahedron	
	Giani et al. [64]	Lacroix et al. [68]	Richardson et al. [45]	Buciuman and Kraushaar-Czarnetzki [44]	Huu et al. [5] with tri. struts	Huu et al. [5] with cyl. struts
Kim et al. [16]	16 %	31 %	44 %	45 %	25 %	35 %
Topin et al. [18]	35 %	49 %	59 %	59 %	74 %	81 %
Dukhan [9]	18 %	21 %	28 %	30 %	18 %	-
Garrido et al. [19]	96 %	42 %	8 %	14 %	-	41 %
Dietrich et al. [20]	87 %	33 %	12 %	12 %	-	29 %
Mancin et al. [22]	17 %	21 %	28 %	29 %	18 %	-
Kumar et al. [71]	4 %	28 %	46 %	43 %	-	28 %
Average	39 %	32 %	32 %	33 %	34 %	43 %

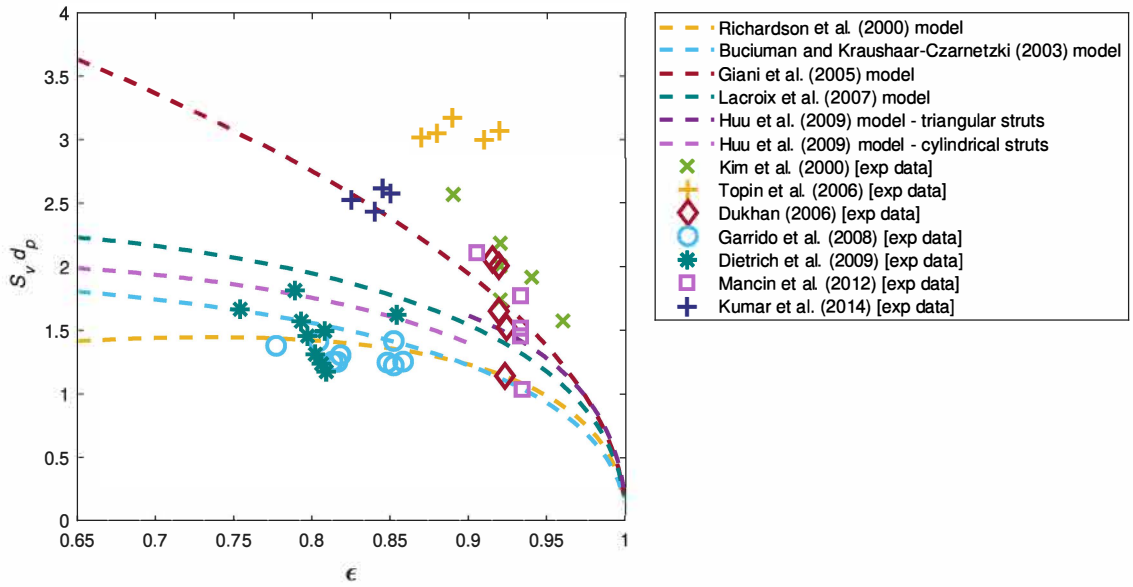

FIGURE 2.16: *Dimensionless specific surface area prediction versus porosity of foam models and data from the literature*

values, where $\epsilon > 0.86$, the cubic unit cell model of Giani et al. [64] is therefore the preferred model. Kumar et al. [71] mentioned the presence of solid accumulation at the strut intersection of foams, as mentioned in Chapter 1. This could possibly be why the specific surface area data provided by them are high and furthermore compare better to the model of Giani et al. [64], since the model of Giani et al. [64] have higher predictions of the specific surface area than the other models obtained from the literature.

In the following section the RUC models considered in this chapter will be compared to each other, as well as to the models and data obtained from the literature.

2.7 Comparison of RUC models

The RUC models in this section will be evaluated similarly to that of the literature models in the previous section, i.e. by including tables that give the relative percentage error between the RUC models and the literature models and data provided in Section 1.3 of Chapter 1, respectively, along with figures that show the graphical comparisons between the relevant model predictions and data. Predictions regarding both the Darcy and Forchheimer permeability coefficients and the specific surface area obtained using the geometric and combined approaches will be considered. In the cases where no models or data obtained from the literature are available, the RUC models will only be compared to each other. These include the cases of the Forchheimer permeability coefficient and specific surface area predictions of fibre-type media. The evaluations will once again be divided into sections for the permeability and specific surface area predictions and then subdivided into the fibre-type and foamlike porous media categories. Porosity values greater than 0.65 were chosen due to the focus of this study being on higher porosity fibrous porous media. Most of the comparisons and concluding results provided in this section were furthermore published by Maré and Woudberg [78].

2.7.1 Permeability predictions

The dimensionless permeability is evaluated in this section and is made dimensionless by dividing by the fibre diameter for the fibre-type media models and data and by dividing by the pore diameter for the foamlike media models and data. In order to obtain the relative percentage error between the predictions of the RUC models and models obtained from the literature, porosity values between $\epsilon = 0.65$ and 1 were chosen consisting of a hundred values between.

Fibre-type media

The predictions for the dimensionless Darcy permeability provided by the RUC models considered to represent fibre-type media, which include the 2D, 3D, two-strut and three-strut RUC models, and the literature models and data from Section 1.3 are compared in Table 2.4 and Figures 2.17 to 2.20.

TABLE 2.4: *Relative percentage error of RUC models that represent fibre-type media compared to K/b^2 predictions and data of Chapter 1*

		RUC models					
		2D		Two-strut		3D	Three-strut
Fibre orientation		in-plane	through plane	in-plane	through plane		
Literature models (Section 1.3.1)							
2D in-plane	Tomadakis and Robertson [60]	19 %	-	36 %	-	-	-
	Van Doormal [61]	93 %	-	53 %	-	-	-
2D through plane	Tomadakis and Robertson [60]	-	8 %	-	36 %	-	-
	Van Doormal [61]	-	58 %	-	56 %	-	-
	Tamayol and Bahrami [54]	-	70 %	-	22 %	-	-
3D	Tomadakis and Robertson [60]	-	-	-	-	17 %	7 %
	Tamayol and Bahrami [54]	-	-	-	-	97 %	96 %
Data (Sections 1.3.3 and 1.3.4)							
2D in-plane	Higdon and Ford [25] (num.)	440 %	-	183 %	-	-	-
	Fotovati et al. [26] (num.)	31 %	-	17 %	-	-	-
2D through plane	Gostick et al. [17] (exp.)	-	50 %	-	54 %	-	-
	Higdon and Ford [25] (num.)	-	317 %	-	254 %	-	-
	Fotovati et al. [26] (num.)	-	61 %	-	21 %	-	-
3D	Manzo et al. [23] (exp.)	-	-	-	-	53 %	53 %
	Theron et al. [24] (exp.)	-	-	-	-	85 %	83 %
	Higdon and Ford [25] (num.)	-	-	-	-	380 %	359 %
	Fotovati et al. [26] (num.)	-	-	-	-	40 %	49 %

The equations considered for comparison of the 2D and two-strut RUC models for in-plane flow are given by equations (2.52) and (2.99), respectively, and the resulting comparisons are given and displayed in Table 2.4 and Figure 2.17. The comparison of relative percentage errors in Table 2.4 and Figure 2.17 of the models and data for 2D in-plane flow of fibre-type media reveal that the two-strut RUC model for in-plane flow performed better in general than the 2D RUC model in comparison to the literature models and numerical data. The RUC models also performed better in general when compared to the data than the literature models, when taking the results provided in Table 2.1 into consideration, the exception being Van Doormal [61] model in comparison with the Higdon and Ford [25] data.

In the case of the models and data representing the Darcy permeability for 2D through plane flow of fibre-type media, the predictions of the two-strut RUC model (provided by

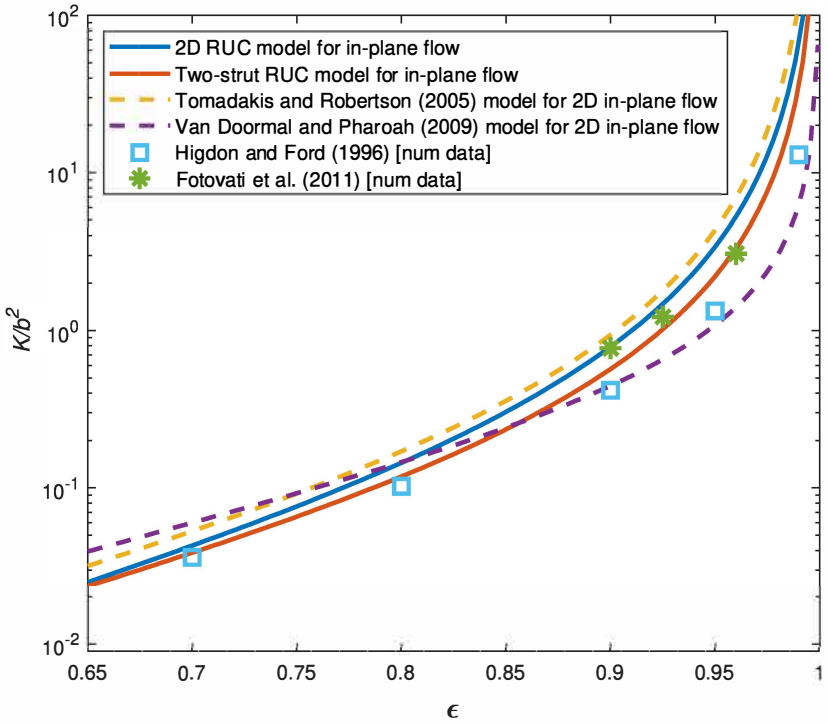

FIGURE 2.17: *Dimensionless Darcy permeability prediction versus porosity of 2D fibre models and data from the literature compared to RUC models for in-plane flow*

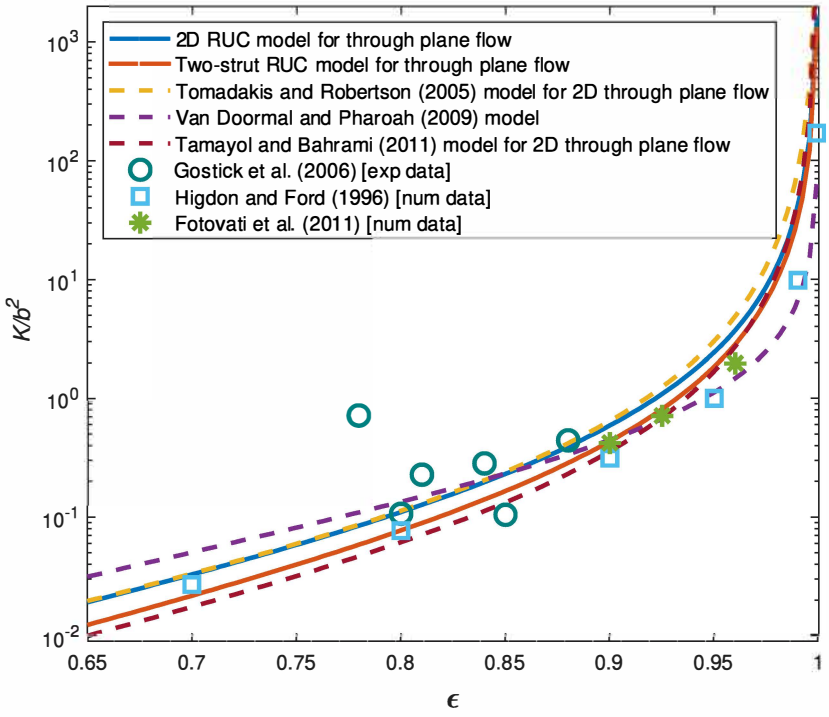

FIGURE 2.18: *Dimensionless Darcy permeability prediction versus porosity of 2D fibre models and data from the literature compared to RUC models for through plane flow*

equation (2.110)) also gave closer average approximations to the literature models and data than the predictions of the 2D RUC model (provided by equation (2.55)), when the relevant results in Table 2.4 and the results shown in Figure 2.18 are considered. It is noted that the Van Doormal [61] model still performed the gave the closest average approximations to the data considered and that the two-strut RUC model corresponds slightly more to the Van Doormal [61] model than the 2D RUC model. Woudberg [55] noted that the 2D RUC model for through plane flow representing a transversely isotropic medium furthermore corresponds well to the model of Tomadakis and Robertson [60] and it is also revealed in this study, deduced from Table 2.4 and Figures 2.17 and 2.18, that the 2D RUC model also corresponds closer to the Tomadakis and Robertson [60] model than the two-strut RUC model. However, in the case of the permeability predictions of the Darcy flow regime, the two-strut RUC model tends to give closer predictions to the models and data obtained from the literature, as provided in this study, than the 2D RUC model.

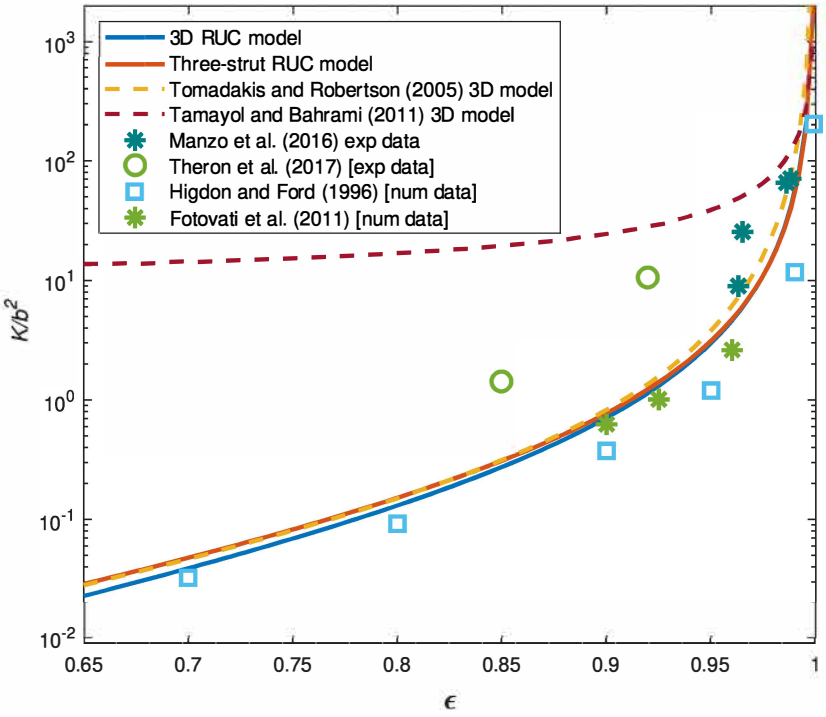

FIGURE 2.19: *Dimensionless Darcy permeability prediction versus porosity of 3D fibre models and data from the literature compared to RUC models*

When comparing the results for the 3D and three-strut RUC model predictions (obtained from equation (2.78) and equation (2.125), respectively), the relative percentage errors in Table 2.4 and the results shown in Figure 2.19, it is concluded that the predictions of the three-strut RUC model are slightly better on average than that of the 3D RUC model. The RUC models furthermore give closer average approximations to the data considered than the models obtained from the literature for 3D fibre-type media, as deduced when comparing the results in Table 2.1 to the results in Table 2.4. It is however noted that the predictions are similar, as is clearly seen in Figure 2.19, between the 3D RUC, three-strut RUC and Tomadakis and Robertson [60] models. The average relative percentage

error of the two RUC models are also similar. One of the data sets, however, correspond better with predictions of the 3D RUC model than that of the three-strut RUC model, and one other data set has the same relative percentage error when compared to both the RUC models. Consequently, one RUC model does not definitively perform better than the other where the Darcy permeability coefficient prediction for 3D fibre-type media are concerned. Woudberg [55] observed that the 3D RUC model agrees well with the analytically weighted model of Tomadakis and Robertson [60], which is satisfactory due to the good correspondence that the model of Tomadakis and Robertson [60] has to the experimental and numerical data, as also mentioned previously in this study. Figure 2.19 also shows that the model of Tamayol and Bahrami [54] give poor correspondence with the data considered, as noted in Section 2.6.1.

The dimensionless Forchheimer permeability predictions of the RUC models representing fibre-type media are shown in Figure 2.20. As previously mentioned, no models or data could be found in the literature by the author for comparison purposes, so only the RUC model predictions are shown. The predicting equations provided by the RUC models for the Forchheimer permeability coefficient are furthermore given as follows: the 2D RUC model for in-plane and through plane flow are given by equations (2.53) and (2.56), respectively, the two-strut RUC model for in-plane and through plane flow are given by equations (2.100) and (2.111), respectively, the 3D RUC model is given by equation (2.79) and the three-strut RUC model equation is given by equation (2.126).

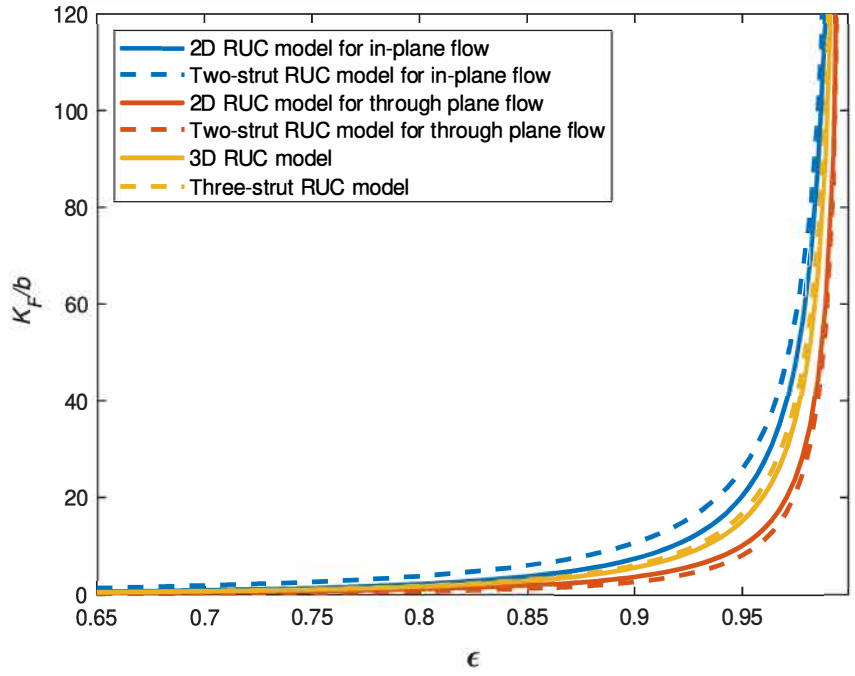

FIGURE 2.20: *Dimensionless Forchheimer permeability prediction versus porosity of fibre RUC models*

From Figure 2.20 it is evident that the RUC models for in-plane flow predict higher K_F/b-values than the RUC models for through plane flow and the RUC models corresponding to 3D fibrous media. This makes sense from a physical point of view since in the case of in-plane flow the resistance to flow is less which makes the fluid flow more easily. Alternatively, the Forchheimer permeability is inversely dependent on the cross-sectional

solid area facing upstream and consequently, the model for in-plane flow with the smaller surface area provides greater Forchheimer permeability predictions. There are furthermore larger discrepancies between the 2D and two-strut RUC models for in-plane flow than between those for through plane flow. The 3D and three-strut RUC models correspond closely to one another, similarly than in the case of the Darcy permeability predictions.

Foamlike media

The equations for predicting the permeability of the RUC models considered to represent foamlike media, i.e. the 3D and three-strut RUC models, are given by equations (2.81) and (2.127), respectively, for the prediction of the Darcy permeability coefficient and equations (2.82) and (2.128), respectively, for the predictions of the Forchheimer permeability coefficient. In Table 2.5 the relative percentage errors of both the permeability predictions for the Darcy and Forchheimer flow regimes are listed. Figure 2.21 furthermore shows the Darcy permeability predictions and Figure 2.22 shows the Forchheimer permeability predictions, both non-dimensionalized with the pore diameter.

TABLE 2.5: *Relative percentage error of RUC models that represent foamlike media compared to K/d_p^2 and K_F/d_p predictions and data of Chapter 1*

Permeability coefficient (dimensionless)		**RUC models**	
		3D	Three-strut
K/d_p^2	**Literature models (Section 1.3.2)**		
	Dietrich et al. [20]	199 %	32 %
	Experimental data (Section 1.3.3)		
	Kim et al. [16]	279 %	33 %
	Bhattacharya et al. [3]	1988 %	403 %
	Topin et al. [18]	2704 %	567 %
	Dukhan [9]	839 %	146 %
	Garrido et al. [19]	1197 %	197 %
	Dietrich et al. [20]	184 %	51 %
	Mancin et al. [21]	895 %	160 %
	Mancin et al. [22]	1900 %	399 %
	Average	1248 %	244 %
K_F/d_p	**Literature models (Section 1.3.2)**		
	Dietrich et al. [20]	75 %	33 %
	Giani et al. [64]	199 %	50 %
	Experimental data (Section 1.3.3)		
	Bhattacharya et al. [3]	254 %	87 %
	Topin et al. [18]	144 %	29 %
	Dukhan [9]	57 %	29 %
	Garrido et al. [19]	13 %	54 %
	Dietrich et al. [20]	59 %	24 %
	Mancin et al. [21]	109 %	50 %
	Mancin et al. [22]	78 %	45 %
	Average	102 %	46 %

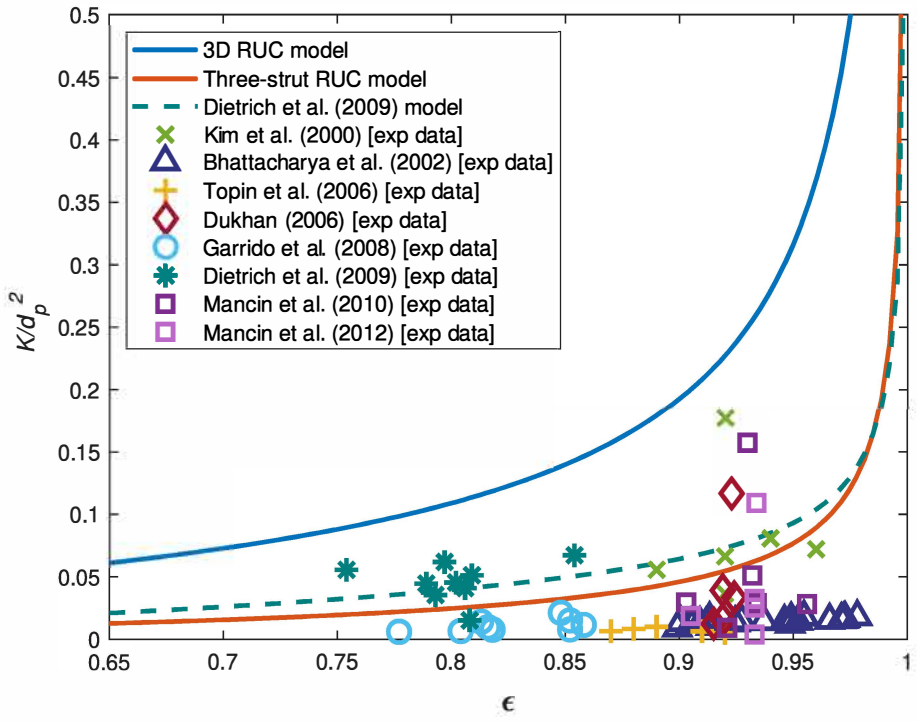

FIGURE 2.21: *Dimensionless Darcy permeability prediction versus porosity of foam models and data from the literature compared to RUC models*

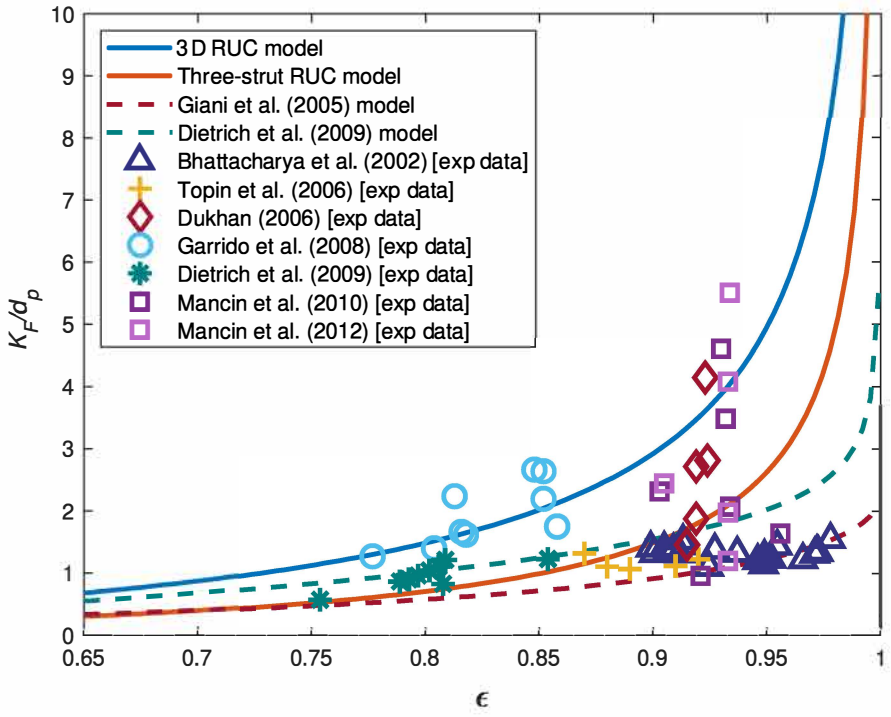

FIGURE 2.22: *Dimensionless Forchheimer permeability prediction versus porosity of foam models and data from the literature compared to RUC models*

The comparison of the 3D and three-strut RUC model performance for predicting the permeability, for both the Darcy and Forchheimer flow regimes, in Table 2.5 and Figures 2.21 and 2.22 clearly reveals that the three-strut RUC model predictions compare better to the models from the literature and experimental data provided in this study than the 3D RUC model, the exception being the comparison with the experimental data for the Forchheimer permeability obtained from Garrido et al. [19]. The permeability predictions of the 3D RUC model are furthermore higher than the predictions of the three-strut RUC model and the literature models for both permeability coefficients, as can be seen in Figures 2.21 and 2.22. When comparing the results of the relative percentage errors in Table 2.2 to those in Table 2.5, it is furthermore noted that the three-strut RUC model provides the best average correspondence to the experimental data amongst all the models considered for the Darcy permeability. The model of Dietrich et al. [20], however, provided a better performance when compared to the experimental data for the Forchheimer permeability than that of the three-strut RUC model and the model of Giani et al. [64] also performed slightly better. The 3D RUC model had the worst average performance amongst all the models when compared to the experimental data and consequently, the three-strut RUC model will be the preferred model for predicting the permeability of foamlike media.

In the following section, the predicting equations provided by the RUC models for the specific surface area obtained using a geometric approach will be evaluated against models and data acquired from the literature.

2.7.2 Specific surface area prediction: Geometric approach

The dimensionless specific surface area obtained using a geometric approach is evaluated in this section. Therefore, due to the models being obtained using a geometric approach, the specific surface area will be multiplied with the fibre diameter in the case of the fibre-type models and the pore diameter in the case of the foamlike models in order to obtain the dimensionless specific surface area. The same method for comparing the models with one another in this section will be used as with the permeability predictions, i.e. porosity values between 0.65 and 1 is utilized. In the case of the fibre-type media, no models from the literature for predicting the specific surface area or experimental data are available and therefore only the RUC models are compared to one another. Models and data from the literature for foamlike media are readily available, however, and therefore a table and figures will be given in order to present the RUC model comparison with the models and data provided.

Fibre-type media

The equations for predicting the specific surface area using a geometric approach provided by the RUC models that represent fibre-type media are given by equations (2.60) and (2.85) for the 2D (or two-strut) RUC model and 3D (or three-strut) RUC model, respectively. It is once again noted that the 2D and two-strut RUC model equations, as well as the 3D and three-strut RUC model equations, in this case, are the same. The predictions for the dimensionless specific surface area for these RUC models are shown in Figure 2.23.

It is evident from Figure 2.23 that the correspondence between the models are close,

especially for very high porosity values, and that the 3D (or three-strut) RUC model provide slightly lower predictions than the 2D (or two-strut) RUC model predictions. The similar predictions between the models representing fibre-type media at higher porosities for the same fibre diameters and porosity values are as expected.

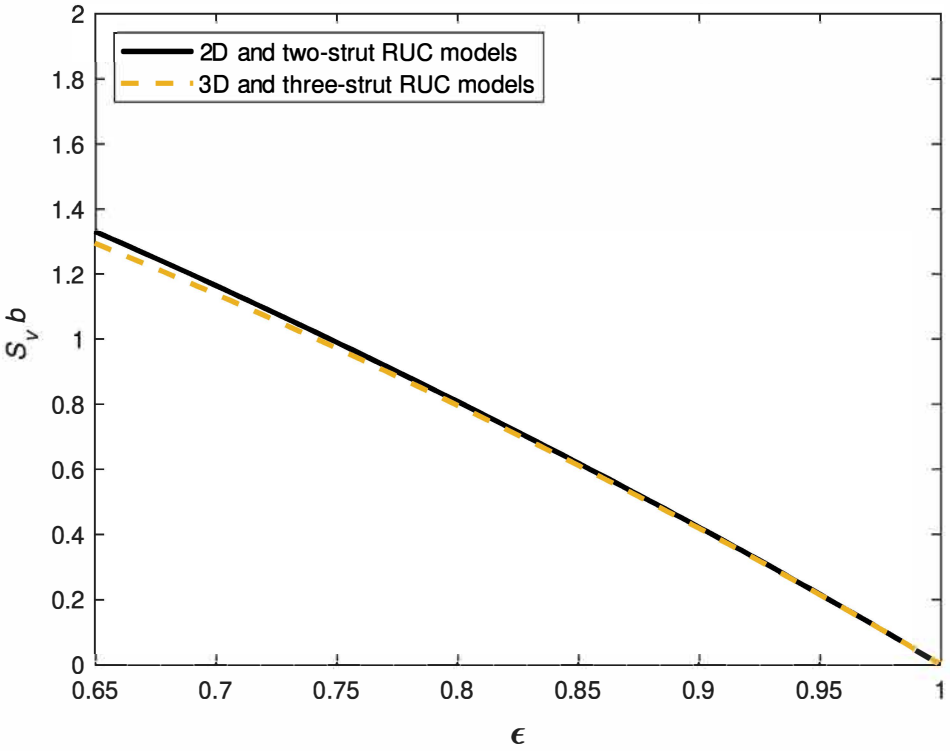

FIGURE 2.23: *Dimensionless specific surface area prediction versus porosity of fibre RUC models*

Foamlike media

Only the 3D (or three-strut) RUC model is once again evaluated against models and experimental data obtained from the literature. The equation of the RUC model for the specific surface area obtained using a geometric approach for foamlike media is furthermore given by equation (2.86) for both the 3D and three-strut RUC models. Multiplying the latter equation with d_p provides the expression for the dimensionless specific surface area considered in this section. The relative percentage errors of the dimensionless specific surface area predictions between the 3D (or three-strut) RUC model and the models and data acquired from the literature (and provided in Section 1.3) are listed in Table 2.6 and the predictions are shown in Figure 2.24.

From Table 2.6 and Figure 2.24 it is seen that the dimensionless specific surface area predicted by the 3D (or three-strut) RUC model give good average approximations to the experimental data and literature models. It is also determined, by comparing Tables 2.3 and 2.6, that the 3D (or three-strut) RUC model has the best average performance amongst all the specific surface area model equations, referring to the literature model equations provided in Section 1.3, when compared to the experimental data considered in this study, for foamlike media.

The equations for the specific surface area based on the combined approach is evaluated against one another and experimental data in the next section.

TABLE 2.6: *Relative percentage error of the RUC model that represents foamlike media compared to $S_v d_p$ predictions and data of Chapter 1*

			RUC model
			3D (or three-strut)
Model type	**Literature models (Section 1.3.2)**		
CUC	Giani et al. [64]		31 %
	Lacroix et al. [68]		10 %
Tetrakaidecahedron	Richardson et al. [45]		23 %
	Buciuman and Kraushaar-Czarnetzki [44]		16 %
Dodecahedron	Huu et al. [5]	with tri. struts	37 %
		with cyl. struts	6 %
Experimental data (Section 1.3.3)			
Kim et al. [16]			30 %
Topin et al. [18]			50 %
Dukhan [9]			21 %
Garrido et al. [19]			31 %
Dietrich et al. [20]			20 %
Mancin et al. [22]			20 %
Kumar et al. [71]			33 %
Average			29 %

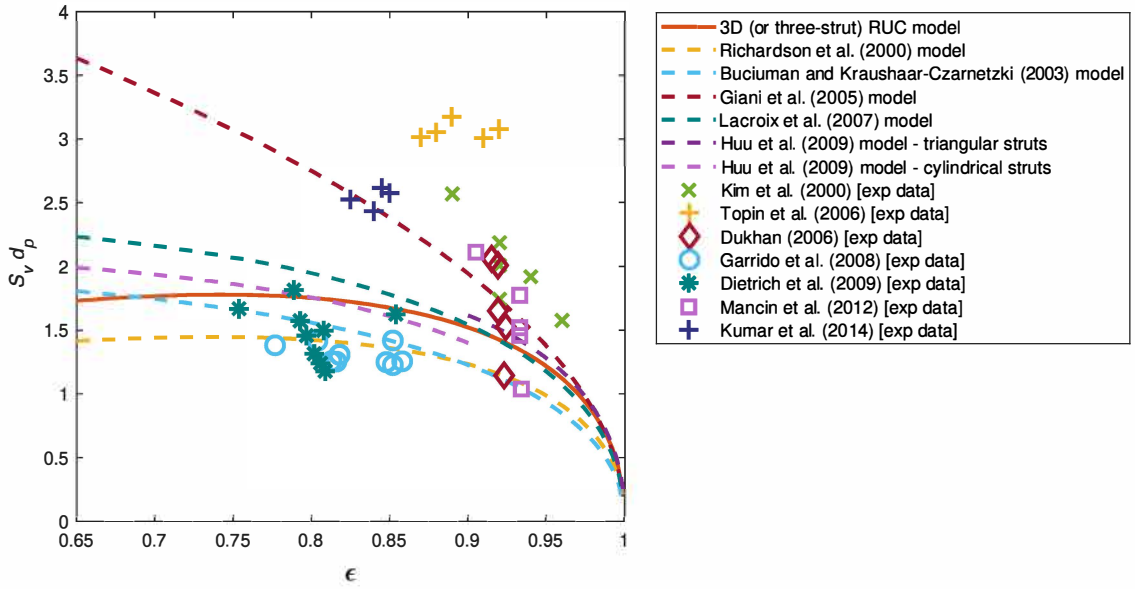

FIGURE 2.24: *Dimensionless specific surface area prediction versus porosity of foam models and data from the literature compared to RUC model using the geometric approach*

2.7.3 Specific surface area prediction: Combined approach

In this section, the dimensionless specific surface area is made dimensionless by respectively multiplying by either the Darcy or Forchheimer permeability coefficient, since the equations for predicting the specific surface area evaluated in this section are obtained using a combined approach. In the case where fibre-type media are considered, only the RUC models are compared to one another due to the lack of specific surface area models and data from the literature. In the case where foamlike media are considered, the RUC models are compared to one another and experimental data provided in the literature using parity diagrams, where both specific surface area and permeability data are required. No models relating the specific surface area and the permeability coefficients from the literature were found to compare the RUC models with either.

Fibre-type media

The equations for the specific surface area in terms of the Darcy permeability coefficient provided by the RUC models are given as follows: equations (2.61) and (2.63) for the 2D RUC model for in-plane and through plane flow, respectively, equations (2.112) and (2.114) for the two-strut RUC model for in-plane and through plane flow, respectively, equation (2.87) for the 3D RUC model and equation (2.129) for the three-strut RUC model. In the same order, the equations of the specific surface area in terms of the Forchheimer permeability coefficient of the RUC models are given by equations (2.62), (2.64), (2.113), (2.115), (2.88) and (2.130). The predictions of these equations are shown

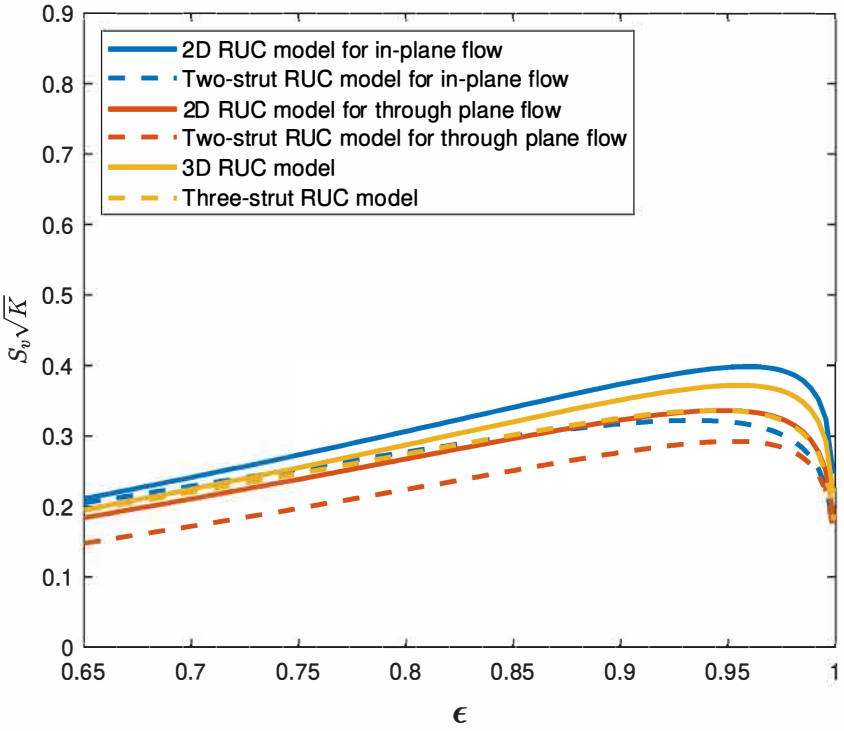

FIGURE 2.25: *Dimensionless specific surface area prediction versus porosity of fibre RUC models using the combined approach with the Darcy permeability coefficient*

in Figures 2.25 and 2.26 for the specific surface area in terms of the Darcy and Forchheimer permeability coefficients, respectively.

In Figure 2.25 it can be seen that the RUC models provide close predictions to one another for the specific surface area in terms of the Darcy permeability. It is noted that the two-strut and three-strut RUC models give lower predictions than their 2D and 3D RUC model counterparts and furthermore, that the three-strut RUC model and 2D RUC model for through plane flow give very similar approximations. The 2D RUC model for in-plane flow give the highest predictions for the porosity range indicated and the two-strut RUC model for through plane flow give the lowest.

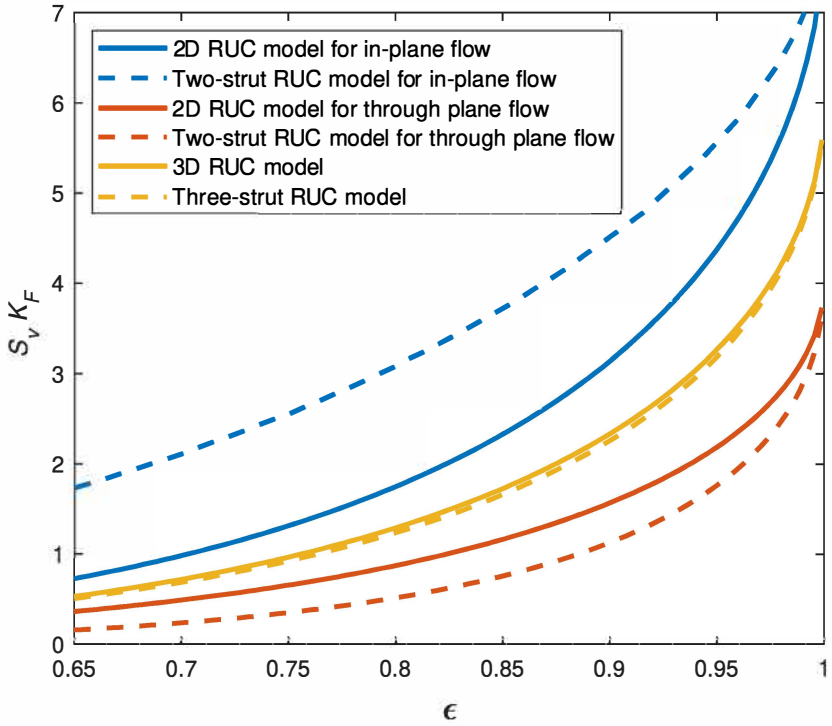

FIGURE 2.26: *Dimensionless specific surface area prediction versus porosity of fibre RUC models using the combined approach with the Forchheimer permeability coefficient*

In Figure 2.26 it is noted that the two-strut RUC model for in-plane flow gives the highest specific surface area predictions for the porosity range indicated with the two-strut RUC model for through plane flow once again giving the lowest prediction. The three-strut and 3D RUC model predictions correspond closely in this model comparison. Due to the specific surface area being non-dimensionalised using the permeability coefficients, the results make physical sense because the 2D fibre orientation with in-plane flow gives the least resistance to flow and therefore will provide the highest permeability. The 2D and two-strut RUC models for through plane flow is expected to provide the lowest predictions for $S_v K_F$ since these models give the lowest predictions for the permeability in Figure 2.20 and give predictions that are practically the same as the predictions of the 3D (or three-strut) RUC model for the specific surface area in Figure 2.23.

The models representing foamlike media will be considered next.

Foamlike media

Due to the availability of corresponding specific surface area and permeability data and the absence of models in the literature for comparison of the specific surface area prediction of foamlike media using the permeability coefficients, parity diagrams are utilized in this section for evaluation of the combined approach predictions of the RUC models. There is furthermore no need to non-dimensionalize the specific surface area. The parity diagrams of the 3D and three-strut RUC models are therefore regarded separately. The RUC models considered are the 3D and three-strut RUC models and the specific surface area equations are respectively given by equations (2.87) and (2.129), in terms of the Darcy permeability, and equations (2.88) and (2.130), in terms of the Forchheimer permeability. It is noted that the equations are the same as those given in the fibre-type media section (i.e. the previous section) for the 3D and three-strut RUC models. The equations provided by the latter models are compared to experimental data in Figures 2.27 to 2.30.

The average relative percentage errors between the respective models and experimental data are indicated on Figures 2.27 to 2.30. These percentage errors reveal that the three-strut RUC model compares more accurately to the experimental data on average than the 3D RUC model where the specific surface area is determined using the Darcy permeability coefficient and that the 3D RUC model compares slightly better when the Forchheimer permeability coefficient is used. It furthermore reveals that the three-strut RUC model performs better on average (with an overall average percentage error of 42%) than the 3D RUC model (with an overall average percentage error of 44%) even though (i) the 3D RUC model provides the closest correspondence with the experimental data when the combined approach using the Forchheimer permeability coefficient is considered and (ii) the error of 2% between the overall average percentage errors of the two models is small.

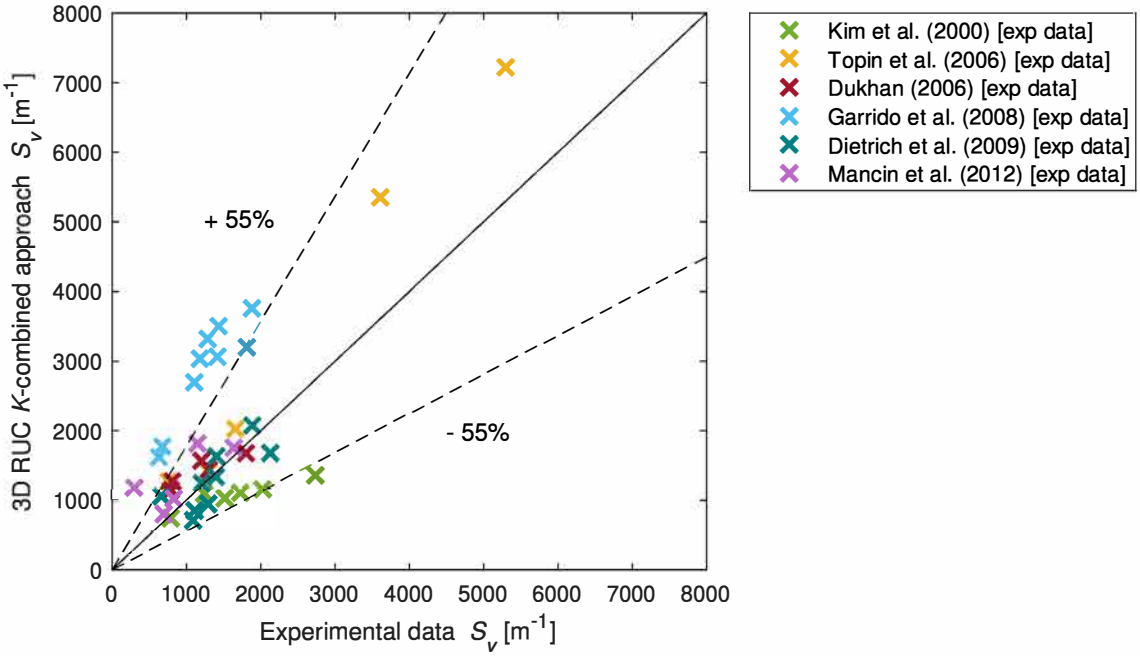

FIGURE 2.27: *Parity diagram of specific surface area: 3D RUC model using the combined approach with the Darcy permeability coefficient versus experimental data*

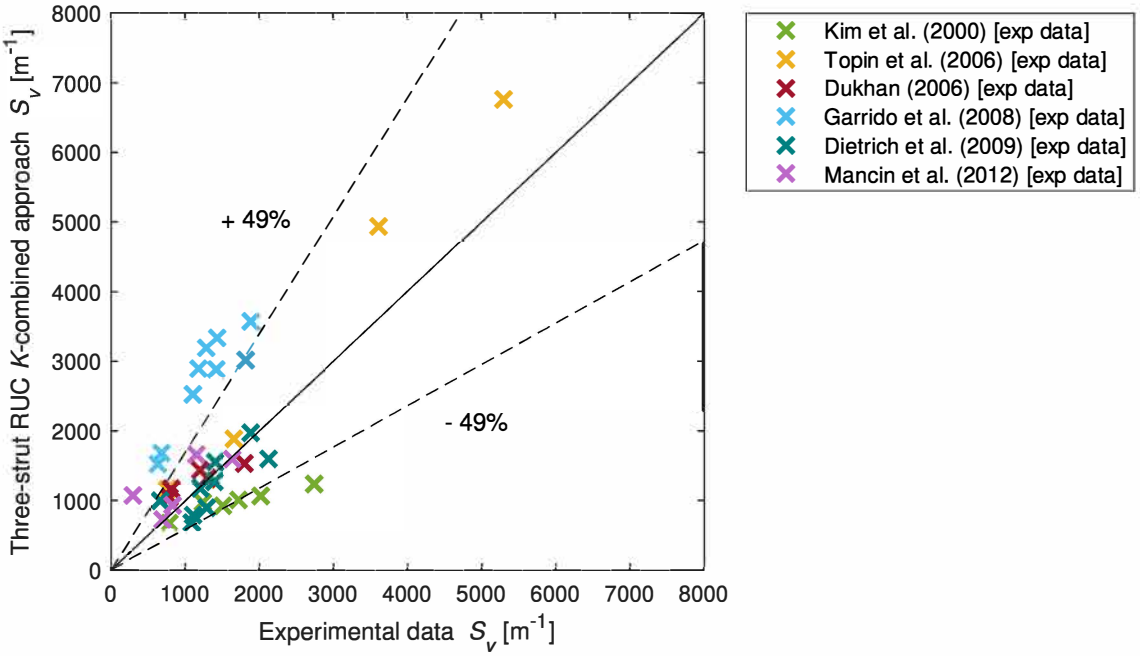

FIGURE 2.28: *Parity diagram of specific surface area: three-strut RUC model using the combined approach with the Darcy permeability coefficient versus experimental data*

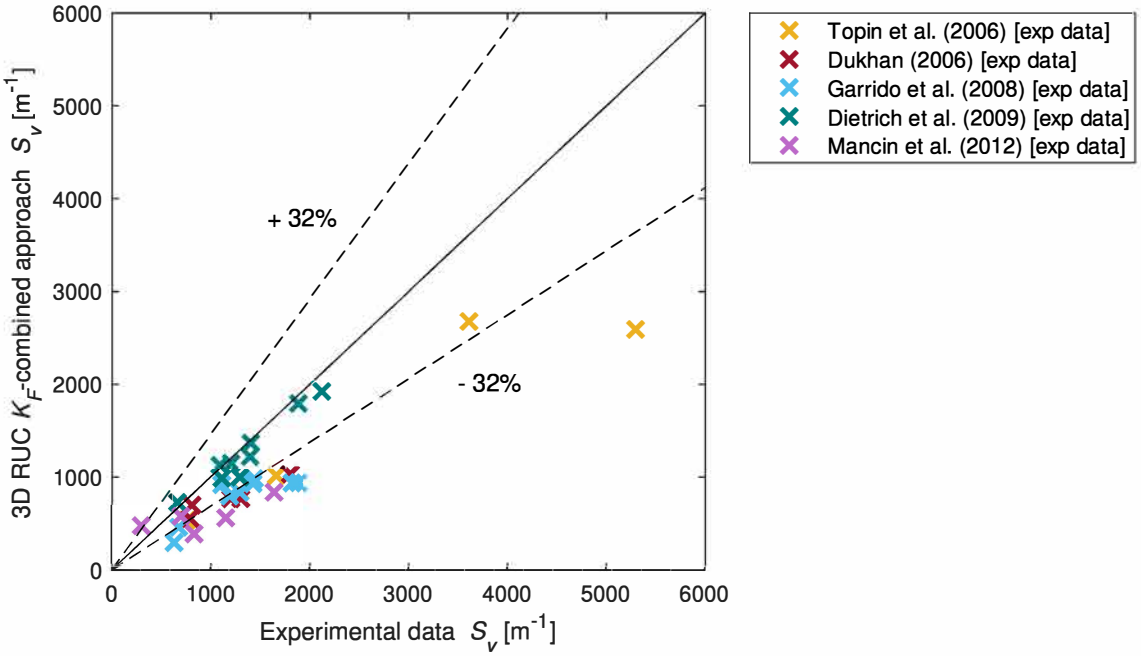

FIGURE 2.29: *Parity diagram of specific surface area: 3D RUC model using the combined approach with the Forchheimer permeability coefficient versus experimental data*

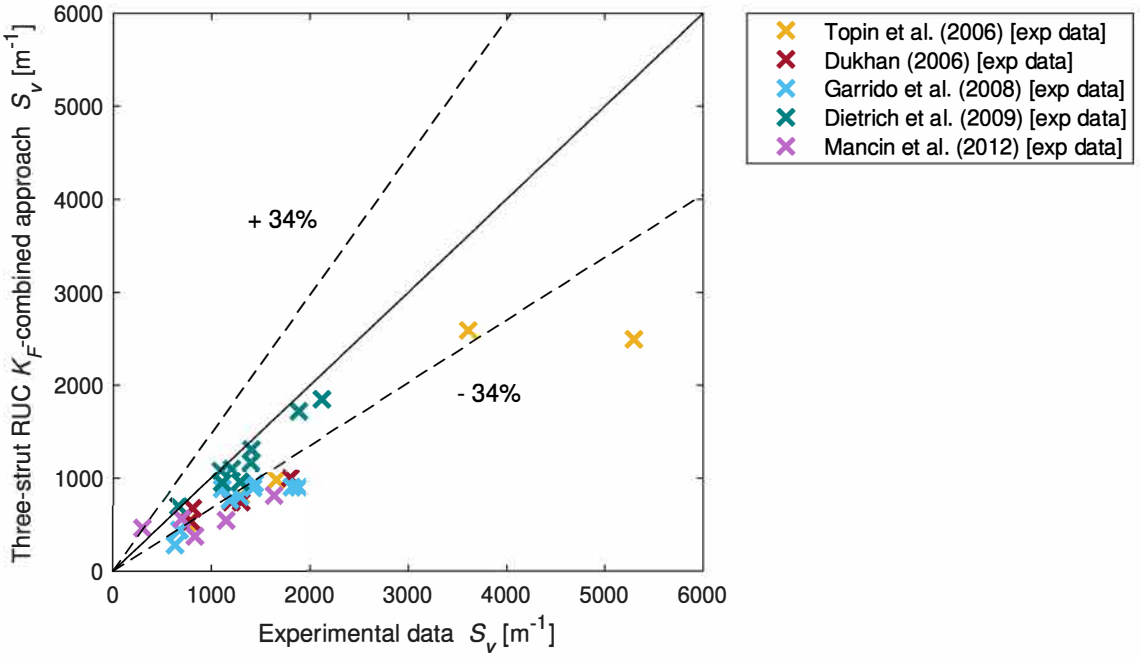

FIGURE 2.30: *Parity diagram of specific surface area: three-strut RUC model using the combined approach with the Forchheimer permeability coefficient versus experimental data*

It consequently does not make a big difference between which model is chosen to obtain the specific surface area using a combined approach for foamlike media. The models evaluated in Figures 2.27 and 2.28 show a relatively even scatter when compared to the experimental data, whereas the models evaluated in Figures 2.29 and 2.30 show a general under prediction of data. Another observation is that the combined approach that makes use of the Forchheimer permeability coefficient tend to give closer correspondence with the experimental data than the combined approach that makes use of the Darcy permeability coefficient. The more accurate performance of the former combined approach can be ascribed to the fact that the Darcy permeability coefficient of which the experimental data is used in the model prediction appears to a power of $-\frac{1}{2}$ in the equation for the specific surface area. Any experimental error will thus also be raised to this power which results in a higher percentage error than in the case of the Forchheimer permeability, which is to a power of -1, due to the permeability measurements being less than 1.

In the following section a table containing a summary of all the model equations obtained in this chapter is provided.

2.8 Chapter summary

In this chapter the 1D, 2D, 3D, two-strut and three-strut RUC models were presented and discussed and the permeability coefficient and specific surface area equations in terms of pore dimensions were provided. The specific surface area in terms of the permeability coefficients were furthermore also provided. All the equations for predicting the permeability and specific surface area of the RUC models discussed in this chapter are listed in Table 2.7. The geometric factor for the 2D (or two-strut) and 3D (or three-strut) RUC

TABLE 2.7: *Summary of permeability coefficient and specific surface area equations acquired based on the collection of RUC models in Chapter 2*

RUC model	Eqn. for	Eqn. i.t.o.	Egn. no.	Eqn.
1D Transverse flow (Section 2.1)	K	b	(2.16)	$b^2\frac{\pi\left(1-\sqrt{1-\epsilon}\right)^3}{4(13.5)(1-\epsilon)^{3/2}}$
	K_F	b	(2.17)	$b\frac{\sqrt{\pi}\,\epsilon\left(1-\sqrt{1-\epsilon}\right)^2}{2(1-\epsilon)}$
	S_v	b	(2.25)	$\frac{8(1-\epsilon)}{\sqrt{\pi}\,b}$
		K	(2.28)	$4\sqrt{\frac{\sqrt{1-\epsilon}\left(1-\sqrt{1-\epsilon}\right)^3}{13.5K}}$
		K_F	(2.30)	$\frac{4\epsilon}{K_F}\left(1-\sqrt{1-\epsilon}\right)^2$
1D Parallel flow (Section 2.1)	K	b	(2.23)	$b^2\frac{\pi\epsilon^3}{192(1-\epsilon)^2}$
	K_F	-	-	-
	S_v	b	(2.25)	$\frac{8(1-\epsilon)}{\sqrt{\pi}\,b}$
		K	(2.31)	$\sqrt{\frac{\epsilon^3}{3K}}$
		K_F	-	-
2D In-plane flow (Section 2.2)	K	b	(2.52)	$b^2\frac{\pi}{4}\left[\frac{1}{2}\left[\frac{48(1-\epsilon)^2}{\epsilon^3}\right]+\frac{1}{2}\left[\frac{13.5(1-\epsilon)^{3/2}}{\left(1-\sqrt{1-\epsilon}\right)^3}\right]\right]^{-1}$
	K_F	b	(2.53)	$b\frac{\sqrt{\pi}\,\epsilon\left(1-\sqrt{1-\epsilon}\right)^2}{1-\epsilon}$
	S_v	b	(2.60)	$\frac{4}{\sqrt{\pi}\,b\psi_1^3}(\psi_1-\epsilon)^2(\psi_1+3\epsilon)$
		K	(2.61)	$\frac{2(\psi_1-\epsilon)^2(\psi_1+3\epsilon)}{\psi_1^3}\sqrt{\frac{2\epsilon^3\left(1-\sqrt{1-\epsilon}\right)^3}{K\left[48(1-\epsilon)^2\left(1-\sqrt{1-\epsilon}\right)^3+13.5\epsilon^3(1-\epsilon)^{3/2}\right]}}$
		K_F	(2.62)	$\frac{4\epsilon(\psi_1-\epsilon)^2(\psi_1+3\epsilon)\left(1-\sqrt{1-\epsilon}\right)^2}{K_F\psi_1^3(1-\epsilon)}$

RUC model	Eqn. for	Eqn. i.t.o.	Egn. no.	Eqn.
2D Through plane flow (Section 2.2)	K	b	(2.55)	$b^2\,\frac{\pi\left(1-\sqrt{1-\epsilon}\right)^3}{54(1-\epsilon)^{3/2}}$
	K_F	b	(2.56)	$b\,\frac{\sqrt{\pi}\,\epsilon\left(1-\sqrt{1-\epsilon}\right)^2}{2(1-\epsilon)}$
	S_v	b	(2.60)	$\frac{4}{\sqrt{\pi}\,b\psi_1^3}(\psi_1-\epsilon)^2(\psi_1+3\epsilon)$
		K	(2.63)	$\frac{2(\psi_1-\epsilon)^2(\psi_1+3\epsilon)}{\psi_1^3}\,\frac{\sqrt{2\left(1-\sqrt{1-\epsilon}\right)^3}}{\sqrt{27K(1-\epsilon)^{3/2}}}$
		K_F	(2.64)	$\frac{2\epsilon(\psi_1-\epsilon)^2(\psi_1+3\epsilon)\left(1-\sqrt{1-\epsilon}\right)^2}{K_F\psi_1^3(1-\epsilon)}$
3D (Section 2.3)	K	b	(2.78)	$b^2\,\frac{\pi}{4}\left[\frac{1}{3}\left[\frac{48(1-\epsilon)^2}{\epsilon^3}\right]+\frac{2}{3}\left[\frac{13.5(1-\epsilon)^{3/2}}{\left(1-\sqrt{1-\epsilon}\right)^3}\right]\right]^{-1}$
		d_p	(2.81)	$d_p^2\,\frac{1-\epsilon}{\left(1-\sqrt{1-\epsilon}\right)^2}\left[\frac{1}{3}\left[\frac{48(1-\epsilon)^2}{\epsilon^3}\right]+\frac{2}{3}\left[\frac{13.5(1-\epsilon)^{3/2}}{\left(1-\sqrt{1-\epsilon}\right)^3}\right]\right]^{-1}$
	K_F	b	(2.79)	$b\,\frac{3\sqrt{\pi}\epsilon\left(1-\sqrt{1-\epsilon}\right)^2}{4(1-\epsilon)}$
		d_p	(2.82)	$d_p\,\frac{3\epsilon\left(1-\sqrt{1-\epsilon}\right)}{2\sqrt{1-\epsilon}}$
	S_v	b	(2.85)	$\frac{3}{\sqrt{\pi}\,b}(3-\psi_2)(\psi_2-1)^2$
		d_p	(2.86)	$\frac{3}{2d_p}(3-\psi_2)(\psi_2-1)^2$
		K	(2.87)	$\frac{3(3-\psi_2)(\psi_2-1)^2}{2}\sqrt{\frac{\epsilon^3\left(1-\sqrt{1-\epsilon}\right)^3}{K\left[16(1-\epsilon)^2\left(1-\sqrt{1-\epsilon}\right)^3+9\epsilon^3(1-\epsilon)^{3/2}\right]}}$
		K_F	(2.88)	$\frac{9\epsilon(3-\psi_2)(\psi_2-1)^2\left(1-\sqrt{1-\epsilon}\right)^2}{4K_F(1-\epsilon)}$
Two-strut In-plane flow (Section 2.4)	K	b	(2.99)	$b^2\,\frac{\pi\epsilon^3\psi_1}{48(\psi_1-\epsilon)^3(3\psi_1+\epsilon)}$
	K_F	b	(2.100)	$b\,\frac{\sqrt{\pi}\,\epsilon^2\psi_1}{2(\psi_1-\epsilon)^2}$
	S_v	b	(2.60)	$\frac{4}{\sqrt{\pi}\,b\psi_1^3}(\psi_1-\epsilon)^2(\psi_1+3\epsilon)$
		K	(2.112)	$(\psi_1+3\epsilon)\sqrt{\frac{\epsilon^3(\psi_1-\epsilon)}{3K\psi_1^5(3\psi_1+\epsilon)}}$
		K_F	(2.113)	$\frac{2\epsilon^2(\psi_1+3\epsilon)}{K_F\psi_1^2}$

RUC model	Eqn. for	Eqn. i.t.o.	Egn. no.	Eqn.
Two-strut Through plane flow (Section 2.4)	K	b	(2.110)	$b^2\frac{\pi\epsilon^4}{48(\psi_1-\epsilon)^3(3\psi_1+\epsilon)}$
	K_F	b	(2.111)	$b\frac{\sqrt{\pi}\epsilon^5}{2\psi_1(\psi_1-\epsilon)^2(\psi_1+\epsilon)}$
	S_v	b	(2.60)	$\frac{4}{\sqrt{\pi}b\psi_1^3}(\psi_1-\epsilon)^2(\psi_1+3\epsilon)$
		K	(2.114)	$\frac{\epsilon^2(\psi_1+3\epsilon)}{\psi_1^3}\sqrt{\frac{\psi_1-\epsilon}{3K(3\psi_1+\epsilon)}}$
		K_F	(2.115)	$\frac{2\epsilon^5(\psi_1+3\epsilon)}{K_F\psi_1^4(\psi_1+\epsilon)}$
Three-strut (Section 2.5)	K	b	(2.125)	$b^2\frac{\epsilon^2}{9\psi_2^2(\psi_2-1)^3}$
		d_p	(2.127)	$d_p^2\frac{\epsilon^2}{9\psi_2^2(3-\psi_2)^2(\psi_2-1)}$
	K_F	b	(2.126)	$b\frac{4\epsilon^3}{\psi_2^2(\psi_2-1)^2(3-\psi_2)}$
		d_p	(2.128)	$d_p\frac{4\epsilon^3}{\psi_2^2(\psi_2-1)(3-\psi_2)^2}$
	S_v	b	(2.85)	$\frac{3}{2b}(3-\psi_2)(\psi_2-1)^2$
		d_p	(2.86)	$\frac{3}{2d_p}(3-\psi_2)^2(\psi_2-1)$
		K	(2.129)	$\frac{\epsilon(3-\psi_2)}{2\psi_2}\sqrt{\frac{\psi_2-1}{K}}$
		K_F	(2.130)	$\frac{6\epsilon^3}{K_F\psi_2^2}$

models are provided by equations (2.44) and (2.72) and are furthermore, respectively, given by

$$\psi_1 = \frac{1}{3} + \frac{2}{3}\sqrt{3\epsilon + 1}\cos\left[\frac{1}{3}\cos^{-1}\left(\frac{9\epsilon - 27\epsilon^2 + 2}{2(3\epsilon + 1)^{3/2}}\right)\right],$$

and

$$\psi_2 = 2 + 2\cos\left[\frac{4\pi}{3} + \frac{1}{3}\cos^{-1}(2\epsilon - 1)\right],$$

in Table 2.7 for easy reference.

All the RUC models considered, with the exception of the 1D RUC models, were evaluated for fibre-type media and the 3D and three-strut RUC models were evaluated for foamlike media by comparing the models to other models and data available in the literature for the respective media types. The model equations in terms of the pore dimensions were evaluated such that it was in terms of the fibre diameter b for fibre-type media and in terms of the pore diameter d_p for foamlike media. (The pore dimensions or permeability coefficients used in the equations given in Table 2.7 are specifically indicated, i.e. whether the equation is given in terms of b, d_p, K or K_F.) It was found that in general, the RUC models compared well or similar to other models in the literature when compared to the data obtained from the literature. Furthermore, the RUC models that performed the best in general amongst the 2D and 3D fibrous porous media types were the two-strut and three-strut RUC models. These models also compared more accurately to the available data from the literature than the other models from the literature.

The expressions for the Darcy and Forchheimer permeability, specific surface area obtained using a geometric approach and specific surface area obtained using a combined approach of the 2D, 3D, two-strut and three-strut RUC models, as well as the novel determination of the permeability predicting equations of the two-strut RUC model for in-plane flow, are published in Maré and Woudberg [78]. Additionally, the evaluation of these models are furthermore included in the aforementioned article.

CHAPTER 3

Foam models including solid lumps at nodes

In foams solid lumps are often present at the intersection of the struts, known as the nodes. Some authors in the literature take these lumps into consideration in their geometric models (e.g., Calmidi and Mahajan [1]). In this chapter these models will be elaborated on and furthermore used to obtain predictive equations for the permeability and specific surface area for given porosity and average pore diameter values. Furthermore, the methods proposed for incorporating solid lumps at the nodes will be replicated into the existing three-strut RUC model. Two options of node adjusted foam RUC models will be considered and evaluated. The models obtained from the literature along with the different RUC model options will be compared to one another and to relevant experimental data obtained from the literature for foams that have different degrees of accumulation of solid matter present at the nodes. The models that take the solid lumps into account will furthermore be compared to the foam models evaluated in Chapter 2 for the data relevant to this chapter. The goal of this chapter is to determine which RUC model with adjustments made to accommodate for solid lumps at the nodes gives the most accurate permeability and specific surface area predictions as well as which methods of determining the foam dimension and node relations give feasible results. The goal is to determine whether the node adjustments to the models do in fact improve model predictions for the relevant data. Only the geometric approach for determining the specific surface area of these RUC models will be included since the changes to the RUC model are limited to the pore-scale parameters and the relations between the specific surface area and permeability coefficients consequently remain unchanged.

3.1 Models from the literature

Six models in the literature representing foamlike porous media that take solid lumps at the nodes of foams into consideration will be discussed in this section and methods for determining the specific surface area will be presented. The models are obtained from Calmidi and Mahajan [1], Boomsma and Poulikakos [2], Bhattacharya et al. [3], Fourie and Du Plessis [4], Huu et al. [5], and Edouard [6]. A seventh node adjusted foam model obtained from Ahmed et al. [7] will also be included in this section for which permeability predictions are provided. It should be noted that the notations used in this section may differ from those used by the aforementioned authors for the sake of consistency throughout the dissertation.

3.1.1 Calmidi and Mahajan [1]

Calmidi and Mahajan [1] developed an analytical model by representing the metal foam structure as a two-dimensional hexagonal array. The edges of the hexagon represent the foam struts and squares at the intersection points of the struts represent the solid lumps that typically appear at the nodes of foams. A unit cell was then identified as shown in Figure 3.1.

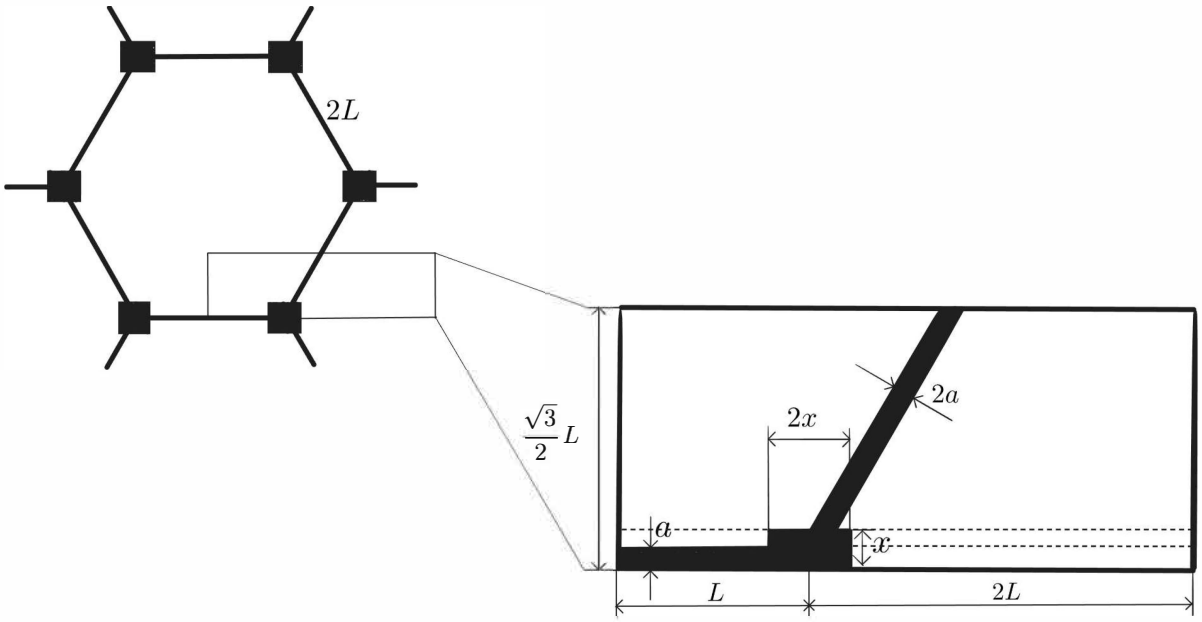

FIGURE 3.1: *Unit cell of 2D hexagonal foam matrix (Calmidi and Mahajan [1])*

The edges of the hexagon therefore have lengths of $2L$, strut widths of $2a$ and node widths of $2x$. In order to obtain the specific surface area, two relations between the model dimensions are defined. The first relation is the area ratio, defined as r_1, and is given by (Calmidi and Mahajan [1])

$$r_1 = \frac{aw}{xw} = \frac{a}{x}, \tag{3.1}$$

where a and x are defined as indicated in Figure 3.1 and w represents the width perpendicular to the plane of the paper. Calmidi and Mahajan [1] determined empirically that $r_1 = 0.09$. This value for the area ratio will also be used in determining the specific surface area. The second ratio is determined by finding an expression for the porosity which is obtained by acquiring the solid and total unit cell volumes, represented by V_s and V_o respectively, from Figure 3.1. Calmidi and Mahajan [1] separated the unit cell into three layers, as indicated in Figure 3.1 by the dashed lines. Therefore, the solid volume is given by adding three volume partitionings of the unit cell and is expressed as

$$V_s = a(L+x)w + 2x(x-a)w + 2a\left[\frac{2}{\sqrt{3}}\left(\frac{\sqrt{3}}{2}L - x\right)\right]. \tag{3.2}$$

The total volume of the unit cell is furthermore given by

$$V_o = 3L\left(\frac{\sqrt{3}}{2}L\right)w. \tag{3.3}$$

Therefore, the solid volume fraction, and hence the porosity, can be determined from equations (3.2) and (3.3):

$$1-\epsilon=\frac{V_s}{V_o}=\frac{a(L+x)+2x(x-a)+\frac{4a}{\sqrt{3}}\left(\frac{\sqrt{3}}{2}L-x\right)}{\frac{3\sqrt{3}}{2}L^2}. \tag{3.4}$$

Using equation (3.1), a can be expressed in terms of the area ratio, i.e. $a=r_1x$. This can, in turn, be substituted into equation (3.4) and rearranged to find the following expression for the relation between x and L, which is the second ratio required (Calmidi and Mahajan [1]):

$$r_2=\frac{x}{L}=\frac{-r_1+\sqrt{r_1^2+\frac{2}{\sqrt{3}}(1-\epsilon)\left[2-r_1\left(1+\frac{4}{\sqrt{3}}\right)\right]}}{\frac{2}{3}\left[2-r_1\left(1+\frac{4}{\sqrt{3}}\right)\right]}. \tag{3.5}$$

An expression for the specific surface area can then be determined in terms of the r_1 and r_2-ratios and the pore diameter. The total surface area can be determined using Figure 3.1 and is given by

$$\begin{aligned}S_{fs}&=2a(L-x)+(L-x)w+2x(2x)+(x-a)w+xw+\left[(2x)w-\frac{4}{\sqrt{3}}aw\right]\\&\quad+2(2a)\left(L-\frac{2}{\sqrt{3}}x\right)+2\left(L-\frac{2}{\sqrt{3}}x\right)w\\&=\left[6r_1xL-\frac{6+8\sqrt{3}}{3}r_1x^2+4x^2\right]+\left[3L+\frac{9-4\sqrt{3}}{3}x-\frac{3+4\sqrt{3}}{3}r_1x\right]w.\end{aligned} \tag{3.6}$$

The specific surface area equation can therefore be determined by dividing the total surface area, i.e. equation (3.6), by the total volume of a unit cell, i.e. equation (3.3), yielding

$$\begin{aligned}S_v&=\frac{1}{w}\left[\frac{4\sqrt{3}}{3}r_1\left(\frac{x}{L}\right)-\frac{16+4\sqrt{3}}{9}r_1\left(\frac{x}{L}\right)^2+\frac{8\sqrt{3}}{9}\left(\frac{x}{L}\right)^2\right]\\&\quad+\frac{1}{L}\left[\frac{2\sqrt{3}}{3}+\frac{6\sqrt{3}-8}{9}\left(\frac{x}{L}\right)-\frac{8+2\sqrt{3}}{9}r_1\left(\frac{x}{L}\right)\right].\end{aligned} \tag{3.7}$$

In this study the width w is assumed to be equal to the strut width, i.e. $2a$. Hence $w=2r_1x$, and r_2 can furthermore be substituted into equation (3.7) to obtain the expression for the specific surface area in terms of the r_1 and r_2-ratios, and L:

$$S_v=\frac{1}{L}\left[\frac{4\sqrt{3}}{3}+\frac{4\sqrt{3}-16}{9}r_2+\frac{4\sqrt{3}}{9r_1}r_2-\frac{8+2\sqrt{3}}{9}r_1r_2\right]. \tag{3.8}$$

The expressions for r_1 and r_2 and calculation thereof, given by equations (3.1), (3.4) and (3.5), were provided by Calmidi and Mahajan [1], whereas the expressions and calculations of the specific surface area, given by equations (3.6) to (3.8), are novel contributions. A relation between the dimension L and the pore diameter is needed in order to obtain the specific surface area in terms of the pore diameter for the purpose of this study. Two options are considered, i.e. one obtained from Buciuman and Kraushaar-Czarnetzki [44]

and the other from Richardson et al. [45], where the foams are represented by tetrakaidecahedron unit cells. The reason for this assumption is that the tetrakaidecahedron cell have predominantly hexagonal faces and the current model considered consists of a 2D hexagonal array. The total volume of the tetrakaidecahedron cells is taken to be equal to the total volume of a hexagon cell, i.e.

$$11.31 l_s^3 = \frac{3\sqrt{3}}{2}(2L)^2 \times w\,, \tag{3.9}$$

where the total tetrakaidecahedron cell volume (left-hand side of equation (3.9)) is given by Buciuman and Kraushaar-Czarnetzki [44] with l_s denoting the side length of a strut in the tetrakaidecahedron cell. The total volume of the hexagonal cell (right-hand side of equation (3.9)) is the area of a hexagon where $2L$ is the side length of the hexagon, and w is the width of the cell.

The equations for the side lengths of the tetrakaidecahedron cell were obtained using relations deduced form the tetrakaidecahedron models provided by Buciuman and Kraushaar-Czarnetzki [44] and Richardson et al. [45], i.e.

$$l_s = \frac{0.64}{1 - 0.62\sqrt{1-\epsilon}} d_p\,, \tag{3.10}$$

and

$$l_s = \frac{0.5498}{1 - 0.971\sqrt{1-\epsilon}} d_p\,, \tag{3.11}$$

respectively. The cell width w of the 2D hexagonal array model can furthermore be written as $w = 2r_1 r_2 L$. Consequently, L can be obtained by substituting the expression for w, as well as equations (3.10) and (3.11), into equation (3.9), resulting in

$$L = \frac{0.64}{1 - 0.62\sqrt{1-\epsilon}} \sqrt[3]{\frac{11.31}{12\sqrt{3}\, r_1 r_2}}\, d_p\,, \tag{3.12}$$

and

$$L = \frac{0.5498}{1 - 0.971\sqrt{1-\epsilon}} \sqrt[3]{\frac{11.31}{12\sqrt{3}\, r_1 r_2}}\, d_p\,, \tag{3.13}$$

respectively. The substitution of equations (3.12) and (3.13) into equation (3.8) therefore leads to two expressions for the specific surface area in terms of the pore diameter, the porosity, r_1 and r_2, where the latter ratio is given by equation (3.5). The predictions acquired for these specific surface area expressions for the porosity range of 0.65 to 0.98, where the dimensionless specific surface area ($S_v d_p$) is used, are shown in Figure 3.2 (by the continuous and dashed bold curves). The predictions of the equations obtained from Calmidi and Mahajan [1] are furthermore compared to the tetrakaidecahedron model without the accumulation of solid at the nodes (and represented by the continuous and dashed slim curves) in Figure 3.2, due to the similarity between the 2D hexagonal array and hexagonal faces of the tetrakaidecahedron model.

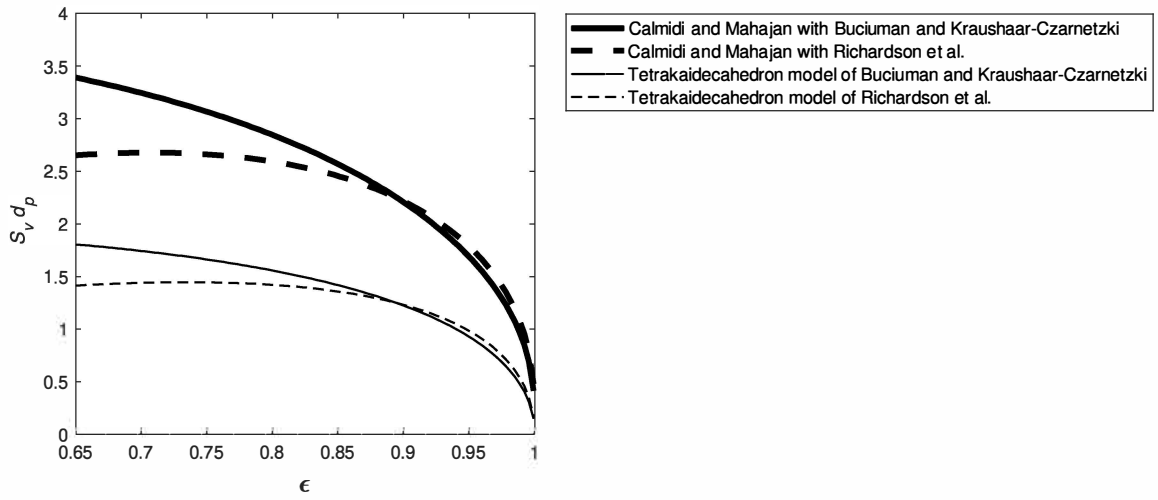

FIGURE 3.2: *Dimensionless specific surface area prediction versus porosity obtained from the node adjusted model of Calmidi and Mahajan [1] and tetrakaidecahedron models from the literature*

The predictions for $\epsilon > 0.65$ are shown for comparison purposes with other models, even though the area ratio determined when compared to the results given by the higher porosity foams in Calmidi and Mahajan [1] were for foams with $\epsilon > 0.9$. Figure 3.2 shows that the predictions between the respective two model options are similar for $\epsilon > 0.85$. This makes sense due to the preference of higher porosity values for the chosen area ratio. Garrido et al. [19] observed an overestimation of specific surface area by the geometric models that do not account for the accumulation of solid at the nodes of the foams, as was mentioned in Chapter 1. Figure 3.2 however reveals that the models that incorporate the solid accumulation give even higher approximations for the specific surface area. Kumar et al. [71] noted, in contrast to Garrido et al. [19], that the accumulation of solid at the nodes lead to an increase in specific surface area. Garrido et al. [19] dealt specifically with ceramic foams with $\epsilon < 0.9$ and mentioned that along with the solid accumulation, some pores in ceramic foams are closed, which logically reduces S_v. Kumar et al. [71] dealt with high porosity metal foams, however, and noted that the strut shape changes with an increase in porosity, which results in accumulation at the nodes. This strut behaviour of metal foams also confirmed the observations of Bhattacharya et al. [3]. Taking all this into consideration, the increase in specific surface area is expected when the solid accumulation at the nodes is taken into account, especially for high porosity metal foams. This increase is also the physically viable result one will expect, barring closed cells in the foam. Lower experimental data values of the specific surface area for ceramic foams at lower porosity values can furthermore also be expected, due to the presence of closed cells (as in the case described by Garrido et al. [19]). The trend of the Calmidi and Mahajan model combined with the side length relation obtained from Richardson et al. [45] is thus preferred in order to accommodate the prediction of the specific surface area for lower and higher porosity open-cell foams.

The model obtained from Boomsma and Poulikakos [2], that represent high porosity foams with solid lumps at the nodes taken into consideration, will be discussed next.

3.1.2 Boomsma and Poulikakos [2]

Boomsma and Poulikakos [2] conducted a similar study as Calmidi and Mahajan [1], the difference being that they presented a three-dimensional generalization of the Calmidi and Mahajan [1] model, i.e. the tetrakaidecahedron. The model has cubic nodes to represent the lumps and has cylindrical struts. A rectangular solid block was inserted into the tetrakaidecahedron to represent the unit cell. The front side and the intersection with the struts and nodes are shown in Figure 3.3 and the square side of the block, the top side, and the intersection with the struts and nodes are shown in Figure 3.4.

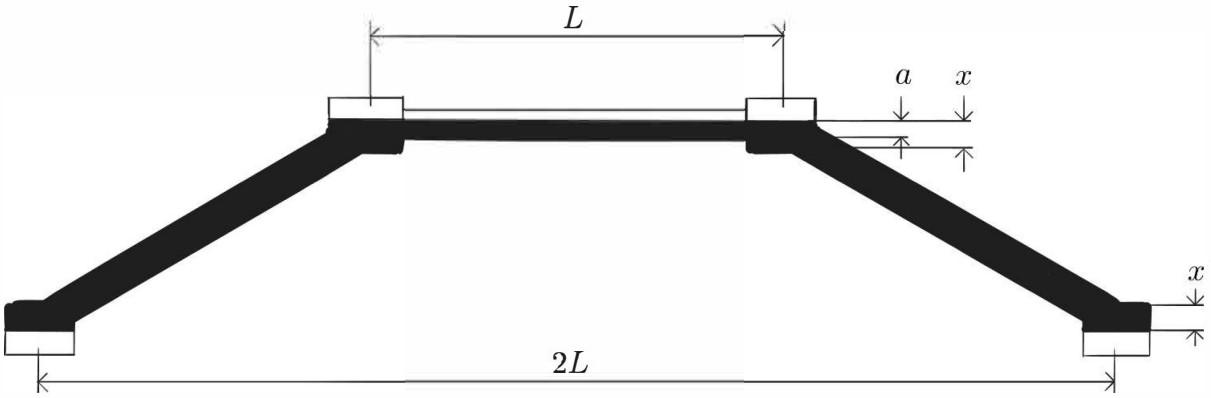

FIGURE 3.3: *Front side view of unit cell of tetrakaidecahedron model (Boomsma and Poulikakos [2])*

In Figure 3.3 the thick lines form part of the rectangular unit cell whilst the thin lines at the nodes and top strut do not form part of the rectangular unit cell but are given for an indication of where the rectangular block intersects with the tetrakaidecahedron structure.

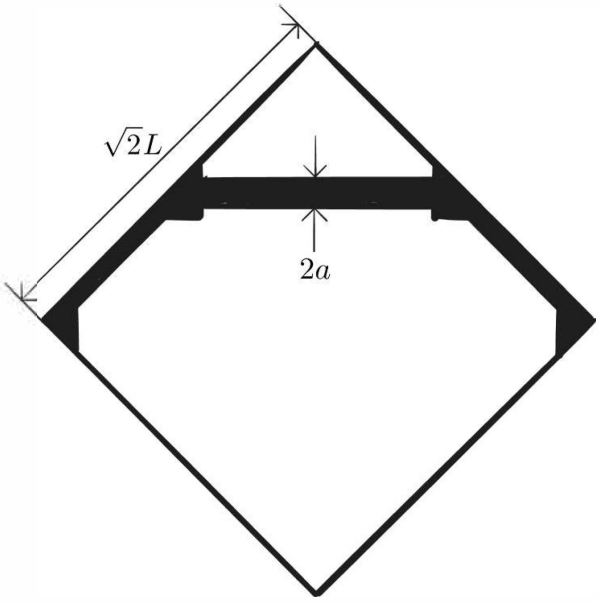

FIGURE 3.4: *Top side view of unit cell of tetrakaidecahedron model (Boomsma and Poulikakos [2])*

From Figures 3.3 and 3.4 the following can be observed and deduced:

- The side length of the strut is denoted by L.
- The diagonals of the square sides of the rectangular unit cell is equal to $2L$.
- The side lengths of the square sides of the rectangular unit cell is equal to $\sqrt{2}L$.
- The height of the rectangular unit cell is equal to $\left(\sqrt{2}/2\right) L$.
- The strut radius is denoted by a.
- The side lengths of the cubic nodes are equal to $2x$.

Once again the determination of the specific surface area of the model includes two ratio values. The r_1-ratio of Boomsma and Poulikakos [2] is defined similar to the r_2-ratio of Calmidi and Mahajan [1], i.e.

$$r_1 = \frac{2x}{L}\,, \tag{3.14}$$

and

$$r_2 = \frac{a}{L}\,, \tag{3.15}$$

which is slightly different than the definition of the r_1-ratio of Calmidi and Mahajan [1]. Boomsma and Poulikakos [2] determined empirically that $r_1 = 0.339$. This value is also used for r_1 in this study. The r_2-ratio is obtained by expressing it in terms of the porosity and r_1. Boomsma and Poulikakos [2] divided their unit cell into four layers in order to determine the solid and total cell volume. This, in turn, is used to find an expression for the porosity. The solid volume of the rectangular unit cell can consequently be determined as follows (Boomsma and Poulikakos [2]):

$$\begin{aligned} V_s &= \left[\frac{\pi a^2(L-2x)}{2} + a(2x)^2\right] + \left[(2x)^2\,(x-a)\right] + \left[\pi a^2\left(L - 4\sqrt{2}\,x\right)\right] + \left[\frac{1}{4}(2x)^3\right] \\ &= \left[r_1^2 + \frac{\pi}{2} r_2 (1-r_1)\right] r_2 L^3 + \left(\frac{1}{2} r_1 - r_2\right) r_1^2 L^3 + \left(1 - 2\sqrt{2}\,r_1\right) \pi r_2^2 L^3 + \frac{1}{4} r_1^3 L^3\,, \end{aligned} \tag{3.16}$$

and the total rectangular cell volume yields (Boomsma and Poulikakos [2]):

$$V_o = \sqrt{2}L \times \sqrt{2}L \times \frac{\sqrt{2}}{2} L = \sqrt{2} L^3\,. \tag{3.17}$$

The porosity can consequently be determined by utilizing equations (3.16) and (3.17), yielding (Boomsma and Poulikakos [2]):

$$\epsilon = 1 - \frac{V_s}{V_o} = 1 - \frac{\sqrt{2}}{2}\left[r_1^2 r_2 + \frac{\pi}{2} r_2^2 (1-r_1) + \left(\frac{1}{2} r_1 - r_2\right) r_1^2 + \pi r_2^2 \left(1 - 2\sqrt{2}\,r_1\right) + \frac{1}{4} r_1^3\right]\,, \tag{3.18}$$

and hence

$$r_2 = \sqrt{\frac{\sqrt{2}\left[2 - \left(\frac{3}{4}\right)\sqrt{2}\, r_1^3 - 2\epsilon\right]}{\pi\left(3 - 4\sqrt{2}\, r_1 - r_1\right)}}\,, \tag{3.19}$$

which is the same expression obtained by Boomsma and Poulikakos [2] with the exception of $\frac{3}{4}$ in equation (3.19) being replaced by $\frac{5}{8}$. This discrepancy could be a calculation error

and therefore the coefficient of $\frac{3}{4}$ will be used in this study. In order to calculate the total surface area of the unit cell, the surface areas were divided into strut and node sections in this study. The total surface area is therefore calculated as follows:

$$\begin{aligned} S_{fs} &= [\text{total surface area of strut section}] + [\text{total surface area of node section}] \\ &= \left[\frac{1}{2} \times 2\pi a(L-2x) + 2 \times \frac{1}{2} \times 2\pi a \left(L - 2\left(\sqrt{2}\,x - a\right)\right)\right] \\ &\quad + \left[6(2x)^2 - \pi a^2 - \pi a\left(\sqrt{2}\,a\right) + \frac{1}{2}(2x)^2 + (2x)^2 - \pi a\left(\sqrt{2}a\right)\right] \\ &= L^2\left[3\pi r_2 - \left(1+2\sqrt{2}\right)\pi r_1 r_2 + \frac{15}{2}r_1^2 + \left(3-2\sqrt{2}\right)\pi r_2^2\right], \end{aligned} \tag{3.20}$$

which, along with equation (3.17) for the total unit cell volume, produces the expression for the specific surface area:

$$S_v = \frac{S_{fs}}{V_o} = \frac{1}{L}\left[\frac{3\sqrt{2}}{2}\pi r_2 - \left(\frac{\sqrt{2}}{2}+2\right)\pi r_1 r_2 + \frac{15\sqrt{2}}{4}r_1^2 + \left(\frac{3\sqrt{2}}{2}-2\right)\pi r_2^2\right]. \tag{3.21}$$

Equations (3.16) to (3.19) were provided by Boomsma and Poulikakos [2], whereas the calculation of the specific surface area given by equations (3.20) and (3.21) are new contributions. Due to the Boomsma and Poulikakos [2] model having a tetrakaidecahedron structure, the side length L can be set equal to the side lengths l_s, given by equations (3.10) and (3.11), based on the tetrakaidecahedron models of Buciuman and Kraushaar-Czarnetzki [44] and Richardson et al. [45], respectively. Therefore, the specific surface area, given by equation (3.21), can be determined from the pore diameter, porosity, r_1 and r_2, with r_2 given by equation (3.19). The resulting predictions for the dimensionless specific surface area as a function of porosity is shown in Figure 3.5.

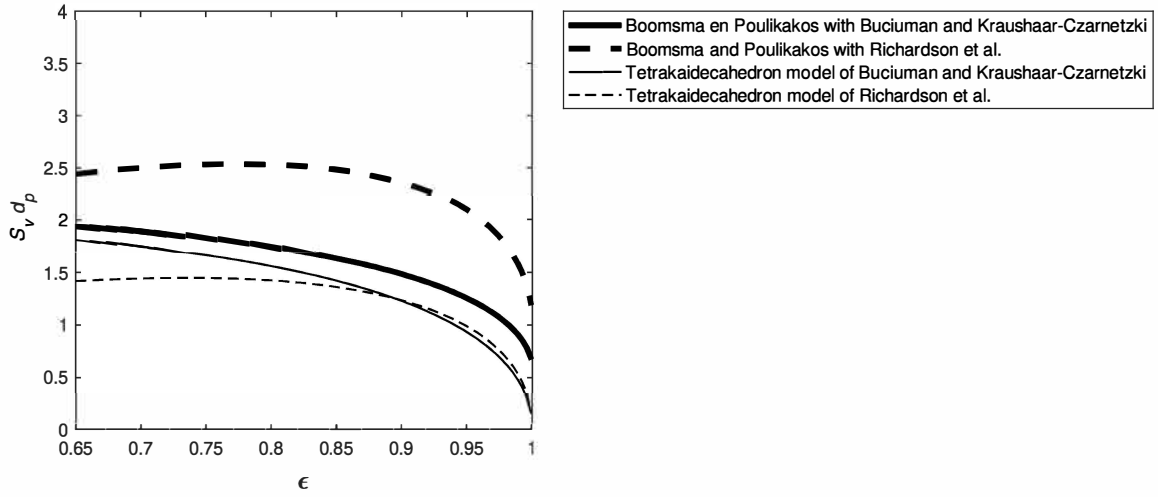

FIGURE 3.5: *Dimensionless specific surface area prediction versus porosity obtained from the node adjusted foam model of Boomsma and Poulikakos [2] and tetrakaidecahedron models from the literature*

Boomsma and Poulikakos [2] stated that their model may lend itself well into the applicability in porosity regimes that are lower than 0.9. The predictions for the dimensionless

specific surface area are shown in Figure 3.5, for $\epsilon > 0.65$ for consistency purposes, along with the tetrakaidecahedron model predictions for comparison purposes. It should be noted that the dimensionless specific surface area model only applies to porosity values for which $\epsilon < 0.98$. Above this porosity limit, the predictions become imaginary and is therefore not plausible. The predictions of the two models obtained from equation (3.21) and equations (3.10) and (3.11), respectively, show closer correspondence at lower porosity values, as well as at very high porosity values. Similarly to the predictions of the model deduced from the work of Calmidi and Mahajan [1], the specific surface area values of the node adjusted models obtained from Boomsma and Poulikakos are higher than those of the tetrakaidecahedron model predictions.

The next discussion will be on the model obtained from Bhattacharya et al. [3].

3.1.3 Bhattacharya et al. [3]

The model of Bhattacharya et al. [3] is similar to the analytical model presented by Calmidi and Mahajan [1], the only difference being that the Bhattacharya et al. [3] model represents the lumps at the nodes as circles where Calmidi and Mahajan [1] represented the lumps as squares. In Figure 3.6 the unit cell of the Bhattacharya et al. [3] model is shown. The specific surface area will be determined in a similar manner than the specific surface area expression obtained using the Calmidi and Mahajan [1] model.

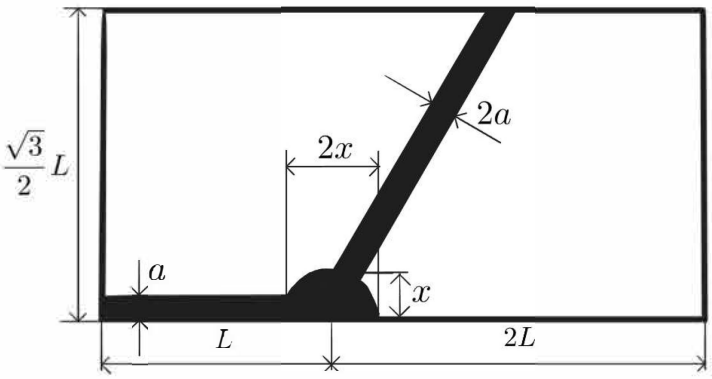

FIGURE 3.6: *Unit cell of 2D hexagonal foam matrix (Bhattacharya et al. [3])*

The r_1-ratio is defined in the same manner as the r_1-ratio in the Calmidi and Mahajan [1] model, given by equation (3.1), i.e. $r_1 = a/x$, but the r_2-ratio is defined as

$$r_2 = \frac{a}{L}. \tag{3.22}$$

For this model the value for r_1 will be the same as that of Calmidi and Mahajan [1], i.e. $r_1 = 0.09$. An expression for the porosity can also be determined by first finding expressions for V_s and V_o. The solid volume of the unit cell shown in Figure 3.6 can be determined as follows, where w once again denotes the width of the unit cell perpendicular

to the plane of the paper:

$$\begin{aligned} V_s &= [\text{strut volume of unit cell}] + [\text{node volume of unit cell}] + [\text{volume of pieces at intersection of struts and node in unit cell}] \\ &= [3a(L-x)w] + \left[\frac{1}{2} \times \pi x^2 w\right] + \left[3 \times \left[a\left(x - \sqrt{x^2-a^2}\right)\right.\right. \\ &\quad \left.\left. -\frac{1}{2} \times \left(\frac{1}{2}x^2\left(\sin^{-1}\left(\frac{2a\sqrt{x^2-a^2}}{x^2}\right) - \frac{2a\sqrt{x^2-a^2}}{x^2}\right)\right)\right] w\right] \\ &= 3aLw - \frac{3}{r_1}a^2 w + \frac{\pi}{2r_1^2}a^2 w + \left[\frac{3}{r_1}\left(1-\sqrt{1-r_1^2}\right) - \frac{3G}{4r_1^2}\right]a^2 w\,, \end{aligned} \tag{3.23}$$

where

$$G = \sin^{-1}\left(2r_1\sqrt{1-r_1^2}\right) - 2r_1\sqrt{1-r_1^2}\,, \tag{3.24}$$

and the total volume is the same as given by equation (3.3). Consequently the porosity is given by

$$\begin{aligned} \epsilon = 1 - \frac{V_s}{V_o} &= 1 - \frac{2}{\sqrt{3}}\left(\frac{a}{L}\right) + \frac{2}{\sqrt{3}\,r_1}\left(\frac{a}{L}\right)^2 - \frac{\pi}{3\sqrt{3}\,r_1^2}\left(\frac{a}{L}\right)^2 \\ &\quad - \left[\frac{2}{\sqrt{3}\,r_1}\left(1-\sqrt{1-r_1^2}\right) - \frac{G}{2\sqrt{3}\,r_1^2}\right]\left(\frac{a}{L}\right)^2. \end{aligned} \tag{3.25}$$

By rearranging equation (3.25) and utilizing equation (3.22), the r_2-ratio can be obtained in terms of r_1, yielding

$$r_2 = \frac{\sqrt{3} + \sqrt{3 + \frac{3\sqrt{3}}{r_1}\left[\frac{\pi}{3r_1} - 2 + 2\left(1-\sqrt{1-r_1^2}\right) - \frac{G}{2r_1}\right](1-\epsilon)}}{-\frac{\sqrt{3}}{r_1}\left[\frac{\pi}{3r_1} - 2 + 2\left(1-\sqrt{1-r_1^2}\right) - \frac{G}{2r_1}\right]}\,. \tag{3.26}$$

The total surface area can be calculated in a similar manner than the solid volume of the unit cell, i.e. by dividing it into the strut section, node section and the section of pieces at the intersection of the strut and node in the unit cell. This results in the following expression for the total surface area:

$$\begin{aligned} S_{fs} &= 6aL - 6\sqrt{1-r_1^2}\,\frac{a^2}{r_1} + 3Lw + \left[\pi - 3\sqrt{1-r_1^2} - 3\sin^{-1}(r_1)\right]\frac{a}{r_1}w \\ &\quad + \left(\pi - \frac{3G}{2}\right)\frac{a^2}{r_1^2}\,, \end{aligned} \tag{3.27}$$

and consequently the specific surface area can be determined by dividing equation (3.27) by equation (3.3), and substituting $w = 2a$, yielding

$$\tilde{S}_v = \frac{2}{3\sqrt{3}\,r_1^2}\cdot\frac{1}{L}\left[6r_1^2 + \left(\pi - 6\sqrt{1-r_1^2} - 3\sin^{-1}(r_1)\right)r_1 r_2 + \left(\frac{\pi}{2} - \frac{3G}{4}\right)r_2\right]. \tag{3.28}$$

The calculation of the porosity and specific surface area, i.e. equations (3.23) to (3.28), are not available elsewhere in the literature. In order to obtain the specific surface area in terms of the pore diameter, L in equation (3.28) can once again be substituted by

equations (3.12) and (3.13), using the models from Buciuman and Kraushaar-Czarnetzki [44] and Richardson et al. [45], respectively. The resulting dimensionless specific surface area predictions (made dimensionless by once again multiplying with the pore diameter) for a given porosity is displayed in Figure 3.7.

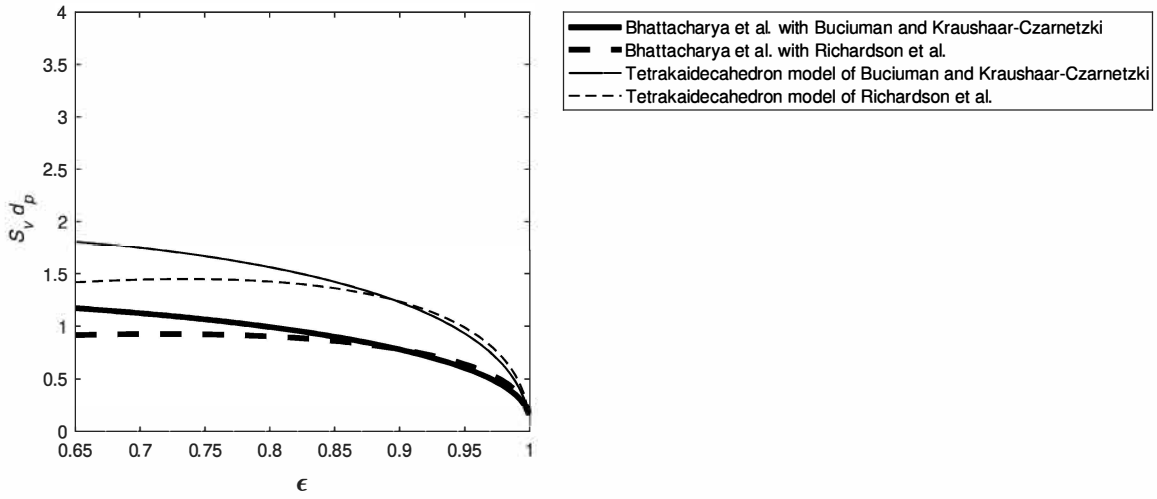

FIGURE 3.7: *Dimensionless specific surface area prediction versus porosity obtained from the node adjusted foam model of Bhattacharya et al. [3] and tetrakaidecahedron models from the literature*

The predictions acquired from the two different combinations are similar, but once more the combination with the Richardson et al. [45] model shows a slight increase in dimensionless specific surface area before decreasing as the porosity increases. The specific surface area predictions deduced from the model provided by Bhattacharya et al. [3] are, however, lower than that of the tetrakaidecahedron models, in contrast to the predictions of the models acquired from Calmidi and Mahajan [1] and Boomsma and Poulikakos [2].

In the following section, the model obtained from Fourie and Du Plessis [4] will be discussed.

3.1.4 Fourie and Du Plessis [4]

Fourie and Du Plessis [4] presented a theoretical model in order to predict the pressure drop for flow through high porosity metallic foams. They developed the three-strut RUC foam model by combining it with the tetrakaidecahedron model in order to find an expression for the pore dimension d (as indicated in Figure 1.5(c)) in terms of the cell size or diameter. In the process they utilized the tetrakaidecahedron model with flares at the strut ends, as shown in Figure 3.8, to represent the lumps at the nodes of a metallic foam, and determined expressions for the porosity and specific surface area of the model. They then equated the specific surface area expression obtained from the three-strut RUC model to the specific surface area expression obtained from the tetrakaidecahedron model with incorporated nodal lumps in order to determine an expression for d. Consequently, the porosity and specific surface area equations were determined from the tetrakaidecahedron model with nodes as shown in Figure 3.8, which will also be utilized in this study.

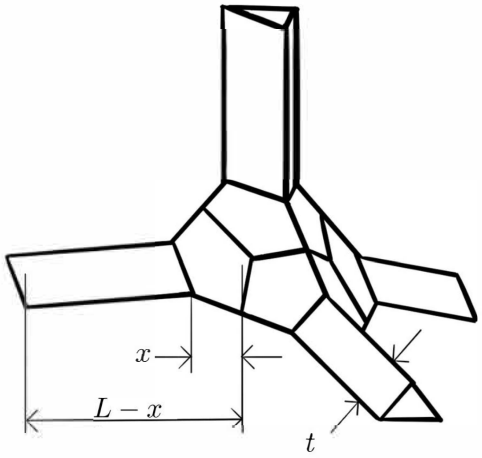

FIGURE 3.8: *Node with pentagonal flares forming solid lump of tetrakaidecahedron model (Fourie and Du Plessis [4])*

In Figure 3.8, L denotes the side length of the struts, x denotes the length of the flares at the end of the struts parallel to the side length of the struts and t denotes the side width of the triangular struts. The equation for the porosity, given by Fourie and Du Plessis [4], is

$$\epsilon = 1 - 3.87\left(\frac{t}{d_c}\right)^2 - 18.5\left(\frac{t}{d_c}\right)^3 , \tag{3.29}$$

where d_c denotes the cell diameter, as defined in Chapter 1, and the equation for the specific surface area for the node adjusted tetrakaidecahedron model is given by (Fourie and Du Plessis [4])

$$S_v = 26.8\frac{t}{d_c^2} - 14.9\frac{t^2}{d_c^3} . \tag{3.30}$$

In order to obtain the specific surface area in terms of the pore diameter, the three-strut RUC model is utilized. Fourie and Du Plessis [4] obtained the relation between the cell diameter of the tetrakaidecahedron model and the pore dimension d, as previously mentioned, for different high porosity values and estimated that $d \approx 0.57 d_c$. The pore dimension in terms of the pore diameter of the three-strut RUC model is given by (Fourie and Du Plessis [4])

$$d = \frac{2d_p}{3 - \chi} , \tag{3.31}$$

where χ, which denotes the tortuosity, is equivalent to ψ of the three-strut model given by equation (2.72). Therefore, equation (3.31) is equivalent to equation (2.75). The specific surface area can therefore be expressed as follows:

$$S_v = \frac{0.57(3 - \chi)}{2d_p}\left[26.8\left(\frac{t}{d_c}\right) - 14.9\left(\frac{t}{d_c}\right)^2\right] , \tag{3.32}$$

where the t/d_c-ratio can be obtained from equation (3.29) for a given porosity and χ from equation (2.72). Equation (3.32) is a novel contribution deduced from the work of Fourie and Du Plessis [4], given by equations (3.29) and (3.30). In Figure 3.9 the predictions obtained for the specific surface area based on the model of Fourie and Du Plessis [4]

are shown, along with the non-adjusted tetrakaidecahedron and three-strut RUC model predictions.

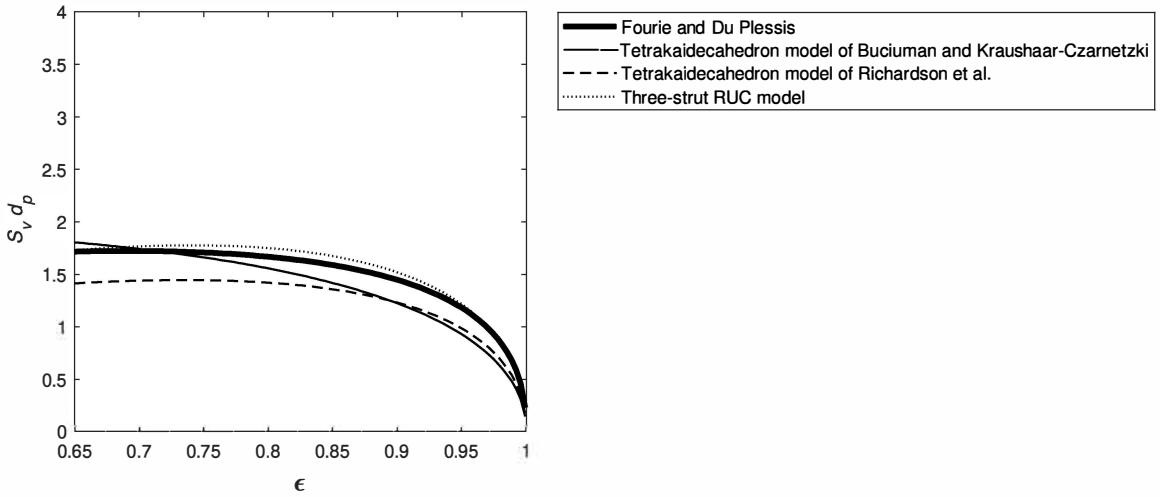

FIGURE 3.9: *Dimensionless specific surface area prediction versus porosity obtained from the node adjusted foam model of Fourie and Du Plessis [4] and models from the literature*

Figure 3.9 shows that the Fourie and Du Plessis [4] model gives very similar predictions for the specific surface area, although slightly lower, than the three-strut RUC model which is not expected, but higher than the tetrakaidecahedron model for porosities higher than 0.7. The model provides the expected results when specifically compared to the tetrakaidecahedron model obtained from Richardson et al. [45].

In the next section, the model obtained from Huu et al. [5] will be discussed.

3.1.5 Huu et al. [5]

Huu et al. [5] introduced the dodecahedron model to represent foams, as mentioned in Chapter 1, where a brief summary of the dodecahedron model is given in Section 1.3.2. As discussed in Chapter 1, Huu et al. [5] made a distinction between foams that have triangular struts versus those that have cylindrical struts, as well as between foams with "slim" and "fat" struts, where the "slim" struts have triangular nodes and the "fat" struts appear more rounded at the edges. The "fat" struts represent foams with lumps at the strut intersections. The dodecahedron model with triangular "slim" and "fat" struts are shown in Figures 3.10(a) and (b), respectively.

In Figure 3.10(a) the strut side length, L, the triangular strut side width, t, and the distance between the strut centre line and edges, x, are shown. The parameters are the same for Figure 3.10(b). A visualized version of the dodecahedron models with cylindrical struts is not shown, since the difference in the calculations consists merely of calculating the volume and surface area of cylinders rather than triangular prisms where the struts are concerned.

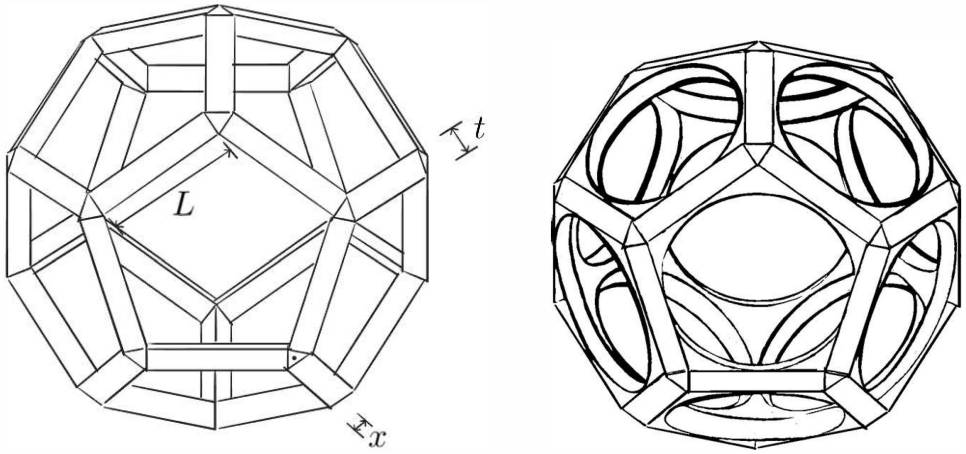

(a) *Triangular "slim" struts* (b) *Triangular "fat" struts*

FIGURE 3.10: *Dodecahedron model of Huu et al. [5]*

Huu et al. [5] provided expressions for the specific surface area of all four model types, but only the expressions for the "fat" strut model will be provided in this section due to the node solid lumps present within this model. The expressions for the "slim" strut model are provided in Chapter 1. A more elaborated discussion on the calculations resulting in the specific surface area equations of the four versions of the dodecahedron model presented by Huu et al. [5] can be found in Maré [65]. As with the aforementioned models, a ratio of dimensions is defined for the dodecahedron model. Only one ratio is however required, in this case, and is defined as $r = t/L$. This ratio is furthermore unique for each type of dodecahedron model and can be expressed in terms of porosity. The ratio for the dodecahedron model with triangular "fat" struts is denoted by r_{tf} and can be calculated from the following expression:

$$\left[-\frac{\sqrt{10}}{3\phi^4}+\frac{Z}{6}-\frac{\sqrt{6}\,W}{36}\right] r_{tf}^3+\left[\frac{\sqrt{15}}{\phi^4}-\sqrt{\frac{2}{3}}\,Z+\frac{W}{2}\right] r_{tf}^2+\left[Z-\frac{\sqrt{6}\,W}{2}\right] r_{tf} + [W-(1-\epsilon)]=0\,, \tag{3.33}$$

where ϕ is the golden ratio, given by

$$\phi=\frac{1+\sqrt{5}}{2}\,, \tag{3.34}$$

and where W and Z are given by

$$W=\frac{5\sin^2\left(\frac{\pi}{5}\right)}{4\sqrt{15}\,(3-\phi)\phi^2}\sqrt{\frac{1}{4}-\frac{\sin^2\left(\frac{\pi}{5}\right)\phi^2}{9-3\phi}}\,, \tag{3.35}$$

and

$$Z=\frac{3}{\sqrt{5}\,\phi^3}\left[\frac{5}{\sqrt{3-\phi}}-\frac{\pi\phi}{3-\phi}\right]\,, \tag{3.36}$$

respectively. Equation (3.33) differs from the manner in which it is represented by Huu et al. [5] and Maré [65] in that equation (3.33) is expressed as a polynomial of r_{tf}. It is written in polynomial form for ease of calculation, given a porosity value. The ratio

of the dodecahedron model with cylindrical "fat" struts is denoted by r_{cf}, which can be calculated using:

$$\left[\frac{\sqrt{10}}{6\phi^4} - \frac{\sqrt{30}\,\pi}{6\phi^4} + \frac{Z}{6} - \frac{\sqrt{6}\,W}{36}\right] r_{cf}^3 + \left[\frac{\sqrt{5}\,\pi}{\phi^4} - \sqrt{\frac{2}{3}}Z + \frac{W}{2}\right] r_{cf}^2 + \left[Z - \frac{\sqrt{6}\,W}{2}\right] r_{cf} + [W - (1-\epsilon)] = 0\,. \tag{3.37}$$

The values of W and Z can, once more, be determined from equations (3.35) and (3.36), respectively. The specific surface area of the dodecahedron model with triangular "fat" struts can hence be determined using the following expression:

$$S_v = \frac{60 r_{tf}\left(1 - \frac{1}{2}\sqrt{\frac{2}{3}}\,r_{tf}\right)^2}{\sqrt{5}\,\phi^3\sqrt{3-\phi}\,d_p} + \frac{\left(1 - \frac{1}{2}\sqrt{\frac{2}{3}}\,r_{tf}\right)}{\phi\sqrt{3-\phi}\,d_p}\left[\frac{12\pi r_{tf}\left(1 - \frac{1}{2}\sqrt{\frac{2}{3}}\,r_{tf}\right)}{\sqrt{5}\,\phi\sqrt{3-\phi}} + \frac{\sqrt{15}\sin^2\left(\frac{\pi}{5}\right)\left(1 - \frac{1}{2}\sqrt{\frac{2}{3}}\,r_{tf}\right)^2}{2(3-\phi)}\right], \tag{3.38}$$

where r_{tf} can be obtained from equation (3.33). Similarly, the predictions for the specific surface area provided by the dodecahedron model with cylindrical "fat" struts can be obtained using the expression:

$$S_v = \frac{20\pi r_{cf}\left(1 - \frac{1}{2}\sqrt{\frac{2}{3}}r_{cf}\right)^2}{\sqrt{5}\,\phi^3\sqrt{3-\phi}\,d_p} + \frac{\left(1 - \frac{1}{2}\sqrt{\frac{2}{3}}\,r_{cf}\right)}{\phi\sqrt{3-\phi}\,d_p}\left[\frac{12\pi r_{cf}\left(1 - \frac{1}{2}\sqrt{\frac{2}{3}}r_{cf}\right)}{\sqrt{3}\,\phi\sqrt{3-\phi}} + \frac{\sqrt{15}\sin^2\left(\frac{\pi}{5}\right)\left(1 - \frac{1}{2}\sqrt{\frac{2}{3}}\,r_{cf}\right)^2}{2(3-\phi)}\right], \tag{3.39}$$

where r_{cf} can be obtained from equation (3.37). The dimensionless specific surface area predictions, determined by once again multiplying the specific surface area equations with d_p, given by equations (3.38) and (3.39), are shown in Figure 3.11.

The dimensionless specific surface area predictions for the dodecahedron model with cylindrical struts are displayed in Figure 3.11 for porosity values of $0.65 < \epsilon < 0.9$ and for the porosity values of $\epsilon > 0.9$ the predictions of the dodecahedron model with triangular struts are shown, according to the distinctions made based on porosity values and strut shapes. It can be noted that there is a discontinuity at the porosity value of 0.9, which is undesirable. The specific surface area predictions of the "fat" dodecahedron model are mainly higher than the predictions of the "slim" model, as expected.

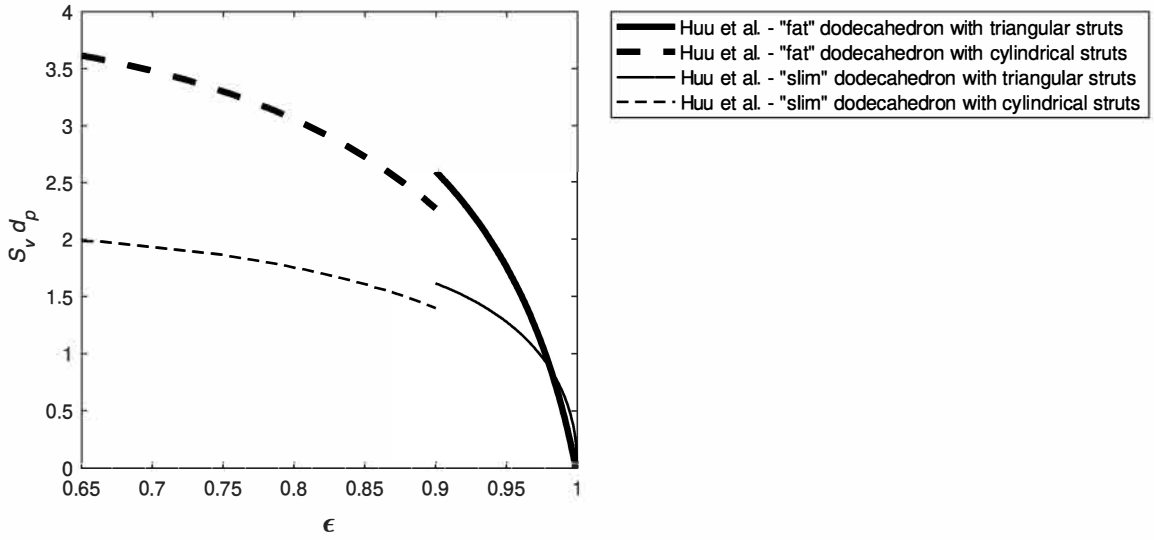

FIGURE 3.11: *Dimensionless specific surface area prediction versus porosity obtained from the dodecahedron foam models of Huu et al. [5] with "fat" and "slim" struts*

The model obtained from Edouard [6] will be considered next.

3.1.6 Edouard [6]

Edouard [6] noted that a ratio was required that relates the strut diameter to the node size, that it differed depending on the unit cell considered (as in Calmidi and Mahajan [1] versus Bhattacharya et al. [3]) and was furthermore restricted to a certain range of porosity values. Edouard [6] therefore highlighted the need for a more representative model, as well as a manner in which to calculate the ratio that relates the strut diameter to the node size, and thus proposed a model accordingly. Similar to the study of Fourie and Du Plessis [4], a combination of two models that represent the structure of solid foams were utilized. In the study of Edouard [6] the two models considered were the dodecahedron and CUC models, where the adjustment of cubic solid lumps at the nodes was made to the CUC model, as displayed in Figure 3.12. The node adjusted CUC model is called the Modified Cubic Lattice (MCL) model, which will also be the manner of reference in this study.

The notion of "slim" and "fat" foams was furthermore adopted and utilized by Edouard [6]. The expression for the ratio in terms of the porosity of the dodecahedron model with triangular struts, for both the "slim" and "fat" dodecahedron models, was compared to the expression for the ratio obtained from the model displayed in Figure 3.12. The ratio obtained from the dodecahedron model, defined in the previous section as r_{tf} for the "fat" model with triangular struts, can be determined using equation (3.33). The ratio for the "slim" dodecahedron model is furthermore determined using equation (1.36) and will be included in this chapter for comparison purposes. The two ratios defined for the MCL model are:

$$r_1 = \frac{a}{L}\,, \tag{3.40}$$

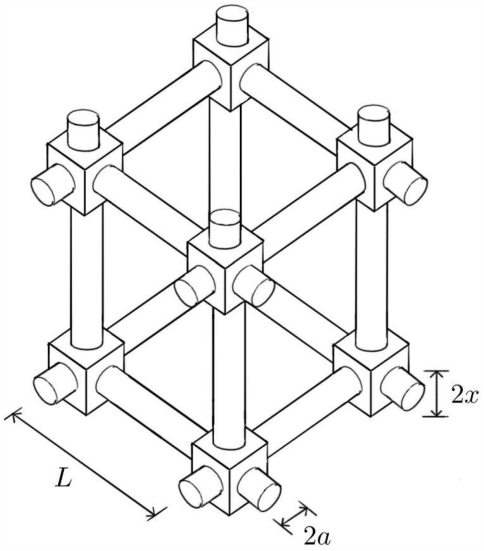

FIGURE 3.12: *MCL model as presented by Edouard [6]*

and

$$r_2 = \frac{x}{a}\,. \tag{3.41}$$

The r_2-ratio can furthermore be defined as

$$r_2 = 1 + \delta\,, \tag{3.42}$$

where δ is an indication of how much matter accumulates at the nodes, i.e. if no matter accumulates $\delta = 0$ and if there is matter that accumulates $\delta > 0$. Consequently, for the "slim" MCL model $r_2 = 1$ and for the "fat" model $r_2 > 1$. In order to obtain these ratio values for a given porosity, an equation for the porosity (based on the MCL model) is determined. The total volume of the unit cell is given by

$$V_o = L^3\,, \tag{3.43}$$

and the solid volume can be determined as follows (Edouard [6]):

$$\begin{aligned} V_s &= 2\left[\pi a^2(L-2x) + 4ax^2\right] + 2\left[4(x-a)x^2\right] + \left[\pi a^2(L-2x)\right] \\ &= 3\pi a^2(L-2x) + 8x^3\,. \end{aligned} \tag{3.44}$$

Therefore, by utilizing equations (3.40) to (3.44), the following equation can be determined for the solid volume fraction in terms of r_1 and δ (Edouard [6]):

$$1 - \epsilon = \frac{V_s}{V_o} = 3\pi r_1^2(1-2r_1) + 8r_1^3 + \delta r_1^3\left(8\delta^2 + 24\delta + 24 - 6\pi\right)\,. \tag{3.45}$$

In order to obtain the values for r_1 and r_2, the ratio values obtained from the dodecahedron model are utilized. It is noted that the expression for the solid volume fraction given by equation (3.45) can be divided into terms excluding the accumulation of matter at the nodes and terms representing the accumulated matter by separating the terms with δ from the terms without δ. Similarly, the expression for the ratio acquired from the dodecahedron model with "slim" triangular struts, that is without matter accumulation at the nodes, is given by equation (1.36) and the expression for the ratio of the model that

includes the node adjustments is given by equation (3.33). Comparing equations (1.36) and (3.33), the terms of the expression for the ratio given by equation (3.33) that represents the model without the accumulated matter taken into consideration and the terms representing the accumulated matter can be distinguished. The solid volume fractions can be equated and two equations can be obtained, i.e. the expression equating the terms of the equations for the ratio without the node lumps taken into consideration and the expression equating the part of the equations for the ratio representing the accumulated matter terms. This then yields

$$\frac{\sqrt{15}}{\phi^4} r_{tf}^2 - \frac{\sqrt{10}}{3\phi^4} r_{tf}^3 = 3\pi r_1^2(1-2r_1) + 8r_1^3\,, \tag{3.46}$$

and

$$\begin{aligned} &\left[\frac{Z}{6} - \frac{\sqrt{6}W}{36}\right] r_{tf}^3 + \left[-\sqrt{\frac{2}{3}}\,Z + \frac{W}{2}\right] r_{tf}^2 + \left[Z - \frac{\sqrt{6}\,W}{2}\right] r_{tf} + W \\ &= \delta r_1^3 \left(8\delta^2 + 24\delta + 24 - 6\pi\right)\,, \end{aligned} \tag{3.47}$$

respectively. The r_{tf}-ratio in both equations (3.46) and (3.47) can be obtained from equation (3.33) for a given porosity and W and Z can be obtained from equations (3.35) and (3.36), respectively. Consequently, r_1 can be obtained from equation (3.46) and by substituting the value obtained for r_1 into equation (3.47), the value for δ, and hence r_2, can be acquired.

The aforementioned calculation of the ratio values was provided by Edouard [6]. The following calculation of the specific surface area is, however, newly presented in this study. The total surface area can be determined from Figure 3.12 and is given by

$$\begin{aligned} S_{fs} &= 3\left[2\pi a(L-2x)\right] + \left[6\left(4x^2 - \pi a^2\right)\right] \\ &= 6L^2\left[\pi r_1 + r_1^2\left(4r_2^2 - 2\pi r_2 - \pi\right)\right]\,. \end{aligned} \tag{3.48}$$

Dividing equation (3.48) by the total volume of the cubic unit cell, given by equation (3.43), and there-upon substituting equations (3.40) and (3.41) into the resulting expression, leads to the following expression for the specific surface area in terms of L, r_1 and r_2:

$$S_v = \frac{6\pi r_1 + 6r_1^2\left(4r_2^2 - 2\pi r_2 - \pi\right)}{L}\,. \tag{3.49}$$

By equating the face diameter to L, the specific surface area in terms of the pore diameter can be determined by utilizing the expression for r_1, given by equation (3.40). The face diameter L equals $d_p + 2a$ and therefore

$$L = \frac{d_p}{1-2r_1}\,. \tag{3.50}$$

Consequently

$$S_v = \frac{(1-2r_1)\left[6\pi r_1 + 6r_1^2\left(4r_2^2 - 2\pi r_2 - \pi\right)\right]}{d_p}\,. \tag{3.51}$$

The predictions for the dimensionless specific surface area are shown in Figure 3.13 as a function of porosity. Both the specific surface area predictions of the "fat" and "slim" MCL models are shown, as well as the predictions of the CUC models for comparison

purposes. The predictions for the "slim" MCL model were obtained by setting $r_2 = 1$ and calculating r_1 using equation (3.46), but using r_{ts} instead of r_{tf} where r_{ts} is calculated from equation (1.36).

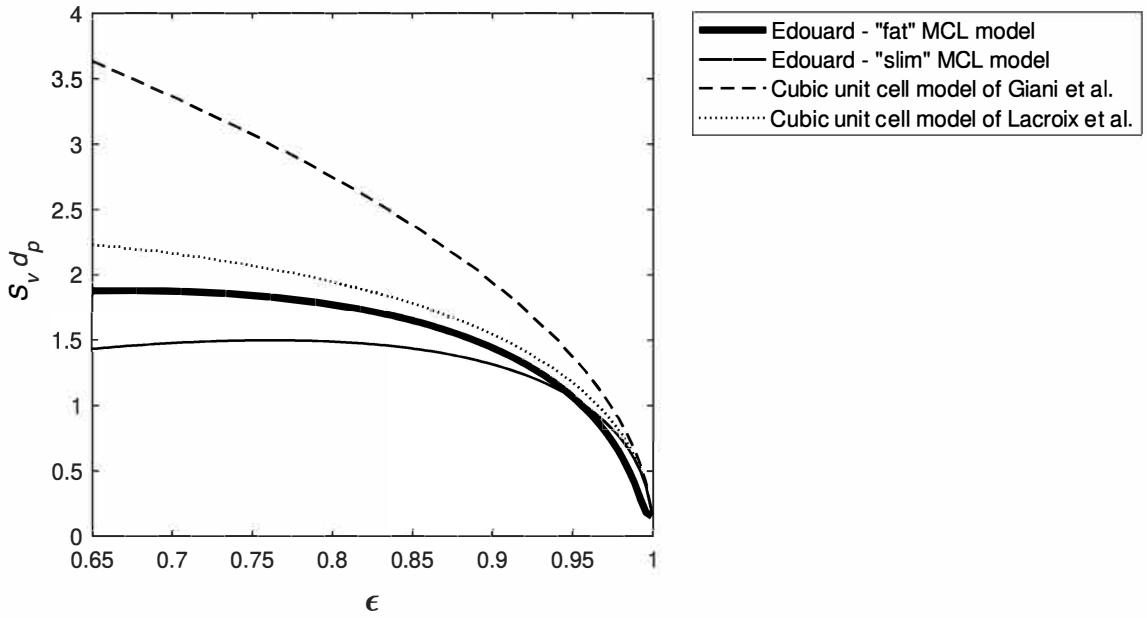

FIGURE 3.13: *Dimensionless specific surface area prediction versus porosity obtained from the node adjusted foam model of Edouard [15] and cubic unit cell models from the literature*

It is evident from Figure 3.13 that when the predictions of the "fat" and "slim" models of Edouard [15] are compared to one another, the predictions of the "fat" model are mainly higher than that of the "slim" model as expected (except for $\epsilon > 0.95$). The predictions of the CUC models are, however, higher than the predictions of both the Edouard [15] models. In the next section the study of the MCL model, as given by Edouard et al. [6], will be expanded as done by Ahmed et al. [7].

3.1.7 Ahmed et al. [7]

Ahmed et al. [7] presented a model to predict the tortuosity and pressure drop of foams where the solid lumps at the node intersections were taken into account. In order to attain these predictions, they utilized the MCL model as given by Edouard et al. [6] (shown in Figure 3.12), and used the method of Du Plessis et al. [82] for obtaining the tortuosity, as well as the pressure drop for this model. From the expression for the pressure drop they furthermore derived the Darcy permeability and inertial coefficient (from which the Forchheimer permeability can be deduced) for the MCL model. Ahmed et al. [7] also adopted the "slim" and "fat" model cases for validation purposes and the "slim" MCL model will be included in this study for comparison purposes.

Ahmed et al. [7] followed the modelling procedure of Bhattacharya et al. [3] who suggested that the RUC model presented by Du Plessis et al. [82] and Fourie and Du Plessis [4] over-predicts the permeability due to the solid lumps at the strut intersections not being taken into consideration, which causes extra resistance to flow and a more tortuous flow path.

Bhattacharya et al. [3] modified the tortuosity, which is equal to the geometric factor, as given by equation (2.72) in this study, by making use of a shape function. Ahmed et al. [7] noted, however, that Bhattacharya et al. [3] used an incorrect definition of the tortuosity, but used the idea of adjusting the tortuosity to account for solid lumps present at the nodes of a foam. The tortuosity for the MCL model, as presented by Ahmed et al. [7], is given by

$$\chi = \frac{\epsilon L^2}{A_p} = \frac{\epsilon}{1 - 4r_1 + 4r_1^2\left(2r_2 - r_2^2\right)}\,, \tag{3.52}$$

where A_p is the constant cross-sectional flow area (equivalent to $A_{p_\parallel}$ of the RUC model) and r_1 and r_2 are as defined by equations (3.40) and (3.41), respectively. The same manner in which Edouard et al. [6] determined r_1 and r_2, by making use of both the MCL model and the dodecahedron model, was used by Ahmed et al. [7] to determine the ratios in terms of the porosity. Consequently, the tortuosity can be determined, given the porosity, by using equation (3.52).

In order to derive the pressure drop, and hence the permeability coefficients, the following expression was utilized by Ahmed et al. [7]:

$$\left(\frac{dp}{dx}\right) = -\frac{\mu}{\epsilon} q f\,, \tag{3.53}$$

In equation (3.53), f is the shear factor such that $f = f_v + f_f$, with f_v being the magnitude of the drag force for low Reynolds number flow and f_f being the magnitude of the drag force for high Reynolds number flow, such that

$$f_v = \frac{C_{D,v}\rho v_p^2 S_{fs}}{2}\,, \tag{3.54}$$

and

$$f_f = \frac{C_{D,f}\rho v_p^2 A_{fr}}{2}\,. \tag{3.55}$$

In equations (3.54) and (3.55), v_p is the average pore velocity for the cubic unit cell in a longitudinally oriented pore (equivalent to $w_\parallel$ of the RUC model), $C_{D,v}$ is the friction coefficient for low Reynolds number flow, $C_{D,f}$ is the form drag coefficient for high Reynolds number flow, S_{fs} is the total wetted surface and A_{fr} is the frontal area subject to recirculation. The average pore velocity is furthermore related to q by dividing the volumetric flow rate by the constant cross-sectional area of the cubic unit cell i.e.

$$v_p = \frac{qL^2}{A_p}\,, \tag{3.56}$$

which leads to an expression for v_p in terms of the tortuosity when comparing equation (3.56) with equation (3.52):

$$v_p = \frac{\chi}{\epsilon} q\,. \tag{3.57}$$

The magnitude of the drag force can also be expressed as

$$f = -\epsilon \frac{dp}{dx} L^3\,, \tag{3.58}$$

which, in conjunction with equations (3.53) to (3.55), leads to

$$f_v = \frac{C_{D,v}\rho q \left(\chi/\epsilon\right)^2 S_{fs}}{2\mu L^3}\,, \tag{3.59}$$

and

$$f_f = \frac{C_{D,f}\rho q \left(\chi/\epsilon\right)^2 A_{fr}}{2\mu L^3}\,. \tag{3.60}$$

Ahmed et al. [7] furthermore used the expression obtained by Du Plessis et al. [82], Fourie and Du Plessis [4] and Du Plessis and Van der Westhuizen [52] for the friction coefficient $C_{D,v}$, given by the latter authors as $C_{D,v} = 12\mu/(\rho v_p d_{p_{MCL}})$ (where $d_{p_{MCL}}$ is the characteristic length of the equivalent pore diameter of the MCL model). Ahmed et al. [7] approximated that $d_{p_{MCL}} = \sqrt{A_p}$ for small δ. In combination with equation (3.56), this leads to the following expression for the friction coefficient for low Reynolds number flow:

$$C_{D,v} = \frac{12\mu\sqrt{A_p}}{\rho q L^2}\,. \tag{3.61}$$

The approximation for the friction coefficient for high Reynolds number flow as the drag coefficient of a cylinder in cross-flow was used by Ahmed et al. [7], given by

$$C_{D,f} = 1 + \frac{10}{\mathrm{Re}^{0.667}}\,. \tag{3.62}$$

Only the asymptotic value of $C_{D,f}$ for high Reynolds number flow, which is $C_{D,f} = 1$, was utilized by Ahmed et al. [7] due to corresponding fluid velocities of experimental data not being available in the data sets they considered. Consequently, by substituting equations (3.61) and (3.62) into equations (3.59) and (3.60), respectively, and there-upon substituting the resulting equations into equation (3.53), leads to

$$-\left(\frac{dp}{dx}\right) = \frac{\rho q^2 \chi^2}{\epsilon^3 L^3}\left(\frac{C_{D,v}S_{fs} + C_{D,f}A_{fr}}{2}\right)\,. \tag{3.63}$$

Ahmed et al. [7] compared equation (3.63) to the well-known Forchheimer-type equation, given by

$$-\left(\frac{dp}{dx}\right) = \frac{\mu}{K}q + \frac{\rho C_E}{\sqrt{K}}q^2\,, \tag{3.64}$$

which is similar to equation (1.1) and can be used to obtain the expressions for both the Darcy and Forchheimer permeabilities. The following expression for the Darcy permeability can consequently be deduced from equations (3.61), (3.63) and (3.64):

$$K = \frac{\epsilon^3 \mu L^3}{\rho q \chi^2}\left(\frac{2}{C_{D,v}S_{fs}}\right) = \frac{\epsilon^3 L^5}{6\chi^2\sqrt{A_p}\,S_{fs}}\,. \tag{3.65}$$

The constant cross-sectional flow area, A_p, can be obtained from equation (3.52), in terms of the tortuosity, and S_{fs} is equivalent to that in Section 3.1.6, given by equation (3.48). Ahmed et al. [7] furthermore obtained the relation between L and the observable pore diameter by adopting the assumption of Du Plessis et al. [82] that the observable pore diameter is quasi-three-dimensional. The observable pore diameter is defined similarly to d_c in this study and therefore equation (3.50) is utilized once again to acquire the

relationship between L and d_p. Substituting the expressions obtained from equations (3.48), (3.50) and (3.52) into equation (3.65) leads to the following expression for the Darcy permeability:

$$K = \frac{\epsilon^{2.5}}{36\chi^{1.5}\left[\pi r_1 + r_1^2\left(4r_2^2 - 2\pi r_2 - \pi\right)\right]} \cdot \frac{d_p^2}{1 + 2\left(\epsilon/\chi\right)}, \tag{3.66}$$

where χ is given by equation (3.52) and r_1 and r_2 are determined in the same manner as in the case of the model of Edouard et al. [6], as previously stated. In order to obtain an expression for the Forchheimer permeability coefficient, equation (3.63) is set equal to equation (1.1), with $-\frac{dp}{dx} = \frac{\Delta p}{L}$, which then leads to:

$$K_F = \frac{\epsilon^3 L^3}{\chi^2}\left(\frac{2}{C_{D,f}A_{fr}}\right). \tag{3.67}$$

The frontal cross-sectional area subject to recirculation, A_{fr}, was determined by Ahmed et al. [7] based on the condition given by Fourie and Du Plessis [4], which states that "the contribution to drag force from the solid aligned with the mean flow direction is neglected", and is given as follows:

$$A_{fr} = (L - 2x)(2\pi a) = 2\pi L^2 r_1\left(1 - 2r_1 r_2\right). \tag{3.68}$$

Substituting equations (3.50) and (3.68) into equation (3.67) then leads to the following expression for the Forchheimer permeability:

$$K_F = \frac{\epsilon^3}{\chi^2 C_{D,f}\left(\pi r_1 - 2\pi r_1^2 r_2\right)} \cdot \frac{d_p}{\sqrt{1 + 2\left(\epsilon/\chi\right)}}, \tag{3.69}$$

where it is assumed that $C_{D,f} = 1$, as previously stated, where χ can once again be determined from equation (3.52) and where r_1 and r_2 are determined as in the case of the model of Edouard et al. [6].

The resulting predictions for the dimensionless Darcy and Forchheimer permeability for the porosity range of 0.65 to 1 obtained from equations (3.66) and (3.69) are shown in Figures 3.14 and 3.15, respectively. Both the "fat" and "slim" models are shown in order to note the change that occurs when taking the accumulation of solid at the nodes into account. In each case, the corresponding permeability predictions for the three-strut RUC model are also shown for comparison.

In Figure 3.14 it can be seen that the "fat" MCL model predictions of the Darcy permeability are slightly lower than that of the "slim" MCL model, except for very high porosity values where $\epsilon > 0.93$. The lower predictions are as expected due to the extra resistance to flow caused by the accumulated solid at the nodes. The predictions between the "fat" and "slim" models are however close, as was noted by Ahmed et al. [7] who stated that the permeability does not seem to be sensitive to the solid accumulation at the strut intersections. The three-strut RUC model predictions for the Darcy permeability are lower than both the "slim" and "fat" MCL model predictions but are still relatively similar.

Figure 3.15 shows that the "fat" MCL model predictions for the Forchheimer permeability are higher than the predictions of the "slim" MCL model. The predictions provided by the "slim" MCL model furthermore corresponds closely to that of the three-strut RUC model. Ahmed et al. [7] noted the dependency of the frontal area subject to recirculation on the Forchheimer term.

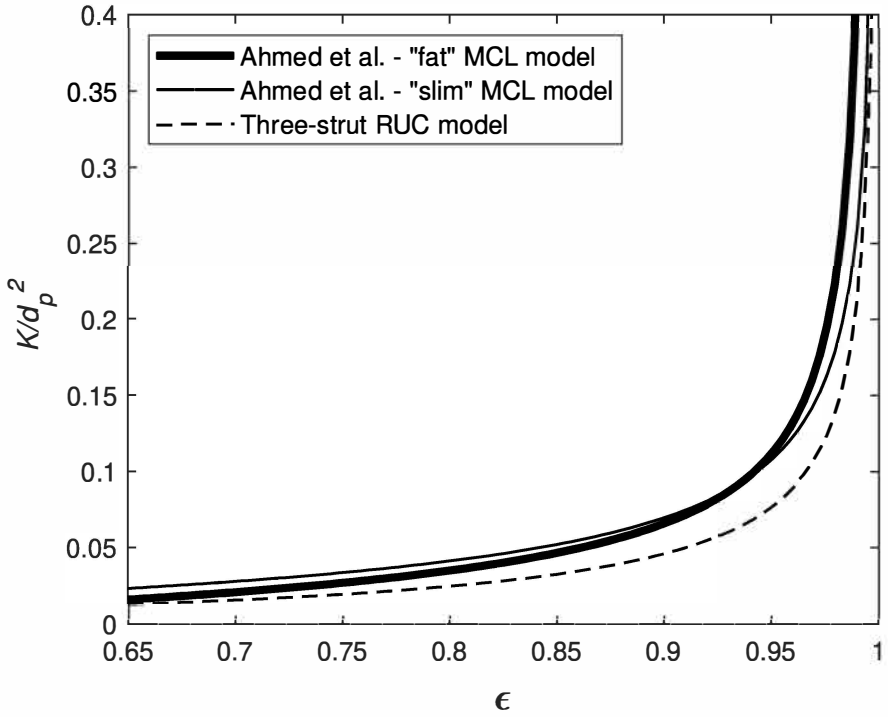

FIGURE 3.14: *Dimensionless Darcy permeability prediction versus porosity obtained from node adjusted foam model of Ahmed et al. [7] and three-strut RUC model*

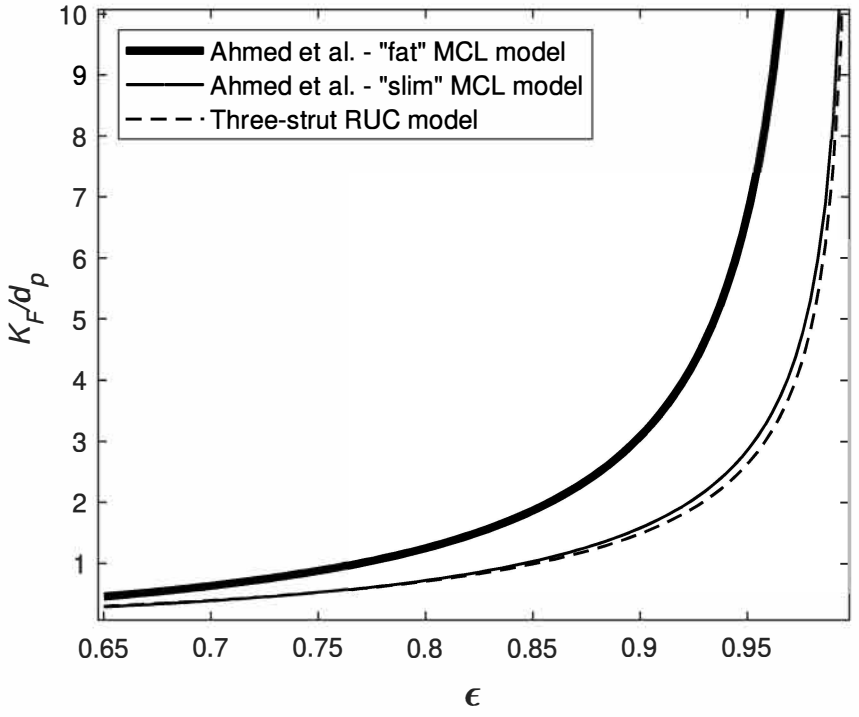

FIGURE 3.15: *Dimensionless Forchheimer permeability prediction versus porosity obtained from node adjusted foam model of Ahmed et al. [7] and three-strut RUC model*

This area is defined such that the nodes are excluded, as can be deduced from equation (3.68), and therefore larger nodes will lessen this area. The exclusion of the nodes in the calculation of A_{fr}, in turn, leads to larger K_F-values due to the dependency of K_F on A_{fr}, which is apparent in equation (3.67). The pressure drop is expected to increase with the accumulation of solid matter at the nodes of a foam, however, and the dependency of the Forchheimer permeability coefficient on the pressure drop as given in equation (1.1) indicates that the permeability will decrease and not increase with the solid addition. Consequently, the predictions of the permeability coefficients of the model obtained from Ahmed et al. [7] are higher than expected with the addition of solid at the nodes of a foam.

In the following section the foam models obtained from the literature that take the accumulation of matter at the strut intersections into account will be compared to one another, as well as to foam models that do not include lumps at the nodes and experimental data also obtained from the literature.

3.1.8 Comparison of literature models

The literature models and data are compared using tables containing the relative percentage errors and figures showing the predictions for a graphical comparison of the dimensionless parameters under consideration. The evaluations are divided into three sections: the Darcy permeability, Forchheimer permeability and specific surface area section. Only one model containing node adjustments with permeability predicting equations was found by the author and included in this study, i.e. the Ahmed et al. [7] model. Consequently, in the Darcy and Forchheimer permeability sections only this model will be evaluated against available models from the literature and data as provided in Chapter 1, Section 1.3. Specific surface area equations, in terms of the pore diameter, were obtained from the six other models acquired from the studies of Calmidi and Mahajan [1], Boomsma and Poulikakos [2], Bhattacharya et al. [3], Fourie and Du Plessis [4], Huu et al. [5] and Edouard [6], and will be evaluated in the relevant sub-section. The experimental data utilized in this chapter for the evaluation of the node adjusted models are limited to the data that had an indication in the respective literature sources of how much solid accumulation were present in the foam samples used in the experiments. These indications included images of the foams utilized or specific mention of the presence of solid accumulation. The experimental data utilized were consequently the data sets obtained from Bhattacharya et al. [3], Garrido et al. [19], Dietrich et al. [20], Mancin et al. [21], Mancin et al. [22] and Kumar et al. [71]. Due to varying degrees of solid accumulation at the nodes of foams, i.e. some foams have a higher degree of accumulation than other foams, the total average percentage error of the collection of data sets compared to the node adjusted models will not be provided. Rather, the performance of the models compared to the individual experimental data sets will be discussed to ascertain whether the node adjusted model behaviour compares as expected to the individual data sets.

Darcy permeability

The dimensionless Darcy permeability predictions (made dimensionless by dividing by the square of the pore diameter) of the Ahmed et al. [7] model, given by equation (3.66), are evaluated in this section against the Darcy permeability equation obtained from Dietrich

et al. [20], given by equation (1.27), the three-strut RUC model, given by equation (2.127), and the relevant experimental data provided in Section 1.3.3. Both the average percentage errors for the "fat" and "slim" MCL model are included, the latter results for the purpose of evaluating the "fat" MCL model against the "slim" model. The calculated relative percentage errors are given in Table 3.1 and the predictions are shown in Figure 3.16.

TABLE 3.1: *Relative percentage error of node adjusted models from the literature compared to* K/d_p^2 *predictions and data of Chapter 1*

	Literature models (Section 3.1) Ahmed et al. [7]	
	"slim" MCL model	"fat" MCL model
Experimental data (Section 1.3.3)		
Bhattacharya et al. [3]	611 %	641 %
Garrido et al. [19]	387 %	323 %
Dietrich et al. [20]	36 %	40 %
Mancin et al. [21]	262 %	260 %
Mancin et al. [22]	606 %	599 %

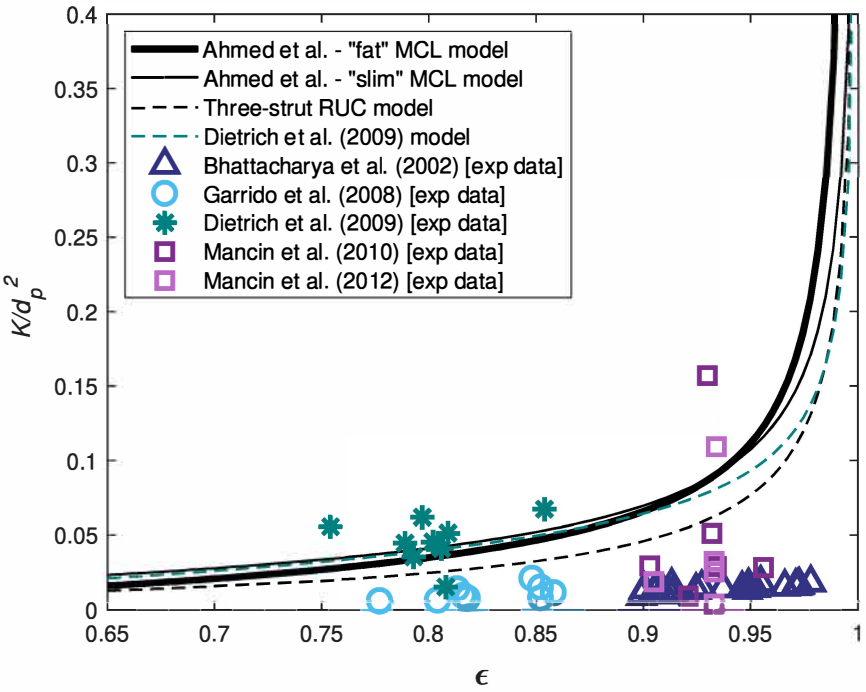

FIGURE 3.16: *Dimensionless Darcy permeability prediction versus porosity obtained from foam models with and without incorporated node solid lumps compared to experimental data*

Bhattacharya et al. [3] specifically addressed the accumulation of solid matter at the nodes of foams and the image they provided showed moderate solid accumulation. Their experimental data are located in the higher porosity data range (i.e. mainly for $\epsilon > 0.9$) and therefore, since the "fat" MCL model gives higher permeability predictions than the

"slim" MCL model for the higher porosity range, it is noticed in Table 3.1 and Figure 3.16 that the "slim" model gives closer correspondence to the data than the "fat" model. This is contrary to what is expected due to the expectation being that models with solid accumulation have lower permeability than those without, as discussed in Section 3.1.7. The Darcy permeability experimental data provided by Garrido et al. [19] is also located lower than the model predictions provided by the models with and without node-lump adjustments. This may be due to the presence of closed pores. As previously mentioned, in Section 3.1.1, Garrido et al. [19] focused on ceramic foams within the lower porosity range. Therefore, the "fat" MCL model furthermore performed better in this case than the "slim" MCL model, since the "fat" model permeability predictions are lower than the "slim" model predictions for the lower porosity range. The image of one of their foam samples furthermore revealed that their foams contained a significant addition of solid matter at the nodes. Dietrich et al. [20] also investigated ceramic foams, but as can be noted from Figure 3.16, the experimental data of the Darcy permeability provided by them are higher than the Garrido et al. [19] data in the same porosity range. An image of their foam sample revealed moderate accumulation of solid matter at the nodes. Table 3.1 reveals that the average percentage error between the "slim" and "fat" MCL models is not large, even though the "slim" model performed slightly better. Mancin et al. [21] provided an image of their 10 PPI aluminium foam sample, which showed little to no solid accumulation at the nodes. In Figure 3.16 the two highest data points of the Mancin et al. [21] experimental data sets are, respectively, for their 20 PPI and 40 PPI foam samples. The majority of experimental data are slightly higher than those provided by Bhattacharya et al. [3], but still lower than the model predictions. The copper foam samples of Mancin et al. [22], however, show moderate accumulation of solid at the nodes and as expected, the experimental data points are predominantly slightly lower than the data of Mancin et al. [21] (which show little to no accumulation of solid at the nodes). All the models follow the tendency of over-predicting the Darcy permeability at high porosities. In general, the three-strut RUC model still performed better when compared to the experimental data where the presence of solid accumulation is noted, because the Darcy permeability predictions of the three-strut RUC model are lower than the predictions of the other models, even lower than that of the "fat" MCL model. In order to represent the experimental data of foams with the presence of solid accumulation at the nodes of the foams better, a model adjustment that assures the prediction of lower Darcy permeability values is thus required.

Forchheimer permeability

The Forchheimer permeability is made dimensionless in this section by dividing by the pore diameter. The prediction for the Forchheimer permeability obtained from the model provided by Ahmed et al. [7] is given by equation (3.69). These predictions are compared to the predictions of the literature models provided by Dietrich et al. [20] and Giani et al. [64], given by equations (1.28) and (1.29), respectively, and the experimental data provided in Section 1.3.3. The Forchheimer permeability predictions of the three-strut RUC model, given by equation (2.128), are also included. Similar to the Darcy permeability section and for the same purpose, both the "fat" and "slim" MCL model average percentage errors and graphical predictions are given. The resulting relative percentage errors and predictions are provided and shown in Table 3.2 and Figure 3.17, respectively.

TABLE 3.2: *Relative percentage error of node adjusted models from the literature compared to K_F/d_p predictions and data of Chapter 1*

	Literature models (Section 3.1) Ahmed et al. [7]	
	"slim" MCL model	"fat" MCL model
Experimental data (Section 1.3.3)		
Bhattacharya et al. [3]	103 %	404 %
Garrido et al. [19]	53 %	20 %
Dietrich et al. [20]	22 %	35 %
Mancin et al. [21]	54 %	150 %
Mancin et al. [22]	47 %	102 %

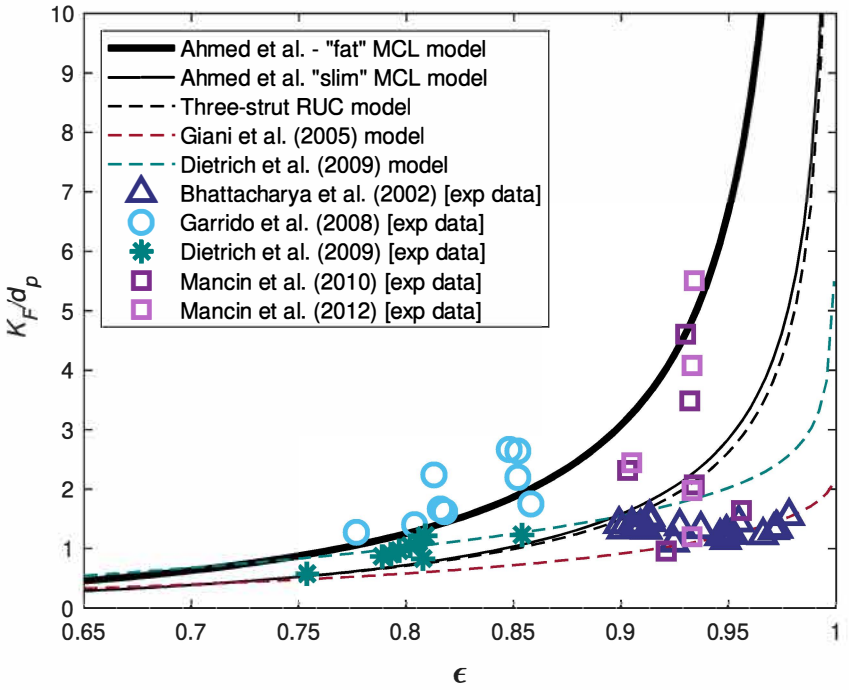

FIGURE 3.17: *Dimensionless Forchheimer permeability prediction versus porosity obtained from foam models with and without incorporated node solid lumps compared to experimental data*

Due to the reasons given in Section 3.1.7, it is expected that the Forcheimer permeability decreases with the presence of solid accumulation at the nodes of the foam, i.e. the pressure drop of the foam increases and therefore the Forchheimer permeability decreases much like the Darcy permeability. The two experimental data sets that seem to confirm the theory of Ahmed et al. [7] (i.e. the theory that the Forchheimer permeability increases with the presence of solid accumulation at the nodes), however, are the data sets obtained from Mancin et al. [21] and Mancin et al. [22]. As mentioned in the previous section where the Darcy permeability was addressed, the foams used by Mancin et al. [21] had little to no solid accumulation, whereas Mancin et al. [22] used foams with moderate solid accumulation at the nodes. In Figure 3.17 it can be seen that most of the data points provided by Mancin et al. [22] is slightly greater than the data points provided by

Mancin et al. [21]. The experimental data points of these two literature sources differ only slightly, however, which might suggest that the Forchheimer permeability is not affected significantly by the presence of solid lumps at the nodes. The model predictions of the "slim" MCL model, however, still corresponds closer to both these data sets than the "fat" MCL model as noted in Table 3.2. The "fat" MCL model furthermore corresponds the best to the Forchheimer permeability data provided by Garrido et al. [19]. The experimental data provided by Dietrich et al. [20] still corresponds closer to the "slim" MCL model, as noted in Table 3.2, but in Figure 3.17 it is observed that the data points lie between the "fat" and "slim" MCL models. In contrast, the data of Bhattacharya et al. [3] lie lower in comparison to the MCL model predictions of the Forchheimer permeability. This coincides with the expectation as described before (i.e. the expectation that the Forchheimer permeability decreases with the presence of solid lumps at the nodes). In conclusion, the data generally corresponds closer to the models that do not take node-lumps into consideration which lends credit to the presumption that the Forchheimer permeability should decrease slightly when the solid accumulation at the nodes are taken into consideration. The data of Bhattacharya et al. [3] especially shows favour to this expectation. The data sets obtained from Mancin et al. [21] and Mancin et al. [22] seem to support the theory of Ahmed et al. [7] (that the Forchheimer permeability increases when solid accumulation at the nodes is taken into consideration), however, and therefore more experimental data of the Forchheimer permeability that specifically identifies the degree of solid accumulation at the nodes of foams is consequently desired to confirm what the preferred outcome should be.

Specific surface area

The specific surface area equations (in terms of the pore diameter) obtained from the literature are evaluated in this section. The model predictions determined from the node adjusted models from the literature under evaluation are given by the following equations and authors: equation (3.8) obtained from the work of Calmidi and Mahajan [1], equation (3.21) obtained from the work of Boomsma and Poulikakos [2], equation (3.28) obtained from the work of Bhattacharya et al. [3], equation (3.32) obtained from the work of Fourie and Du Plessis [4], equations (3.38) and (3.39) obtained from the work of Huu et al. [5] (for the triangular and cylindrical struts, respectively) and equation (3.51) obtained from the work of Edouard [6]. The equations provided by Calmidi and Mahajan [1], Boomsma and Poulikakos [2] and Bhattacharya et al, [3] furthermore require combinations with other equations in order to find the expressions for the specific surface area in terms of the pore diameter. These added combination equations are specified where necessary in this section. The model equations obtained from other literature resources that do not include the node adjustments (provided in Section 1.3.2) are furthermore given by equation (1.30) (Giani et al. [64]), equation (1.32) (Lacroix et al. [68]), equation (1.33) (Richardson et al. [45], i.e. the corrected version), equation (1.34) (Buciuman and Kraushaar-Czarnetzki [44]) and equations (1.35) and (1.37) (Huu et al. [5] for triangular and cylindrical struts, respectively). The relevant experimental data used for evaluation purposes are once again obtained from Section 1.3.3. The resulting relative percentage errors are given in

TABLE 3.3: *Relative percentage error of node adjusted models from the literature compared to $S_v d_p$ predictions and data of Chapter 1*

		Experimental data (Section 1.33)			
		Garrido et al. [19]	Dietrich et al. [20]	Mancin et al. [22]	Kumar et al. [71]
Literature models (Section 3.1)					
Calmidi and Mahajan [1]	with eq. (3.12)	107 %	94 %	29 %	4 %
	with eq. (3.13)	93 %	77 %	33 %	3 %
Boomsma and Poulikakos [2]	with eq. (3.10)	27 %	19 %	23 %	36 %
	with eq. (3.11)	91 %	73 %	41 %	3 %
Bhattacharya et al. [3]	with eq. (3.12)	28 %	32 %	54 %	64 %
	with eq. (3.13)	32 %	38 %	53 %	66 %
Fourie and Du Plessis [4]		25 %	16 %	22 %	37 %
Huu et al. [5]	with tri. struts	-	-	44 %	-
	with cyl. struts	121 %	108 %	-	25 %
Edouard [6]	"slim" MCL	12 %	12 %	26 %	43 %
	"fat" MCL	31 %	21 %	23 %	34 %

Table 3.3 and the model predictions are displayed in Figures 3.18 to 3.20. The node adjusted models obtained from the literature exceed the number of experimental data sets for comparison. The comparison in Table 3.3 is therefore structured differently from the other average percentage error tables in this study so far. The average percentage errors between the "slim" MCL model (acquired from the work of Edouard et al. [6]) are also included in Table 3.3, similar to the evaluation of the permeability models acquired from the study of Ahmed et al. [7]. The "slim" dodecahedron models are, however, not included because the average percentage error results are already provided in Table 2.3 for reference. Furthermore, the literature models are displayed in their different categories: tetrakaidecahedron-type geometry, dodecahedron geometry and cubic unit cell type geometry in Figures 3.18, 3.19 and 3.20, respectively. This manner of display was chosen in order to better evaluate each of the models due to the number of models under consideration, i.e. to minimize the clutter in a single figure. The specific surface area predictions of the three-strut RUC model are added for reference purposes in each of the figures, along with the relevant non-adjusted literature models for comparison purposes.

Experimental data for the specific surface area acquired from Kumar et al. [71] are shown in addition to experimental data sets acquired from sources already addressed in the sections regarding the Darcy and Forchheimer permeability evaluation. Kumar et al. [71] obtained their experimental data from casted Kelvin cell foams, i.e. foams that have tetrakaidecahedron-type geometry for every cell, and noted that the node accumulation led to an increase of the specific surface area in their results. As expected, when taking Table 2.3, Table 2.6, Table 3.3 and Figures 3.18 to 3.20 into account, the experimental data obtained from Kumar et al. [71] is resembled more accurately by the node adjusted models than their non-adjusted counterparts, i.e. by the models acquired from the work of Calmidi and Mahajan [1], Boomsma and Poulikakos [2] (combined with the pore diameter relation from Richardson et al. [45]) and the "fat" dodecahedron model of Huu et al. [5].

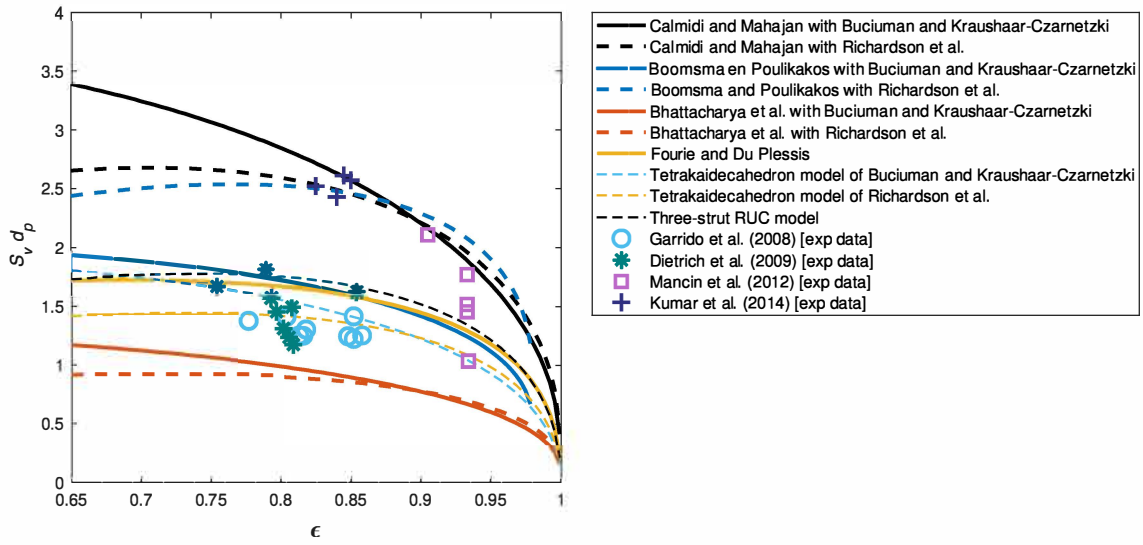

FIGURE 3.18: *Dimensionless specific surface area predictions versus porosity obtained from foam models with and without incorporated node solid lumps compared to experimental data: tetrakaidecahedron-type geometry*

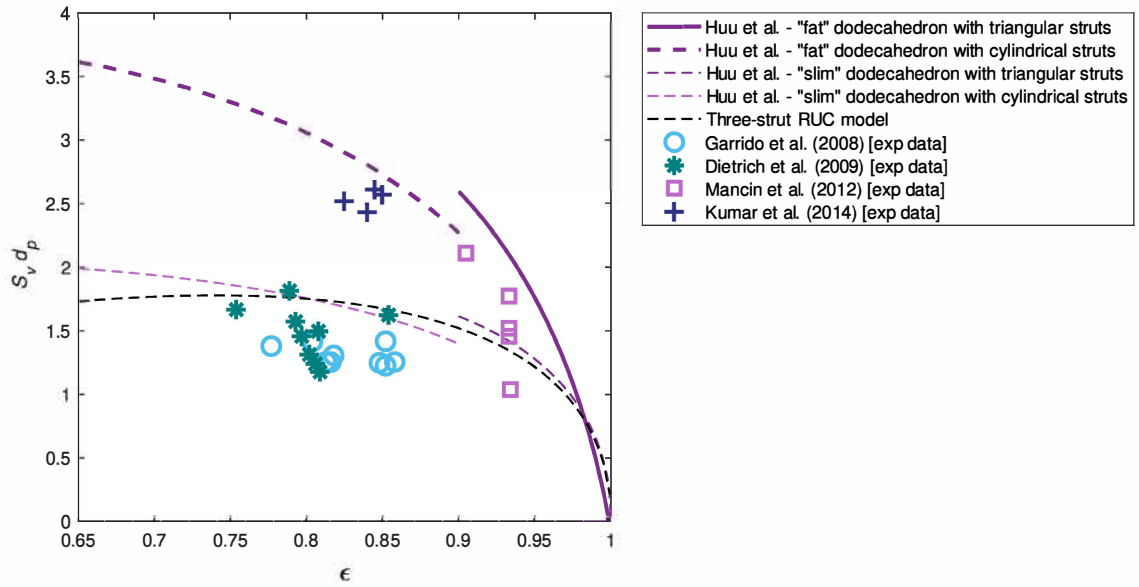

FIGURE 3.19: *Dimensionless specific surface area predictions versus porosity obtained from foam models with and without incorporated node solid lumps compared to experimental data: dodecahedron geometry*

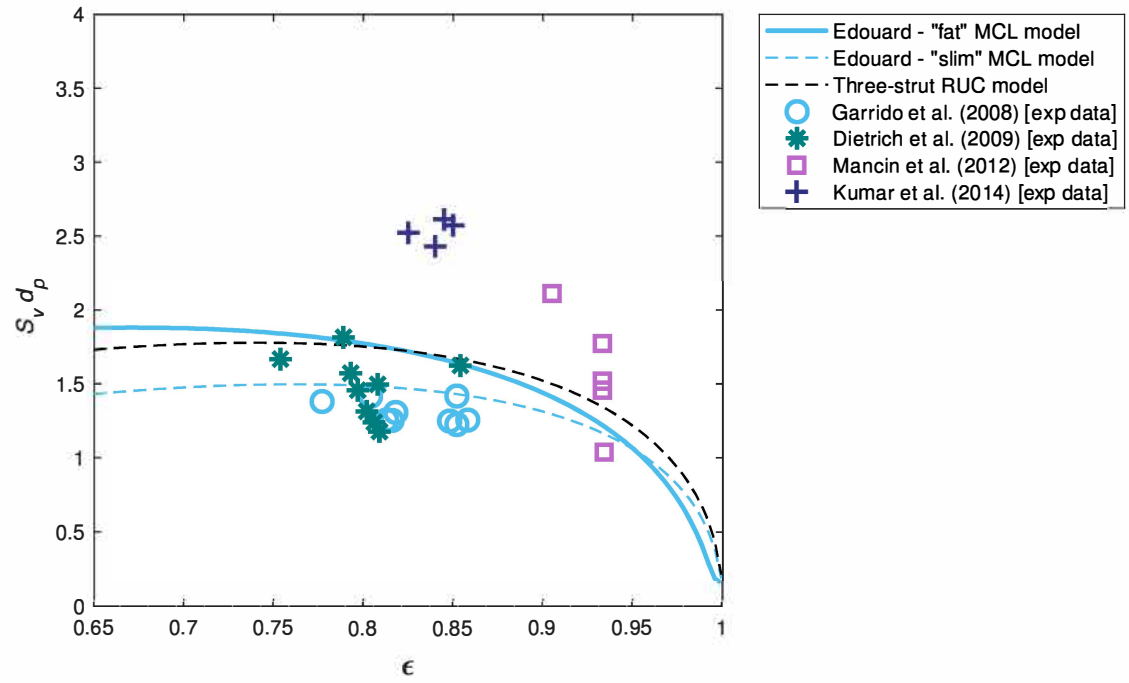

FIGURE 3.20: *Dimensionless specific surface area predictions versus porosity obtained from foam models with and without incorporated node solid lumps compared to experimental data: cubic unit cell type geometry*

These models furthermore represent the trend of the experimental data provided by Mancin et al. [22] more accurately, even though the average percentage errors reveal that the approximations of the specific surface area of these models perform almost equal

to some of the non-adjusted foam models. Figure 3.18 also confirms that the predictions provided by the model attained from the work of Bhattacharya et al. [3] are much lower than expected. This model will therefore not be recommended for predicting the specific surface area of foams with solid accumulation present at the nodes. The experimental specific surface area obtained from Garrido et al. [19] and Dietrich et al. [20], appear lower than expected when it is regarded that node accumulation leads to an increase in surface area. The over-prediction of the specific surface area by literature models was noted by Garrido et al. [19], as mentioned earlier in this chapter. The existence of closed pores, as also mentioned by these authors, could possibly be the reason for the lower prediction of the specific surface area. Nevertheless, the node adjusted models that consequently give better overall approximations for the data sets considered are the literature models obtained from the work of Boomsma and Poulikakos [2] (combined with the pore dimension relation from Buciuman and Kraushaar-Czarnetzki [44]), Fourie and Du Plessis [4] and Edouard [6]. It is, however, noted that the models obtained from the work of Calmidi and Mahajan [1], Boomsma and Poulikakos [2] (combined with the pore dimension relation from Richardson et al. [45]) and "fat" dodecahedron model of Huu et al. [5] compare well with the data of Kumar et al. [71].

In the following section the RUC models that are modified to incorporate the presence of solid lumps at the nodes of a foam are introduced.

3.2 Node Adjusted RUC (NARUC) model

In this section two different ways of adjusting the foam (or three-strut) RUC model are shown to accommodate the presence of solid matter at strut intersections, one using cubic nodes and the other using nodes that resemble curved wedges. The foam RUC model adjusted to accommodate the presence of solid matter accumulated at the nodes of the foam will be referred to as the Node Adjusted RUC (NARUC) model. The permeability equations for both the Darcy and Forchheimer regimes will be presented for each of the NARUC model options, as well as the specific surface area equations obtained using the geometric approach. Furthermore, three different manners of obtaining the necessary ratios of the node adjusted model using cubic nodes are presented, which involves the combination of the NARUC model with the dodecahedron model, MCL model and node adjusted tetrakaidecahedron model, respectively. (The node adjusted tetrakaidecahedron model will be referred to as the modified tetrakaidecahedron model in the remainder of the chapter.) The geometry of the NARUC model with nodes that resemble curved wedges is chosen in such a manner that a combination with another geometric model is not required to obtain the necessary ratios. The different NARUC model options and the different ratios obtained due to the different model combinations are all evaluated to determine the model and model combination that gives the most physically sound and accurate predictions. The ratios are defined in a similar manner as in Edouard [6], i.e.

$$r_1 = \frac{a}{d}, \tag{3.70}$$

and

$$r_2 = \frac{x}{a}, \tag{3.71}$$

where $d_s = 2a$. For all the NARUC model options, U_o still remains the same as in the case of the three-strut foam RUC model, that is $U_o = d^3$. The following relations between

the dimensions d, d_p and d_s apply to all the NARUC model options and are derived from equation (3.70) as well as the fact that $d_s = 2a$ and $d = d_p + d_s$:

$$d = \frac{d_s}{2r_1}\,, \tag{3.72}$$

$$d = \frac{d_p}{1 - 2r_1}\,, \tag{3.73}$$

and

$$d_p = \frac{(1 - 2r_1)d_s}{2r_1}\,. \tag{3.74}$$

The NARUC model that represents the accumulation of solid matter as cubes at the strut intersection (similar to the MCL model) and the NARUC model that represents the accumulation as curved wedges at the strut intersection (similar to the "fat" dodecahedron model) are shown in Figures 3.21(a) and (b), respectively. In Figure 3.21 the visual representation of the manner in which the two NARUC model options are acquired are furthermore illustrated, as will be discussed below.

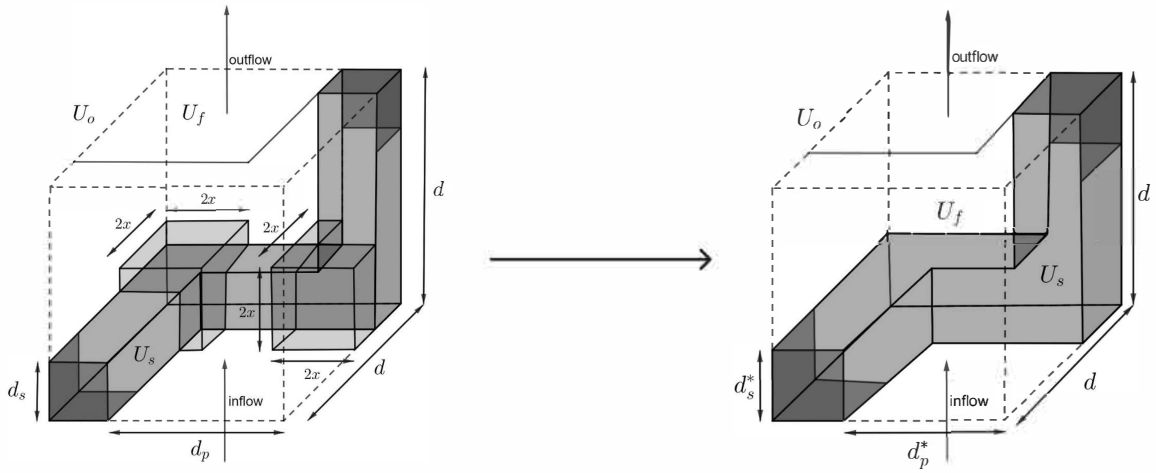

(a) *Node volumes represented by cubes*

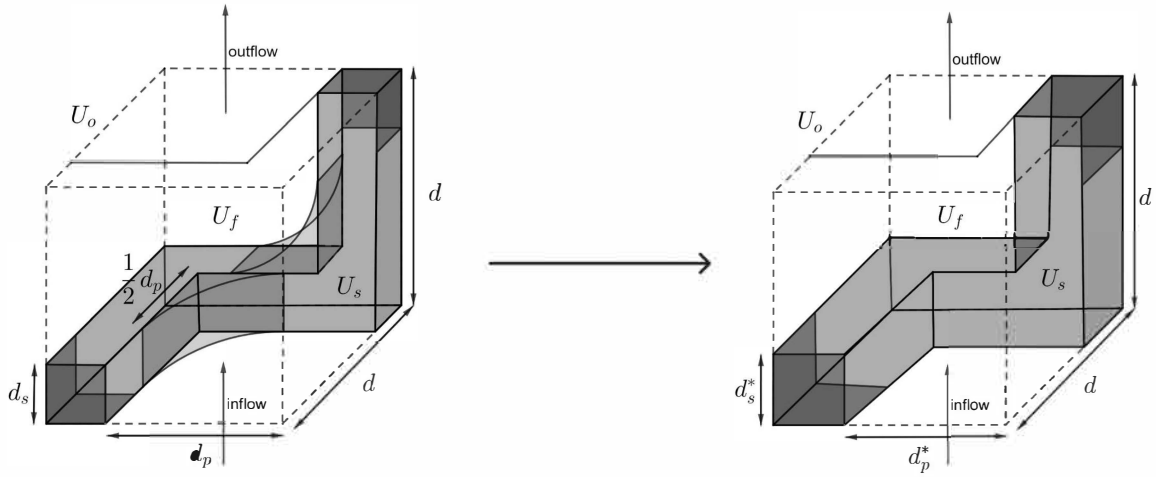

(b) *Node volumes represented by curved wedges*

FIGURE 3.21: *NARUC model options*

On the left-hand side of Figure 3.21(a) it can be seen that the node lumps are represented as cubes that are moulded into the intersection of two struts. Similarly, in Figure 3.21(b) the node lumps are added to the strut intersections and resembles a shape that would be acquired if a cylinder with diameter d_p was partially cut out of a square prism, where the square side lengths are assumed to also be equal to d_p. The shape then resembles one of the corners that will be left in the square prism and is hence described as a curved wedge. The foam RUC models with the respective shapes of volumes added in order to represent the nodes (the left-hand sides of Figures 3.21(a) and (b)) are then utilized to acquire a novel foam RUC model with adjusted parameters, represented by the right-hand side of Figures 3.21(a) and (b), respectively. The NARUC models with adjusted parameters are identical visual portrayals of the non-adjusted foam (three-strut) RUC model as illustrated in Figure 2.8(b), but with adjusted linear dimensions. The adjusted parameters are represented by d_s^* and d_p^* and ascribe to the parameter relations provided in Section 2.3.1. The transition between the models with the nodes and the models with the adjusted parameters are implemented by setting the porosity of these RUC models equal, as well as the cell sizes. Consequently, the solid volumes of these two RUC models (the left- and right-hand sides of Figure 3.21) are the same.

As mentioned in Chapter 1, the d_s and d_p measurements acquired from foams are usually located where the struts are the thinnest. Therefore, when the accumulation of solid around the nodes are taken into account, the average diameter of the entire strut will increase. Equivalently, the average diameter of the entire pore will decrease. This reasoning led to the construction of the NARUC model with adjusted pore-scale parameters. This construction furthermore provides a result where all the benefits of the RUC model and the rectangular geometry thereof is preserved.

It is noted that only two nodes are added to each of the models shown in Figure 3.21. In this study, however, provision is made in the model equations to add any number of nodes to either of the two model options and the number of nodes is furthermore denoted by k. As noted before, some foams have higher degrees of solid accumulation than other foams at similar porosities and consequently, in the case of the NARUC models, the added number of nodes can portray the degree of accumulation. However, only $k = 3$ for the NARUC model with cubic nodes is considered and is restricted in such a manner due to the number of places where two struts would intersect in the RUC. Beyond this number, the model will not be theoretically and geometrically viable. In order to remain within a reasonable number of nodes ascribed to the NARUC model with curved wedge nodes, it is however recommended that either 3, 6, 9 or 12 nodes be added. The two nodes are therefore added in Figure 3.21 for illustration purposes, but the rest of the numbers of nodes are chosen to assign either 1, 2, 3 or 4 nodes to each of the three main directions of flow. The use of more than 12 nodes will not make sense in the context of the rectangular geometry of the RUC model. In the case of the NARUC model obtained using curved wedge nodes, the model with 3 nodes will ideally represent the foam with less solid accumulation and the model with 12 nodes the foam with a high degree of solid accumulation. No variation in the number of nodes is however considered in the case of the NARUC model obtained using cubic nodes.

It is also noted that r_2 will only be required in the NARUC model option where cubic nodes are utilized. r_2 can also be defined as $r_2 = 1 + \delta$, as in the case of Edouard [6] given by equation (3.42), although it is not required in the calculations and equations related to the NARUC models. The derivation of the permeability and specific surface

area equations, as well as the different manners in which the ratios are acquired, will be presented next for the NARUC model where cubic nodes are utilized, as shown in Figure 3.21(a).

3.2.1 NARUC model with cubic nodes

In order to determine the expressions for the permeability and specific surface area of the NARUC model with adjusted pore-scale parameters, the ratio between the original and adjusted parameters is needed, e.g. the value of a factor R such that

$$d_s^* = R d_s \,. \tag{3.75}$$

The factor R, as defined in equation (3.75), can furthermore be used to obtain the relation between d_p^* and d_p by noting that $d_s^* = d - d_p^*$ and by applying the dimension relations given by equations (3.73) and (3.74) to obtain d_p. This results in

$$d_p^* = \frac{1 - 2r_1 R}{1 - 2r_1} \, d_p \,. \tag{3.76}$$

Once R is acquired, the permeability and specific surface area equations for the three-strut RUC model can be utilized using the adjusted parameters (d_s^* and d_p^*). As mentioned previously, the porosity and cell sizes of the foam RUC model with the nodes included into the geometry of the model (shown on the left-hand side of Figure 3.21 (a)) and the NARUC model with adjusted parameters (shown on the right-hand side of Figure 3.21 (a)) are assumed to be equal, i.e. $\epsilon = \epsilon^*$ and $d = d^*$. Due to these assumptions, expressions for the porosity for each of the models can be determined and set equal to one another in order to acquire an equation from which a factor describing the transition between the pore-scale parameters (in this case chosen to be the factor R, as defined by equation (3.75)), can be determined. An expression for the porosity of the model on the left-hand side of Figure 3.21(a) is determined first. The volume added to the solid volume of the foam RUC model of one cubic node can be determined from Figure 3.21(a) and is given by

$$U_{s_{\text{node}}} = (2x)^3 - \left[d_s^3 + 2\,(2x - d_s)\,d_s^2\right] \,. \tag{3.77}$$

The total solid volume is therefore the addition of the solid volume of the three-strut RUC model, given by $U_s = 3d_s^2 d_p + d_s^3$ (as provided in Chapter 2, Section 2.3.1) and the number of nodes times the volume of one node (given by equation (3.77)). Furthermore, utilizing equations (3.70), (3.71) and $d_s = 2a$, leads to the following expression for the solid volume:

$$\begin{aligned} U_s &= 3d_s^2(d - d_s) + d_s^3 + k\left[(2x)^3 - \left[d_s^3 + 2\,(2x - d_s)\,d_s^2\right]\right] \\ &= \left[\frac{3}{2r_1} - 2\right](2a)^3 + k\left[r_2^3 - 2r_2 + 1\right](2a)^3 \,. \end{aligned} \tag{3.78}$$

Consequently the solid volume fraction is determined as follows:

$$1 - \epsilon = \frac{U_s}{U_o} = 12r_1^2 - 16r_1^3 + 8kr_1^3\left(r_2^3 - 2r_2 + 1\right) \,. \tag{3.79}$$

The porosity of the NARUC model with adjusted parameters (i.e. shown on the right-hand side of Figure 3.21(a)) can similarly be determined by starting with the expression

of the solid volume. Due to the resemblance to the three-strut RUC model and also that $d = d_p^* + d_s^*$, the solid volume is given by

$$U_s^* = 3d_s^{*2}d_p^* + d_s^{*3} = 3dd_s^{*2} - 2d_s^{*3}\,. \tag{3.80}$$

The expression for the solid volume fraction in terms of both d_s^* and d_s can therefore be calculated using both equations (3.72) and (3.80), resulting in

$$1 - \epsilon = \frac{U_s^*}{U_o} = 12r_1^2\left(\frac{d_s^*}{d_s}\right)^2 - 16r_1^3\left(\frac{d_s^*}{d_s}\right)^3\,. \tag{3.81}$$

Setting equations (3.79) and (3.81) equal consequently results in the following third-degree polynomial of R (as defined in equation (3.75)):

$$\left[16r_1^3\right]R^3 + \left[-12r_1^2\right]R^2 + \left[12r_1^2 - 16r_1^3 + 8kr_1^3\left(r_2^3 - 2r_2 + 1\right)\right] = 0\,, \tag{3.82}$$

from which R can be determined by making use of the Cardanic method, as discussed in Appendix A. The expression for R is hence given by

$$R = \frac{1}{2\sqrt{r_1}}\cos\left[\frac{1}{3}\cos^{-1}\left[1 + 8r_1^2\left(4r_1 - 3\right) - 16r_1^3k\left(r_2^3 - 2r_2 + 1\right)\right] + \frac{4}{3}\pi\right] + \frac{1}{4r_1}\,. \tag{3.83}$$

The permeability and specific surface area equations for the NARUC model are similar to that of the three-strut RUC model, as mentioned previously, given by equations (2.127), (2.128) and (2.86). For convenience, these equations are given below in terms of the adjusted parameters as follows:

$$K = d_p^{*2}\frac{\epsilon^2}{9\psi^2(\psi - 1)(3 - \psi)^2}\,, \tag{3.84}$$

$$K_F = d_p^*\frac{4\epsilon^3}{\psi^2(\psi - 1)(3 - \psi)^2}\,, \tag{3.85}$$

and

$$S_v = \frac{3}{2d_p^*}(3 - \psi)^2(\psi - 1)\,, \tag{3.86}$$

where ψ is given by equation (2.72). Substituting equation (3.76) into equations (3.84) to (3.86) yields

$$K = d_p^2\frac{\epsilon^2\left(1 - 2r_1R\right)^2}{9\psi^2(\psi - 1)(3 - \psi)^2\left(1 - 2r_1\right)}\,, \tag{3.87}$$

$$K_F = d_p\frac{4\epsilon^3\left(1 - 2r_1R\right)}{\psi^2(\psi - 1)(3 - \psi)^2\left(1 - 2r_1\right)}\,, \tag{3.88}$$

and

$$S_v = \frac{3(3 - \psi)^2(\psi - 1)\left(1 - 2r_1\right)}{2d_p\left(1 - 2r_1R\right)}\,. \tag{3.89}$$

The Darcy permeability, Forchheimer permeability and specific surface area of the NARUC model, adjusted using cubic nodes, can therefore be determined from equations (3.87), (3.88) and (3.89), respectively, where R is given by equation (3.83).

A method of determining the r_1- and r_2-ratios is needed in order to complete the calculation of the permeability and specific surface area. In order to do this, a similar approach is followed as done by Edouard [6] in that two models are combined to obtain the ratio values. Three NARUC model combinations are introduced to obtain the ratio values where the NARUC model obtained using cubic nodes is combined with some of the node adjusted models discussed in Section 3.1. The node adjusted models considered for combination with the NARUC model are those obtained from Huu et al. [5] (dodecahedron model), Edouard [6] (MCL model) and Fourie and Du Plessis [4] (modified tetrakaidecahedron model). The strategy for obtaining the ratio values is discussed and evaluated for each of the combinations considered. Once the r_1- and r_2-ratio values are obtained, it can be substituted into equations (3.87), (3.88) and (3.89) to determine the permeabilities and specific surface area, respectively.

Dodecahedron model combination

The combination of the NARUC model with cubic nodes and the "fat" dodecahedron model provided by Huu et al. [5], discussed in Section 3.1.5, is done very similar to the method used by Edouard [6], discussed in Section 3.1.6, in order to obtain the ratio values. In this section, however, combinations with both the triangular and cylindrical strut shaped models are included. Once again, the terms of the ratio expressions of both the dodecahedron model and NARUC model, representing those associated with and without the accumulation of matter at the nodes, are equated and results in equations for the determination of r_1 and r_2. The "fat" dodecahedron model with triangular struts is considered first.

The part of the solid volume fraction for the dodecahedron model, with triangular struts, without the node adjustments included, is represented by equation (1.36) (or the left-hand side of equation (3.46)). The values of the r_{tf}-ratio are determined from the porosity by using equation (3.33), which is then substituted into the left-hand side of equation (3.46), such that a value C_t can be determined, i.e.

$$C_t = \frac{\sqrt{15}}{\phi^4} r_{tf}^2 - \frac{\sqrt{10}}{3\phi^4} r_{tf}^3 \,. \tag{3.90}$$

The C_t-value is then equated to the sum of the terms of the solid volume fraction (given by equation (3.79)) that does not include the accumulated matter at the nodes of the model. This sum is given by $12r_1^2 - 16r_1^3$. Therefore, r_1 can be determined using the following expression:

$$16r_1^3 - 12r_1^2 + C_t = 0 \,. \tag{3.91}$$

The results for porosity values between 0.9 and 1, for the NARUC model combined with the "fat" dodecahedron model with triangular struts, are displayed in Figure 3.22.

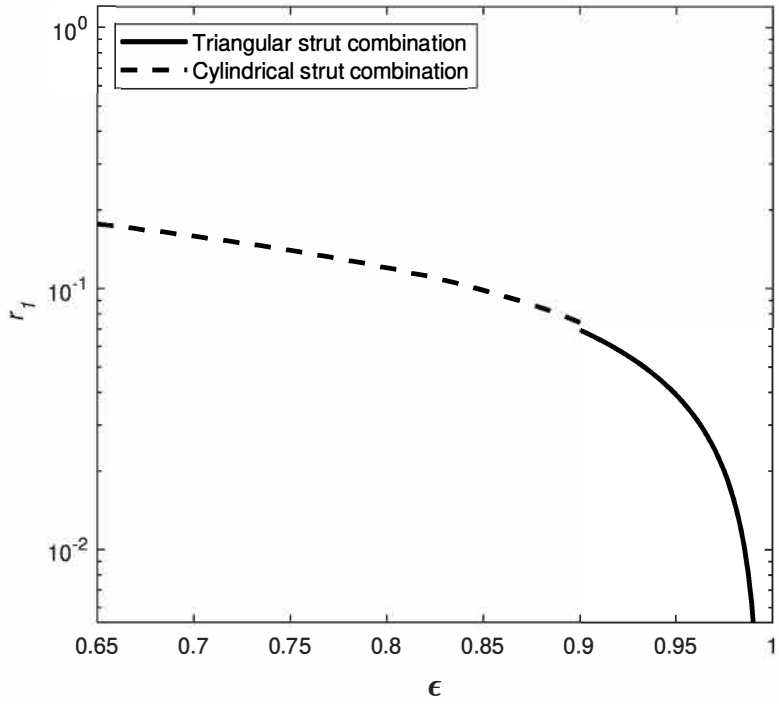

FIGURE 3.22: *Ratio of strut radius to face diameter versus porosity of NARUC model with cubic nodes combined with "fat" dodecahedron model obtained from Huu et al. [5]*

In order to determine r_2, the terms of the solid volume fraction of both the dodecahedron and NARUC model that represents only the accumulated matter are utilized. The calculation thereof is commenced by substituting the value obtained for r_{tf} into the left-hand side of equation (3.47) to obtain C_{node}, i.e.

$$C_{\text{node}} = \left[\frac{Z}{6} - \frac{\sqrt{6}\,W}{36}\right] r_{tf}^3 + \left[-\sqrt{\frac{2}{3}}\,Z + \frac{W}{2}\right] r_{tf}^2 + \left[Z - \frac{\sqrt{6}\,W}{2}\right] r_{tf} + W\,, \tag{3.92}$$

where W and Z are given by equations (3.35) and (3.36), respectively. It is noted that the sum of the terms of the solid volume fraction of the dodecahedron model that represents the added node lumps is the same, irrespective of whether triangular or cylindrical struts are used. Hence, when the dodecahedron model with cylindrical struts are considered, r_{tf} in equation (3.92) becomes r_{cf} in order to determine C_{node}. The value of C_{node} is then equated to the sum of the terms of the solid volume fraction of the NARUC model (given by equation (3.79)) that represents the accumulated matter, yielding

$$\left(8kr_1^3\right) r_2^3 + \left(-16kr_1^3\right) r_2 + \left(8kr_1^3 - C_{\text{node}}\right) = 0\,, \tag{3.93}$$

where r_1 is determined from equation (3.91). The resulting predictions of r_2 for a given porosity and for a node number of 3 are shown in Figure 3.23.

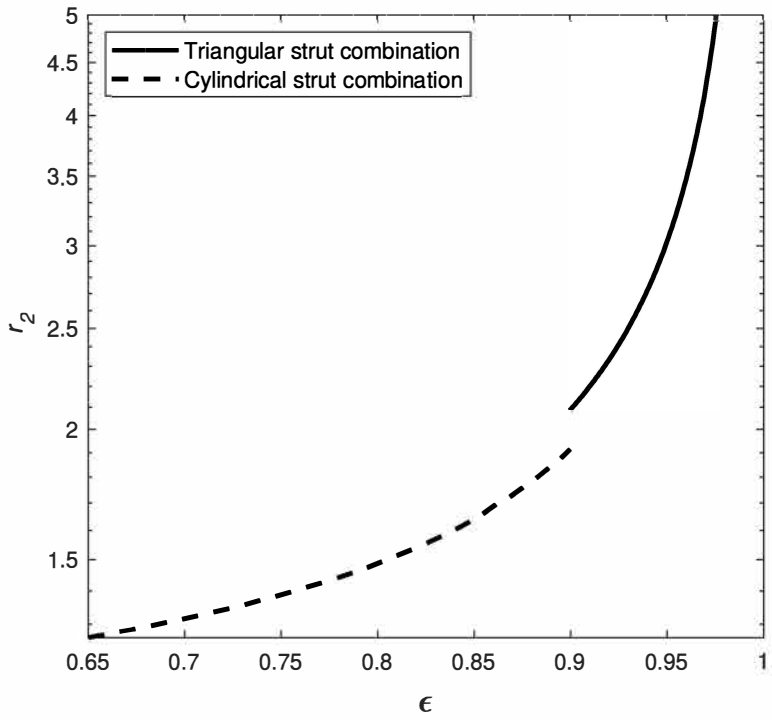

FIGURE 3.23: *Ratio of cubic node lump edge width to strut radius versus porosity of NARUC model with cubic nodes combined with "fat" dodecahedron model obtained from Huu et al. [5]*

The "fat" dodecahedron model with cylindrical struts is considered next. The part of the solid volume fraction that represents the dodecahedron model with cylindrical struts that do not take the added node lumps into consideration is given by the left-hand side of equation (1.38), without $(1-\epsilon)$. In this case r_{cf} is determined from equation (3.37) using porosity as input. The value of C_c can hence be determined from

$$C_c = \left(\frac{\sqrt{10}}{6\phi^4} - \frac{\sqrt{5}\pi}{2\phi^4}\sqrt{\frac{2}{3}} \right) r_{cf}^3 + \frac{\sqrt{5}\pi}{\phi^4} r_{cf}^2 \,. \tag{3.94}$$

The calculation of r_1 and r_2 are furthermore similar to that in the case of the triangular struts, the only differences being that C_c replaces C_t in equation (3.91) and r_{cf} replaces r_{tf} in equation (3.92), as already mentioned. The resulting predictions for the ratio values of r_1 and r_2, for the combination of the "fat" dodecahedron model with cylindrical struts with the NARUC model, are respectively shown in Figure 3.22 and 3.23 for porosity values between 0.65 and 0.9.

In Figure 3.22 the ratio of the foam strut radius to the face diameter, r_1, is displayed and it is noted that for both the cases of triangular and cylindrical struts, r_1 decreases as the porosity increases. This is as would be expected for high porosity foams as the struts are expected to become thinner as the porosity increases. It is furthermore noted that the ratio is never higher than 0.5, as expected since $d_s < d$ and therefore $a < 0.5d$. Therefore, r_1 as determined in this section by combining the "fat" dodecahedron model and NARUC models is a viable approach. There is not a significant difference between the predictions of the combinations with the dodecahedron with triangular and cylindrical strut types at $\epsilon = 0.9$. In Figure 3.23 the ratio $r_2 = x/a$ is displayed and it can be seen that the trend

of the r_2-predictions increases with increasing porosity. The values of r_2 furthermore remain above 1, which makes sense since the node sizes remain larger than the strut sizes. In the case of r_2, however, there is a greater difference between the predictions of the combinations with the dodecahedron with triangular and cylindrical strut types where the transition occurs, which is not ideal, but similar to other observations where the dodecahedron model was evaluated earlier in this study. The dodecahedron model combination therefore proves to be a viable approach for determining r_2.

The resulting dimensionless permeabilities and dimensionless specific surface area predictions of the NARUC model obtained using cubic nodes and combined with the "fat" dodecahedron model in order to find the r_1- and r_2-ratio values are shown in Figures 3.24, 3.25 and 3.26, respectively.

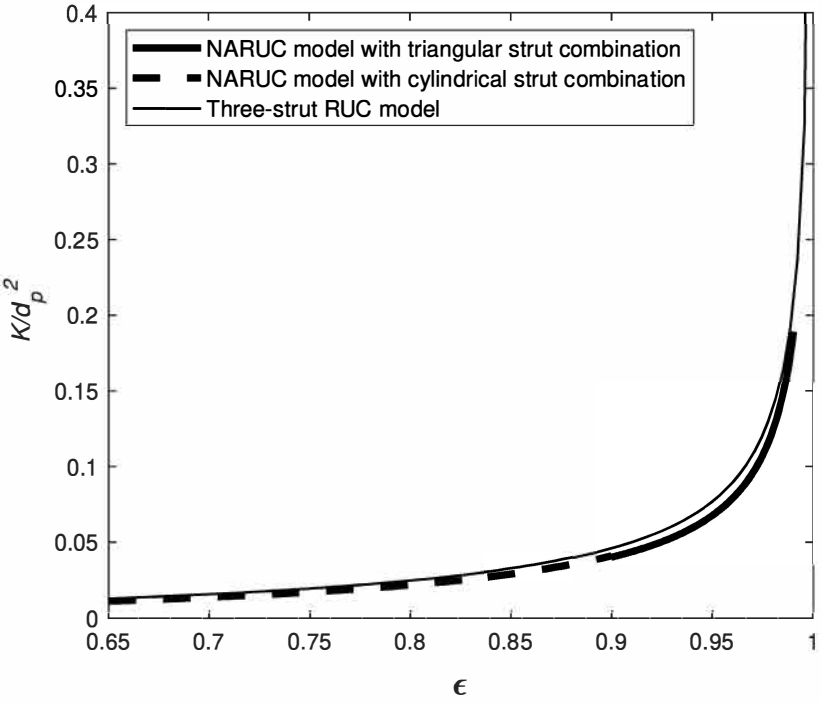

FIGURE 3.24: *Dimensionless Darcy permeability prediction versus porosity obtained from NARUC model adjusted using cubic nodes and combined with "fat" dodecahedron model and three-strut RUC model*

In Figure 3.24, the predictions for the Darcy permeability of the NARUC model are slightly lower than the predictions of the three-strut RUC model, as would be expected. Furthermore, the combination of the NARUC model with the "fat" dodecahedron model with triangular and cylindrical struts give similar predictions at the transition point where $\epsilon = 0.9$ (also in Figures 3.25 and 3.26 for the predictions of the Forchheimer permeability and specific surface area, respectively), which is a satisfactory result. The predictions for the Darcy permeability of the NARUC model are not significantly lower than that of the three-strut RUC model, which corresponds to the observation of Ahmed et al. [7] who mentioned that the permeability is not extremely sensitive to solid accumulation.

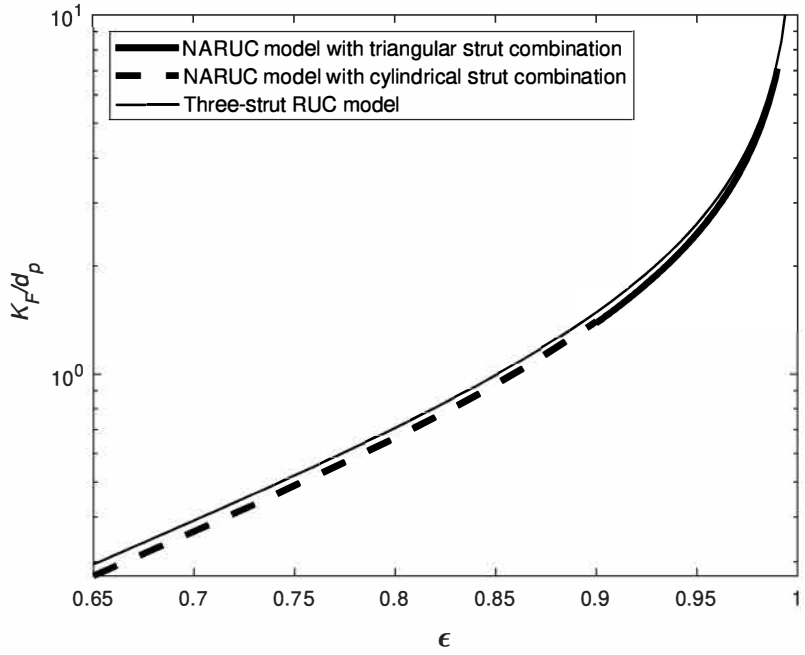

FIGURE 3.25: *Dimensionless Forchheimer permeability prediction versus porosity obtained from NARUC model adjusted using cubic nodes and combined with "fat" dodecahedron model and three-strut RUC model*

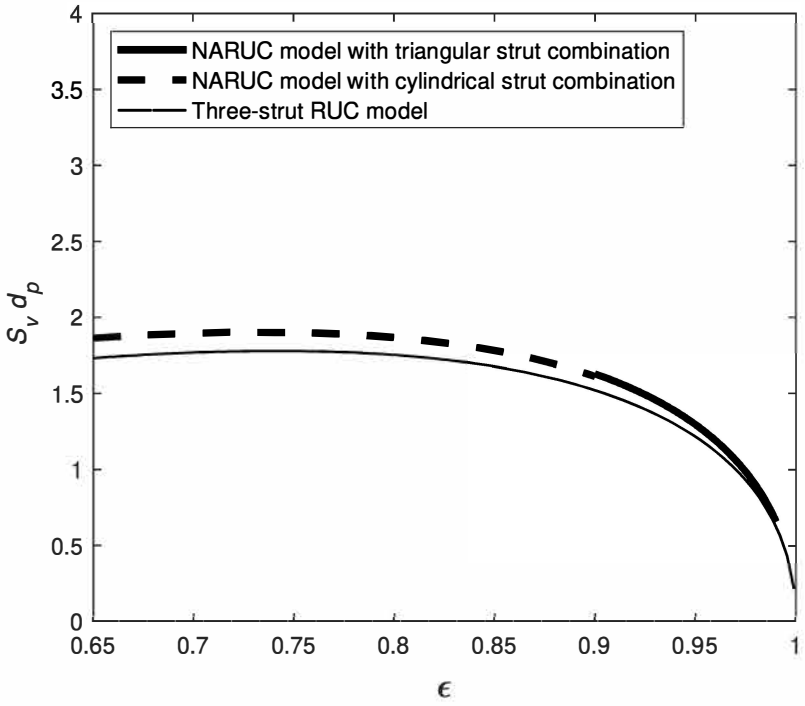

FIGURE 3.26: *Dimensionless specific surface area prediction versus porosity obtained from NARUC model adjusted using cubic nodes and combined with "fat" dodecahedron model and three-strut RUC model*

The predictions for the Forchheimer permeability are shown in Figure 3.25. The NARUC model combined with the "fat" dodecahedron model give lower predictions (although once again only slightly lower) than the three-strut RUC model, as expected and explained in Section 3.1.7. The close estimation of the Forchheimer permeability predictions of the NARUC model combination under consideration to the predictions of the three-strut RUC model led to the decision to use a semilog plot so that the decrease in the prediction of the Forchheimer permeability can be observed. The close approximation of the two models, however, lessens the usefulness of the model combination where the Forchheimer permeability is concerned.

In Figure 3.26 the predictions of the dimensionless specific surface area are shown for both the NARUC model and three-strut RUC model and once again, the predictions are as expected in that the predictions of the NARUC model are higher than the predictions of the three-strut RUC model, although not significantly higher.

The combination of the modified cubic lattice model, given by Edouard [6], and the NARUC model is considered next.

MCL model combination

Edouard [6] provided an expression for r_1 and δ in terms of the porosity, given by equation (3.45), and furthermore proposed that $r_2 = 1 + \delta$. The solid volume fraction in terms of r_1 and r_2 can therefore be expressed for the MCL model as follows:

$$1 - \epsilon = 3\pi r_1^2 (1 - 2r_1 r_2) + 8 r_1^3 r_2^3 . \tag{3.95}$$

Consequently, equation (3.95) in combination with the NARUC model with cubic nodes equation for the solid volume fraction (given by equation (3.79)) is used to obtain values for r_1 and r_2. In this section it is assumed that the r_1- and r_2-ratio values for each of the two models (MCL model and NARUC model) are equal. The values are determined by solving both polynomials with the two variables simultaneously. The root for r_1, for each porosity input value, is chosen such that it is real and positive and makes sense in context, i.e. $r_1 < 0.5$. Similarly, the root chosen for r_2, for each porosity input, is real and positive, but also such that $r_2 > 1$. The results are shown in Figures 3.27 and 3.28 for r_1 and r_2, respectively, for $k = 3$.

In Figure 3.27 it is evident that the r_1 predictions using the NARUC model in combination with the MCL model, are similar to the predictions obtained using the NARUC model in combination with the "fat" dodecahedron model, i.e. the predictions are below 0.5 for all porosity values and decreases as the porosity increases. The MCL model combination is therefore also a viable approach for determining r_1. In Figure 3.28 the predictions of r_2 for the NARUC model combined with the MCL model is shown. The r_2 results of the present model combination are also similar to the results of the NARUC and "fat" dodecahedron model combination since the r_2-value also increases with increasing porosity, although to a slightly lesser degree. Consequently this approach also proves to be viable for determining r_2. The permeability results observed in Figures 3.29 and 3.30 of the NARUC model are generally as expected.

The predictions for the Darcy permeability, Forchheimer permeability and specific surface area of the NARUC model combined with the MCL model are shown in Figures 3.29, 3.30 and 3.31, respectively.

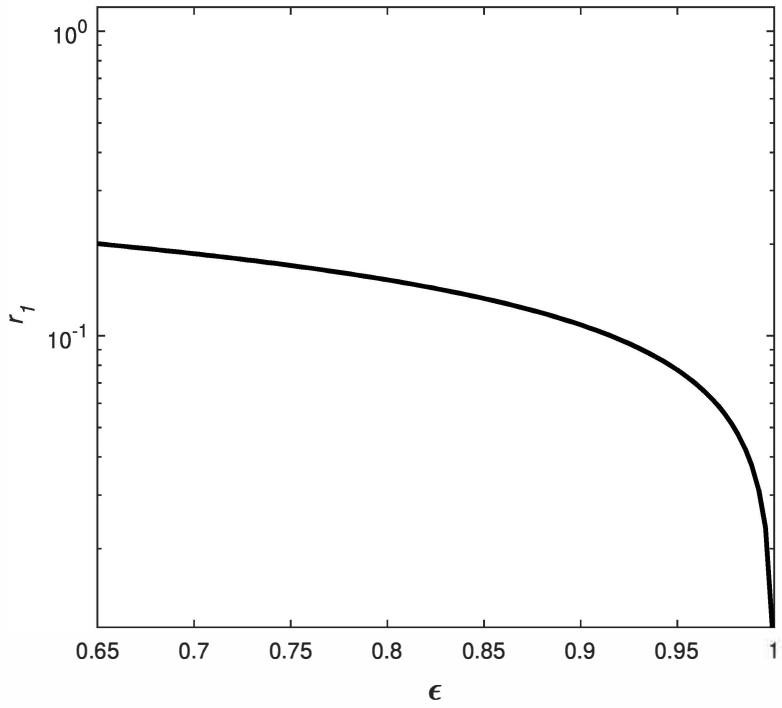

FIGURE 3.27: *Ratio of strut radius to face diameter versus porosity of NARUC model with cubic nodes combined with MCL model obtained from Edouard [6]*

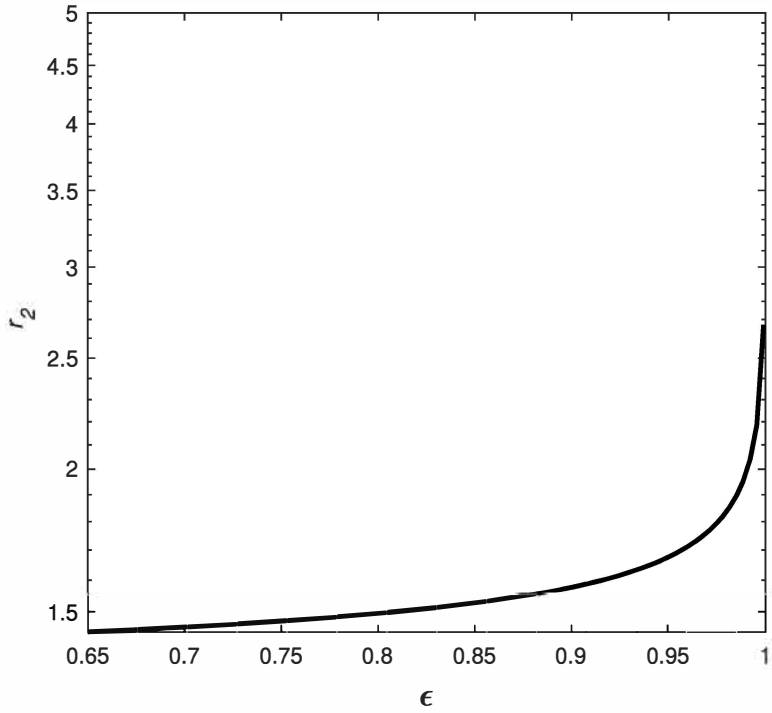

FIGURE 3.28: *Ratio of cubic node lump edge width to strut radius versus porosity of NARUC model with cubic nodes combined with MCL model obtained from Edouard [6]*

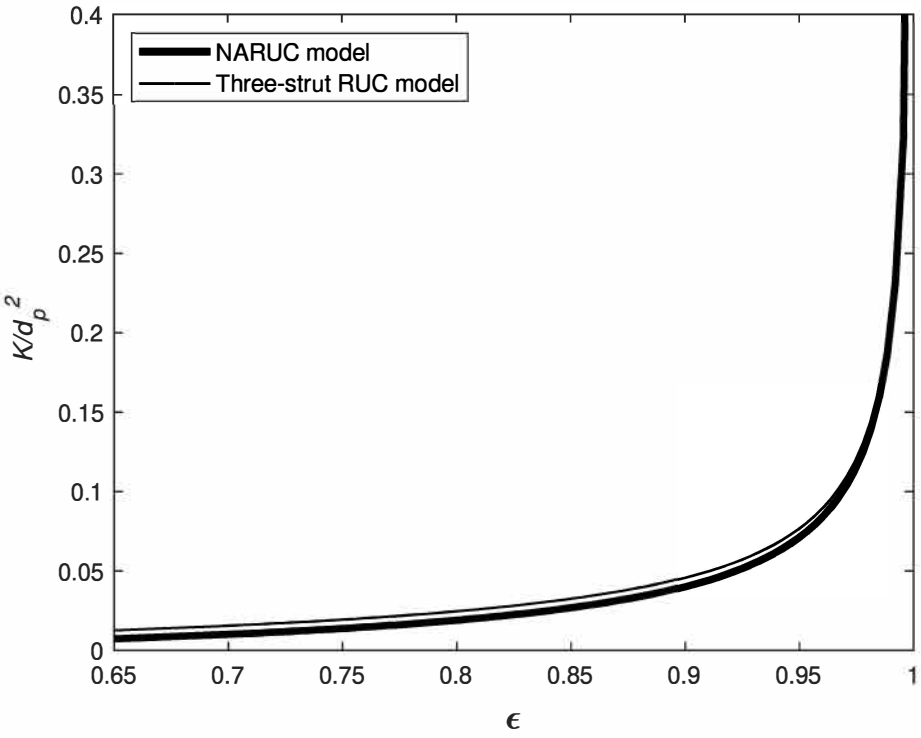

FIGURE 3.29: *Dimensionless Darcy permeability prediction versus porosity obtained from NARUC model adjusted using cubic nodes and combined with MCL model and three-strut RUC model*

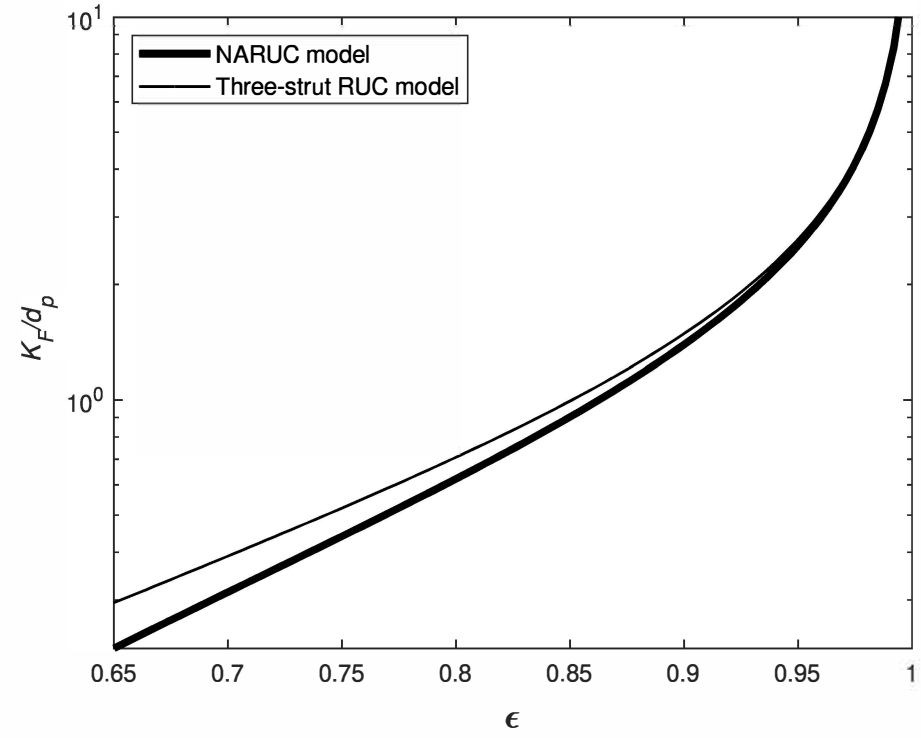

FIGURE 3.30: *Dimensionless Forchheimer permeability prediction versus porosity obtained from NARUC model adjusted using cubic nodes and combined with MCL and three-strut RUC model*

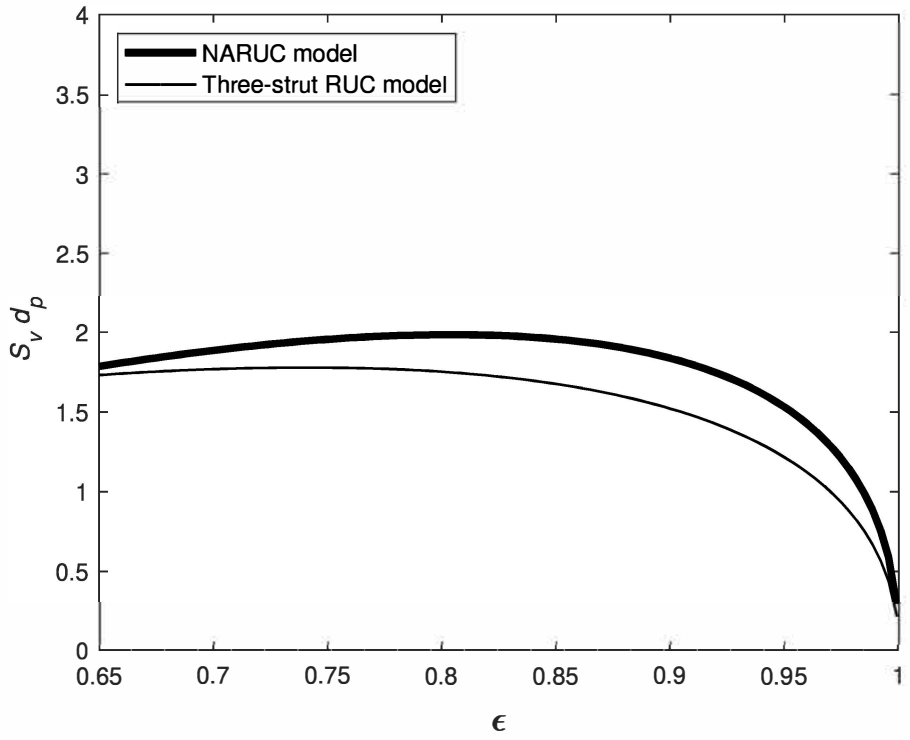

FIGURE 3.31: *Dimensionless specific surface area prediction versus porosity obtained from NARUC model adjusted using cubic nodes and combined with MCL model and three-strut RUC model*

The predictions for the Darcy permeability of the NARUC model are also slightly lower than that of the three-strut RUC model, as in the case of the predictions of the NARUC model combined with the "fat" dodecahedron model in Figure 3.24 and the Ahmed et al. [7] model in Figure 3.14. Consequently, the predictions of the Darcy permeability of the NARUC model combined with the MCL model are a valid representation. The predictions for the Forchheimer permeability shown in Figure 3.30 are lower than those of the three-strut RUC model, which are similar to the predictions observed for the NARUC model combined with the 'fat" dodecahedron model. The trend of the current model combination differs from the "fat" dodecahedron model combination, however, in that the permeability prediction decreases more than the prediction of the "fat" dodecahedron model combination as the porosity decreases. The predictions for the dimensionless specific surface area of the NARUC model combined with the MCL model, shown in Figure 3.31, are slightly different than the predictions of the NARUC model combined with the "fat" dodecahedron model in terms of the predictive trend. The predictions for the specific surface area of the NARUC model combined with the MCL model are lower than that of the three-strut RUC model for lower porosity values (though not shown in Figure 3.31, this is true for $\epsilon < 0.6$). Furthermore, the model combination is only valid for porosity values greater than 0.34. The model predictions also increase before decreasing as the porosity increases (where the turning point occurs at approximately $\epsilon = 0.85$). This phenomenon can potentially be a good portrayal of the observations reported by Kumar et al. [71] (who noted that the strut shape changes with an increase in porosity, which results in accumulation at the nodes, as previously mentioned in Section 3.1.1).

In conclusion, although the NARUC model combination with the MCL model provides

predictions that correspond with the predictions of the "fat" dodecahedron model for the most part, it is not a viable model combination for all porosity values.

The combination of the modified tetrakaidecahedron model, as provided by Fourie et al. [4], and the NARUC model adjusted using cubic nodes will lastly be discussed.

Modified tetrakaidecahedron model combination

For this model combination the expression for the porosity given by Fourie et al. [4], i.e. equation (3.29) is used. The strut edge width in this equation, denoted by t, represents the edge width of a triangular strut, whereas the strut of the NARUC model is square. For this reason the strut edge width for the tetrakaidecahedron model in terms of the strut dimension of the RUC model a, such that $d_s = 2a$, is first determined. In order to determine this expression, the cross-sectional areas of the struts are set equal, thus

$$\frac{\sqrt{3}}{4}t^2 = 4a^2\,, \tag{3.96}$$

and therefore

$$t = \frac{4}{\sqrt{\sqrt{3}}}a\,. \tag{3.97}$$

The cell diameter of the tetrakaidecahedron model, d_c, is furthermore expressed in terms of the RUC dimension d, i.e. the face diameter. The cell diameter for the RUC model is defined as the diagonal of the RUC and is thus equal to $\sqrt{3}\,d$. The cell diameter of the tetrakaidecahedron model can therefore be expressed as

$$d_c = \sqrt{3}\,d\,. \tag{3.98}$$

Substituting equations (3.97) and (3.98) into equation (3.29), therefore leads to the following expression for the solid volume fraction:

$$\begin{aligned} 1-\epsilon &= 3.87\left(\frac{4}{\sqrt{\sqrt{3}}}\right)^2\frac{1}{(\sqrt{3})^2}\left(\frac{a}{d}\right)^2 + 18.5\left(\frac{4}{\sqrt{\sqrt{3}}}\right)^3\frac{1}{(\sqrt{3})^3}\left(\frac{a}{d}\right)^3 \\ &= 11.92\,r_1^2 + 99.96\,r_1^3\,, \end{aligned} \tag{3.99}$$

from which values for r_1 can consequently be obtained. The predictions for r_1 are shown in Figure 3.32.

In Figure 3.32 it can be seen that the predictions for r_1 once more decreases as porosity increases and that for all the porosity values r_1 is below 0.5. The tetrakaidecahedron model combination is therefore also a viable approach for determining r_1.

The r_2-ratio can then be obtained by substituting the values obtained for r_1 into the solid volume fraction equation of the NARUC model with cubic nodes (given by equation (3.79)) with $k = 3$. The positive real roots are chosen in each case. The resulting predictions for r_2 are shown in Figure 3.33.

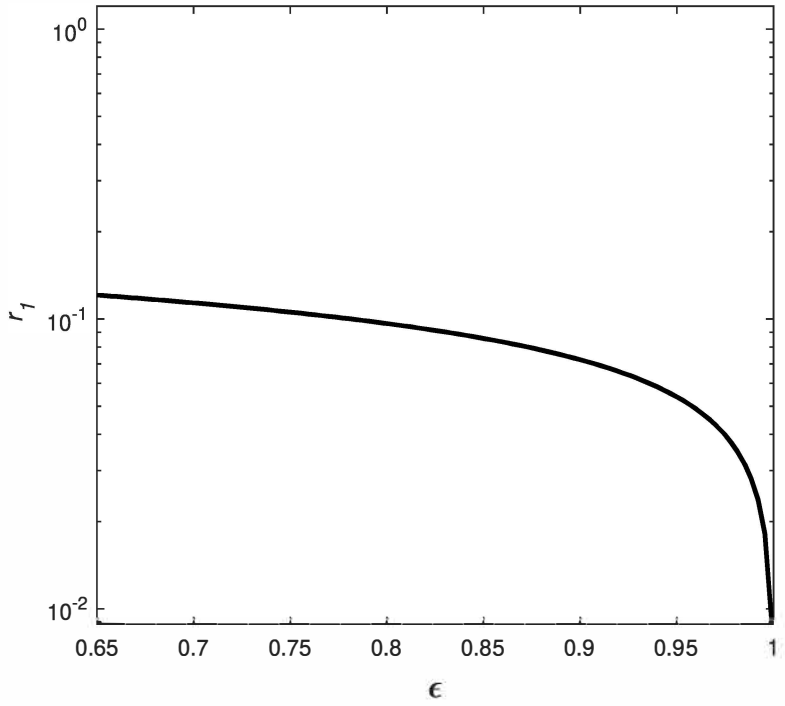

FIGURE 3.32: *Ratio of strut radius to face diameter versus porosity of NARUC model with cubic nodes combined with modified tetrakaidecahedron model obtained from Fourie et al. [4]*

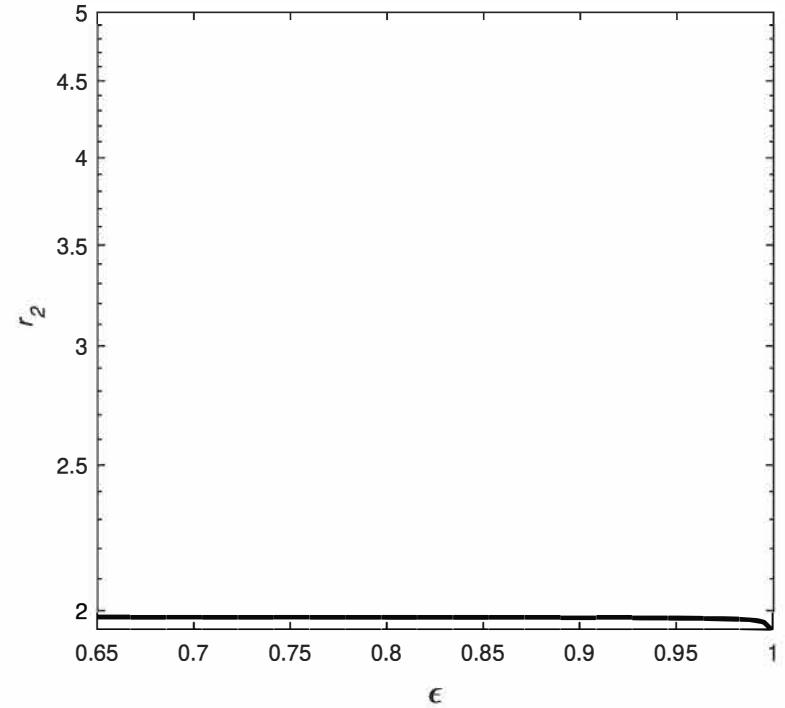

FIGURE 3.33: *Ratio of cubic node lump edge width to strut radius versus porosity of NARUC model with cubic nodes combined with modified tetrakaidecahedron model obtained from Fourie et al. [4]*

It shows that there is a slight decrease in r_2 predictions with an increase in porosity, which is a different trend observed than for the other model combination predictions. Another difference that can be noted is that the predictions for r_2 in this model combination are lower than those in the other model combinations where $\epsilon > 0.7$. All the ratio values are, however, greater than 1. This approach therefore also seems to be viable for determining r_2.

In Figures 3.34, 3.35 and 3.36 the predictions for the dimensionless Darcy and Forchheimer permeability and dimensionless specific surface area are, respectively, shown.

In Figures 3.34, 3.35 and 3.36 the results are as expected and similar to the results obtained with the combination of the "fat" dodecahedron model. The predictions for the dimensionless specific surface area of the NARUC model combined with the modified tetrakaidecahedron model in Figure 3.36 are, however, generally higher than the predictions of the "fat" dodecahedron model, which is the preferred result since the distinction between the model with and without nodes is therefore more prominent. The predictions of the NARUC model combination with the modified tetrakaidecahedron for the dimensionless specific surface area furthermore corresponds with the three-strut RUC model at very high porosity values, as expected. The predictions for the Forchheimer permeability of the NARUC model combined with the modified tetrakaidecahedron model provide such close estimation to the predictions of the three-strut RUC model that it was therefore once again chosen to use a semilog plot so that the decrease in the prediction of the Forchheimer permeability can be observed. The combination of the NARUC and modified tetrakaidecahedron models is also considered a viable method to adjust the RUC model in order to accommodate the presence of solid accumulation at the nodes of a foam.

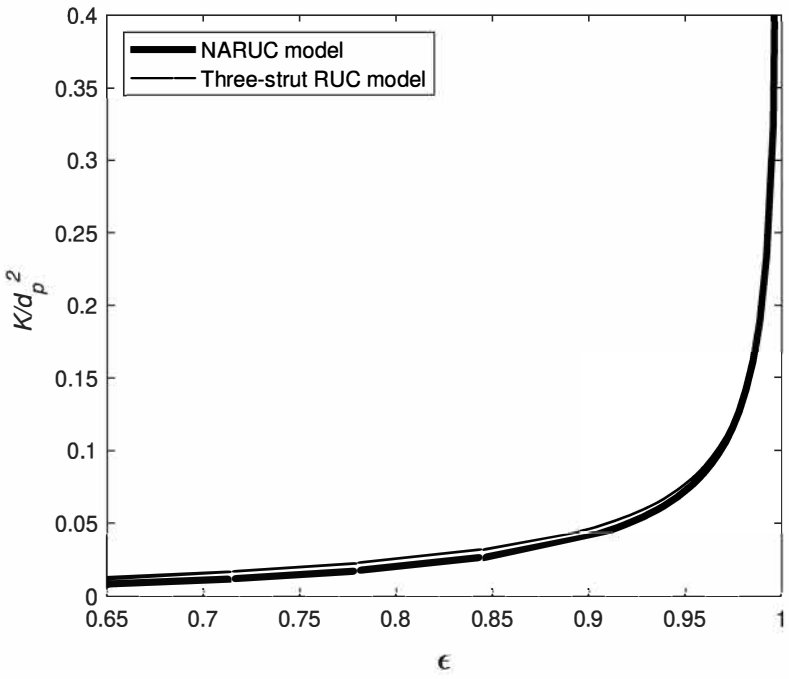

FIGURE 3.34: *Dimensionless Darcy permeability prediction versus porosity obtained from NARUC model adjusted using cubic nodes and combined with modified tetrakaidecahedron model and three-strut RUC model*

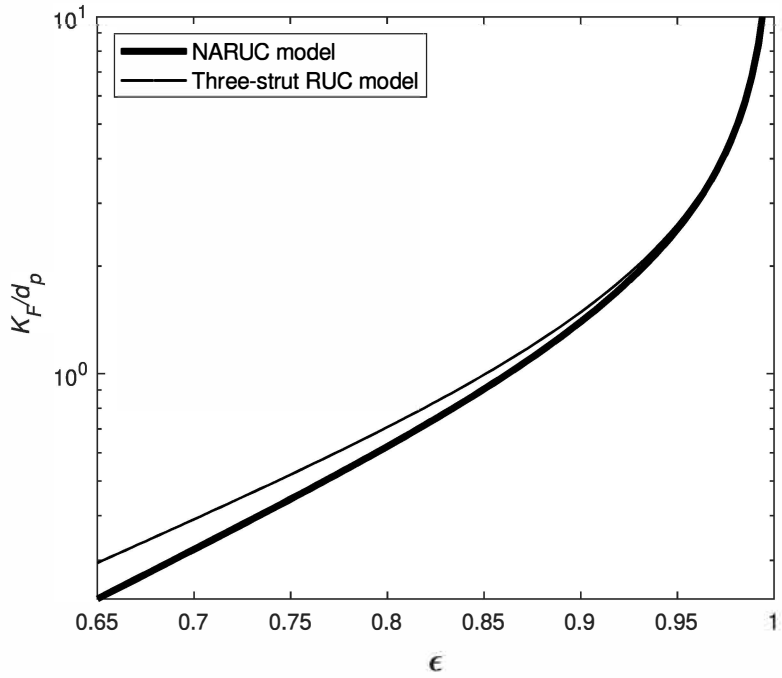

FIGURE 3.35: *Dimensionless Forchheimer permeability prediction versus porosity obtained from NARUC model adjusted using cubic nodes and combined with modified tetrakaidecahedron model and three-strut RUC model*

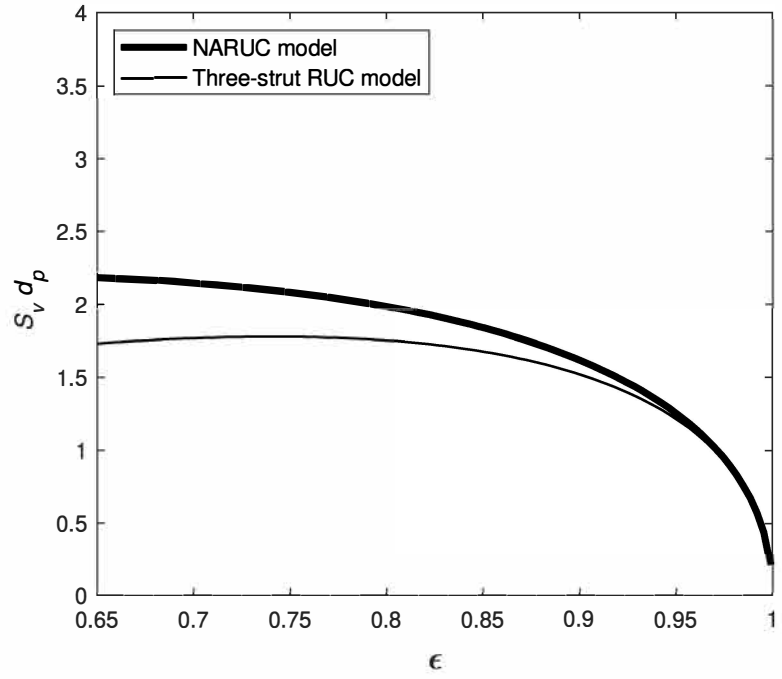

FIGURE 3.36: *Dimensionless specific surface area prediction versus porosity obtained from NARUC model adjusted using cubic nodes and combined with modified tetrakaidecahedron model and three-strut RUC model*

In the next section the NARUC model with nodes that resemble curved wedges, shown in Figure 3.21(b), is discussed.

3.2.2 NARUC model with curved wedge nodes

The NARUC model with curved wedges at the nodes is the model where the geometry is chosen in such a manner that no model combination is needed to obtain the r_1- and r_2-ratio values for the calculation of the permeability coefficients and specific surface area. The extra node volumes added resemble sections that remain at the corners if a circular prism were cut out of a square prism (in this case with the circular diameter equal to d_p), as shown in Figure 3.21(b). The node volumes are only added to the two sections where the struts meet perpendicularly in the RUC in Figure 3.21(b), but the number of nodes, denoted by k, is incorporated in order to represent the degree of solid accumulation. In this case, k representing the numbers 3, 6, 9 and 12 are considered and evaluated in this section.

In order to calculate the permeability and specific surface area of the NARUC model with adjusted pore-scale parameters, equations (3.75) and (3.76) can once again be utilized. The expression for R for the NARUC model with curved wedge nodes is furthermore determined in a similar manner to that of the NARUC model with cubic nodes by first finding the expressions for the porosity of both the left and right-hand sides of the models shown in Figure 3.21(b). The equation for the porosity of the model on the left-hand side of Figure 3.21(b) is determined first by finding the expression for the solid volume of this model. The volume of a single node that resembles a curved wedge with the given parameters is determined as follows:

$$U_{s_{\text{node}}} = \frac{1}{4} \times \left(d_p^2 - \frac{\pi}{4} d_p^2\right) \times d_s = \frac{1}{4}\left(1 - \frac{\pi}{4}\right) d_s d_p^2 \,. \tag{3.100}$$

The total solid volume of the NARUC model with k curved wedge nodes is then equal to the solid volume of the three-strut RUC model plus k of the volumes given by equation (3.100), i.e.

$$\begin{aligned} U_s &= 3d_s^2(d - d_s) + d_s^3 + k\left[\frac{1}{4}\left(1 - \frac{\pi}{4}\right)(d - d_s)^2 d_s\right] \\ &= \left[\frac{3}{2r_1} - 2\right](2a)^3 + \frac{k}{4}\left(1 - \frac{\pi}{4}\right)\left[\frac{1}{4r_1^2} - \frac{1}{r_1} + 1\right](2a)^3 \,. \end{aligned} \tag{3.101}$$

The solid volume fraction is therefore given by

$$1 - \epsilon = \frac{U_s}{U_o} = 12r_1^2 - 16r_1^3 + k\left(1 - \frac{\pi}{4}\right)\left[2r_1^3 - 2r_1^2 + \frac{r_1}{2}\right] \,. \tag{3.102}$$

The model structure on the right-hand side of both Figures 3.21(a) and (b) are the same. The total solid volume and consequently the porosity of the NARUC models with adjusted parameters (i.e. using cubic nodes and curve wedge nodes) are given by the same expression, i.e. equations (3.80) and (3.81). Therefore, setting equation (3.102) equal to equation (3.81) leads to the following third-degree polynomial of R:

$$\left[16r_1^3\right] R^3 + \left[-12r_1^2\right] R^2 + \left[12r_1^2 - 16r_1^3 + k\left(1 - \frac{\pi}{4}\right)\left(2r_1^3 - 2r_1^2 + \frac{r_1}{2}\right)\right] = 0 \,, \tag{3.103}$$

which, can in turn, be determined by making use of the Cardanic method (Appendix A) and results in

$$R = \frac{1}{2\sqrt{r_1}} \cos\left[\frac{1}{3}\cos^{-1}\left[1 + 8r_1^2\left(4r_1 - 3\right) - k\left(1 - \frac{\pi}{4}\right)\left(4r_1^3 - 4r_1^2 + r_1\right)\right] + \frac{4}{3}\pi\right] + \frac{1}{4r_1}\,. \tag{3.104}$$

The Darcy permeability, Forchheimer permeability and specific surface area of the NARUC model with adjusted parameters, using the curved wedge nodes, can be determined using equations (3.87), (3.88) and (3.89), respectively, due to the same geometry of the NARUC models with adjusted parameters shown on the right-hand side of Figures 3.21(a) and (b). The difference between the NARUC models with adjusted parameters is introduced through the calculation of the R and r_1-value. The value of R in the case of the model with curved wedges is determined by using equation (3.104).

The only value that is still needed to determine the permeability and specific surface area at a specified porosity, pore diameter and node number, is the value of r_1. Due to the circular geometry used to determine the extra node volume, the r_2-ratio is not needed to determine the permeability coefficients and specific surface area of the NARUC model with curved wedge nodes. The r_1-ratio can furthermore be determined from the porosity by using equation (3.102) after expressing the result as a polynomial of r_1 and then solving for r_1, i.e. solving for r_1 from the following polynomial:

$$\left[16 - 2k\left(1 - \frac{\pi}{4}\right)\right] r_1^3 + \left[-12 + 2k\left(1 - \frac{\pi}{4}\right)\right] r_1^2 + \left[-\frac{k}{2}\left(1 - \frac{\pi}{4}\right)\right] r_1 + (1 - \epsilon) = 0\,. \tag{3.105}$$

The root chosen for each porosity value is the smallest positive number because r_1 is expected to be small. Figure 3.37 shows the dependence of r_1 on porosity. (The colour gradient in Figure 3.37 was chosen to represent the gradual change in prediction with number of nodes.)

From Figure 3.37 it can be seen that the r_1-ratio values behave as expected in that as the porosity increases, the ratio values decrease. One would expect the strut diameter of higher porosity foams to be smaller and therefore this behaviour makes physical sense. Also, the ratio value is below 0.5 for the porosity range which is necessary for it to be considered as valid, since the strut diameter will be less than the face diameter for any actual foam. The r_1-values of the NARUC model with curved wedge nodes decrease at the same porosity value as the number of nodes increase. This makes sense since more nodes being added to the model occupies more of the solid volume, which would intuitively lead to smaller strut diameter values for the same porosity and face diameter value.

The resulting predictions for the dimensionless permeabilities and dimensionless specific surface area of the NARUC model obtained by making use of curved wedge nodes are shown in Figures 3.38 to 3.40.

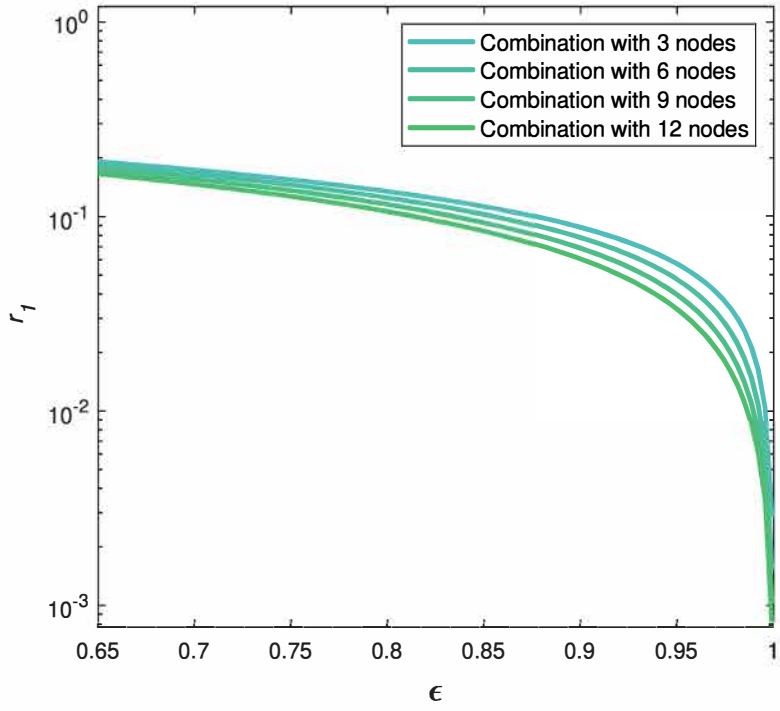

FIGURE 3.37: *Ratio of strut radius to face diameter versus porosity of NARUC model adjusted using curved wedge nodes*

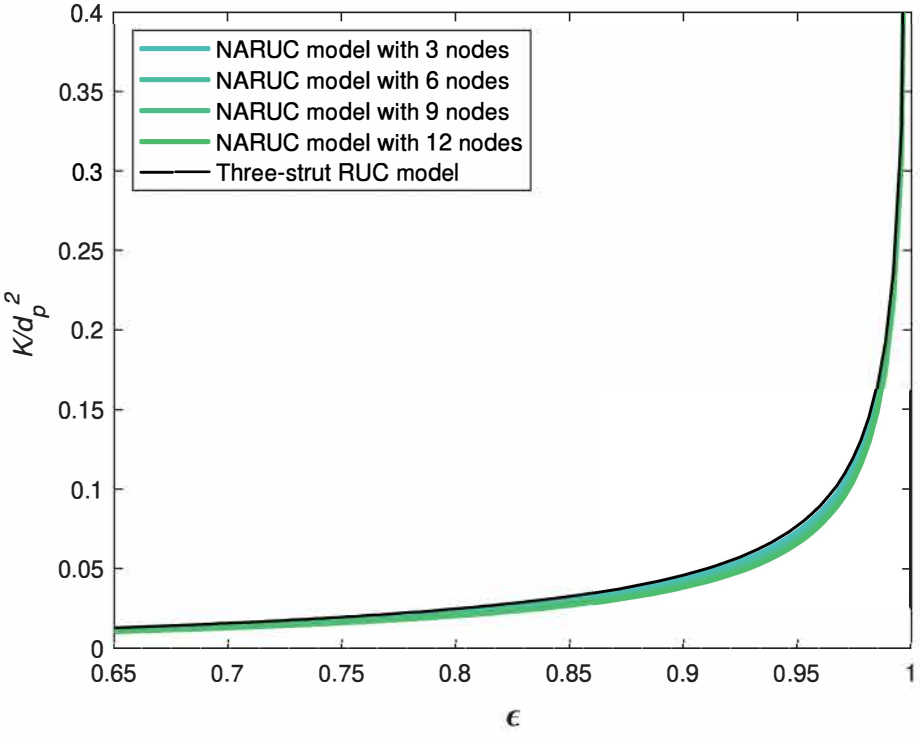

FIGURE 3.38: *Dimensionless Darcy permeability prediction versus porosity obtained from NARUC model adjusted using curved wedge nodes and three-strut RUC model*

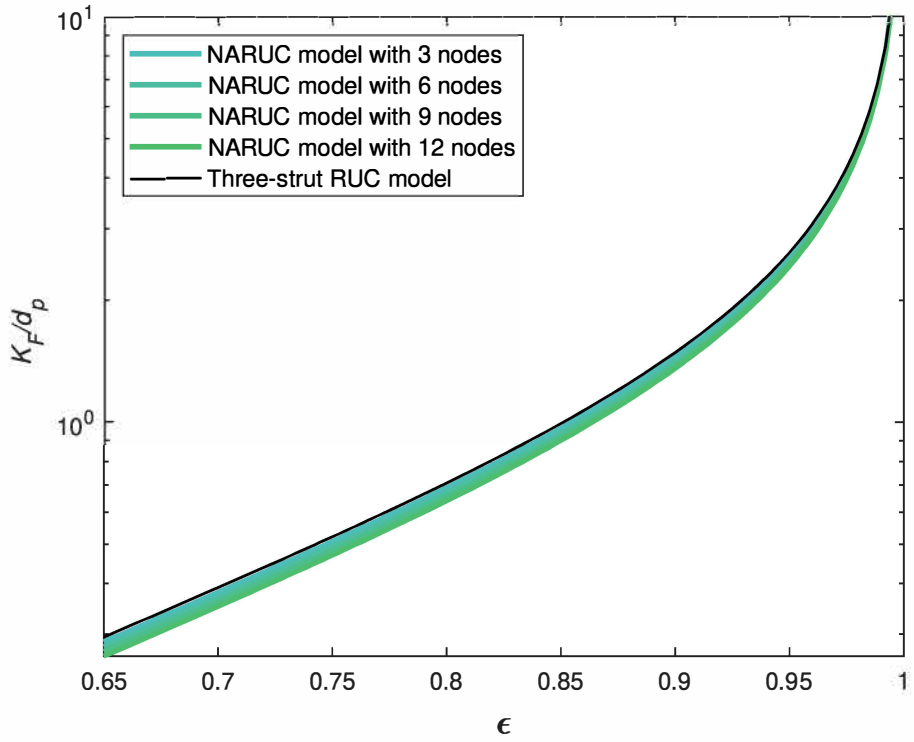

FIGURE 3.39: *Dimensionless Forchheimer permeability prediction versus porosity obtained from NARUC model adjusted using curved wedge nodes and three-strut RUC model*

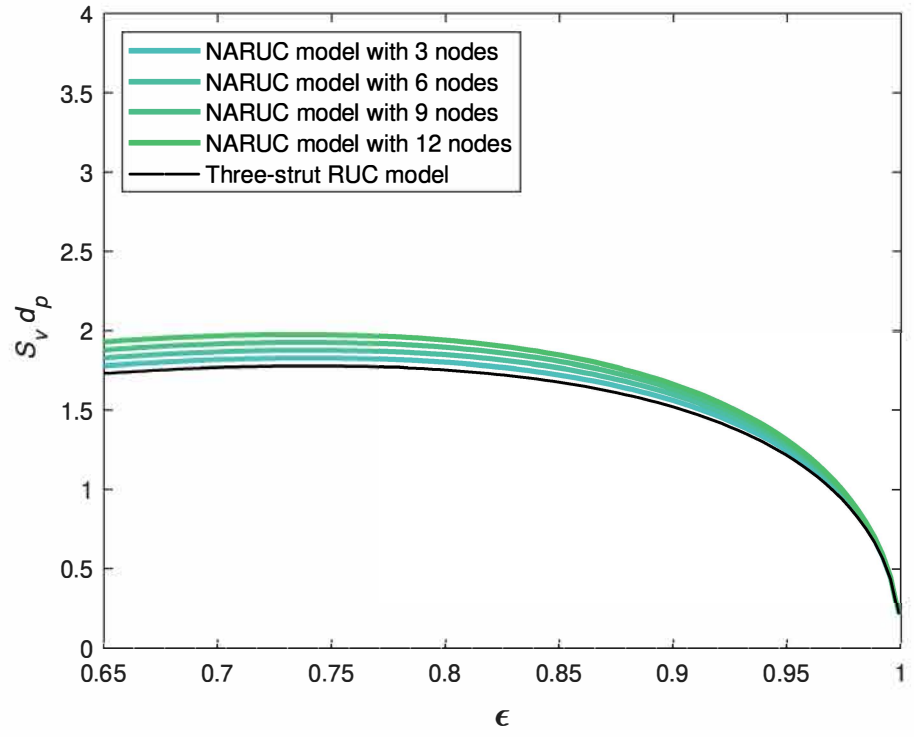

FIGURE 3.40: *Dimensionless specific surface area prediction versus porosity obtained from NARUC model adjusted using curved wedge nodes and three-strut RUC model*

In both Figures 3.38 and 3.39 the permeability predictions for different node numbers of the NARUC model are relatively close to one another. However, in both cases the permeability decreases with an increase in number of nodes at the same porosity value. The predictions for the dimensionless Darcy permeability of the NARUC model are furthermore lower than that of the three-strut RUC model and the predictions for the dimensionless Forchheimer permeability are also lower, as expected.

The predictions for the dimensionless specific surface area of the NARUC and three-strut RUC models are shown in Figure 3.40. The predictions of the NARUC model are higher than those of the three-strut RUC model, as expected, and furthermore increases with increasing node numbers at the same porosity. The results of the NARUC model with curved wedge nodes therefore proves to be satisfactory.

In the following section, the permeability and specific surface area equations of the different NARUC models and model combinations are compared to one another, the literature models with node adjustments given in Section 3.1 and the experimental data provided in Section 1.3.3.

3.2.3 Comparison of NARUC models

The NARUC models (along with all the model combinations in the case of the NARUC model with cubic nodes) will be evaluated in this section using relative percentage error tables and figures containing the model predictions. This section is also divided into sections where each of the foam characteristics of interest in this study is analysed, i.e. both the permeability coefficients and the specific surface area in terms of the pore diameter. The NARUC model options and combinations are evaluated by comparing the resulting predictions to the predictions provided by the node adjusted models from the literature discussed in Section 3.1 and the relevant experimental data provided in Section 1.3.3. In this section the number of nodes is restricted to the maximum number of nodes that makes sense within the context of the nodes being added to the geometrical three-strut RUC model, i.e. $k = 3$ in the case of the NARUC model with cubic nodes and $k = 12$ in the case of the NARUC model with curved wedge nodes. The node number chosen for the NARUC model with cubic nodes is 3 due to the model with cubic nodes being restricted to the number of places where two struts would intersect in the RUC, as explained previously. The use of 3, 6, 9 or 12 nodes for the NARUC model with curved wedge nodes are the recommended number of nodes. In Section 3.2.2 all the aforementioned node numbers were taken into consideration in order to evaluate the effect of the change in the number of nodes on the NARUC model obtained using curved wedge nodes. In the case of this NARUC model, 4 nodes can be assigned to every direction of flow and still be geometrically plausible. Therefore, 12 nodes are viable to use in this case.

Darcy Permeability

The Darcy permeability equation of the NARUC models, given by equation (3.87), combined with the "fat" dodecahedron, MCL and modified tetrakaidecahedron models (where applicable) and as described in Section 3.2.1, are evaluated in this section. The relative percentage errors between the NARUC models and data are given in Table 3.4 and the different models are compared in Figure 3.41. Once again a semilog plot is used so

TABLE 3.4: *Relative percentage error of NARUC models compared to experimental data for K/d_p^2 of Chapter 1*

NARUC model combination:	**NARUC models (Section 3.2)**				
	Cubic nodes ($k = 3$)				Curved wedge nodes ($k = 12$)
	Dodec. with tri. struts	Dodec. with cyl. struts	MCL	Tetra.	
Experimental data (Section 1.3.3)					
Bhattacharya et al. [3]	342 %	-	363 %	368 %	331 %
Garrido et al. [19]	-	162 %	137 %	139 %	144 %
Dietrich et al. [20]	-	54 %	57 %	57 %	56 %
Mancin et al. [21]	132 %	-	139 %	141 %	125 %
Mancin et al. [22]	342 %	-	356 %	360 %	328 %

that clear distinction between the model predictions can be made. The experimental data used to evaluate the NARUC models are the same as the data used to analyse the node adjusted models obtained from the literature in Section 3.1.8, i.e. the data obtained from Bhattacharya et al. [3], Garrido et al. [19], Dietrich et al. [20], Mancin et al. [21] and Mancin et al. [22]. In Figure 3.41 the model predictions of the "fat" MCL model obtained from Ahmed et al. [7] and the three-strut RUC model are also shown for comparison. (The figures provided in this section, e.g. Figure 3.41, are displayed with the table legend

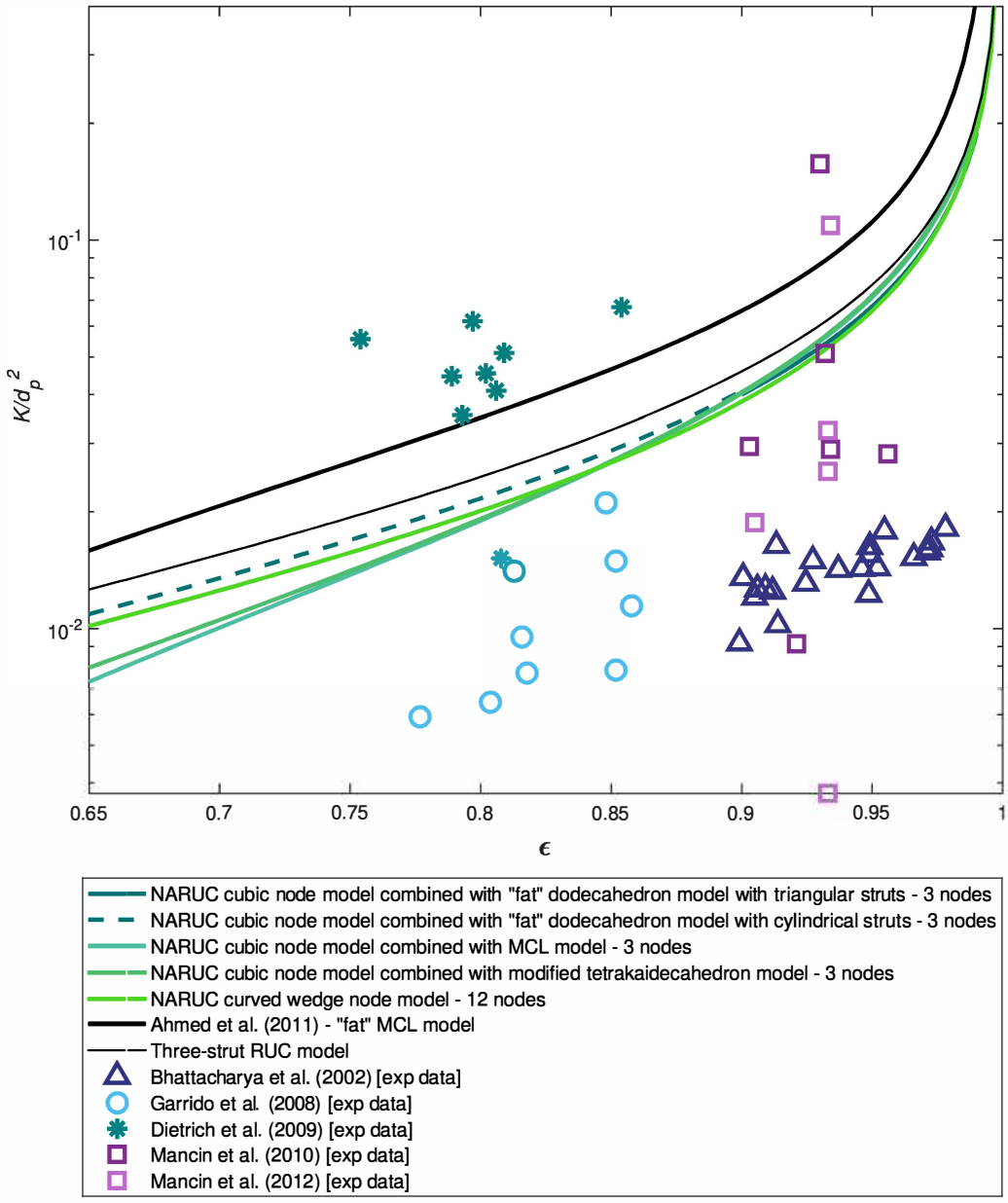

FIGURE 3.41: *Dimensionless Darcy permeability prediction versus porosity obtained from NARUC models compared to node adjusted models and experimental data from the literature*

situated under the figure due to the length of the legend entries. The arrangement of the figures and legends in this manner is to ensure that the text within the legend is legible.)

When the relative percentage errors between the Darcy permeability predictions of the different models and the experimental data in Tables 2.2, 2.5, 3.1 and 3.4 are compared, the following observations can be made:

- With the exception of the data acquired from Dietrich et al. [20], all the experimental data sets compared the best to the NARUC model predictions (i.e. the NARUC model predictions gave the closest average approximations to the data sets when compared to the models obtained from the literature, with and without node adjustments, and the RUC models considered in this study).
- There is up to a 70% improvement in comparison to the data acquired from Mancin et al. [22] (the data representing foams with a moderate degree of node accumulation).
- The average percentage errors of the NARUC models are relatively close to one another.

The predictions shown in Figure 3.41 furthermore confirms the general improvement that the models with lower dimensionless Darcy permeability predictions have when compared to the experimental data of foams with accumulation of solid at the node intersections. The NARUC model with curved wedges give the lowest predictions at the high porosity values which lead to the better approximations when compared to the data acquired from Mancin et al. [22] and Bhattacharya et al. [3]. The NARUC model with cubic nodes combined with the "fat" dodecahedron model generally gives the most accurate predictions when compared to the relevant experimental data from all the model combinations considered. This is also due to the lower predictions of this model at high porosity values when compared to the NARUC model combined with the MCL and tetrakaidecahedron models (although this distinction is not as clearly seen in Figure 3.41 due to the similar predictions of the NARUC models at high porosities). The NARUC models furthermore gave closer average approximations to the experimental data than the "fat" MCL model. This is as expected since the NARUC models give lower predictions for the Darcy permeability than the three-strut RUC model and it was already noted that the three-strut RUC model compared more accurately than the "fat" MCL model in Section 3.1.8. More experimental data at lower porosity values with moderate and high degrees of solid accumulation will complement this study to confirm the expected trend at lower porosities.

Forchheimer Permeability

The NARUC models are combined and evaluated similarly for the Forchheimer permeability predictions than for the Darcy permeability coefficient. Equation (3.88) is furthermore used to predict the Forchheimer permeability for the NARUC models. The NARUC model predictions are compared to the Forchheimer permeability predictions provided by the Ahmed et al. [7] model, calculated using equation (3.69), and experimental data from the literature summarized in Section 1.3.3. The resulting relative percentage errors between the NARUC models and the relevant experimental data are listed in Table 3.5. Figure 3.42 shows the predictions of the NARUC model, "fat" MCL model of Ahmed et

TABLE 3.5: *Relative percentage error of NARUC models compared to experimental data for K_F/d_p of Chapter 1*

NARUC model combination:	**NARUC models (Section 3.2)**				
	Cubic nodes ($k = 3$)				Curved wedge nodes ($k = 12$)
	Dodec.		MCL	Tetra.	
	with tri. struts	with cyl. struts			
Experimental data (Section 1.3.3)					
Bhattacharya et al. [3]	76 %	-	80 %	81 %	74 %
Garrido et al. [19]	-	57 %	59 %	59 %	59 %
Dietrich et al. [20]	-	29 %	33 %	33 %	31 %
Mancin et al. [21]	48 %	-	49 %	49 %	48 %
Mancin et al. [22]	44 %	-	44 %	45 %	44 %

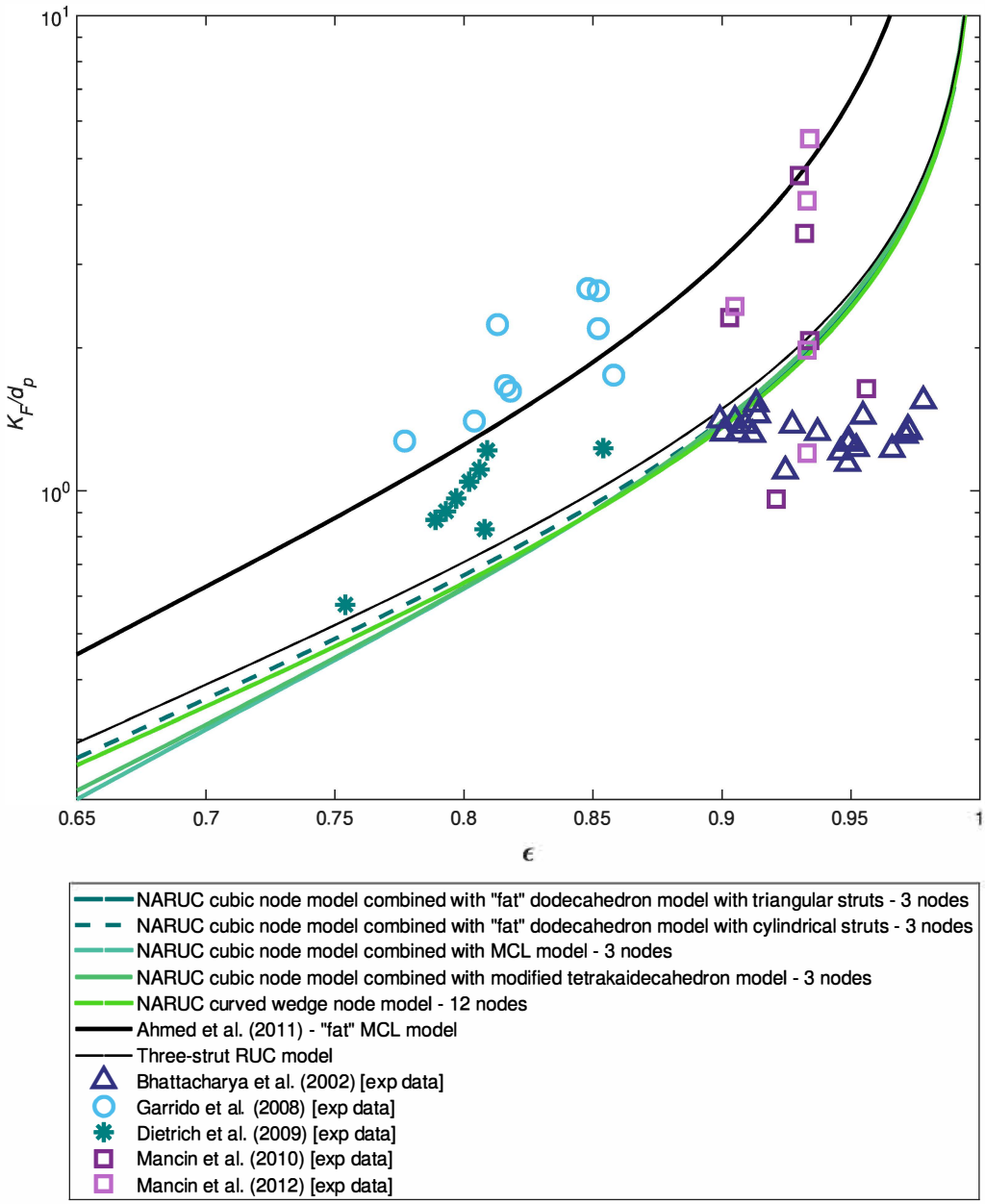

FIGURE 3.42: *Dimensionless Forchheimer permeability prediction versus porosity obtained from NARUC models compared to node adjusted models and experimental data from the literature*

al. [7] and the three-strut RUC model, as well as the relevant experimental data provided by the same literature sources as in the case of the Darcy permeability comparisons.

Comparison of the average relative percentage errors between the Forchheimer permeability predictions and experimental data in Table 3.5 with those in Tables 2.2, 2.5 and 3.2 reveal that the Dietrich et al. [20] model generally still provides the lowest average percentage error compared to the experimental data. The NARUC models provide lower

percentage error averages than the three-strut RUC model for some of the data sets (i.e. Bhattacharya et al. [3], Mancin et al. [21] and Mancin et al. [22]), whilst the data sets where the Forchheimer permeability predictions are higher (i.e. the Garrido et al. [19] and Dietrich et al. [20] data sets) are more closely approximated by the "fat" MCL model of Ahmed et al. [7]. The NARUC model predictions are furthermore relatively close to one another, as seen in Figure 3.42. Consequently, the NARUC model that performs the best is difficult to identify in this case. It is noted, however, that the NARUC model with curved wedge nodes and the NARUC model with cubic nodes combined with the "fat" dodecahedron model performed slightly better than the other NARUC models when compared to the experimental data considered in this section.

Specific surface area: geometric approach

In this section the specific surface area predictions obtained using a geometric approach of the NARUC models and combinations are evaluated against the dimensionless specific surface area predictions of the node adjusted models discussed in Section 3.1 as well as the relevant experimental data provided in this study for the specific surface area of foamlike media.

The node adjusted literature models include the Calmidi and Mahajan [1], Boomsma and Poulikakos [2], Fourie and Du Plessis [4], Huu et al. [5] "fat" dodecahedron and Edouard [6] models whose specific surface area equations are, respectively, given by equations (3.8), (3.21), (3.32), (3.38), (3.39) and (3.51). The model obtained from the work of Bhattacharya et al. [3] is excluded from the evaluation in this section due to the results of this model being counter-intuitive, as explained in Section 3.1.8. The first two literature models mentioned furthermore use either the pore dimension relations obtained from Buciuman and Kraushaar-Czarnetzki [44] or Richardson et al. [45] to yield specific surface area predictions in terms of the pore diameter. The experimental data sets relevant to this chapter, and hence used for evaluation purposes, are acquired from Garrido et al. [19], Dietrich et al. [20], Mancin et al. [22] and Kumar et al. [71]. The specific surface area predicted by the NARUC models in terms of the pore diameter is given by equation (3.89). The manner in which r_1 and R is calculated for the model combinations with the NARUC model with cubic nodes is explained in Section 3.2.1, and for the NARUC model with curved wedge nodes is explained in Section 3.2.2. The relative percentage errors between the predictions of the NARUC models and the experimental data are presented in Table 3.6 and the predictions of the dimensionless specific surface area of the node adjusted models from the literature, the three-strut RUC model, the aforementioned data sets and the NARUC models are shown in Figure 3.43.

It is noted that the experimental data obtained from Garrido et al. [19] and Dietrich et al. [20] are lower than expected, as mentioned in Section 3.1.8. Consequently, the models that approximate these data sets more accurately are the "slim" models. This observation is verified when comparing the average percentage error results of Tables 2.3, 2.6, 3.3 and Table 3.6 along with the predictions shown in Figures 2.24, 3.18, 3.19, 3.20 and 3.43. The comparison furthermore reveals that the "slim" MCL model gives the closest average approximation to these data sets and that the node adjusted model obtained from Fourie and Du Plessis [4] gives the closest approximation compared to all the node adjusted models. It is expected, however, that the specific surface area increases with the presence of solid accumulation at the nodes of the foam and therefore the experimental data sets

TABLE 3.6: *Relative percentage error of NARUC models compared to experimental data for $S_v d_p$ of Chapter 1*

NARUC model combination:	**NARUC models (Section 3.2)**				
	Cubic nodes ($k = 3$)				Curved wedge nodes ($k = 12$)
	Dodec.		MCL	Tetra.	
	with tri. struts	with cyl. struts			
Experimental data (Section 1.3.3)					
Garrido et al. [19]	-	40 %	51 %	46 %	45 %
Dietrich et al. [20]	-	28 %	36 %	35 %	32 %
Mancin et al. [22]	18 %	-	21 %	18 %	17 %
Kumar et al. [71]	28 %	-	22 %	26 %	26 %

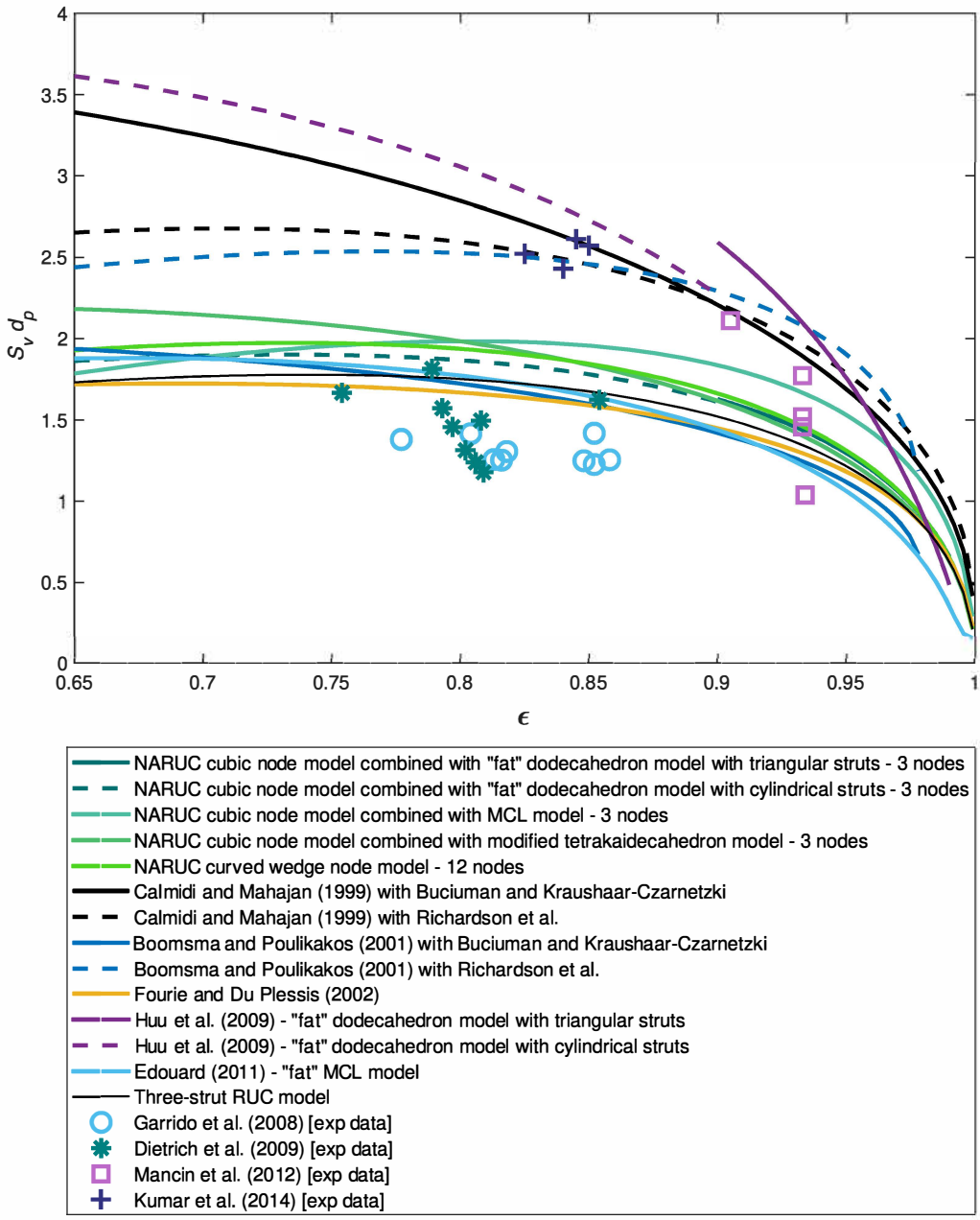

FIGURE 3.43: *Dimensionless specific surface area prediction versus porosity obtained from NARUC models compared to node adjusted models and experimental data from the literature*

obtained from Mancin et al. [22] and Kumar et al. [71] are more appropriate. Comparing the tables listed above reveals that all the NARUC models represent the experimental data acquired from Mancin et al. [22] more accurately than any of the other models, except for the NARUC model with cubic nodes combined with the MCL model.

The NARUC model with curved wedges furthermore provides the closest correspondence to this data set. The data set of Kumar et al. [71] corresponds the best to the node

adjusted models obtained from Calmidi and Mahajan [1] and Boomsma and Poulikakos [2] (using the expression of Richardson et al. [45]). The NARUC model predictions, however, corresponds closer to the data of Kumar et al. [71] than the three-strut RUC model, which reveals an improvement. The NARUC model that compares closest to the latter data set is the NARUC model with cubic nodes combined with the MCL model. The combination of the NARUC model with the "fat" dodecahedron model and the NARUC model with curved wedges also provide satisfactory results, which is worth mentioning since the combination with the MCL model proved to have some flaws, as discussed in Section 3.2.1.

In the following section all the equations provided by the node adjusted models from the literature and the NARUC models presented in this chapter are summarized in Tables 3.7 and 3.8. A summary of the results obtained is also provided.

3.3 Chapter summary

Models from the literature incorporating the solid accumulation that occur at strut intersections obtained, as well as different versions of the node adjusted RUC model were discussed and presented in this chapter. Expressions for the prediction of the permeability, both for the Darcy and Forchheimer regimes, and the specific surface area in terms of the pore diameter were determined. Node adjusted RUC (NARUC) model options were presented with nodes that either represent cubes or curved wedges. The NARUC models with cubic nodes were furthermore combined with the "fat" dodecahedron model, MCL model or modified tetrakaidecahedron model in order to obtain the ratios that determine the node size. All the NARUC models presented, except for the combination with the MCL model, provided satisfying results. Where the NARUC model with cubic nodes is considered, the combination with the dodecahedron model is preferred due to its overall performance. The NARUC model with curved wedges, however, is generally preferred due to the ability to adapt to different degrees of solid accumulation, as well as its satisfying performance. Comparison of the node adjusted literature models with their model counterparts that do not take solid accumulation at the strut intersections of foams into account, revealed that the expected effect on the specific surface area is that it increases with the addition of nodal lumps. Comparison of the Darcy and Forchheimer permeability coefficients, as well as comments from the literature, suggested that the permeability coefficients should decrease with the presence of solid accumulation. The NARUC models proposed in this study fulfils these expectations when compared to the three-strut RUC model and furthermore performs better, for the most part, than any of the other models when compared to relevant experimental data. The NARUC models were furthermore created in such a way as to keep the benefits of the rectangular geometry of the RUC model which maintains its simplicity as well as its satisfactory performance. Further experimental study involving the effect of solid accumulation at the nodes of foams on the permeability will be useful in order to establish the actual trend.

For easy reference in this chapter, the coefficients related to the dodecahedron model are given in Table 3.7 (i.e. the coefficients in Table 3.7 are utilized in Table 3.8 in order to shorten the equations listed). The permeability and specific surface area equations discussed and derived in this chapter, along with the relevant ratio expressions are summarized in Table 3.8. The equation numbers provided in Table 3.8 either references the

TABLE 3.7: *Coefficients related to the dodecahedron model*

Eqn. of	Eqn. no.	Eqn.
r_{tf}	(3.33)	$\left[-\frac{\sqrt{10}}{3\phi^4}+\frac{Z}{6}-\frac{\sqrt{6}W}{36}\right]r_{tf}^3+\left[\frac{\sqrt{15}}{\phi^4}-\sqrt{\frac{2}{3}}Z+\frac{W}{2}\right]r_{tf}^2+\left[Z-\frac{\sqrt{6}W}{2}\right]r_{tf}+[W-(1-\epsilon)]=0$
r_{cf}	(3.37)	$\left[\frac{\sqrt{10}}{6\phi^4}-\frac{\sqrt{30}\pi}{6\phi^4}+\frac{Z}{6}-\frac{\sqrt{6}W}{36}\right]r_{cf}^3+\left[\frac{\sqrt{5}\pi}{\phi^4}-\sqrt{\frac{2}{3}}Z+\frac{W}{2}\right]r_{cf}^2+\left[Z-\frac{\sqrt{6}W}{2}\right]r_{cf}+[W-(1-\epsilon)]=0$
ϕ	(3.34)	$\frac{1+\sqrt{5}}{2}$
W	(3.35)	$\frac{5\sin^2\left(\frac{\pi}{5}\right)}{4\sqrt{15}\,(3-\phi)\phi^2}\sqrt{\frac{1}{4}-\frac{\sin^2\left(\frac{\pi}{5}\right)\phi^2}{9-3\phi}}$
Z	(3.36)	$\frac{3}{\sqrt{5}\,\phi^3}\left[\frac{5}{\sqrt{3-\phi}}-\frac{\pi\phi}{3-\phi}\right]$
C_t	(3.90)	$\frac{\sqrt{15}}{\phi^4}r_{tf}^2-\frac{\sqrt{10}}{3\phi^4}r_{tf}^3$
C_c	(3.94)	$\left(\frac{\sqrt{10}}{6\phi^4}-\frac{\sqrt{5}\pi}{2\phi^4}\sqrt{\frac{2}{3}}\right)r_{cf}^3+\frac{\sqrt{5}\pi}{\phi^4}r_{cf}^2$
$C_{\text{node}}\left(r_{tf}\right)$	(3.92)	$\left[\frac{Z}{6}-\frac{\sqrt{6}W}{36}\right]r_{tf}^3+\left[-\sqrt{\frac{2}{3}}Z+\frac{W}{2}\right]r_{tf}^2+\left[Z-\frac{\sqrt{6}W}{2}\right]r_{tf}+W$
$C_{\text{node}}\left(r_{cf}\right)$	-	$\left[\frac{Z}{6}-\frac{\sqrt{6}W}{36}\right]r_{cf}^3+\left[-\sqrt{\frac{2}{3}}Z+\frac{W}{2}\right]r_{cf}^2+\left[Z-\frac{\sqrt{6}W}{2}\right]r_{cf}+W$

TABLE 3.8: *Summary of permeability coefficient and specific surface area equations presented in Chapter 3*

Literature model	Eqn. for	Eqn. no.	Eqn.
Calmidi and Mahajan [1] (Section 3.1.1)	S_v	(3.8) and (3.12)	$\frac{1}{d_p}\frac{1-0.62\sqrt{1-\epsilon}}{0.64}\sqrt[3]{\frac{12\sqrt{3}r_1r_2}{11.31}}\left[\frac{4\sqrt{3}}{3}+\frac{4\sqrt{3}-16}{9}r_2+\frac{4\sqrt{3}}{9r_1}r_2-\frac{8+2\sqrt{3}}{9}r_1r_2\right]$
		(3.8) and (3.13)	$\frac{1}{d_p}\frac{1-0.97\sqrt{1-\epsilon}}{0.5498}\sqrt[3]{\frac{12\sqrt{3}r_1r_2}{11.31}}\left[\frac{4\sqrt{3}}{3}+\frac{4\sqrt{3}-16}{9}r_2+\frac{4\sqrt{3}}{9r_1}r_2-\frac{8+2\sqrt{3}}{9}r_1r_2\right]$
	r_1	-	0.09
	r_2	(3.5)	$\frac{-r_1+\sqrt{r_1^2+\frac{2}{\sqrt{3}}(1-\epsilon)\left[2-r_1\left(1+\frac{4}{\sqrt{3}}\right)\right]}}{\frac{2}{3}\left[2-r_1\left(1+\frac{4}{\sqrt{3}}\right)\right]}$
Boomsma and Poulikakos [2] (Section 3.1.2)	S_v	(3.21) and (3.10) $[L=l_s]$	$\frac{1}{d_p}\frac{1-0.62\sqrt{1-\epsilon}}{0.64}\left[\frac{3\sqrt{2}}{2}\pi r_2-\left(\frac{\sqrt{2}}{2}+2\right)\pi r_1r_2+\frac{15\sqrt{2}}{4}r_1^2+\left(\frac{3\sqrt{2}}{2}-2\right)\pi r_2^2\right]$
		(3.21) and (3.11) $[L=l_s]$	$\frac{1}{d_p}\frac{1-0.971\sqrt{1-\epsilon}}{0.5498}\left[\frac{3\sqrt{2}}{2}\pi r_2-\left(\frac{\sqrt{2}}{2}+2\right)\pi r_1r_2+\frac{15\sqrt{2}}{4}r_1^2+\left(\frac{3\sqrt{2}}{2}-2\right)\pi r_2^2\right]$
	r_1	-	0.339
	r_2	(3.19)	$\sqrt{\frac{\sqrt{2}\left[2-\left(\frac{3}{4}\right)\sqrt{2}r_1^3-2\epsilon\right]}{\pi\left(3-4\sqrt{2}r_1-r_1\right)}}$
Bhattacharya et al. [3] (Section 3.1.3)	S_v	(3.28) and (3.12)	$\frac{1}{d_p}\frac{1-0.62\sqrt{1-\epsilon}}{0.64}\sqrt[3]{\frac{12\sqrt{3}r_1r_2}{11.31}}\frac{2}{3\sqrt{3}r_1^2}\left[6r_1^2+\left(\pi-6\sqrt{1-r_1^2}-3\sin^{-1}(r_1)\right)r_1r_2+\left(\frac{\pi}{2}-\frac{3G}{4}\right)r_2\right]$
		(3.28) and (3.13)	$\frac{1}{d_p}\frac{1-0.97\sqrt{1-\epsilon}}{0.5498}\sqrt[3]{\frac{12\sqrt{3}r_1r_2}{11.31}}\frac{2}{3\sqrt{3}r_1^2}\left[6r_1^2+\left(\pi-6\sqrt{1-r_1^2}-3\sin^{-1}(r_1)\right)r_1r_2+\left(\frac{\pi}{2}-\frac{3G}{4}\right)r_2\right]$
	G	(3.24)	$\sin^{-1}\left(2r_1\sqrt{1-r_1^2}\right)-2r_1\sqrt{1-r_1^2}$
	r_1	-	0.09
	r_2	(3.26)	$\frac{\sqrt{3}+\sqrt{3+\frac{3\sqrt{3}}{r_1}\left[\frac{\pi}{3r_1}-2+2\left(1-\sqrt{1-r_1^2}\right)-\frac{G}{2r_1}\right](1-\epsilon)}}{-\frac{\sqrt{3}}{r_1}\left[\frac{\pi}{3r_1}-2+2\left(1-\sqrt{1-r_1^2}\right)-\frac{G}{2r_1}\right]}$
Fourie and Du Plessis [4] (Section 3.1.4)	S_v	(3.32)	$\frac{0.57(3-\chi)}{2d_p}\left[26.8\left(\frac{a}{d_c}\right)-14.9\left(\frac{a}{d_c}\right)^2\right]$
	$\chi=\psi$	(2.72)	$2+2\cos\left[\frac{4\pi}{3}+\frac{1}{3}\cos^{-1}(2\epsilon-1)\right]$
	$\left(\frac{t}{d_c}\right)$	(3.29)	$18.5\left(\frac{t}{d_c}\right)^3+3.87\left(\frac{t}{d_c}\right)^2+(\epsilon-1)=0$
Huu et al. [5] (Section 3.1.5) - tri. struts	S_v	(3.38)	$\frac{60r_{tf}\left(1-\frac{1}{2}\sqrt{\frac{2}{3}}r_{tf}\right)^2}{\sqrt{5}\phi^3\sqrt{3-\phi}\,d_p}+\frac{\left(1-\frac{1}{2}\sqrt{\frac{2}{3}}r_{tf}\right)}{\phi\sqrt{3-\phi}\,d_p}\left[\frac{12\pi r_{tf}\left(1-\frac{1}{2}\sqrt{\frac{2}{3}}r_{tf}\right)}{\sqrt{5}\phi\sqrt{3-\phi}}+\frac{\sqrt{15}\sin^2\left(\frac{\pi}{5}\right)\left(1-\frac{1}{2}\sqrt{\frac{2}{3}}r_{tf}\right)^2}{2(3-\phi)}\right]$
- cyl. struts	S_v	(3.39)	$\frac{20\pi r_{cf}\left(1-\frac{1}{2}\sqrt{\frac{2}{3}}r_{cf}\right)^2}{\sqrt{5}\phi^3\sqrt{3-\phi}\,d_p}+\frac{\left(1-\frac{1}{2}\sqrt{\frac{2}{3}}r_{cf}\right)}{\phi\sqrt{3-\phi}\,d_p}\left[\frac{12\pi r_{cf}\left(1-\frac{1}{2}\sqrt{\frac{2}{3}}r_{cf}\right)}{\sqrt{3}\phi\sqrt{3-\phi}}+\frac{\sqrt{15}\sin^2\left(\frac{\pi}{5}\right)\left(1-\frac{1}{2}\sqrt{\frac{2}{3}}r_{cf}\right)^2}{2(3-\phi)}\right]$

Literature model	Eqn. for	Eqn. no.	Eqn.
Edouard [6] (Section 3.1.6)	S_v	(3.51)	$\frac{1}{d_p}(1-2r_1)\left[6\pi r_1+6r_1^2\left(4r_2^2-2\pi r_2-\pi\right)\right]$
	r_1	(3.46)	$(8-6\pi)r_1^3+(3\pi)r_1^2-C_t=0$
	r_2	(3.42) and (3.47)	$\sqrt[3]{\frac{C_{\text{node}}(r_{tf})}{8r_1^3}}+1+\frac{3\pi}{4}$
Ahmed et al. (Section 3.1.7)	K	(3.66)	$\frac{\epsilon^{2.5}}{36\chi^{1.5}\left[\pi r_1+r_1^2\left(4r_2^2-2\pi r_2-\pi\right)\right]}\frac{d_p^2}{1+2(\epsilon/\chi)}$
	K_F	(3.69)	$\frac{\epsilon^3}{\chi^2\left(\pi r_1-2\pi r_1^2 r_2\right)}\frac{d_p}{\sqrt{1+2(\epsilon/\chi)}}$
	χ	(3.52)	$\frac{\epsilon}{1-4r_1+4r_1^2\left(2r_2-r_2^2\right)}$
	r_1	(3.46)	$(8-6\pi)r_1^3+(3\pi)r_1^2+C_t=0$
	r_2	(3.42) and (3.47)	$\sqrt[3]{\frac{C_{\text{node}}(r_{tf})}{8r_1^3}}+1+\frac{3\pi}{4}$
NARUC models (Section 3.2)			
	K	(3.87)	$d_p^2\frac{\epsilon^2(1-2r_1R)^2}{9\psi^2(\psi-1)(3-\psi)^2(1-2r_1)}$
	K_F	(3.88)	$d_p\frac{4\epsilon^3(1-2r_1R)}{\psi^2(\psi-1)(3-\psi)^2(1-2r_1)}$
	S_v	(3.89)	$\frac{3(3-\psi)^2(\psi-1)(1-2r_1)}{2d_p(1-2r_1R)}$
	ψ	(2.72)	$2+2\cos\left[\frac{4\pi}{3}+\frac{1}{3}\cos^{-1}(2\epsilon-1)\right]$
NARUC: cubic nodes (Section 3.2.1)	R	(3.83)	$\frac{1}{2\sqrt{r_1}}\cos\left[\frac{1}{3}\cos^{-1}\left[1+8r_1^2(4r_1-3)-16r_1^3k\left(r_2^3-2r_2+1\right)\right]+\frac{4}{3}\pi\right]+\frac{1}{4r_1}$
Combinations:			
Dodecahedron - tri. struts	r_1	(3.91)	$16r_1^3-12r_1^2+C_t=0$
	r_2	(3.93)	$\left(8kr_1^3\right)r_2^3+\left(-16kr_1^3\right)r_2+\left(8kr_1^3-C_{\text{node}(r_{tf})}\right)=0$
Dodecahedron - cyl. struts	r_1	-	$16r_1^3-12r_1^2+C_c=0$
	r_2	(3.93)	$\left(8kr_1^3\right)r_2^3+\left(-16kr_1^3\right)r_2+\left(8kr_1^3-C_{\text{node}(r_{cf})}\right)=0$
MCL (solve eqns. simultaneously)	r_1 & r_2	(3.79)	$1-\epsilon=12r_1^2-16r_1^3+8kr_1^3\left(r_2^3-2r_2+1\right)$
	r_1 & r_2	(3.95)	$1-\epsilon=3\pi r_1^2(1-2r_1r_2)+8r_1^3r_2^3$
Tetrakaidecahedron	r_1	(3.99)	$99.96r_1^3+11.92r_1^2+(\epsilon-1)=0$
	r_2	(3.79)	$\left(8kr_1^3\right)r_2^3+\left(-16kr_1^3\right)r_2+\left(12r_1^2-16r_1^3+8kr_1^3+\epsilon-1\right)=0$
NARUC: curved wedge nodes (Section 3.2.2)	R	(3.104)	$\frac{1}{2\sqrt{r_1}}\cos\left[\frac{1}{3}\cos^{-1}\left[1+8r_1^2(4r_1-3)-k\left(1-\frac{\pi}{4}\right)\left(4r_1^3-4r_1^2+r_1\right)\right]+\frac{4}{3}\pi\right]+\frac{1}{4r_1}$
	r_1	(3.105)	$\left[16-2k\left(1-\frac{\pi}{4}\right)\right]r_1^3+\left[-12+2k\left(1-\frac{\pi}{4}\right)\right]r_1^2+\left[-\frac{k}{2}\left(1-\frac{\pi}{4}\right)\right]r_1+(1-\epsilon)=0$

equation provided in the table, or the equations provided in the chapter from which the equation in the table can be deduced. In the case where no equation numbers are provided, the equation provided in the table was deduced as explained in the text of the relevant section listed. In Table 3.7 (and Table 3.8), $C_{\text{node}}(r_{tf})$ refers to the C_{node} expression determined using r_{tf} and $C_{\text{node}}(r_{cf})$ refers to the C_{node} expression determined using r_{cf}. The latter expression was not provided explicitly as an equation in this chapter, but the derivation thereof is explained in Section 3.2.1. Some of the equations are direct expressions for the respective parameters (or variables) and others are given as polynomials which need to be solved in order to obtain the specified parameter (or variable).

CHAPTER 4

Compressed and rectangular fibre and foam RUC models

In the literature the topic of compression of fibre-type and foamlike media are often addressed (e.g. Jaganathan et al. [10] and Akaydin et al. [11]). Soft fibre-type materials are readily deformed in practice, as noted by Jaganathan et al. [10], due the high degree of flexibility and the compressible nature thereof. They also explored the influence of compression on the pore size distribution in non-woven fibrous porous media, demonstrating an exponential decrease in the mean pore diameter with increasing compressive stress. Akaydin et al. [11] noted that the change in the permeability of a soft compressible fibrous material decreases by more than one order of magnitude when comparing the measurements of the uncompressed and highest compressed state of the material sample, whereas the porosity only decreases slightly (i.e. by approximately 3%). Antohe et al. [40] and Dukhan et al. [9] mentioned the advantages of compressed metal foams in that with compression, the density of the foam increases and consequently improves heat transfer and structural rigidity. The only geometric models that accommodate the structural changes induced by compression, as found by the author in the literature, are the streamwisely compressed two-strut and three-strut RUC models (Van Heyningen [57] and Woudberg et al. [83]). Compression in the transverse direction (i.e. perpendicular to the direction of flow) is another consideration since it does appear in experimental studies available in the literature. For example, Ouagne and Bréard [84] examined resin film infusion processes using transverse compression of fibres and Hong et al. [85] investigated the controlling of microfluidic flow in microphysiological systems by also compressing foams in a transverse direction. In addition to structural changes of a porous medium caused by compression, a fibrous medium can also be manufactured in such a way that it will be better represented by an anisotropic structure (or rectangular in terms of the RUC geometry), rather than by an isotropic or cubic one. Examples of considerations that include the idea of anisotropic foams in the literature are provided by Perrot et al. [86], Magnico [87] and De Jaeger et al. [12]. In this chapter the two-strut and three-strut RUC models presented in Chapter 2 are adjusted to accommodate such structural changes. The models adjusted to accommodate compression induced structural changes will be referred to as the two-strut and three-strut Compression Adjusted RUC (CARUC) models. The models presented retain the rectangular nature but is adjusted to facilitate different pore dimensions for each of the three principal directions. The models are applicable to streamwise or transverse compression, of hard or soft fibres (or struts) (i.e. in cases where the fibres (or struts) also deform with compression), or to anisotropic structures by implementing structural conditions to the

CARUC models presented. The conditions necessary to apply the models for compression or anisotropic applications, as well as the methods in which the models can be utilized for each of the different cases described by the aforementioned properties, are also discussed in this chapter. Additionally, a compression factor, denoted by e_x, is introduced to relate the dimensions of the uncompressed models to the dimensions of the compressed models, where $0 < e_x \leq 1$. The subscript x in this chapter represents '$\parallel$', '$\perp_1$' or '$\perp_2$' to denote compression in the streamwise direction and two possible transverse directions (e.g. $e_\parallel$ denotes the streamwise compression factor). When $e_x = 1$, the pore dimension corresponds to the uncompressed state. The adjustment of the RUC models to represent an anisotropic structure is furthermore a special case of the compression adjusted models where $e_x = 1$ for all the pore dimensions. Expressions for the permeability, of both the Darcy and Forchheimer regime, and the specific surface area for both the two-strut and three-strut CARUC models are provided. In the case of the CARUC models, more than one dimension is required in order to calculate the permeability or specific surface area predictions. In order to obtain the specific surface area using a combined approach, only one of the dimensions can be replaced by a permeability coefficient. Consequently, there are multiple options of how the specific surface area can be determined using either of the permeability coefficients, but each of the options also requires information regarding at least one other pore dimension. Either of the permeability coefficients can be used to substitute an unavailable pore dimension using the combined approach method of determining the specific surface area, as described for all the RUC models in Chapter 2. An example of replacing one of the pore dimensions using the Darcy permeability will be included in this chapter for each of the CARUC models presented. Along with other examples provided in this chapter to demonstrate different scenarios of compression, the application of the two-strut CARUC model for through plane flow and three-strut CARUC model with streamwise compression and hard fibres (or struts) are described in greater detail. The expressions derived for these specific scenarios are published in Woudberg et al. [77], of which the author of this dissertation is a co-author. Finally, examples of how the CARUC models are applied to specific scenarios are illustrated using available experimental data for the permeability coefficients and specific surface area. The expressions acquired for the permeability coefficients and specific surface area of the three-strut CARUC model in this chapter, as well as the application of the model to the experimental data obtained from Dukhan [9], was presented at the 12th International Conference on Porous Metals and Metallic Foams hosted in Dresden, Radebeul, Germany, from 5-7 July 2023. A peer-reviewed paper is yet to be published in the conference proceedings.

The model predictions for the permeability and specific surface area of the two-strut CARUC model for both in-plane and through plane flow will be determined first.

4.1 Two-strut Compression Adjusted RUC (CARUC) model

The two-strut CARUC model is presented for both in-plane and through plane flow and are shown in Figure 4.1(a) and (b), respectively. The streamwise flow directions are indicated in Figure 4.1 as "flow direction", similar to the manner in which they are indicated in Figure 2.4, as well as the adjustable dimensions in the three principal directions. The derivation of the permeability coefficients and specific surface area for the two-strut CARUC model, for both in-plane and through plane flow, are consequently presented in this section.

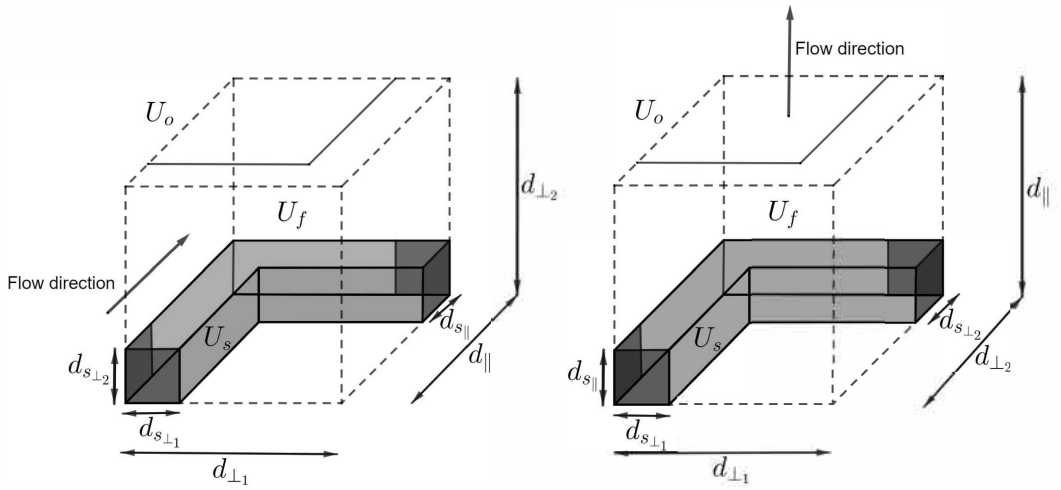

(a) *In-plane flow* (b) *Through plane flow*

FIGURE 4.1: *Two-strut CARUC models*

It is once again noted, and furthermore illustrated in Figure 4.1, that the subscripts of the dimensions in this chapter denote the directions in which the dimensions are orientated with respect to the streamwise flow direction, i.e. the streamwise direction defined as the direction of the superficial flow velocity, $\underline{q}$. For example, $d_\parallel$ denotes the face diameter orientated parallel to the streamwise flow direction and $d_{\perp_1}$ and $d_{\perp_2}$ refer to the two directions perpendicular to the streamwise flow directions, respectively. The two-strut CARUC model is dependent on the geometrical parameters as shown in Figure 4.1 in order to obtain the expressions that relate the model dimensions and equations for the permeability coefficients and specific surface area. The expressions of the two-strut CARUC model are not provided in terms of the fibre diameter, as in Chapter 2 for the two-strut RUC model, due the adjusted model also being dependent on the other dimensions other than the strut diameter indicated in Figure 4.1. An adjustment from the rectangular strut diameters to the fibre diameter is consequently not incorporated into the CARUC model equations, but can easily be incorporated by implementing the assumption that $\{d_{s_\parallel}, d_{s_{\perp_1}}, d_{s_{\perp_2}}\} = \sqrt{\pi}/2\,\{b_\parallel, b_{\perp_1}, b_{\perp_2}\}$. The manner in which the model dimension relations can be acquired, based on the geometry, as provided in Figures 4.1(a) and (b) for both the in-plane and through plane flow models, respectively, is acquired next.

4.1.1 Porosity in terms of model dimensions

The porosity equations for both the two-strut CARUC models for in-plane and through plane flow are determined in this section. It is first stated that the total volume of all the CARUC models presented in this chapter is given by

$$U_o = d_\parallel d_{\perp_1} d_{\perp_2}\,. \tag{4.1}$$

The expressions for the solid volume differ, however, and consequently results in different porosity expressions. Equation (1.6) is utilized to determine the porosity, and, in turn, the porosity equation determined based on the CARUC model is utilized to acquire relations

between the model dimensions. These equations are dependent on the conditions made for each of the CARUC models, as well as the information and data available when the model is implemented.

Two-strut CARUC model: In-plane flow

The solid volume of the two-strut CARUC model for in-plane flow can be determined from Figure 4.1(a) and is given by

$$U_s = d_{s_{\perp_1}} d_{s_{\perp_2}} d_{\parallel} + d_{s_{\parallel}} d_{s_{\perp_2}} d_{\perp_1} - d_{s_{\parallel}} d_{s_{\perp_1}} d_{s_{\perp_2}} \,. \tag{4.2}$$

The expression for the porosity is consequently determined as follows:

$$\begin{aligned} \epsilon &= \frac{d_{\parallel} d_{\perp_1} d_{\perp_2} - d_{s_{\perp_1}} d_{s_{\perp_2}} d_{\parallel} - d_{s_{\parallel}} d_{s_{\perp_2}} d_{\perp_1} + d_{s_{\parallel}} d_{s_{\perp_1}} d_{s_{\perp_2}}}{d_{\parallel} d_{\perp_1} d_{\perp_2}} \\ &= 1 - \frac{d_{s_{\perp_1}} d_{s_{\perp_2}}}{d_{\perp_1} d_{\perp_2}} - \frac{d_{s_{\parallel}} d_{s_{\perp_2}}}{d_{\parallel} d_{\perp_2}} + \frac{d_{s_{\parallel}} d_{s_{\perp_1}} d_{s_{\perp_2}}}{d_{\parallel} d_{\perp_1} d_{\perp_2}} \,. \end{aligned} \tag{4.3}$$

Similarly, the porosity for the two-strut CARUC model for through plane flow is acquired next.

Two-strut CARUC model: Through plane flow

In the case of the two-strut CARUC model for through plane flow, the porosity is deduced from Figure 4.1(b), where the solid volume is

$$U_s = d_{s_{\parallel}} d_{s_{\perp_1}} d_{\perp_2} + d_{s_{\parallel}} d_{s_{\perp_2}} d_{\perp_1} - d_{s_{\parallel}} d_{s_{\perp_1}} d_{s_{\perp_2}} \,, \tag{4.4}$$

and therefore yields

$$\epsilon = 1 - \frac{d_{s_{\parallel}} d_{s_{\perp_1}}}{d_{\parallel} d_{\perp_1}} - \frac{d_{s_{\parallel}} d_{s_{\perp_1}}}{d_{\parallel} d_{\perp_2}} + \frac{d_{s_{\parallel}} d_{s_{\perp_1}} d_{s_{\perp_2}}}{d_{\parallel} d_{\perp_1} d_{\perp_2}} \,. \tag{4.5}$$

The derivation of the permeability coefficients is subsequently presented.

4.1.2 Permeability prediction

In this section, equation (1.10) is adjusted and utilized to acquire the pressure drop for the Darcy flow regime, yielding

$$\Delta p = \frac{S_{\parallel_1} \tau_{w_{\parallel_1}} + S_{\parallel_2} \tau_{w_{\parallel_2}} + S_{\perp_1} \tau_{w_{\perp_1}} + S_{\perp_2} \tau_{w_{\perp_2}}}{A_{p_{\parallel}}} \,. \tag{4.6}$$

Equation (1.19) can be utilized as provided in Chapter 1, and therefore require no adjustments, in order to obtain the pressure gradient of the Forchheimer flow regime. The subscripts in equation (4.6) (i.e. '1' and '2') are shown to distinguish between the different allocations of parallel and perpendicular channels, as will be illustrated in Figures 4.2 and 4.3. For the two-strut CARUC model, $\xi = 1$ (once again) and the magnitude of the average wall shear stresses are determined using equation (1.12). The process of acquiring the permeability of the two-strut CARUC model for in-plane flow is considered first.

Two-strut CARUC model: In-plane flow

The streamwise and transverse surfaces of the two-strut CARUC model for in-plane flow are shown in Figure 4.2. Due to the adjustments made to the model dimensions, the surfaces are divided further such that it is assured that each surface allocation represents surfaces across the same channel width and with the same average channel velocity. For example, the surfaces shown in Figure 4.2(b) representing $S_{\perp_1}$ are bounding a channel width of $d_{\parallel} - d_{s_{\parallel}}$, whereas the surfaces shown in Figure 4.2(c) are bounding a channel width of $d_{\perp_1} - d_{s_{\perp_1}}$. In the case of the two-strut CARUC model for in-plane flow, the surfaces parallel to the streamwise direction are all bounding the same channel width and the streamwise cross-sectional flow area bordering these surface areas is the same. Therefore, the streamwise average channel velocity also remains the same and consequently, a distinction in this case is not required.

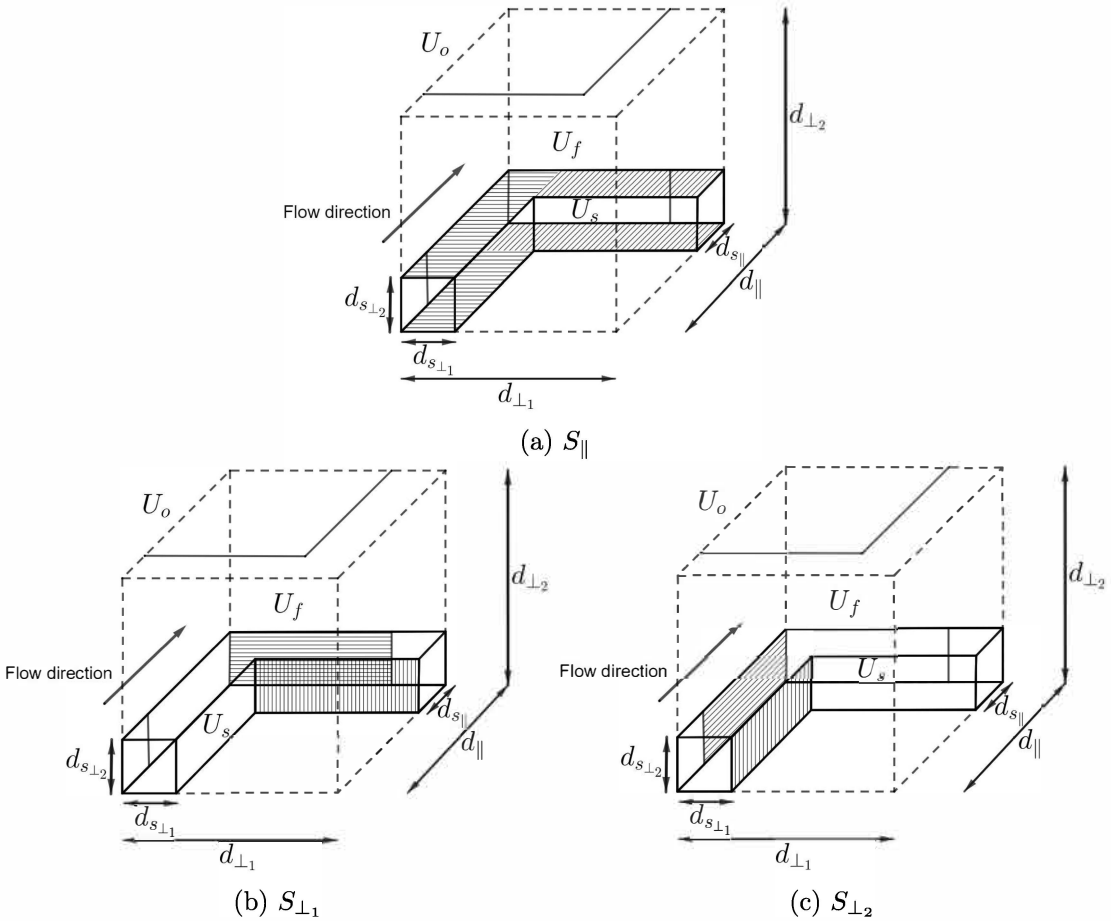

(a) $S_{\parallel}$

(b) $S_{\perp_1}$ (c) $S_{\perp_2}$

FIGURE 4.2: *Solid surfaces of two-strut CARUC model for in-plane flow*

From Figure 4.2 the surface areas parallel to the streamwise and transverse flow directions consequently yields

$$S_{\parallel} = 2d_{s_{\perp_1}}\left(d_{\parallel} - d_{s_{\parallel}}\right) + 2d_{s_{\parallel}}\left(d_{\perp_1} - d_{s_{\perp_1}}\right) + 2d_{s_{\parallel}}d_{s_{\perp_1}}\,, \tag{4.7}$$

$$S_{\perp_1} = 2d_{s_{\perp_2}}\left(d_{\perp_1} - d_{s_{\perp_1}}\right)\,, \tag{4.8}$$

and

$$S_{\perp_2} = 2d_{s_{\perp_2}} \left(d_{\parallel} - d_{s_{\parallel}} \right) . \tag{4.9}$$

The total cross-sectional area (as defined in Chapter 1) is given by

$$A_o = d_{\perp_1} d_{\perp_2} , \tag{4.10}$$

and the expression for the streamwise cross-sectional flow area can be determined from Figure 4.1(a), yielding

$$A_{p_{\parallel}} = d_{\perp_1} \left(d_{\perp_2} - d_{s_{\perp_2}} \right) . \tag{4.11}$$

Once again, equation (1.13) can be utilized together with equations (4.10) and (4.11), leading to

$$w_{\parallel} = \frac{d_{\perp_2}}{d_{\perp_2} - d_{s_{\perp_2}}} \, q . \tag{4.12}$$

It can be noted from Figures 4.2(b) and (c) that the respective transverse cross-sectional flow areas are equal, i.e.

$$A_{p_{\perp_1}} = A_{p_{\perp_2}} = A_{p_{\perp}} = \left(d_{\parallel} - d_{s_{\parallel}} \right) \left(d_{\perp_1} - d_{s_{\perp_1}} \right) . \tag{4.13}$$

Also, equation (1.14) still applies to the CARUC models and therefore the magnitude of the average channel velocity in both transverse flow directions is given by

$$w_{\perp} = \frac{A_{p_{\parallel}}}{A_{p_{\perp}}} \, w_{\parallel} = \frac{d_{\perp_1} d_{\perp_2}}{\left(d_{\parallel} - d_{s_{\parallel}} \right) \left(d_{\perp_1} - d_{s_{\perp_1}} \right)} \, q . \tag{4.14}$$

(Due to the equality of the two transverse cross-sectional flow areas, the expressions for the magnitude of the transverse average channel velocities are equal, i.e. $w_{\perp_1} = w_{\perp_2} = w_{\perp}$.) The magnitude of the streamwise and transverse average wall shear stresses are determined by implementing equation (1.12) and leads to

$$\tau_{w_{\parallel}} = \frac{6\mu w_{\parallel}}{d_{\perp_2} - d_{s_{\perp_2}}} = \frac{6 d_{\perp_2}}{\left(d_{\perp_2} - d_{s_{\perp_2}} \right)^2} \mu q , \tag{4.15}$$

$$\tau_{w_{\perp_1}} = \frac{6\mu w_{\perp}}{d_{\parallel} - d_{s_{\parallel}}} = \frac{6 d_{\perp_1} d_{\perp_2}}{\left(d_{\parallel} - d_{s_{\parallel}} \right)^2 \left(d_{\perp_1} - d_{s_{\perp_1}} \right)} \mu q , \tag{4.16}$$

and

$$\tau_{w_{\perp_2}} = \frac{6\mu w_{\perp}}{d_{\perp_1} - d_{s_{\perp_1}}} = \frac{6 d_{\perp_1} d_{\perp_2}}{\left(d_{\parallel} - d_{s_{\parallel}} \right) \left(d_{\perp_1} - d_{s_{\perp_1}} \right)^2} \mu q . \tag{4.17}$$

Substituting the surface area equations, given by equations (4.7) to (4.9), and average wall shear stress equations, given by equations (4.15) to (4.17), along with the streamwise

cross-sectional flow area (given by equation (4.11)), into equation (4.6), results in the following expression for the pressure gradient of the Darcy flow regime:

$$\frac{\Delta p}{d_{\parallel}} = \frac{12 d_{\perp_2} \mu q}{d_{\parallel} d_{\perp_1} \left(d_{\perp_2} - d_{s_{\perp_2}}\right)} \left[\frac{d_{s_{\perp_1}} \left(d_{\parallel} - d_{s_{\parallel}}\right) + d_{s_{\parallel}} \left(d_{\perp_1} - d_{s_{\perp_1}}\right) + d_{s_{\parallel}} d_{s_{\perp_1}}}{\left(d_{\perp_2} - d_{s_{\perp_2}}\right)^2} + \frac{d_{s_{\perp_2}} d_{\perp_1}}{\left(d_{\parallel} - d_{s_{\parallel}}\right)^2} + \frac{d_{s_{\perp_2}} d_{\perp_1}}{\left(d_{\perp_1} - d_{s_{\perp_1}}\right)^2} \right] . \tag{4.18}$$

The pressure gradient for the Forchheimer flow regime is determined from equation (1.19) for which the expressions for U_o and $w_{\parallel}$ are given by equations (4.1) and (4.12), respectively. S_{face} can be determined using Figure 4.1(a), leading to

$$S_{\text{face}} = d_{s_{\perp_2}} \left(d_{\perp_1} - d_{s_{\perp_1}}\right) , \tag{4.19}$$

and the pressure gradient can therefore be calculated as follows:

$$\begin{aligned} -\nabla \langle p \rangle_f &= \frac{d_{s_{\perp_2}} \left(d_{\perp_1} - d_{s_{\perp_1}}\right)}{d_{\parallel} d_{\perp_1} d_{\perp_2} \epsilon} \rho \cdot \left(\frac{q d_{\perp_2}}{d_{\perp_2} - d_{s_{\perp_2}}} \right)^2 \underline{\hat{n}} \\ &= \frac{d_{s_{\perp_2}} d_{\perp_2} \left(d_{\perp_1} - d_{s_{\perp_1}}\right)}{d_{\parallel} d_{\perp_1} \epsilon \left(d_{\perp_2} - d_{s_{\perp_2}}\right)^2} \rho q^2 \underline{\hat{n}} . \end{aligned} \tag{4.20}$$

The Ergun-type equation of the two-strut CARUC model for in-plane flow is consequently given by

$$\frac{\Delta p}{d_{\parallel}} = \frac{12 d_{\perp_2}}{d_{\parallel} d_{\perp_1} \left(d_{\perp_2} - d_{s_{\perp_2}}\right)} \left[\frac{d_{s_{\perp_1}} \left(d_{\parallel} - d_{s_{\parallel}}\right) + d_{s_{\parallel}} \left(d_{\perp_1} - d_{s_{\perp_1}}\right) + d_{s_{\parallel}} d_{s_{\perp_1}}}{\left(d_{\perp_2} - d_{s_{\perp_2}}\right)^2} + \frac{d_{s_{\perp_2}} d_{\perp_1}}{\left(d_{\parallel} - d_{s_{\parallel}}\right)^2} + \frac{d_{s_{\perp_2}} d_{\perp_1}}{\left(d_{\perp_1} - d_{s_{\perp_1}}\right)^2} \right] \mu q + \frac{d_{s_{\perp_2}} d_{\perp_2} \left(d_{\perp_1} - d_{s_{\perp_1}}\right)}{d_{\parallel} d_{\perp_1} \epsilon \left(d_{\perp_2} - d_{s_{\perp_2}}\right)^2} \rho q^2 , \tag{4.21}$$

from which the following expressions for the Darcy and Forchheimer permeability coefficients are deduced:

$$K = \frac{d_{\parallel} d_{\perp_1} \left(d_{\perp_2} - d_{s_{\perp_2}}\right)}{12 d_{\perp_2}} \left[\frac{d_{s_{\perp_1}} \left(d_{\parallel} - d_{s_{\parallel}}\right) + d_{s_{\parallel}} \left(d_{\perp_1} - d_{s_{\perp_1}}\right) + d_{s_{\parallel}} d_{s_{\perp_1}}}{\left(d_{\perp_2} - d_{s_{\perp_2}}\right)^2} + \frac{d_{s_{\perp_2}} d_{\perp_1}}{\left(d_{\parallel} - d_{s_{\parallel}}\right)^2} + \frac{d_{s_{\perp_2}} d_{\perp_1}}{\left(d_{\perp_1} - d_{s_{\perp_1}}\right)^2} \right]^{-1} , \tag{4.22}$$

and

$$K_F = \frac{d_{\parallel} d_{\perp_1} \epsilon \left(d_{\perp_2} - d_{s_{\perp_2}}\right)^2}{d_{s_{\perp_2}} d_{\perp_2} \left(d_{\perp_1} - d_{s_{\perp_1}}\right)} . \tag{4.23}$$

The Ergun-type equation and permeability coefficients of the two-strut CARUC model for through plane flow will be considered next.

Two-strut CARUC model: Through plane flow

Similar to the case of the two-strut CARUC model for in-plane flow, the streamwise and transverse surface areas for the two-strut CARUC model for through plane flow are shown in Figure 4.3. In this case, however, a distinction between the streamwise surface areas

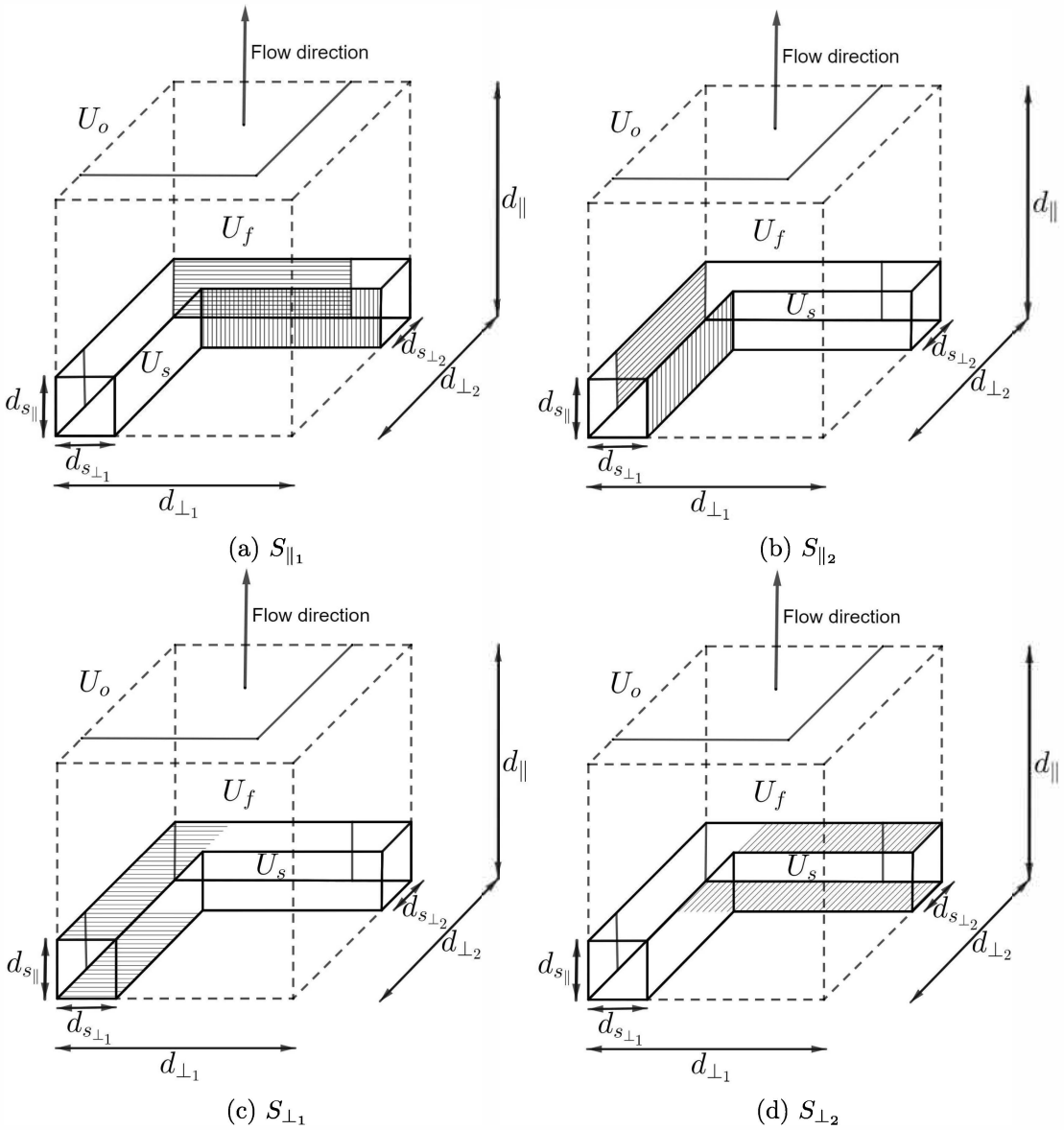

(a) $S_{\parallel_1}$ (b) $S_{\parallel_2}$

(c) $S_{\perp_1}$ (d) $S_{\perp_2}$

FIGURE 4.3: *Solid surfaces of two-strut CARUC model for through plane flow*

are required due to different channel widths and a distinction between the transverse surface areas are required due to different cross-sectional flow areas and hence different transverse average channel velocities.

The streamwise and transverse surface areas are consequently determined from Figure 4.3 and results in the following expressions:

$$S_{\parallel_1} = 2d_{s_\parallel}\left(d_{\perp_1} - d_{s_{\perp_1}}\right), \tag{4.24}$$

$$S_{\parallel_2} = 2d_{s_\parallel}\left(d_{\perp_2} - d_{s_{\perp_2}}\right), \tag{4.25}$$

and

$$S_{\perp_1} = 2d_{s_{\perp_1}}\left(d_{\perp_2} - d_{s_{\perp_2}}\right) + d_{s_{\perp_1}}d_{s_{\perp_2}}, \tag{4.26}$$

$$S_{\perp_2} = 2d_{s_{\perp_2}}\left(d_{\perp_1} - d_{s_{\perp_1}}\right) + d_{s_{\perp_1}}d_{s_{\perp_2}}, \tag{4.27}$$

and the streamwise cross-sectional flow area is given by

$$A_{p_\parallel} = \left(d_{\perp_1} - d_{s_{\perp_1}}\right)\left(d_{\perp_2} - d_{s_{\perp_2}}\right). \tag{4.28}$$

Utilizing equations (1.13), (4.10) and (4.28) then leads to the magnitude of the streamwise average channel velocity, i.e.

$$w_\parallel = \frac{d_{\perp_1}d_{\perp_2}}{\left(d_{\perp_1} - d_{s_{\perp_1}}\right)\left(d_{\perp_2} - d_{s_{\perp_2}}\right)}\,q\,. \tag{4.29}$$

(It is noted that $A_{p_{\parallel_1}} = A_{p_{\parallel_2}} = A_{p_\parallel}$ and consequently $w_{\parallel_1} = w_{\parallel_2} = w_\parallel$ in this case.) Two transverse cross-sectional flow areas are present in the two-strut CARUC model for through plane flow and are given by

$$A_{p_{\perp_1}} = d_{\perp_2}\left(d_\parallel - d_{s_\parallel}\right) \qquad \text{and} \qquad A_{p_{\perp_2}} = d_{\perp_1}\left(d_\parallel - d_{s_\parallel}\right). \tag{4.30}$$

Implementing the equation for conservation of mass, i.e. equation (1.14), to both the latter transverse cross-sectional flow areas therefore leads to the following magnitudes of the transverse average channel velocities:

$$w_{\perp_1} = \frac{A_{p_\parallel}}{A_{p_{\perp_1}}}\,w_\parallel = \frac{d_{\perp_1}}{d_\parallel - d_{s_\parallel}}\,q\,, \tag{4.31}$$

and

$$w_{\perp_2} = \frac{A_{p_\parallel}}{A_{p_{\perp_2}}}\,w_\parallel = \frac{d_{\perp_2}}{d_\parallel - d_{s_\parallel}}\,q\,. \tag{4.32}$$

The expressions for the magnitude of the streamwise and transverse average wall shear stress, determined using equation (1.12) together with equations (4.29), (4.31) and (4.32),

are consequently given as follows:

$$\tau_{w_{\parallel_1}} = \frac{6\mu w_{\parallel}}{d_{\perp_2} - d_{s_{\perp_2}}} = \frac{6 d_{\perp_1} d_{\perp_2}}{\left(d_{\perp_1} - d_{s_{\perp_1}}\right)\left(d_{\perp_2} - d_{s_{\perp_2}}\right)^2}\,\mu q\,, \tag{4.33}$$

$$\tau_{w_{\parallel_2}} = \frac{6\mu w_{\parallel}}{d_{\perp_1} - d_{s_{\perp_1}}} = \frac{6 d_{\perp_1} d_{\perp_2}}{\left(d_{\perp_1} - d_{s_{\perp_1}}\right)^2\left(d_{\perp_2} - d_{s_{\perp_2}}\right)}\,\mu q\,, \tag{4.34}$$

$$\tau_{w_{\perp_1}} = \frac{6\mu w_{\perp_1}}{d_{\parallel} - d_{s_{\parallel}}} = \frac{6 d_{\perp_1}}{\left(d_{\parallel} - d_{s_{\parallel}}\right)^2}\,\mu q\,, \tag{4.35}$$

and

$$\tau_{w_{\perp_2}} = \frac{6\mu w_{\perp_2}}{d_{\parallel} - d_{s_{\parallel}}} = \frac{6 d_{\perp_2}}{\left(d_{\parallel} - d_{s_{\parallel}}\right)^2}\,\mu q\,. \tag{4.36}$$

Substituting all the relevant expressions determined for the two-strut CARUC model for through plane flow into equation (4.6), yields the pressure gradient expression for the Darcy flow regime, i.e.

$$\frac{\Delta p}{d_{\parallel}} = \frac{12\mu q}{d_{\parallel}\left(d_{\perp_1} - d_{s_{\perp_1}}\right)\left(d_{\perp_2} - d_{s_{\perp_2}}\right)}\left[\frac{d_{s_{\parallel}} d_{\perp_1} d_{\perp_2}}{\left(d_{\perp_2} - d_{s_{\perp_2}}\right)^2} + \frac{d_{s_{\parallel}} d_{\perp_1} d_{\perp_2}}{\left(d_{\perp_1} - d_{s_{\perp_1}}\right)^2}\right. \tag{4.37}$$

$$\left. + \frac{d_{s_{\perp_1}} d_{\perp_1}\left(d_{\perp_2} - \frac{1}{2} d_{s_{\perp_2}}\right) + d_{s_{\perp_2}} d_{\perp_2}\left(d_{\perp_1} - \frac{1}{2} d_{s_{\perp_1}}\right)}{\left(d_{\parallel} - d_{s_{\parallel}}\right)^2}\right]. \tag{4.38}$$

The pressure gradient for the Forchheimer flow regime is once again calculated using equation (1.19) which requires the expressions for U_o, $w_{\parallel}$ and S_{face}. The total volume is given by equation (4.1), $w_{\parallel}$ is given by equation (4.29) for the two-strut CARUC model for through plane flow and S_{face} can be determined using Figure 4.1(b), leading to

$$S_{\text{face}} = d_{s_{\perp_1}} d_{\perp_2} + d_{s_{\perp_2}} d_{\perp_1} - d_{s_{\perp_1}} d_{s_{\perp_2}}\,. \tag{4.39}$$

The pressure gradient for the Forchheimer flow regime is therefore given by

$$-\nabla\langle p\rangle_f = \frac{d_{\perp_1} d_{\perp_2}\left(d_{s_{\perp_1}} d_{\perp_2} + d_{s_{\perp_2}} d_{\perp_1} - d_{s_{\perp_1}} d_{s_{\perp_2}}\right)}{d_{\parallel}\epsilon\left(d_{\perp_1} - d_{s_{\perp_1}}\right)^2\left(d_{\perp_2} - d_{s_{\perp_2}}\right)^2}\,\rho q^2 \underline{\hat{n}}\,, \tag{4.40}$$

and consequently an Ergun-type equation for the two-strut CARUC model for through

plane flow is obtained:

$$\frac{\Delta p}{d_{\parallel}} = \frac{12}{d_{\parallel}\left(d_{\perp_1}-d_{s_{\perp_1}}\right)\left(d_{\perp_2}-d_{s_{\perp_2}}\right)}\left[\frac{d_{s_{\parallel}}d_{\perp_1}d_{\perp_2}}{\left(d_{\perp_2}-d_{s_{\perp_2}}\right)^2}+\frac{d_{s_{\parallel}}d_{\perp_1}d_{\perp_2}}{\left(d_{\perp_1}-d_{s_{\perp_1}}\right)^2}\right.$$
$$\left.+\frac{d_{s_{\perp_1}}d_{\perp_1}\left(d_{\perp_2}-\frac{1}{2}d_{s_{\perp_2}}\right)+d_{s_{\perp_2}}d_{\perp_2}\left(d_{\perp_1}-\frac{1}{2}d_{s_{\perp_1}}\right)}{\left(d_{\parallel}-d_{s_{\parallel}}\right)^2}\right]\mu q$$
$$+\frac{d_{\perp_1}d_{\perp_2}\left(d_{s_{\perp_1}}d_{\perp_2}+d_{s_{\perp_2}}d_{\perp_1}-d_{s_{\perp_1}}d_{s_{\perp_2}}\right)}{d_{\parallel}\epsilon\left(d_{\perp_1}-d_{s_{\perp_1}}\right)^2\left(d_{\perp_2}-d_{s_{\perp_2}}\right)^2}\rho q^2\,. \tag{4.41}$$

Hence, the Darcy permeability is given by

$$K=\frac{d_{\parallel}\left(d_{\perp_1}-d_{s_{\perp_1}}\right)\left(d_{\perp_2}-d_{s_{\perp_2}}\right)}{12}\left[\frac{d_{s_{\parallel}}d_{\perp_1}d_{\perp_2}}{\left(d_{\perp_2}-d_{s_{\perp_2}}\right)^2}+\frac{d_{s_{\parallel}}d_{\perp_1}d_{\perp_2}}{\left(d_{\perp_1}-d_{s_{\perp_1}}\right)^2}\right.$$
$$\left.+\frac{d_{s_{\perp_1}}d_{\perp_1}\left(d_{\perp_2}-\frac{1}{2}d_{s_{\perp_2}}\right)+d_{s_{\perp_2}}d_{\perp_2}\left(d_{\perp_1}-\frac{1}{2}d_{s_{\perp_1}}\right)}{\left(d_{\parallel}-d_{s_{\parallel}}\right)^2}\right]^{-1}. \tag{4.42}$$

and the Forchheimer permeability by

$$K_F=\frac{d_{\parallel}\epsilon\left(d_{\perp_1}-d_{s_{\perp_1}}\right)^2\left(d_{\perp_2}-d_{s_{\perp_2}}\right)^2}{d_{\perp_1}d_{\perp_2}\left(d_{s_{\perp_1}}d_{\perp_2}+d_{s_{\perp_2}}d_{\perp_1}-d_{s_{\perp_1}}d_{s_{\perp_2}}\right)}\,. \tag{4.43}$$

The specific surface area of the two-strut CARUC model will now be addressed.

4.1.3 Specific surface area prediction: Geometric approach

The specific surface area is determined using the two-strut geometry as shown in Figure 4.1. Due to the different orientations of the struts and the specification of the dimensions, the results are dependent on the direction of flow, i.e. in-plane or through plane.

Two-strut CARUC model: In-plane flow

The specific surface area determined using a geometric approach entails the total surface area being divided by the total volume. The total surface area is calculated by utilizing Figure 4.1(a) and leads to

$$\begin{aligned}S_{fs}&=2d_{s_{\perp_1}}\left(d_{\parallel}-d_{s_{\parallel}}\right)+d_{s_{\parallel}}d_{s_{\perp_1}}+2d_{s_{\parallel}}\left(d_{\perp_1}-d_{s_{\perp_1}}\right)+d_{s_{\parallel}}d_{s_{\perp_1}}+2d_{s_{\perp_2}}\left(d_{\perp_1}-d_{s_{\perp_1}}\right)\\&\quad+2d_{s_{\perp_2}}\left(d_{\parallel}-d_{s_{\parallel}}\right)\\&=2\left(d_{\parallel}-d_{s_{\parallel}}\right)\left(d_{s_{\perp_1}}+d_{s_{\perp_2}}\right)+2\left(d_{\perp_1}-d_{s_{\perp_1}}\right)\left(d_{s_{\parallel}}+d_{s_{\perp_2}}\right)+2d_{s_{\parallel}}d_{s_{\perp_1}}\,,\end{aligned} \tag{4.44}$$

and the total volume is given by equation (4.1). The specific surface area equation is therefore

$$S_v = \frac{2\left[\left(d_{\parallel} - d_{s_{\parallel}}\right)\left(d_{s_{\perp_1}} + d_{s_{\perp_2}}\right) + \left(d_{\perp_1} - d_{s_{\perp_1}}\right)\left(d_{s_{\parallel}} + d_{s_{\perp_2}}\right) + d_{s_{\parallel}} d_{s_{\perp_1}}\right]}{d_{\parallel} d_{\perp_1} d_{\perp_2}} . \tag{4.45}$$

Relations between the model dimensions present in equation (4.45) can be determined by rearranging equation (4.3).

Two-strut CARUC model: Through plane flow

The specific surface area determined for the two-strut CARUC model for through plane flow is determined similarly to that of the model for in-plane flow, but utilizing Figure 4.1(b) in this case. The total surface area is consequently determined to be

$$\begin{aligned} S_{fs} &= 2d_{s_{\parallel}}\left(d_{\perp_1} - d_{s_{\perp_1}}\right) + 2d_{s_{\parallel}}\left(d_{\perp_2} - d_{s_{\perp_2}}\right) + 2d_{s_{\perp_1}}\left(d_{\perp_2} - d_{s_{\perp_2}}\right) + d_{s_{\perp_1}} d_{s_{\perp_2}} \\ &\quad + 2d_{s_{\perp_2}}\left(d_{\perp_1} - d_{s_{\perp_1}}\right) + d_{s_{\perp_1}} d_{s_{\perp_2}} \\ &= 2d_{s_{\parallel}}\left(d_{\perp_1} + d_{\perp_2} - d_{s_{\perp_1}} - d_{s_{\perp_2}}\right) + 2\left(d_{s_{\perp_1}} d_{\perp_2} + d_{s_{\perp_2}} d_{\perp_1}\right) - 2d_{s_{\perp_1}} d_{s_{\perp_2}} , \end{aligned} \tag{4.46}$$

and the equation for the specific surface area is hence given by

$$S_v = \frac{2\left[d_{s_{\parallel}}\left(d_{\perp_1} + d_{\perp_2} - d_{s_{\perp_1}} - d_{s_{\perp_2}}\right) + \left(d_{s_{\perp_1}} d_{\perp_2} + d_{s_{\perp_2}} d_{\perp_1}\right) - d_{s_{\perp_1}} d_{s_{\perp_2}}\right]}{d_{\parallel} d_{\perp_1} d_{\perp_2}} . \tag{4.47}$$

In this case, the model dimension relations acquired from equation (4.5) can be used to determine the dimensions in equation (4.47), that is, the model dimension relations acquired for the two-strut CARUC model for through plane flow.

4.1.4 Specific surface area prediction: Combined approach

In order to determine the specific surface area using a combined approach, one of the pore dimensions in the equations for the specific surface area determined using the geometric approach (i.e. equation (4.45) or (4.47) in the case of the two-strut CARUC model for in-plane and through plane flow, respectively), needs to be replaced with one of the permeability coefficients for the corresponding streamwise flow directions, as previously explained. As an example, the streamwise face diameter will be replaced by the Darcy permeability coefficient for in-plane and through plane flow to determine the expression for the specific surface area of the respective streamwise flow directions obtained using a combined approach. It should be noted that in order to determine the specific surface area by making use of the combined approach, experimental permeability data is required.

Two-strut CARUC model: In-plane flow

In the case of the two-strut CARUC model for in-plane flow, equation (4.45) first needs to be rearranged to determine $d_{\parallel}$ in terms of the specific surface area. This yields

$$d_{\parallel} = \frac{2s - 2d_{s_{\parallel}} r}{d_{\perp_1} d_{\perp_2} S_v - 2r} , \tag{4.48}$$

where $s = \left(d_{\perp_1} - d_{s_{\perp_1}}\right)\left(d_{s_\parallel} + d_{s_{\perp_2}}\right) + d_{s_\parallel} d_{s_{\perp_1}}$ and $r = d_{s_{\perp_1}} + d_{s_{\perp_2}}$. Equation (4.48) is then substituted into equation (4.22) and rearranged in order to obtain the following third-degree polynomial in terms of S_v from which the latter parameter can be solved:

$$a' S_v^3 + b' S_v^2 + c' S_v + g' = 0 \tag{4.49}$$

where

$$\begin{aligned}
a' &= d_{\perp_1}^3 d_{\perp_2}^3 K \left(-d_{s_\parallel}^3 d_{s_{\perp_1}} + d_{s_\parallel}^2 l z + d_{s_{\perp_2}} d_{\perp_1} z\right) \\
b' &= -6 d_{\perp_1}^2 d_{\perp_2}^2 K r \left(-d_{s_\parallel}^3 d_{s_{\perp_1}} + d_{s_\parallel}^2 l z + d_{s_{\perp_2}} d_{\perp_1} z\right) \\
&\quad + 2 d_{s_\parallel} d_{\perp_1}^2 d_{\perp_2}^2 \left(s - d_{s_\parallel} r\right)\left(3 d_{s_\parallel} d_{s_{\perp_1}} K - 2 K l z - d_{s_\parallel} m z\right) \\
c' &= 12 d_{\perp_1} d_{\perp_2} K r^2 \left(-d_{s_\parallel}^3 d_{s_{\perp_1}} + d_{s_\parallel}^2 l z + d_{s_{\perp_2}} d_{\perp_1} z\right) \\
&\quad - 8 d_{s_\parallel} d_{\perp_1} d_{\perp_2} r \left(s - d_{s_\parallel} r\right)\left(3 d_{s_\parallel} d_{s_{\perp_1}} K - 2 K l z - d_{s_\parallel} m z\right) \\
&\quad + 4 d_{\perp_1} d_{\perp_2} \left(s - d_{s_\parallel} r\right)^2 \left(-3 d_{s_\parallel} d_{s_{\perp_1}} K + K l z + 2 d_{s_\parallel} m z\right) \\
g' &= -8 K r^3 \left(-d_{s_\parallel}^3 d_{s_{\perp_1}} + d_{s_\parallel}^2 l z + d_{s_{\perp_2}} d_{\perp_1} z\right) \\
&\quad + 8 d_{s_\parallel} r^2 \left(s - d_{s_\parallel} r\right)\left(3 d_{s_\parallel} d_{s_{\perp_1}} K - 2 K l z - d_{s_\parallel} m z\right) \\
&\quad - 8 r \left(s - d_{s_\parallel} r\right)^2 \left(-3 d_{s_\parallel} d_{s_{\perp_1}} K + K l z + 2 d_{s_\parallel} m z\right) \\
&\quad + 8 \left(s - d_{s_\parallel} r\right)^3 \left(d_{s_{\perp_1}} K - m z\right) .
\end{aligned} \tag{4.50}$$

In the coefficients in equation (4.50), $m = \frac{d_{\perp_1}\left(d_{\perp_2} - d_{s_{\perp_2}}\right)}{12 d_{\perp_2}}$, $l = \frac{d_{s_\parallel}\left(d_{\perp_1} - d_{s_{\perp_1}}\right) + d_{s_\parallel} d_{s_{\perp_1}}}{\left(d_{\perp_2} - d_{s_{\perp_2}}\right)^2} + \frac{d_{s_{\perp_2}} d_{\perp_1}}{\left(d_{\perp_1} - d_{s_{\perp_1}}\right)^2}$ and $z = \left(d_{\perp_2} - d_{s_{\perp_2}}\right)^2$. The substitutions of s, r, m, l and z are included in this section for convenience sake with regards to displaying the equations required to determine the specific surface area.

Two-strut CARUC model: Through plane flow

The combined approach for determining the specific surface area of the two-strut CARUC model for through plane flow is done in a similar manner as in the case of the two-strut CARUC model for in-plane flow. In this case, equation (4.47) is rearranged in order to obtain the following expression

$$d_\parallel = \frac{s}{S_v} , \tag{4.51}$$

where $s = \frac{2\left[d_{s_\parallel}\left(d_{\perp_1} + d_{\perp_2} - d_{s_{\perp_1}} - d_{s_{\perp_2}}\right) + \left(d_{s_{\perp_1}} d_{\perp_2} + d_{s_{\perp_2}} d_{\perp_1}\right) - d_{s_{\perp_1}} d_{s_{\perp_2}}\right]}{d_{\perp_1} d_{\perp_2}}$. Substituting equation (4.51) into equation (4.42) and rearranging then leads to third-degree polynomial, as

given by equation (4.49), with the following coefficients:

$$\begin{aligned} a' &= K\left(d_{s_\parallel}^2 l + r\right) \\ b' &= -d_{s_\parallel} s\left(2Kl + d_{s_\parallel} m\right) \\ c' &= s^2\left(Kl + 2d_{s_\parallel} m\right) \\ g' &= -ms^2 . \end{aligned} \tag{4.52}$$

In equation (4.52), $m = \frac{\left(d_{\perp_1} - d_{s_{\perp_1}}\right)\left(d_{\perp_2} - d_{s_{\perp_2}}\right)}{12}$, $l = \frac{d_{s_\parallel} d_{\perp_1} d_{\perp_2}}{\left(d_{\perp_2} - d_{s_{\perp_2}}\right)^2} + \frac{d_{s_\parallel} d_{\perp_1} d_{\perp_2}}{\left(d_{\perp_1} - d_{s_{\perp_1}}\right)^2}$ and $r = d_{s_{\perp_1}} d_{\perp_1}\left(d_{\perp_2} - \frac{1}{2} d_{s_{\perp_2}}\right) + d_{s_{\perp_2}} d_{\perp_2}\left(d_{\perp_1} - \frac{1}{2} d_{s_{\perp_1}}\right)$.

The three-strut CARUC model is considered next.

4.2 Three-strut Compression Adjusted RUC (CARUC) model

The three-strut CARUC model, adapted in such a way that the dimensions can be adjusted, is shown in Figure 4.4. Only the high porosity model is shown in this case.

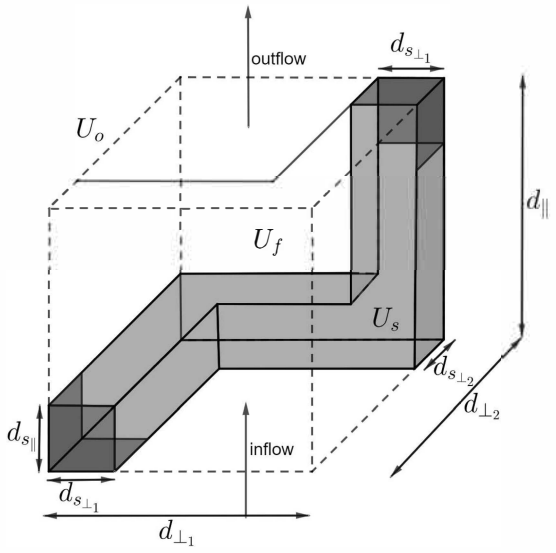

FIGURE 4.4: *Three-strut CARUC model*

Expressions for the model dimensions can be determined using Figure 4.4. Where the three-strut CARUC model is used to predict the properties of fibre-type media, the transition between the strut and fibre diameters as provided in the two-strut CARUC model section, i.e. $\{d_{s_\parallel}, d_{s_{\perp_1}}, d_{s_{\perp_2}}\} = \sqrt{\pi}/2\,\{b_\parallel, b_{\perp_1}, b_{\perp_2}\}$, can be utilized. The porosity as a function of the model dimensions is presented next.

4.2.1 Porosity in terms of model dimensions

The total volume of the CARUC model is given by equation (4.1) and the solid volume of the three-strut CARUC model can be acquired from Figure 4.4, which yields

$$U_s = d_{s_\parallel} d_{s_{\perp_1}} \left(d_{\perp_2} - d_{s_{\perp_2}} \right) + d_{s_\parallel} d_{s_{\perp_2}} \left(d_{\perp_1} - d_{s_{\perp_1}} \right) + d_{s_{\perp_1}} d_{s_{\perp_2}} d_\parallel \,. \tag{4.53}$$

The porosity is then determined to be

$$\epsilon = 1 - \frac{U_s}{U_o} = 1 - \frac{d_{s_\parallel} d_{s_{\perp_1}}}{d_\parallel d_{\perp_1}} - \frac{d_{s_\parallel} d_{s_{\perp_2}}}{d_\parallel d_{\perp_2}} - \frac{d_{s_{\perp_1}} d_{s_{\perp_2}}}{d_{\perp_1} d_{\perp_2}} + \frac{2 d_{s_\parallel} d_{s_{\perp_1}} d_{s_{\perp_2}}}{d_\parallel d_{\perp_1} d_{\perp_2}} \,. \tag{4.54}$$

Using equation (4.54), relations between the pore-scale dimensions and porosity can be attained.

In the following section, the expressions for the permeability coefficients of the three-strut CARUC model are determined.

4.2.2 Permeability prediction

The adjusted equation of the pressure drop for the Darcy flow regime also has to accommodate the third perpendicular strut present in the three-strut RUC model, i.e. equation (1.10) becomes

$$\Delta p = \frac{S_{\parallel_1} \tau_{w_{\parallel_1}} + S_{\parallel_2} \tau_{w_{\parallel_2}} + S_{\perp_{1,1}} \tau_{w_{\perp_{1,1}}} + S_{\perp_{1,2}} \tau_{w_{\perp_{1,2}}} + S_{\perp_{2,1}} \tau_{w_{\perp_{2,1}}} + S_{\perp_{2,2}} \tau_{w_{\perp_{2,2}}}}{A_{p_\parallel}} \,. \tag{4.55}$$

Once again, $\xi = 1$, and the expressions for the magnitude of the average wall shear stress of the model are determined using equation (1.12). All the surface areas and the grouping thereof are indicated in Figure 4.5. The subscripts of '1' and '2' appearing as the second numerical subscript in the case of the transverse parameters are utilized in order to distinguish between the surface areas bounding the same channels in the different transverse flow directions as well as the areas bordering the same cross-sectional flow areas in the different flow directions.

The six sets of surface areas determined for the three-strut CARUC model, based on Figure 4.5, are given as follows:

$$S_{\parallel_1} = 2 d_{s_\parallel} \left(d_{\perp_1} - d_{s_{\perp_1}} \right) \,, \tag{4.56}$$

$$S_{\parallel_2} = 2 d_{s_\parallel} \left(d_{\perp_2} - d_{s_{\perp_2}} \right) \,, \tag{4.57}$$

$$S_{\perp_{1,1}} = 2 d_{s_{\perp_1}} \left(d_{\perp_2} - d_{s_{\perp_2}} \right) \,, \tag{4.58}$$

$$S_{\perp_{1,2}} = 2 d_{s_{\perp_1}} \left(d_\parallel - d_{s_\parallel} \right) \,, \tag{4.59}$$

$$S_{\perp_{2,1}} = 2 d_{s_{\perp_2}} \left(d_{\perp_1} - d_{s_{\perp_1}} \right) \,, \tag{4.60}$$

and

$$S_{\perp_{2,2}} = 2 d_{s_{\perp_2}} \left(d_\parallel - d_{s_\parallel} \right) \,. \tag{4.61}$$

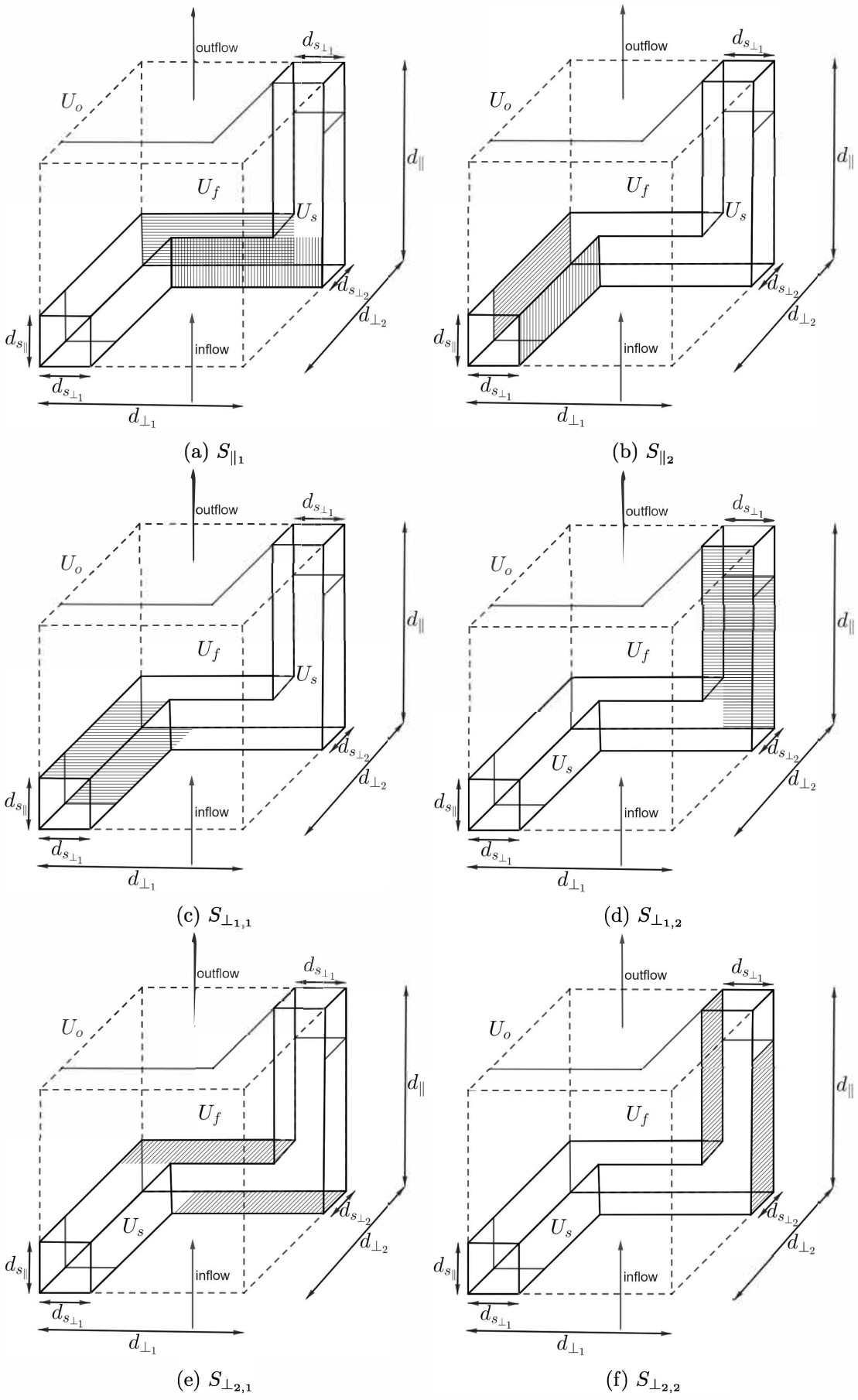

(a) $S_{\parallel_1}$ (b) $S_{\parallel_2}$

(c) $S_{\perp_{1,1}}$ (d) $S_{\perp_{1,2}}$

(e) $S_{\perp_{2,1}}$ (f) $S_{\perp_{2,2}}$

FIGURE 4.5: *Solid surfaces of three-strut CARUC model*

The streamwise cross-sectional flow area for the three-strut CARUC model is the same as that of the two-strut CARUC model for through plane flow, i.e. it is also given by equation (4.28), and the total cross-sectional area is given by equation (4.10). Consequently, the streamwise average channel velocity is acquired by utilizing equation (1.13), yielding

$$w_{\parallel} = \frac{d_{\perp_1} d_{\perp_2}}{\left(d_{\perp_1} - d_{s_{\perp_1}}\right)\left(d_{\perp_2} - d_{s_{\perp_2}}\right)} q \,. \tag{4.62}$$

The following transverse cross-sectional areas can furthermore be deduced from Figure 4.5:

$$A_{p_{\perp_{1,1}}} = A_{p_{\perp_{1,2}}} = A_{p_{\perp_1}} = \left(d_{\parallel} - d_{s_{\parallel}}\right)\left(d_{\perp_2} - d_{s_{\perp_2}}\right) , \tag{4.63}$$

and

$$A_{p_{\perp_{2,1}}} = A_{p_{\perp_{2,2}}} = A_{p_{\perp_2}} = \left(d_{\parallel} - d_{s_{\parallel}}\right)\left(d_{\perp_1} - d_{s_{\perp_1}}\right) . \tag{4.64}$$

From the implementation of equation (1.14), the magnitude of the average channel velocities in the transverse directions are determined to be

$$w_{\perp_1} = \frac{A_{p_{\parallel}}}{A_{p_{\perp_1}}} w_{\parallel} = \frac{d_{\perp_1} d_{\perp_2}}{\left(d_{\parallel} - d_{s_{\parallel}}\right)\left(d_{\perp_2} - d_{s_{\perp_2}}\right)} q \,, \tag{4.65}$$

and

$$w_{\perp_2} = \frac{A_{p_{\parallel}}}{A_{p_{\perp_2}}} w_{\parallel} = \frac{d_{\perp_1} d_{\perp_2}}{\left(d_{\parallel} - d_{s_{\parallel}}\right)\left(d_{\perp_1} - d_{s_{\perp_1}}\right)} q \,. \tag{4.66}$$

The expressions for the magnitude of the average wall shear stress for the different flow directions in the three-strut CARUC model are therefore given by

$$\tau_{w_{\parallel_1}} = \frac{6\mu w_{\parallel}}{d_{\perp_2} - d_{s_{\perp_2}}} = \frac{6 d_{\perp_1} d_{\perp_2}}{\left(d_{\perp_1} - d_{s_{\perp_1}}\right)\left(d_{\perp_2} - d_{s_{\perp_2}}\right)^2} \mu q \,, \tag{4.67}$$

$$\tau_{w_{\parallel_2}} = \frac{6\mu w_{\parallel}}{d_{\perp_1} - d_{s_{\perp_1}}} = \frac{6 d_{\perp_1} d_{\perp_2}}{\left(d_{\perp_1} - d_{s_{\perp_1}}\right)^2\left(d_{\perp_2} - d_{s_{\perp_2}}\right)} \mu q \,, \tag{4.68}$$

$$\tau_{w_{\perp_{1,1}}} = \frac{6\mu w_{\perp_1}}{d_{\parallel} - d_{s_{\parallel}}} = \frac{6 d_{\perp_1} d_{\perp_2}}{\left(d_{\parallel} - d_{s_{\parallel}}\right)^2\left(d_{\perp_2} - d_{s_{\perp_2}}\right)} \mu q \,, \tag{4.69}$$

$$\tau_{w_{\perp_{1,2}}} = \frac{6\mu w_{\perp_1}}{d_{\perp_2} - d_{s_{\perp_2}}} = \frac{6 d_{\perp_1} d_{\perp_2}}{\left(d_{\parallel} - d_{s_{\parallel}}\right)\left(d_{\perp_2} - d_{s_{\perp_2}}\right)^2} \mu q \,, \tag{4.70}$$

$$\tau_{w_{\perp_{2,1}}} = \frac{6\mu w_{\perp_2}}{d_{\parallel} - d_{s_{\parallel}}} = \frac{6 d_{\perp_1} d_{\perp_2}}{\left(d_{\parallel} - d_{s_{\parallel}}\right)^2\left(d_{\perp_1} - d_{s_{\perp_1}}\right)} \mu q \,, \tag{4.71}$$

and

$$\tau_{w_{\perp_{2,2}}} = \frac{6\mu w_{\perp_2}}{d_{\perp_1} - d_{s_{\perp_1}}} = \frac{6 d_{\perp_1} d_{\perp_2}}{\left(d_{\parallel} - d_{s_{\parallel}}\right)\left(d_{\perp_1} - d_{s_{\perp_1}}\right)^2} \mu q \,. \tag{4.72}$$

Substituting equations (4.56) to (4.61), equations (4.67) to (4.72) and equation (4.28) into equation (4.55), leads to the following equation for the pressure gradient of the Darcy flow regime:

$$\frac{\Delta p}{d_{\parallel}} = \frac{12 d_{\perp_1} d_{\perp_2} \mu q}{d_{\parallel}\left(d_{\perp_1} - d_{s_{\perp_1}}\right)\left(d_{\perp_2} - d_{s_{\perp_2}}\right)} \left[\frac{d_{s_{\perp_1}} + d_{s_{\perp_2}}}{\left(d_{\parallel} - d_{s_{\parallel}}\right)^2} + \frac{d_{s_{\parallel}} + d_{s_{\perp_2}}}{\left(d_{\perp_1} - d_{s_{\perp_1}}\right)^2} + \frac{d_{s_{\parallel}} + d_{s_{\perp_1}}}{\left(d_{\perp_2} - d_{s_{\perp_2}}\right)^2} \right] . \tag{4.73}$$

The cross-sectional solid area that faces upstream, as determined from Figure 4.4, is given by

$$\begin{aligned} S_{\text{face}} &= d_{s_{\perp_1}}\left(d_{\perp_2} - d_{s_{\perp_2}}\right) + d_{s_{\perp_2}}\left(d_{\perp_1} - d_{s_{\perp_1}}\right) \\ &= d_{s_{\perp_1}} d_{\perp_2} + d_{s_{\perp_2}} d_{\perp_1} - 2 d_{s_{\perp_1}} d_{s_{\perp_2}} . \end{aligned} \tag{4.74}$$

The pressure gradient of the Forchheimer flow regime can thus be obtained using equations (1.19), (4.1), (4.62) and (4.74), which yields

$$-\nabla \langle p \rangle_f = \frac{d_{\perp_1} d_{\perp_2} \left(d_{s_{\perp_1}} d_{\perp_2} + d_{s_{\perp_2}} d_{\perp_1} - 2 d_{s_{\perp_1}} d_{s_{\perp_2}} \right)}{d_{\parallel} \epsilon \left(d_{\perp_1} - d_{s_{\perp_1}}\right)^2 \left(d_{\perp_2} - d_{s_{\perp_2}}\right)^2} \rho q^2 \underline{\hat{n}} . \tag{4.75}$$

The Ergun-type equation consequently leads to

$$\frac{\Delta p}{d_{\parallel}} = \frac{12 d_{\perp_1} d_{\perp_2}}{d_{\parallel}\left(d_{\perp_1} - d_{s_{\perp_1}}\right)\left(d_{\perp_2} - d_{s_{\perp_2}}\right)} \left[\frac{d_{s_{\perp_1}} + d_{s_{\perp_2}}}{\left(d_{\parallel} - d_{s_{\parallel}}\right)^2} + \frac{d_{s_{\parallel}} + d_{s_{\perp_2}}}{\left(d_{\perp_1} - d_{s_{\perp_1}}\right)^2} + \frac{d_{s_{\parallel}} + d_{s_{\perp_1}}}{\left(d_{\perp_2} - d_{s_{\perp_2}}\right)^2} \right] \mu q + \frac{d_{\perp_1} d_{\perp_2} \left(d_{s_{\perp_1}} d_{\perp_2} + d_{s_{\perp_2}} d_{\perp_1} - 2 d_{s_{\perp_1}} d_{s_{\perp_2}} \right)}{d_{\parallel} \epsilon \left(d_{\perp_1} - d_{s_{\perp_1}}\right)^2 \left(d_{\perp_2} - d_{s_{\perp_2}}\right)^2} \rho q^2 , \tag{4.76}$$

and comparing equation (4.76) with equation (1.1) yields the expressions of the Darcy and Forchheimer permeability coefficients of the three-strut CARUC model, i.e.

$$K = \frac{d_{\parallel}\left(d_{\perp_1} - d_{s_{\perp_1}}\right)\left(d_{\perp_2} - d_{s_{\perp_2}}\right)}{12 d_{\perp_1} d_{\perp_2}} \left[\frac{d_{s_{\perp_1}} + d_{s_{\perp_2}}}{\left(d_{\parallel} - d_{s_{\parallel}}\right)^2} + \frac{d_{s_{\parallel}} + d_{s_{\perp_2}}}{\left(d_{\perp_1} - d_{s_{\perp_1}}\right)^2} + \frac{d_{s_{\parallel}} + d_{s_{\perp_1}}}{\left(d_{\perp_2} - d_{s_{\perp_2}}\right)^2} \right]^{-1} . \tag{4.77}$$

and

$$K_F = \frac{d_{\parallel} \epsilon \left(d_{\perp_1} - d_{s_{\perp_1}}\right)^2 \left(d_{\perp_2} - d_{s_{\perp_2}}\right)^2}{d_{\perp_1} d_{\perp_2} \left(d_{s_{\perp_1}} d_{\perp_2} + d_{s_{\perp_2}} d_{\perp_1} - 2 d_{s_{\perp_1}} d_{s_{\perp_2}} \right)} . \tag{4.78}$$

The specific surface area of the three-strut CARUC model is determined next.

4.2.3 Specific surface area: Geometric approach

The total surface area of the three-strut CARUC model can be determined from Figure 4.4 and results in

$$S_{fs} = 2\left[\left(d_{\parallel} - d_{s_{\parallel}}\right)\left(d_{s_{\perp_1}} + d_{s_{\perp_2}}\right) + \left(d_{\perp_1} - d_{s_{\perp_1}}\right)\left(d_{s_{\parallel}} + d_{s_{\perp_2}}\right) + \left(d_{\perp_2} - d_{s_{\perp_2}}\right)\left(d_{s_{\parallel}} + d_{s_{\perp_1}}\right)\right] . \tag{4.79}$$

Dividing equation (4.79) by the total volume (equation (4.1)) leads to the equation for the specific surface area, i.e.

$$S_v = \frac{2}{d_{\parallel}d_{\perp_1}d_{\perp_2}}\left[\left(d_{\parallel} - d_{s_{\parallel}}\right)\left(d_{s_{\perp_1}} + d_{s_{\perp_2}}\right) + \left(d_{\perp_1} - d_{s_{\perp_1}}\right)\left(d_{s_{\parallel}} + d_{s_{\perp_2}}\right) + \left(d_{\perp_2} - d_{s_{\perp_2}}\right)\left(d_{s_{\parallel}} + d_{s_{\perp_1}}\right)\right] . \tag{4.80}$$

Due to the dependence of the specific surface area on the geometry of the three-strut CARUC model, the porosity equation determined in Section 4.2.1 (i.e. equation (4.54)) can be used to relate the dimensions in equation (4.80).

4.2.4 Specific surface area: Combined approach

Acquiring the specific surface area using a combined approach for the three-strut CARUC model is done in a similar manner as in the cases for the two-strut CARUC models. The streamwise face diameter will once again be replaced by the Darcy permeability coefficient as an example of determining the specific surface area equations using the combined approach. Consequently, equation (4.80) is first rearranged to determine the following expression for the streamwise face diameter in terms of the specific surface area:

$$d_{\parallel} = \frac{2s - 2d_{s_{\parallel}}r}{d_{\perp_1}d_{\perp_2}S_v - 2r} , \tag{4.81}$$

where $s = \left(d_{\perp_1} - d_{s_{\perp_1}}\right)\left(d_{s_{\parallel}} + d_{s_{\perp_2}}\right) + \left(d_{\perp_2} - d_{s_{\perp_2}}\right)\left(d_{s_{\parallel}} + d_{s_{\perp_1}}\right)$ and $r = d_{s_{\perp_1}} + d_{s_{\perp_2}}$ in this case. Substituting equation (4.81) into equation (4.77) and rearranging once again leads to a third-degree polynomial in terms of S_v, as given by equation (4.49). The coefficients acquired for the three-strut CARUC model is, however, given by

$$\begin{aligned}
a' &= -d_{\perp_1}^3 d_{\perp_2}^3 K\left(r + d_{s_{\parallel}}^2 l\right)\\
b' &= 6d_{\perp_1}^3 d_{\perp_2}^3 Kr\left(r + d_{s_{\parallel}}^2 l\right) + 2d_{s_{\parallel}} d_{\perp_1}^2 d_{\perp_2}^2\left(s - d_{s_{\parallel}} r\right)\left(d_{s_{\parallel}} m + 2Kl\right)\\
c' &= -12d_{\perp_1}d_{\perp_2}Kr^2\left(r + d_{s_{\parallel}}^2 l\right) - 8d_{s_{\parallel}}d_{\perp_1}d_{\perp_2}r\left(s - d_{s_{\parallel}} r\right)\left(d_{s_{\parallel}} m + 2Kl\right)\\
&\quad - 4d_{\perp_1}d_{\perp_2}\left(s - d_{s_{\parallel}} r\right)^2\left(2d_{s_{\parallel}} m + Kl\right)\\
g' &= 8Kr^3\left(r + d_{s_{\parallel}}^2 l\right) + 8d_{s_{\parallel}} r^2\left(s - d_{s_{\parallel}} r\right)\left(d_{s_{\parallel}} m + 2Kl\right)\\
&\quad + 8r\left(s - d_{s_{\parallel}} r\right)^2\left(2d_{s_{\parallel}} m + Kl\right) + 8m\left(s - d_{s_{\parallel}} r\right)^3 ,
\end{aligned} \tag{4.82}$$

with $m = \frac{\left(d_{\perp_1} - d_{s_{\perp_1}}\right)\left(d_{\perp_2} - d_{s_{\perp_2}}\right)}{12 d_{\perp_1} d_{\perp_2}}$ and $l = \frac{d_{s_\parallel} + d_{s_{\perp_2}}}{\left(d_{\perp_1} - d_{s_{\perp_1}}\right)^2} + \frac{d_{s_\parallel} + d_{s_{\perp_1}}}{\left(d_{\perp_2} - d_{s_{\perp_2}}\right)^2}$.

The application of the CARUC models in different scenarios of deformation is explained in the following section.

4.3 Application of CARUC models

The conditions applicable to different scenarios of compression will be addressed in this section. Three different directions of compression is possible: the streamwise and the two transverse directions. Compression in either of the transverse directions of the two-strut CARUC model for through plane flow and three-strut CARUC model, however, yields identical results, i.e. the results for changes in $d_{\perp_1}$ yields the same results as the same changes in $d_{\perp_2}$, and are therefore treated as equivalent in these cases. For the two-strut CARUC model for in-plane flow, it is essential to differentiate between the two dimensions oriented perpendicular to the streamwise direction since compression in the '$\perp_1$'-direction results in the lengthwise compression of a strut, whereas compression in the '$\perp_2$'-direction does not cause such deformation. The compression factor, as defined in the introduction section of this chapter, and the manner in which it is utilized will be discussed first. Two types of models that represent fibrous porous media under compression will furthermore be considered in this section: the hard and soft models. The hard model refers to the CARUC model where the struts do not compress with compression of the porous medium. The soft model refers to the CARUC model where the struts compress with compression and represents softer fibres/foam struts that will deform under compression along with the medium, that is, the strut diameter decreases in the direction in which the compression takes place. Two scenarios of each model type will also be considered: one in which lateral expansion of the medium under compression is not incorporated, due to (for example) a confinement wall or container that prohibits the expansion, and therefore the dimensions orientated transverse to the direction of compression remain unchanged, and one in which lateral expansion is incorporated in which case the aforementioned solid dimensions are allowed to increase as the dimension in the direction of compression decreases. Finally, a special case in which the CARUC models represent a fibrous porous medium with a rectangular structure without compression is discussed, i.e. an uncompressed state of the CARUC model, and will furthermore be referred to as the rectangular CARUC model.

The three-strut CARUC model will be used as the general illustrative example in order to demonstrate the implementation of the different model scenarios (i.e. the conditions implemented for the different model scenarios on the three-strut CARUC model equations as provided in Section 4.2 can also be implemented on the two-strut CARUC model equations provided in Section 4.1 in a similar manner). The resulting permeability coefficients and specific surface area equations for each of the compression scenarios will be deduced by applying the conditions of each of the scenarios to the equations of the three-strut CARUC model provided in Section 4.2. An illustrative example of the two-strut CARUC model for through plane flow will, however, also be added in the description of one of the compression scenarios (i.e. the streamwise compression scenario) in order to show how this model is adjusted. This example will furthermore be used to demonstrate the validity of the equations obtained in Section 4.1 by determining the Darcy permeability and specific surface area equations from the scenario-specific model (i.e. the streamwise

compressed two-strut RUC model for through plane flow). The resulting expressions deduced directly from the scenario-specific model (i.e. the streamwise compressed two-strut RUC model for through plane flow) are then compared to the expressions obtained when implementing the conditions associated with the compression scenario (i.e. the conditions associated with streamwise compression), to the equations provided in Section 4.1. Due to the length of the equations obtained for solving the specific surface area using a combined approach, the implementation of conditions on these equations are only provided for one compression scenario, i.e. in the illustrative example of the streamwise compression of the two-strut CARUC model for through plane flow and the three-strut CARUC model. (For easy reference, a diagram (Figure 4.23) is provided at the end of the chapter to summarize the conditions associated with the different compression scenarios discussed in this section.)

4.3.1 Compression factor

The compression factor e_x is given by the following ratio (Van Heyningen [57]):

$$e_x = \frac{h}{h_o}\,, \tag{4.83}$$

where h_o and h are the uncompressed and post-compression thickness of the porous medium sample in question, respectively, and x represents the direction of compression, i.e. '$\parallel$', '$\perp_1$' or '$\perp_2$'. Consequently, the compression factors are given by

$$e_\parallel = \frac{d_\parallel}{d_{\parallel_o}}\,, \qquad e_{\perp_1} = \frac{d_{\perp_1}}{d_{\perp_{1_o}}} \qquad \text{and} \qquad e_{\perp_2} = \frac{d_{\perp_2}}{d_{\perp_{2_o}}}\,, \tag{4.84}$$

for streamwise and transverse compression in the first and second manner, respectively, where the subscript 'o' denotes the uncompressed state. If a fibrous medium undergoes compression in the streamwise direction, for example, then $d_\parallel < d_{\parallel_o}$ and consequently $e_\parallel < 1$. If no lateral expansion occurs in this example, $e_{\perp_1} = e_{\perp_2} = 1$ since the transverse face diameters remain unchanged. In this study, $e_x > 1$ will thus refer to the expansion of the medium in the direction that is specified by x.

In the case of soft fibrous media, the strut diameters also undergo compression with compression of the porous medium, whereas for the hard models the strut diameters do not undergo compression. For the soft model, a compression function that depends on the compression factor is assumed to define the relation between pre- and post-compressed strut diameters, such that

$$f_\parallel\left(e_\parallel\right) = \frac{d_{s_\parallel}}{d_{s_{\parallel_o}}}\,, \qquad f_{\perp_1}\left(e_{\perp_1}\right) = \frac{d_{s_{\perp_1}}}{d_{s_{\perp_{1_o}}}} \qquad \text{and} \qquad f_{\perp_2}\left(e_{\perp_2}\right) = \frac{d_{s_{\perp_2}}}{d_{s_{\perp_{2_o}}}}\,. \tag{4.85}$$

When the strut diameter remains hard with compression, the uncompressed and post-compressed strut dimension is the same with different states of compression and consequently $f_x(e_x) = 1$, i.e. $d_{s_\parallel} = d_{s_{\parallel_o}}$, $d_{s_{\perp_1}} = d_{s_{\perp_{1_o}}}$ and $d_{s_{\perp_2}} = d_{s_{\perp_{2_o}}}$.

A general relationship between the porosity and compression factor provided in the literature (Van Heyningen [57] and Dukhan [9]), is given by

$$\epsilon = 1 - \frac{1-\epsilon_o}{e_x}\,, \tag{4.86}$$

where ϵ_o denotes the porosity of the uncompressed state and ϵ denotes the porosity at any state of compression. Equation (4.86) is deduced by first equating the total volume of the uncompressed media (i.e. U_o) and the total volume of the compressed media (denoted by U) as $U_o = Ah_o$ and $U = Ah$, respectively, where A denotes the base area of the container enclosing the porous medium. Consequently,

$$U_s = U_o - U_{f_o} = U_o\,(1 - \epsilon_o) = Ah_o\,(1 - \epsilon_o)\ , \tag{4.87}$$

if it is assumed that the solid volumes of the uncompressed and compressed states are equal (i.e $U_s = U_{s_o}$). Utilizing equation (1.6), equation (4.87) and the expression for U, equation (4.86) can therefore be attained. Equation (4.86) is, however, determined based on the assumption that the medium under compression does not undergo any lateral expansion due to the assumption that A remains constant, and that changes in the strut with compression take place due to the assumption that U_s remains constant. Equation (4.86) is therefore not valid in conditions where non-negligible lateral expansion occurs. Consequently, equation (4.86) is applicable to the case in which a porous medium undergoes no lateral expansion. Furthermore, a constant U_s is another condition for the use of equation (4.86). This implies that e.g. the three-strut CARUC model undergoing compression in the streamwise direction and with constant $d_\perp$, due to no lateral expansion, adjustments to the strut volume are then required to preserve a constant solid volume. If the corresponding porosity and compression factor data are provided, an empirical relation between ϵ and e_x can be determined from equation (4.86), i.e.

$$\epsilon = 1 - \frac{C}{e_x}\,, \tag{4.88}$$

where C is determined by substituting all the corresponding porosity and compression factor data into equation (4.88) and taking the average. Equation (4.88) consequently does not require the porosity of the uncompressed state of the medium. Given the reliance of equation (4.88) on available experimental data, certain relaxations can be made regarding the conditions associated with equation (4.86), i.e. that it is only applicable to the compression scenario of a fibrous porous medium with constant solid volume and where no lateral expansion takes place. Equation (4.88) will be utilized later in this chapter in order to facilitate a comparative analysis between predictions obtained from equation (4.88) and those obtained directly using the provided porosity and compression factor data, in scenarios that do not strictly adhere to the conditions of no lateral expansion and constant U_s. The use of equation (4.88) is furthermore demonstrated in Woudberg et al. [77] (and in the chapter to follow) where it is applied to the experimental data obtained from Le Coq [13].

As already mentioned, in the case where the compression of soft fibrous media is considered, a function $f_x(e_x)$ is required that defines the relationship between the uncompressed and compressed strut diameter, i.e. as given in equation (4.85). To the author's knowledge, there is a lack of existing literature exploring the characteristics of this function. More details concerning the relationship between the strut deformation and the compressive strain are, however, beyond the scope of this study. Considering that the strut diameter is likely to experience a different level of compression compared to the entire porous medium (i.e. it cannot be adequately described by $f_x(e_x) = e_x$), this study assumes the necessity of a function. It is expected that the strut diameter will compress less than the entire medium and therefore it is assumed, in this study for illustration

purposes and as an example, that the strut diameter of the soft porous medium compresses at half the rate of the face diameter, i.e. $f_x(e_x) = (1 + e_x)/2$. For example, if $e_x = 0.8$ then $f_x(e_x) = 0.9$, implying that with compression a face diameter loses 20% of the uncompressed length, whereas the strut diameter only loses 10% of the uncompressed length.

In order to determine the values of the dimensions that are necessary to calculate the required predictions for the permeability coefficients and specific surface area provided by the CARUC models, information regarding the direction of compression and compression factor are essential.

The application of compression of the CARUC models with the assumption that the model remains hard under compression is discussed next.

4.3.2 Hard model

As previously mentioned, the hard models refer to the models where the strut diameters do not change with the compression of the porous medium. $f_x(e_x) < 1$ is therefore not valid in this scenario. This assumption is implemented in cases where the fibre-type or foamlike medium consists of material that does not undergo changes (in terms of fibre or strut diameter changes) and are therefore considered "hard" materials, e.g. materials such as glass, metal and ceramics. In this study it will be assumed, in the case where the CARUC models represent "hard" materials, that the strut diameter is the same in all directions of compression, i.e. $d_{s_\parallel} = d_{s_{\perp_1}} = d_{s_{\perp_2}} = d_s$. Where possible, it is furthermore assumed that $d_s = d_{s_o}$. In some scenarios and when utilizing some of the CARUC models, however, in order to accommodate the conditions of a constant solid volume, d_s is allowed to increase to meet this condition. Further detailed explanation of this exception will be provided later in this section. For illustration purposes, the two-strut CARUC model for through plane flow and the three-strut CARUC model with streamwise compression will be used as examples. Consequently, for this example, $e_{\perp_1} = e_{\perp_2} = e_\perp$ and the face diameter in the streamwise direction can be determined from the left-hand side expression in equation (4.84), i.e.

$$d_\parallel = e_\parallel d_{\parallel_o}\,. \tag{4.89}$$

It is furthermore assumed that $d_{\perp_1} = d_{\perp_2} = d_\perp$. Firstly, the conditions applied to the three-strut CARUC model with streamwise compression, will be shown for the scenarios of lateral expansion and no lateral expansion, respectively. The conditions utilized in the scenarios can similarly be applied to the two-strut CARUC model for in-plane flow. Next, the method in which the expressions for the permeability coefficients and specific surface area can be attained for the hard two-strut CARUC model for through plane flow with streamwise compression will be shown and compared to the relevant conditions applied to the equations presented in Section 2.1. The hard two-strut CARUC model for through plane flow with streamwise compression is furthermore an exception: it is unable to expand laterally due to its geometrical structure. The condition of including or excluding lateral expansion therefore has no effect on this model.

Lateral expansion

In the scenario where lateral expansion is allowed, the dimensions transverse to the direction of compression are allowed to expand/increase as the dimension in the direction of compression changes/decreases. Consequently, $e_\perp > 1$, i.e. $d_\perp > d_{\perp_o}$, where the direction of compression is in the streamwise direction, for the compressed state. In Figure 4.6, the geometrical changes of the hard three-strut CARUC model with streamwise compression where lateral expansion is allowed, are shown, for which the uncompressed model (where $e_\parallel = 1$) is shown on the left-hand side and the compressed model (where $e_\parallel < 1$) is shown on the right-hand side.

It can be noted from Figure 4.6 that $d_s = d_{s_o}$ (since the lateral expansion makes provision for the redistribution of solid volume) and that $d_\parallel$ decreases with streamwise compression. It can furthermore be seen that $d_\perp$ changes with compression by expanding. Implementing the dimension-based conditions associated with this scenario into equation (4.54), leads to the following unique expression for the porosity:

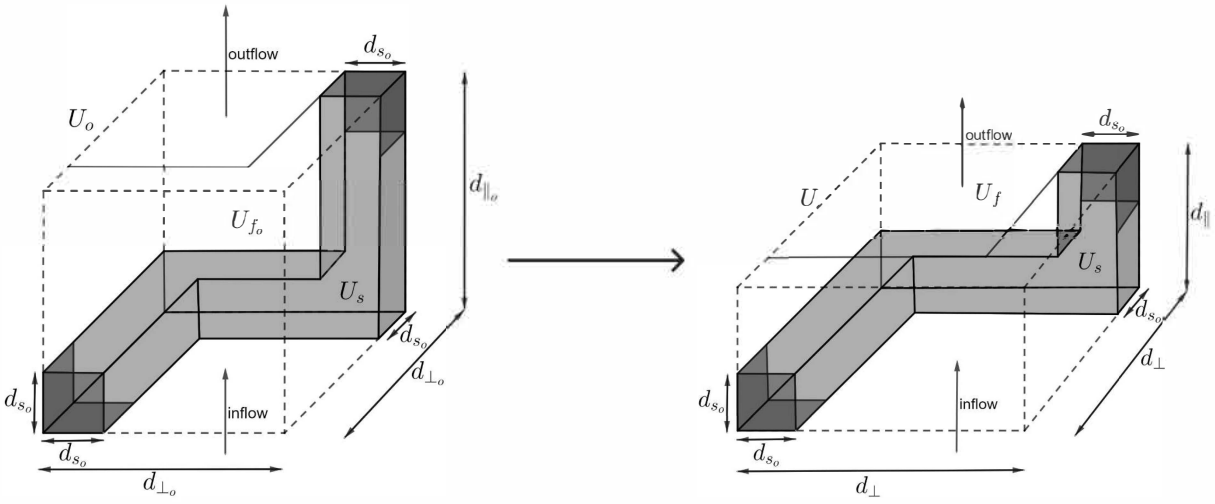

FIGURE 4.6: *Geometrical changes of hard three-strut CARUC model with streamwise compression and lateral expansion*

$$\epsilon = 1 - \frac{2d_s^2}{d_\parallel d_\perp} - \frac{d_s^2}{d_\perp^2} + \frac{2d_s^3}{d_\parallel d_\perp^2}\,. \tag{4.90}$$

Equation (4.90) can then be rearranged to find an expression for the face diameter in the transverse direction, i.e.

$$d_\perp = \frac{d_s\left[d_s + \sqrt{d_s^2 + d_\parallel\left(d_\parallel - 2d_s\right)(1-\epsilon)}\right]}{d_\parallel(1-\epsilon)}\,. \tag{4.91}$$

$d_\perp$ therefore depends on $d_\parallel$ and ϵ for the different states of compression. (It is noted that $d_s = d_{s_o}$ is implemented in both equations (4.90) and (4.91) in this compression scenario.) The expressions for the permeability coefficients and specific surface area can be determined by implementing the same dimension-based conditions as used for equation (4.90) into equations (4.77), (4.78) and (4.80). This results in the following equations for

the hard three-strut CARUC model with streamwise compression:

$$K = \frac{d_{\parallel}\left(d_{\perp} - d_s\right)^2}{24 d_s d_{\perp}^2}\left[\frac{2}{\left(d_{\perp} - d_s\right)^2} + \frac{1}{\left(d_{\parallel} - d_s\right)^2}\right]^{-1}, \tag{4.92}$$

$$K_F = \frac{d_{\parallel}\epsilon}{2 d_s d_{\perp}^2}, \tag{4.93}$$

and

$$S_v = \frac{4 d_s}{d_{\parallel} d_{\perp}^2}\left[\left(d_{\parallel} - d_s\right) + 2\left(d_{\perp} - d_s\right)\right], \tag{4.94}$$

where $d_{\parallel}$ can be acquired from equation (4.89), $d_{\perp}$ from equation (4.91) and $d_s = d_{s_o}$. Equations (4.90) to (4.92) are given by Woudberg et al. [83]. In order to obtain the specific surface area using a combined approach the conditions associated with this compression scenario is applied to equation (4.82). This yields the third-degree polynomial in terms of S_v, given by equation (4.49), with coefficients

$$\begin{aligned}
a' &= 48 d_s^3 d_{\perp}^8 K + 24 d_s d_{\perp}^8 K m \\
b' &= -768 d_s^3 d_{\perp}^7 K + 576 d_s^4 d_{\perp}^6 K - 8 d_s^3 d_{\perp}^5 m^2 + 12 d_s^4 d_{\perp}^4 m^2 - 288 d_s^2 d_{\perp}^6 K m \\
c' &= 3072 d_s^3 d_{\perp}^6 K - 3072 d_s^4 d_{\perp}^5 K + 128 d_s^3 d_{\perp}^4 m^2 - 320 d_s^4 d_{\perp}^3 m^2 + 192 d_s^5 d_{\perp}^2 m^2 + 1152 d_s^3 d_{\perp}^4 K m \\
g' &= -512 d_s^3 d_{\perp}^3 m^2 + 1792 d_s^4 d_{\perp}^2 m^2 - 2048 d_s^5 d_{\perp} m^2 + 768 d_s^6 m^2 - 12288 d_s^4 d_{\perp}^4 K \\
&\quad + 24576 d_s^5 d_{\perp}^3 K - 12288 d_s^6 d_{\perp}^2 K - 1536 d_s^4 d_{\perp}^2 K m,
\end{aligned} \tag{4.95}$$

where m is equal to $\left(d_{\perp} - d_s\right)^2$. The derivation of the third-degree polynomial in terms of S_v with coefficients, as given in equation (4.95), is published in Woudberg et al. [77]. In order to determine the Darcy permeability, Forchheimer permeability and specific surface area using a geometric and combined approach from equations (4.92) to (4.95), respectively, information regarding $e_{\parallel}$, ϵ, $d_{\parallel_o}$ and d_{s_o} are needed from experimental measurements.

No lateral expansion

In the scenario where no lateral expansion is allowed, the dimensions transverse to the direction of compression remain equal to the uncompressed dimensions. In the case where streamwise compression is considered (as in the illustrative example considered in this section), it therefore implies that $d_{\perp} = d_{\perp_o}$. A visual representation of the three-strut CARUC model compressed in the streamwise direction where no lateral expansion is allowed, is shown in Figure 4.7. The uncompressed model is once again represented by the three-strut CARUC model on the left-hand side of Figure 4.7 and the compressed model is shown on the right-hand side.

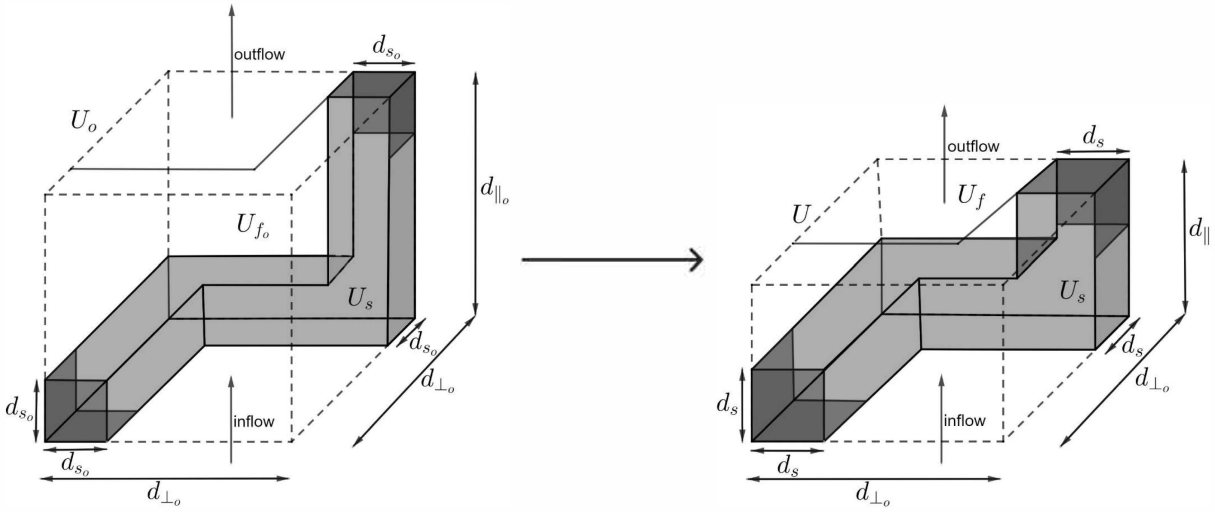

FIGURE 4.7: *Geometrical changes of hard three-strut CARUC model with streamwise compression and no lateral expansion*

As can be seen in Figure 4.7, $d_\perp$ remains the same, for both the uncompressed and compressed states, where-as the streamwise face diameter $d_\parallel$ changes due to the streamwise compression. Applying the relevant conditions for streamwise compression to the three-strut CARUC model once again leads to equations (4.90) and (4.91). In this compression scenario where no lateral expansion is allowed, however, $d_\perp = d_{\perp_o}$ needs to be implemented and consequently, only the values for the dimensions in the uncompressed state are utilized in equation (4.91) to determine the transverse face diameter. To preserve the validity of equation (4.90) and the assumption of constant $d_\perp$ (i.e. the validity of equation (4.91) with conditions associated with the current compression scenario), a constant solid volume needs to be implemented for different states of compression and therefore a redistribution of solid volume is required. In order to accommodate this condition, the strut diameter is allowed to increase with compression. One possible approach is to consider that the strut diameter increases due to struts or fibers of actual media breaking or bending, thereby maintaining hardness while accommodating the solid distribution associated with confined compression. In this scenario, $d_\perp$ can be determined, as already explained (where $d_s = d_{s_o}$), and then d_s can be determined from a new arrangement of equation (4.90), i.e.

$$2d_s^3 - \left(2d_{\perp_o} + d_\parallel\right) d_s^2 + (1-\epsilon)\, d_\parallel d_{\perp_o}^2 = 0\,. \tag{4.96}$$

The permeability coefficients and specific surface area can once again be determined from equations (4.92) to (4.95), respectively, for which $d_\parallel$ can be determined from equation (4.89). Furthermore, $d_\perp = d_{\perp_o}$ and d_s is determined from equation (4.96). Information from experimental measurements regarding $e_\parallel$, ϵ, $d_{\parallel_o}$ and d_{s_o} are also required in this scenario where lateral expansion is not allowed.

Two-strut CARUC model for through plane flow

The derivation presented in this section is published in Woudberg et al. [77] and is therefore also presented here. It will additionally be explained how the same predictive equations result from Section 4.1 by incorporating the same conditions. The model equations deduced from the compression of the two-strut CARUC model for through plane

flow are also newly proposed and is an extension of the work done by Van Heyningen [57]. A novel contribution is the incorporation of the combined approach for determining the specific surface area by replacing $d_{\parallel}$ with K (i.e. the Darcy permeability coefficient). In this section, it can be assumed that $d_s = d_{s_o}$ and will therefore be employed in this compression scenario.

In Figure 4.8, a visual representation of the compression of the hard two-strut CARUC model for through plane flow is shown, where the uncompressed model is on the left-hand side and the compressed model is on the right-hand side. It is noted that for this particular scenario, even if lateral expansion is allowed, the solid volume remains constant with compression and consequently, no lateral expansion does in fact, occur. The model equations obtained for the two-strut CARUC model for through plane flow in this scenario is therefore equal to the model equations obtained for the scenario where no lateral expansion is allowed.

In order to demonstrate the validity of the equations obtained in Section 4.1, the conditions for the hard model will be implemented in the equations involved in the modelling steps that lead to the expressions for the Darcy permeability coefficient and specific surface area of this scenario. It will be shown that the final expressions resemble those for the Darcy permeability and specific surface area if the conditions were implemented in

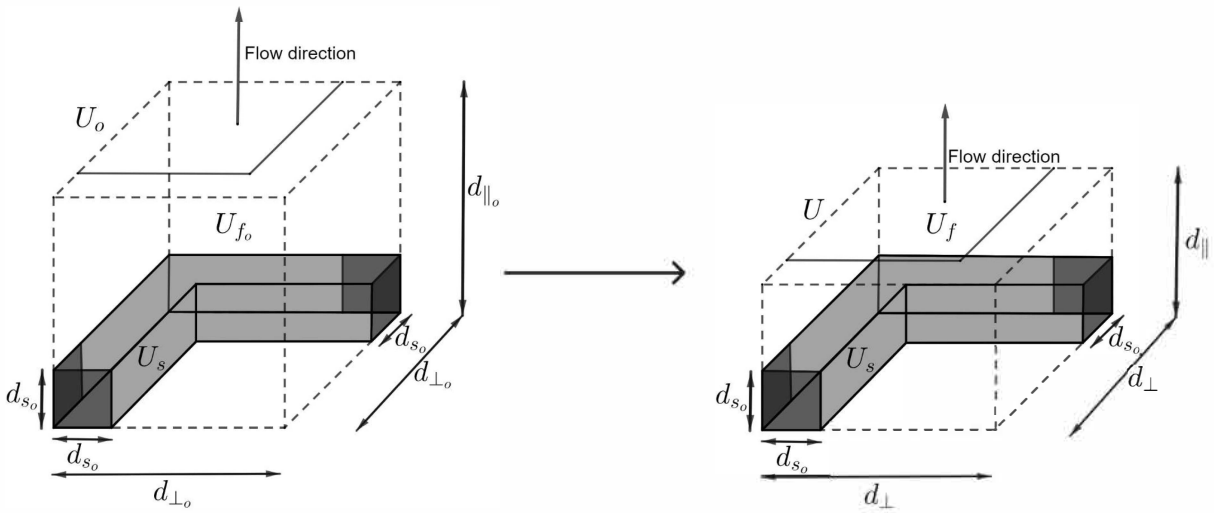

FIGURE 4.8: *Geometrical changes of hard two-strut CARUC model for through plane flow with streamwise compression*

these equations directly, as mentioned previously. (The aforementioned conditions refer to the equality of the strut diameters, i.e. $d_{s_\parallel} = d_{s_{\perp_1}} = d_{s_{\perp_2}} = d_s = d_{s_o}$, and the equality of the face diameters perpendicular to the streamwise flow direction, i.e. $d_{\perp_1} = d_{\perp_2} = d_\perp$.) The modelling process of the hard two-strut CARUC model for through plane flow presented as follows is published in Woudberg et al. [77].

From Figure 4.8 the following expression for the solid volume can be deduced:

$$U_s = 2d_s^2 d_\perp - d_s^3\,, \tag{4.97}$$

and consequently, the equation for the porosity is given by

$$\epsilon = \frac{d_\parallel d_\perp^2 - 2d_s^2 d_\perp + d_s^3}{d_\parallel d_\perp^2}\,, \tag{4.98}$$

(since it is evident that $U_o = d_{\parallel} d_{\perp}^2$). The transverse RUC dimension $d_{\perp}$ can be determined from equation (4.98), yielding

$$d_{\perp} = \frac{d_s \left(d_s + \sqrt{d_s^2 + d_s d_{\parallel} \left(\epsilon - 1 \right)} \right)}{d_{\parallel} \left(1 - \epsilon \right)} , \tag{4.99}$$

where $d_{\parallel}$ is given by equation (4.89). The pressure drop over a porous medium can be determined from equation (1.10) where $\xi = 1$, yielding

$$\Delta p = \frac{S_{\parallel} \tau_{w_{\parallel}} + S_{\perp} \tau_{w_{\perp}}}{A_{p_{\parallel}}} . \tag{4.100}$$

The streamwise and transverse solid surfaces can then be quantified as follows:

$$S_{\parallel} = 4 d_s \left(d_{\perp} - d_s \right) \qquad \text{and} \qquad S_{\perp} = 4 d_s \left(d_{\perp} - d_s \right) + 2 d_s^2 . \tag{4.101}$$

The expressions for the magnitude of the average shear stresses on the streamwise and transverse surfaces are to be determined next. The magnitude of the streamwise average pore velocity can be determined using equation (1.13), where $A_o = d_{\perp}^2$ and

$$A_{p_{\parallel}} = \left(d_{\perp} - d_s \right)^2 , \tag{4.102}$$

as determined from Figure 4.8, consequently yielding

$$w_{\parallel} = \frac{d_{\perp}^2}{\left(d_{\perp} - d_s \right)^2} q . \tag{4.103}$$

Using equation (1.14) where $A_{p_{\perp}} = d_{\perp} \left(d_{\parallel} - d_s \right)$, the following expression for $w_{\perp}$ can therefore be deduced:

$$w_{\perp} = \frac{d_{\perp}}{d_{\parallel} - d_s} q . \tag{4.104}$$

The magnitude of the streamwise and transverse average wall shear stresses can then be quantified as follows:

$$\tau_{w_{\parallel}} = \frac{6 \mu w_{\parallel}}{\left(d_{\perp} - d_s \right)} = \frac{6 d_{\perp}^2}{\left(d_{\perp} - d_s \right)^3} \mu q , \tag{4.105}$$

and

$$\tau_{w_{\perp}} = \frac{6 \mu w_{\perp}}{\left(d_{\parallel} - d_s \right)} = \frac{6 \mu \beta w_{\parallel}}{\left(d_{\parallel} - d_s \right)} = \frac{6 d_{\perp}}{\left(d_{\parallel} - d_s \right)^2} \mu q , \tag{4.106}$$

where it is deduced from Figure 4.8 that $B = d_{\perp} - d_s$ in equation (4.105) and $B = d_{\parallel} - d_s$ in equation (4.106) (B refers to the distance between parallel plates as defined in equation (1.12)). Substituting equations (4.101), (4.102), (4.105) and (4.106) into equation (4.100) leads, after simplification, to the following expression for the pressure gradient:

$$\frac{\Delta p}{d_{\parallel}} = \frac{24 d_s d_{\perp}^2 \mu q}{d_{\parallel} \left(d_{\perp} - d_s \right)^2} \left[\frac{1}{\left(d_{\perp} - d_s \right)^2} + \frac{2 d_{\perp} - d_s}{2 d_{\perp} \left(d_{\parallel} - d_s \right)^2} \right] , \tag{4.107}$$

Consequently, the Darcy permeability is given by

$$K = \frac{d_{\parallel} \left(d_{\perp} - d_s \right)^2}{24 d_s d_{\perp}^2} \left[\frac{1}{\left(d_{\perp} - d_s \right)^2} + \frac{2 d_{\perp} - d_s}{2 d_{\perp} \left(d_{\parallel} - d_s \right)^2} \right]^{-1} . \tag{4.108}$$

The permeability is presented by Van Heyningen [57] as

$$K = \frac{d_{\parallel}\left(d_{\perp}-d_s\right)^4\left(d_{\parallel}-d_s\right)^2}{24d_sd_{\perp}^2\left(d_{\parallel}-d_s\right)^2+12d_sd_{\perp}\left(2d_{\perp}-d_s\right)\left(d_{\perp}-d_s\right)^2}\,. \tag{4.109}$$

which is equivalent to equation (4.108). If the conditions for a hard model is implemented in equation (4.42), i.e. if $d_{\perp_1}=d_{\perp_2}=d_{\perp}$ and $d_{s_{\parallel}}=d_{s_{\perp_1}}=d_{s_{\perp_2}}=d_s$ is implemented in the expression for the Darcy permeability coefficient of the two-strut CARUC model for through plane flow, it leads to

$$K = \frac{d_{\parallel}\left(d_{\perp}-d_s\right)^2}{12}\left[\frac{2d_sd_{\perp}^2}{\left(d_{\perp}-d_s\right)^2}+\frac{2d_sd_{\perp}\left(d_{\perp}-\frac{1}{2}d_s\right)}{\left(d_{\parallel}-d_s\right)^2}\right]^{-1}\,, \tag{4.110}$$

which can be simplified further to obtain equation (4.108). The final expression for the Darcy permeability coefficient is therefore equivalent to the equations of this chapter where the required conditions are implemented. According to the geometric approach the specific surface area S_v is calculated as the ratio of the total outer solid surface area to the total volume of the RUC, which can be determined by making use of Figure 4.8, yielding

$$S_v = \frac{8d_s\left(d_{\perp}-d_s\right)+2d_s^2}{d_{\parallel}d_{\perp}^2} = \frac{2d_s\left(4d_{\perp}-3d_s\right)}{d_{\parallel}d_{\perp}^2}\,. \tag{4.111}$$

Implementing the required conditions of the hard CARUC model, as previously mentioned, in equation (4.47) leads to

$$S_v = \frac{2\left[d_s\left(2d_{\perp}-2d_s\right)+2d_sd_{\perp}-d_s^2\right]}{d_{\parallel}d_{\perp}^2}\,, \tag{4.112}$$

and is furthermore equivalent to equation (4.111). In this section a manner in which the combined approach is utilized in order to determine the specific surface area is furthermore included. This is done by replacing $d_{\parallel}$ with the Darcy permeability coefficient. In this approach the equation for the permeability is first written as a polynomial in terms of $d_{\parallel}$ by rearranging equation (4.108), resulting in:

$$\begin{aligned}-2d_{\perp}m^2d_{\parallel}^3+\left(48d_sd_{\perp}^3K+4d_sd_{\perp}m^2\right)d_{\parallel}^2+\left(-96d_s^2d_{\perp}^3K-2d_s^2d_{\perp}m^2\right)d_{\parallel}+48d_s^3d_{\perp}^3K\\+24d_sd_{\perp}^2Km\left(2d_{\perp}-d_s\right)=0\,,\end{aligned} \tag{4.113}$$

with $m=\left(d_{\perp}-d_s\right)^2$. The streamwise face diameter of the two-strut RUC model for through plane flow in this scenario can be expressed in terms of the specific surface area by making use of equation (4.111). This leads to

$$d_{\parallel} = \frac{8d_s\left(d_{\perp}-d_s\right)+2d_s^2}{d_{\perp}^2S_v} = \frac{2d_s\left(4d_{\perp}-3d_s\right)}{d_{\perp}^2S_v}\,. \tag{4.114}$$

Replacing $d_{\parallel}$ in equation (4.113) with equation (4.114), multiplying each term with $S_v^3d_{\perp}^6$ and rearranging terms, yields the following third-degree polynomial in terms of S_v:

$$a'S_v^3+b'S_v^2+c'S_v+g'=0\,,$$

with

$$\begin{aligned} a' &= 48d_s^3 d_\perp^9 K + 24 d_s d_\perp^8 K m \left(2d_\perp - d_s\right) \\ b' &= -192 d_s^3 d_\perp^7 K \left(4d_\perp - 3d_s\right) - 4 d_s^3 d_\perp^5 m^2 \left(4d_\perp - 3d_s\right) \\ c' &= 192 d_s^3 d_\perp^5 K \left(4d_\perp - 3d_s\right)^2 + 16 d_s^3 d_\perp^3 m^2 \left(4d_\perp - 3d_s\right)^2 \\ g' &= -16 d_s^3 d_\perp m^2 \left(4d_\perp - 3d_s\right)^3 . \end{aligned} \tag{4.115}$$

The predicted values for the specific surface area are then obtained for the hard two-strut CARUC model for through plane flow subject to streamwise compression by solving equation (4.115) for experimentally measured values of the permeability. Applying the conditions as already specified in this section to equation (4.52), the same coefficients are acquired as given in equation (4.115). The application of conditions associated with different compression scenarios to the adjusted models provided in Sections 4.1 and 4.2 will similarly lead to equivalent expressions should it be derived for each compressed model case. The model equations are therefore valid, provided that the correct conditions are applied to the equations provided in Sections 4.1 and 4.2.

4.3.3 Soft model

In the case where the fibrous porous medium is considered as soft, the strut diameter changes (by decreasing) with compression of the porous medium. Hence, $f_x(e_x) < 1$, where x represents the direction of compression, and f_x becomes dependant on the compression factor e_x. The expressions presented by equation (4.85) are therefore utilized in this section. Soft materials are assumed to include fibres made of polyester, wool or silk and foams made of polyurethane. In such cases, the average strut diameter is likely to deform as the medium is compressed. In the work of Woudberg [88], the three-strut RUC model was adjusted to represent soft fibrous porous media. In the aforementioned study, the average strut diameter was however considered to be constant and therefore resembled the hard three-strut CARUC model where lateral expansion is allowed in this study. The adjustment of the average strut diameter for soft media was introduced by Van Heiningen [57], who assigned specific ratios to the strut diameter values in the directions parallel and perpendicular to the directions of compression of the two-strut RUC model for through plane flow. In this study, a similar approach is followed to incorporate changes in the strut diameter, where soft fibrous porous media are under consideration. The ratio assigned is described by $f_x(e_x)$. A scenario where no lateral expansion is allowed and another in which lateral expansion is allowed, respectively, will be addressed once again. For illustration purposes, the example of the three-strut CARUC model with transverse compression will be used. Therefore,

$$d_{\perp_1} = e_{\perp_1} d_{\perp_{1_o}} = d_\perp = e_\perp d_{\perp_o} , \tag{4.116}$$

and $d_\parallel = d_{\perp_2} = d$. Furthermore, $d_{s_{\perp_1}} = f_{\perp_1}\left(e_{\perp_1}\right) d_{s_{\perp_1}} = d_{s_\perp} = f_\perp\left(e_\perp\right) d_{s_\perp}$ and $d_{s_\parallel} = d_{s_{\perp_2}} = d_s$. Note that for transverse compression the dimensions orientated parallel to the direction of compression are indicated by the subscript '$\perp$' and the dimensions orientated transverse to the direction of compression have no subscript. A soft model furthermore requires that the strut diameter orientated in the direction of compression is described by the ratio given by $f_x(e_x)$. As previously stated, $f_x(e_x) = (1 + e_x)/2$ is utilized in this study in order to describe the change of the strut diameter in the direction of compression

(i.e. $f_\perp(e_\perp) = (1 + e_\perp)/2$ in this case). Consequently, for the current example

$$d_{s_\perp} = \frac{1 + e_\perp}{2} d_{s_o} . \tag{4.117}$$

It is also assumed in this study that $d_{s_{\parallel_o}} = d_{s_{\perp_{1_o}}} = d_{s_{\perp_{2_o}}} = d_{s_o}$, i.e. in the uncompressed state the strut diameters orientated in all three principle directions are equal. In the case where no lateral expansion is allowed, i.e. $d = d_o$, it is assumed that d_s is allowed to expand within the confined porous medium, i.e. $f_\parallel(e_\parallel) = f_{\perp_2}(e_{\perp_2}) = f(e) > 1$. In the case where lateral expansion is allowed it is, however, assumed that the medium expands along the length of the face diameters only and therefore $d_s = d_{s_o}$ and $f(e) = 1$.

Lateral expansion

In this scenario, the face diameters transverse to the direction of compression are allowed to expand (while the strut diameters transverse to the direction of compression are kept constant). The soft three-strut CARUC model compressed in the transverse direction that allows for lateral expansion is shown in Figure 4.9. The left-hand side shows the uncompressed model (where $e_\perp = 1$) and the right-hand side the compressed model (where $e_\perp < 1$).

In the case where transverse compression is considered, for the soft three-strut CARUC model, equation (4.54) can be rewritten as follows:

$$\epsilon = 1 - \frac{2 d_s d_{s_\perp}}{d d_\perp} - \frac{d_s^2}{d^2} + \frac{2 d_s^2 d_{s_\perp}}{d^2 d_\perp} . \tag{4.118}$$

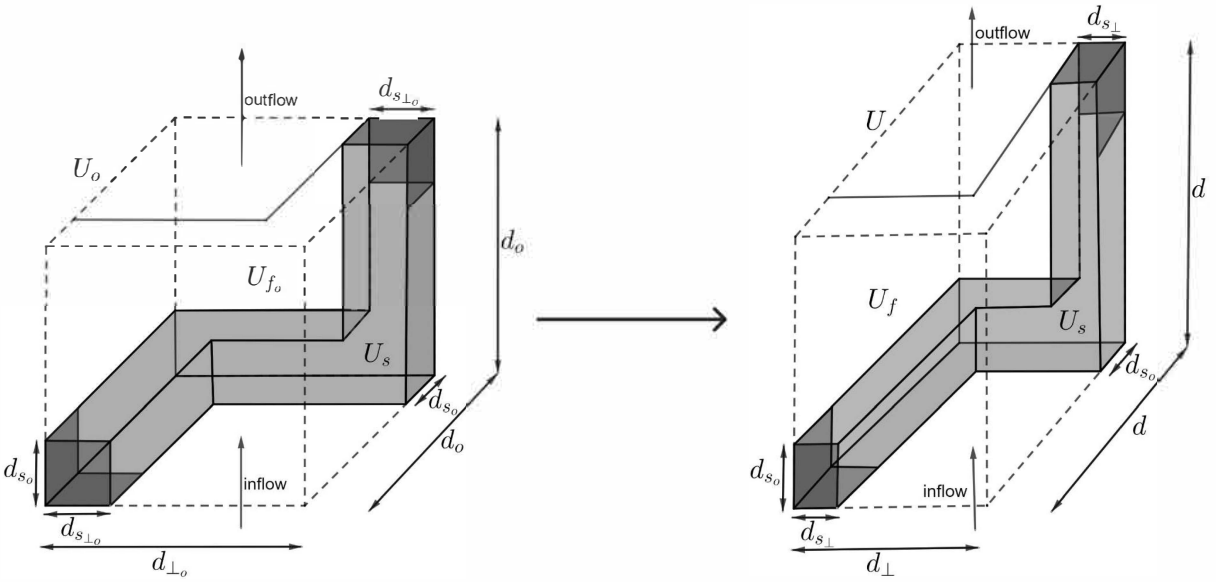

FIGURE 4.9: *Geometrical changes of soft three-strut CARUC model with transverse compression and lateral expansion*

The expression for d deduced from equation (4.118) yields

$$d = \frac{d_s \left[d_{s_\perp} + \sqrt{d_{s_\perp}^2 + d_\perp \left(d_\perp - 2 d_{s_\perp} \right) (1 - \epsilon)} \right]}{d_\perp (1 - \epsilon)} , \tag{4.119}$$

where $d_s = d_{s_o}$ and $d_\perp$ and $d_{s_\perp}$ can be determined from equations (4.116) and (4.117), respectively. Applying the conditions associated for the current scenario (i.e. $d_{\perp_1} = d_\perp$, $d_\parallel = d_{\perp_2} = d$, $d_{s_{\perp_1}} = d_{s_\perp}$ and $d_{s_\parallel} = d_{s_{\perp_2}} = d_s = d_{s_o}$), to equations (4.77), (4.78) and (4.80), the expressions for the Darcy permeability, Forchheimer permeability and specific surface area for the soft three-strut CARUC model under transverse compression can be determined. This results in

$$K = \frac{(d - d_s)(d_\perp - d_{s_\perp})}{12 d_\perp} \left[\frac{2(d_{s_\perp} + d_s)}{(d - d_s)^2} + \frac{2 d_s}{(d_\perp - d_{s_\perp})^2} \right]^{-1}, \tag{4.120}$$

$$K_F = \frac{\epsilon (d_\perp - d_{s_\perp})^2 (d - d_s)^2}{d_\perp (d_{s_\perp} d + d_s d_\perp - 2 d_s d_{s_\perp})}, \tag{4.121}$$

and

$$S_v = \frac{4}{d^2 d_\perp} \left[(d - d_s)(d_{s_\perp} + d_s) + d_s (d_\perp - d_{s_\perp}) \right], \tag{4.122}$$

respectively. The calculations involved in this analysis necessitate the availability of data for $e_\perp$, ϵ, $d_{\perp_o}$ and d_{s_o}.

No lateral expansion

As in the case where hard models were considered, the scenario where no lateral expansion is allowed implies that the face diameters orientated perpendicular to the direction of compression remains constant at different stages of compression. In the example where the three-strut CARUC model is compressed in the direction transverse to the direction of flow, d (denoting the values for both $d_\parallel$ and $d_{\perp_2}$) is equal to d_o. In Figure 4.10 a visual representation of the soft three-strut CARUC model under compression in the direction transverse to the streamwise direction is shown.

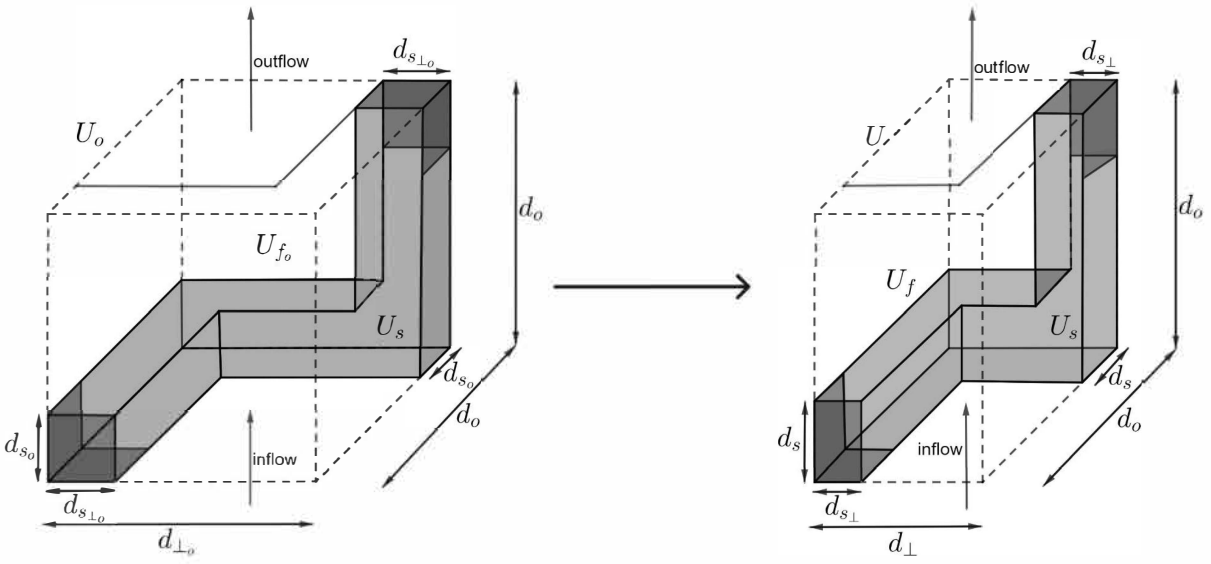

FIGURE 4.10: *Geometrical changes of soft three-strut CARUC model with transverse compression and no lateral expansion*

It can be noted in Figure 4.10 that the strut diameter in the direction of compression, $d_{s_\perp}$, decreases with compression and the other strut diameters transverse to this direction, d_s,

increases with compression, whilst d, however, remains constant. Equation (4.118) also applies to this compression scenario, where $d = d_o$ in this case. Equation (4.119) can also be utilized in order to acquire d using pore-scale dimensions of the uncompressed state, i.e. where $d_{s_\perp} = d_s = d_{s_o}$, $d_\perp = d_{\perp_o}$ and $\epsilon = \epsilon_o$. By once again rearranging equation (4.118), the following expression for the strut diameters orientated in the directions transverse to the direction of compression can be determined:

$$d_s = \frac{d\left[d_{s_\perp} - \sqrt{d_{s_\perp}^2 + d_\perp\left(d_\perp - 2d_{s_\perp}\right)(1-\epsilon)}\right]}{2d_{s_\perp} - d}\,, \tag{4.123}$$

where $d = d_o$. Having acquired the aforementioned pore-scale parameters, equations (4.120) to (4.122) can consequently be utilized to determine the Darcy permeability, Forchheimer permeability and specific surface area, respectively. In order to determine the permeability coefficients and specific surface area, $d_\perp$ is therefore acquired using equation (4.116), $d_{s_\perp}$ using equation (4.117), d using equation (4.119) in the uncompressed state and d_s using equation (4.123). Experimental data are once again required in order to determine the permeability coefficients and specific surface area of the soft three-strut CARUC model compressed in the direction transverse to the streamwise flow direction which includes $e_\perp$, ϵ, $d_{\perp_o}$ and d_{s_o}.

In both scenarios of soft models where no expansion is allowed and where expansion is allowed, additional information regarding the nature of $f_x(e_x)$ will be beneficial. This topic could consequently be considered for future studies.

In the case where values of the required dimensions in the uncompressed model states are not available, for any of the compression scenarios, an assumption can be made that the uncompressed model resembles the isotropic or cubic models presented in Chapter 2. For example if $d_{\parallel_o}$ is not available in the case where streamwise compression of the three-strut CARUC model is considered, $d_{\parallel_o}$ is then assumed to be equal to $d_{\perp_o}$ and can furthermore be determined using the porosity and strut diameter of the uncompressed model by utilizing equation (2.73), i.e.

$$d_o = \frac{2}{\psi_o - 1}\, d_{s_o}\,, \tag{4.124}$$

where $d_o = d_{\parallel_o} = d_{\perp_o}$ with

$$\psi_o = 2 + 2\cos\left[\frac{4\pi}{3} + \frac{1}{3}\cos^{-1}\left(2\epsilon_o - 1\right)\right]\,, \tag{4.125}$$

which is similar to equation (2.72).

4.3.4 Rectangular geometry

The conditions required in order to evaluate the CARUC models that take a rectangular form to account for anisotropy are similar to those applied to the models with compression, the exception being that a compression factor is no longer required. Other information is, however, needed in order to determine the values of the dimensions that are essential for predicting the permeability and specific surface area.

Generally, data for two cell or pore diameters are provided where the rectangular nature of a porous medium is accentuated (e.g. De Jaeger et al. [12]). In such cases, the dimension

in the third principal direction is assumed to be equal to one of the two dimensions provided. Information regarding which of these two dimensions the third dimension is equal to is furthermore required. Other information required in order to determine the predictions for the permeability and specific surface area are which dimensions are oriented in which directions, i.e. parallel or perpendicular to the streamwise direction. It is furthermore generally assumed that $d_{s_\parallel} = d_{s_{\perp_1}} = d_{s_{\perp_2}}$, unless specified otherwise. If more than one strut diameter is provided for the three different principal directions, the same requirements that are applicable to the face or pore diameters are applicable to the strut diameter in order to incorporate the information into the model. The remaining dimensions can be determined from the porosity equation of the CARUC model chosen to represent the porous medium.

As an illustrative example, the rectangular three-strut CARUC model with a shorter streamwise and longer transverse dimensions are chosen, i.e. $d_\parallel < d_\perp$ where $d_{\perp_1} = d_{\perp_2} = d_\perp$. A visual representation of the rectangular three-strut model with the latter specifications is shown in Figure 4.11.

Implementing the aforementioned conditions leads to the deduction that equation (4.90) is furthermore valid for the rectangular three-strut CARUC model with a streamwise adjustment, as well as the expressions for the permeability coefficients and specific surface area given by equations (4.92) to (4.95). The information from experiments required in order to implement this model scenario, however, includes the complete data set of ϵ and corresponding data sets of either two of the three pore-scale dimensions d_s, $d_\parallel$ and $d_\perp$. The remaining pore-scale dimension can then be determined by rearranging the equation

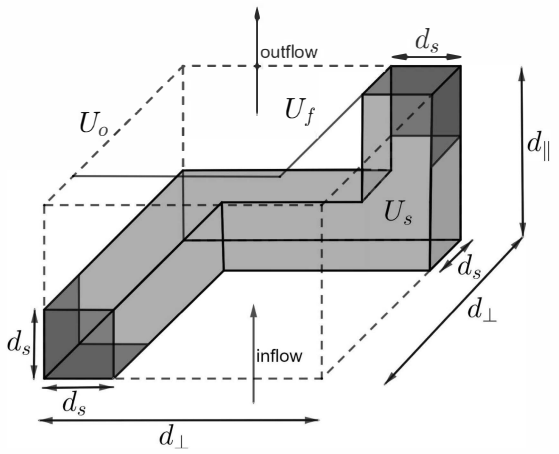

FIGURE 4.11: *Rectangular three-strut CARUC model with streamwise adjustment*

for the porosity, which in this case is equation (4.90). For example, if the data set for $d_\perp$ at different porosity values is not available, equation (4.91) can be utilized to determine $d_\perp$ from the data sets of ϵ, d_s and $d_\parallel$.

In the following section, the manner in which the CARUC models can be applied to available experimental data from the literature is shown and the predictions acquired are compared to the corresponding uncompressed model predictions and experimental data values provided.

4.4 Comparison of CARUC models

Six experimental data sets that will be utilized for the purpose of evaluation and comparison in this chapter are provided in this section and not in Chapter 1 due to the specific application to compressed and rectangular fibres and foams. The data sets acquired are from Jackson and James [8], Boomsma and Poulikakos [2], Dukhan [9], Jaganathan et al. [10], Akaydin et al. [11] and De Jaeger et al. [12].

4.4.1 Jackson and James [8]:

Jackson and James [8] investigated the permeability of fibrous media, specifically the Darcy permeability, and provided experimental permeability data for a wide variety of fibrous media from the literature along with model equations for predicting the Darcy permeability. The data which they used was acquired from Ingmanson et al. [89] and was obtained for nylon and glass fibres. The latter data will be utilized in this study and is listed in Table 4.1.

TABLE 4.1: *Experimental data obtained from Jackson and James [8] for nylon and glass fibre-type media*

Fibre type	ϵ	$K \times 10^9\,[\mathrm{m}^2]$
Nylon fibres: $b_o = 0.193\,\mathrm{mm}$	0.742	2.79
	0.768	3.63
	0.79	4.66
	0.80	5.12
	0.83	7.45
	0.85	9.03
	0.86	10.3
	0.87	12.4
	0.90	17.9
Glass fibres: $b_o = 0.164\,\mathrm{mm}$	0.68	1.01
	0.71	1.48
	0.71	4.17
	0.80	3.70
	0.83	5.31
	0.85	6.7
	0.87	10
	0.90	13
	0.91	17
	0.92	20
	0.93	26
	0.94	35
	0.955	54

Ingmanson et al. [89] studied the internal pressure distributions in compressible mats under fluid stress. The data set provided is therefore suitable for fibre-type media that are randomly distributed subject to streamwise compression. Jackson and James [8] did not, however, provide $e_{\parallel}$-data or information regarding uncompressed dimensions, such as $d_{\parallel_o}$, that are required in order to utilize the three-strut CARUC model for the prediction

of the Darcy permeability for comparison. In order to utilize the data provided by Jackson and James [8], the method described in Section 4.3 where the uncompressed medium is assumed to resemble the isotropic three-strut RUC model is used, i.e. equations (4.124) and (4.125) are used to determine $d_{\|_o}$ (since it is assumed that $d_{\|_o} = d_{\perp_o} = d_o$) where $\epsilon_o = 0.9$ for the nylon fibres and $\epsilon_o = 0.955$ for the glass fibres. It is unclear whether nylon fibres should be categorized as soft material or hard material and consequently, both the soft and hard three-strut CARUC models are utilized in order to predict the Darcy permeability of these compressed fibres. Glass fibres are furthermore assumed to be hard and therefore the hard three-strut CARUC model is considered in this case. Since no compression factor data is provided it is assumed that the relation between the porosity and compression factor given by equation (4.86) is valid in this case, i.e. it is assumed that no lateral expansion occurs and that the total solid volume of the medium remains constant.

The method of attaining the model equations for the soft three-strut CARUC model with no lateral expansion can, consequently, be attained similarly to the scenario provided in Section 4.3.3. Applying the required conditions to equation (4.54) and rearranging leads to an expression for the strut diameter orientated transverse to the streamwise direction (and transverse to the compression direction due to the compression occurring in the streamwise direction), that is similar to equation (4.123). The strut diameter orientated in the streamwise direction is furthermore given by $d_{s_\|} = f(e_\|)d_{s_o}$, where $f(e_\|) = (1+e_\|)/2$ for illustration purposes, as already mentioned.

In the case of the glass fibres, the scenario described in Section 4.3.2 for the hard three-strut CARUC model with no lateral expansion can be used due to its resemblance to the current scenario. It should be noted, however, that the use of equation (4.86) necessitates the use of equation (4.96) to determine the strut diameter at different compression states.

Model validation

In Figure 4.12 the predictions for the Darcy permeability obtained from the CARUC models, subject to the given conditions, their uncompressed counterparts and the experimental data provided in Table 4.1 for the nylon fibres are shown. Similarly, the predictions and data of the glass fibres are shown in Figure 4.13.

In both Figures 4.12 and 4.13 it is noted that the majority of the data provided by Jackson and James [8] is situated between the predictions of the compressed and uncompressed models. Furthermore, the average correspondence of the experimental data to the compressed models is closer than that of the uncompressed models. It consequently indicates that the compressed models provide an improved method of predicting the permeability of compressed fibre-type media. The soft and hard models provide similar predictions in Figure 4.12 in the case where nylon fibres are considered. A soft model assumption in this case is thus unnecessary. It is also noted that the assumptions that had to be made due to the lack of compression factor data and information regarding the uncompressed conditions may be the reason for the deviations observed. An improvement of the compressed model performance may result from the availability of additional information. Van Heyningen [57] observed that the relation between the porosity and compression factor had a significant impact on the prediction of the Darcy permeability. Taking the absence of the compression factor data into account in this case, along with the satisfying perfor-

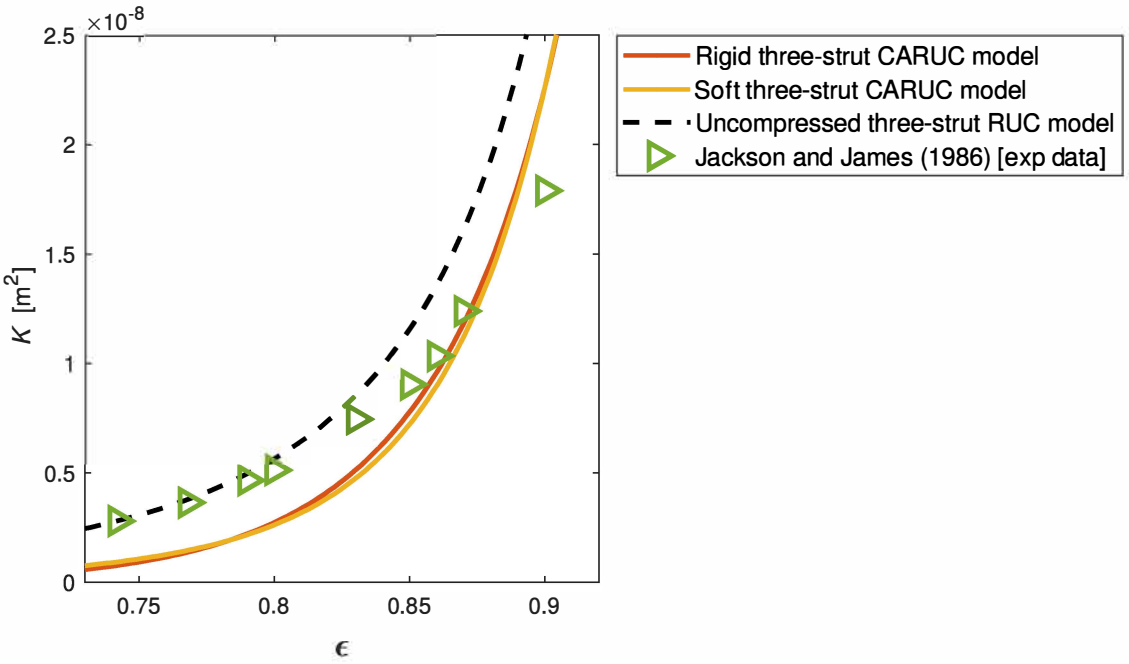

FIGURE 4.12: *Darcy permeability prediction versus porosity of CARUC models and nylon fibre experimental data under compression from Jackson and James [8]*

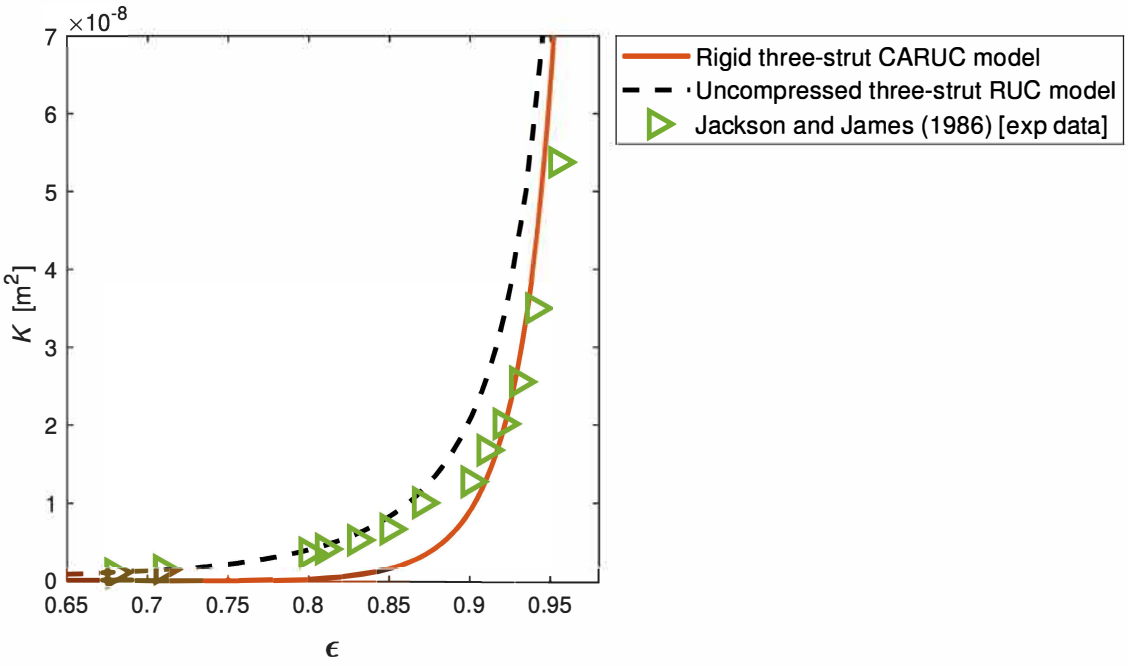

FIGURE 4.13: *Darcy permeability prediction versus porosity of CARUC models and glass fibre experimental data under compression from Jackson and James [8]*

mance of the three-strut CARUC models despite the lack thereof, adds credibility to the performance of the compressed model.

The following data set that will be considered is obtained from Boomsma and Poulikakos [2].

4.4.2 Boomsma and Poulikakos [2]

In the study of Boomsma and Poulikakos [2] the effects of compression on the flow characteristics of metal foams are considered and data provided accordingly. The Darcy and Forchheimer permeability data sets of the two samples of compressed metal foams are listed in Table 4.2.

TABLE 4.2: *Experimental data obtained from Boomsma and Poulikakos [2] for aluminium foams with* $d_{p_o} = 2.3\,mm$

Foam sample	ϵ	$e_\perp$	$K \times 10^9$ [m^2]	$K_F \times 10^3$ [m]
Sample 1: $\epsilon_o = 0.95$	0.608	0.125	0.246	0.115
	0.689	0.167	0.525	0.212
	0.805	0.250	0.197	0.369
	0.882	0.500	0.444	0.856
Sample 2: $\epsilon_o = 0.92$	0.669	0.167	0.388	0.181
	0.722	0.200	0.807	0.246
	0.761	0.250	1.39	0.298
	0.825	0.333	2.30	0.560
	0.874	0.500	3.67	0.876

Boomsma and Poulikakos [2] stated that the compressed foams were allowed to expand laterally, which apparently allows for the isotropy of the foam to be more maintained. The corresponding data sets of the porosity, compression factor, PPI number (from which the pore diameter was calculated) and permeability coefficients reduce the number of conditions necessary in order to implement the data and evaluate the CARUC models. The foam dimensions provided by Boomsma and Poulikakos [2] enabled the deduction that the compression of the foam samples occurred in the direction orientated perpendicular to the streamwise direction. Since foamlike media is under consideration, the three-strut CARUC model is utilized for the evaluation of these experimental data sets. The conditions implemented in order to accommodate transverse compression are therefore similar to those described in Section 4.3.3 for transverse compression, i.e. the use of equation (4.116) and that $d_\parallel = d_{\perp_2} = d$. It is not clear from Boomsma and Poulikakos [2] whether the struts undergo deformation under compression and consequently both the implementations of hard and soft struts are considered in order to illustrate the effect on the permeability predictions. For the hard model application $d_{s_\parallel} = d_{s_{\perp_1}} = d_{s_{\perp_2}} = d_s$. Furthermore, $d_s = d_{s_o}$ since lateral expansion is allowed and therefore distribution of the solid volume by increasing the strut diameters are not necessary. The parameter d can consequently be calculated using an equation similar to equation (4.91), but applying the conditions for transverse compression rather than that for streamwise compression. For the soft model application, the strut diameter parallel to the direction of compression is given by equation (4.117) and $d_{s_\parallel} = d_{s_{\perp_2}} = d_{s_o}$. For this scenario, d can be calculated using equation (4.119) due to the conditions of the transverse compression of a soft porous medium. The lateral expansion of the foam samples during compression implies that equation (4.86) does not theoretically apply to this scenario. Boomsma and Poulikakos [2], however, showed that the calculated porosity values, determined using the aforementioned equation and corresponding e-data, and experimentally measured porosity values are very close. Due to this information, as well as the corresponding ϵ-e data sets, equation (4.88)

will be employed in this section and compared to the predictions acquired using the e-data directly. In the case where Sample 1 in Table 4.2 is used to acquire C in equation (4.88), it follows that $C = 0.0521$, and in the case where Sample 2 is utilized, $C = 0.0584$.

The data sets provided by Boomsma and Poulikakos [2] does not include a value for $d_{\perp_o}$ or a manner in which $d_{\perp_o}$ can be attained. Only a value for d_{p_o} was provided. Consequently, and similar to the previous section where data acquired from Jackson and James [8] were considered, the initial conditions in this case are assumed to resemble the isotropic three-strut RUC model provided in Chapter 2. From the dimension relations provided in Chapter 2, Section 2.3.1, values for $d_{\perp_o}$ and d_{s_o} are therefore determined (using equations (2.72), (2.74) and (2.75), where $d_{\perp_o} = d$, $d_{s_o} = d_s$ and $d_{p_o} = d_p$ in these equations). The necessary conditions for the hard three-strut CARUC model under transverse compression can therefore be implemented in equations (4.77) and (4.78) in order to obtain predictions for the Darcy and Forchheimer permeability coefficients, respectively.

Model validation

The Darcy permeability predictions of the CARUC models and uncompressed model, along with the experimental data given in Table 4.2, are shown in Figure 4.14. The Forchheimer permeability predictions and data are shown in Figure 4.15. The two samples are distinguished in each figure by different colour shades of the markers, i.e. sample 1 displays darker/duller and sample 2 displays lighter/brighter. The predictions of the CARUC models indicated with 'o' markers make use of the data provided in Table 4.2 directly, whereas the solid lines make use of equation (4.88), with $C = 0.0521$ and $C = 0.0584$ for Samples 1 and 2, respectively, in order to obtain the values for the compression factor.

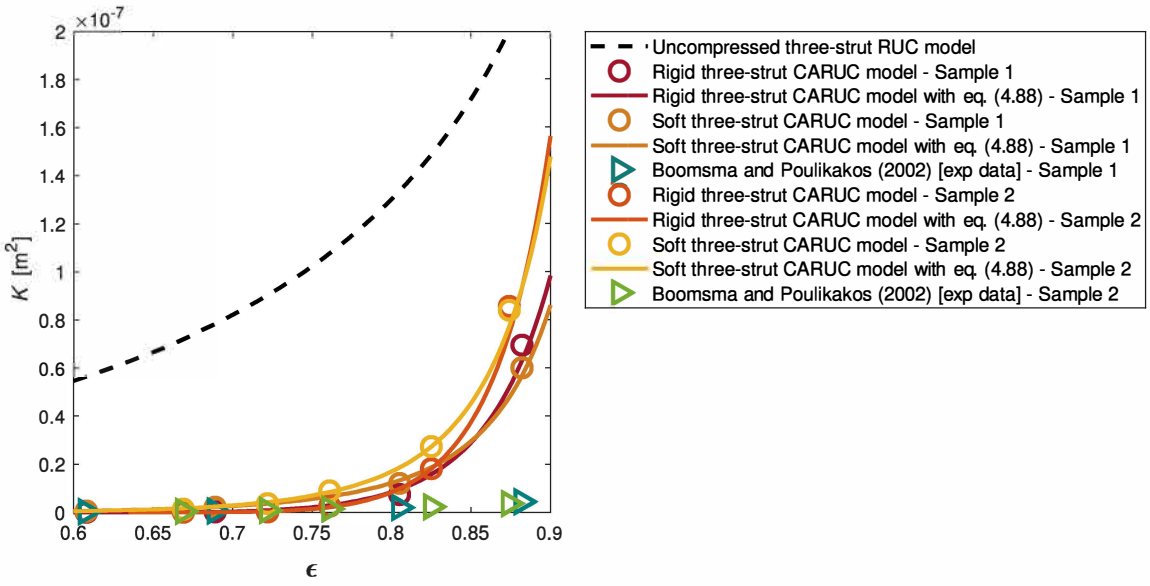

FIGURE 4.14: *Darcy permeability prediction versus porosity of CARUC models and metal foam experimental data under compression from Boomsma and Poulikakos [2]*

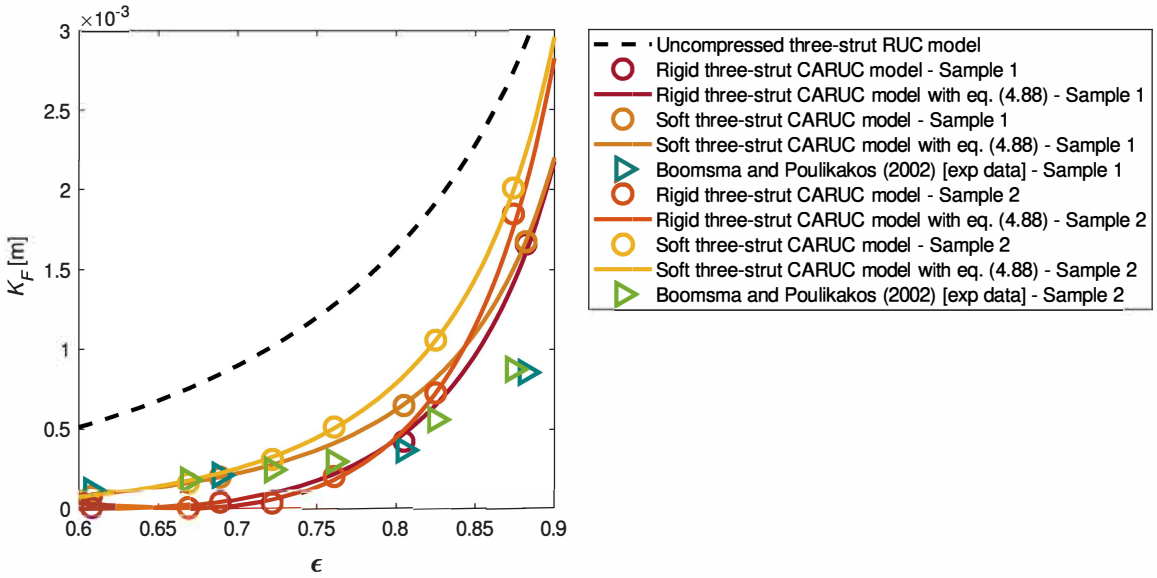

FIGURE 4.15: *Forchheimer permeability prediction versus porosity of CARUC models and metal foam experimental data under compression from Boomsma and Poulikakos [2]*

In Figure 4.14 it can first be noticed that the permeability predictions of the CARUC model that makes use of the data provided in Table 4.2 versus the predictions acquired by making use of equation (4.88) give similar results. It is also evident that the uncompressed three-strut CARUC model significantly overestimates the experimental data of the Darcy permeability compared to the compressed models. Consequently, the model predictions that correspond closest to the experimental data of both samples are the three-strut CARUC models. The hard three-strut CARUC model provides a closer average correspondence to the experimental data than the soft model, but both the CARUC models do however not provide satisfactory predictions at the higher porosity values compared to the experimental data, and show a significant increase in this region (of higher porosity values). A reason for the deviation between the experimental data and the predictions of the CARUC models, may be the fact that the PPI number was used to obtain d_{p_o} and furthermore, that an isotropic uncompressed state was assumed.

The model predictions that supply the most accurate predictions when compared to the experimental data of the Forchheimer permeability in Figure 4.15 is clearly accredited to the three-strut CARUC models, since the uncompressed model once again overpredicts the data significantly. Furthermore, the hard CARUC model provides a closer average correspondence to the data over the entire porosity domain considered, whilst the soft model provides more accurate predictions at lower porosity values. The model predictions obtained for the Forchheimer permeability are more satisfactory than in the case of that for the Darcy permeability.

The data considered next for evaluation is obtained from Dukhan [9].

4.4.3 Dukhan [9]

Dukhan [9] investigated the correlations of pressure drop for air flow through different foam samples, of which some were compressed. Permeability and specific surface area

data for four of these foam samples that were compressed in the streamwise direction were acquired by them and are consequently listed in Table 4.3.

TABLE 4.3: *Experimental data obtained from Dukhan [9] for aluminium foams*

ϵ_o	ϵ	$e_{\parallel}$	d_{p_o} [μm]	$K \times 10^9$ [m^2]	$K_F \times 10^3$ [m]	S_v [m^{-1}]
0.921	0.679	0.246	1300	0.66	0.323	5104.3
0.921	0.774	0.350	1300	0.10	0.500	3593.7
0.922	0.682	0.245	2500	0.10	0.588	3169.3
0.922	0.794	0.379	2500	0.21	0.00012	2053.1

The initial porosity and PPI numbers (which enables the determination of the initial pore diameter) were provided by Dukhan [9], along with corresponding porosity and compression factor data, which are also listed in Table 4.3. The compression factor data, however, was determined by Dukhan [9] by using equation (4.86) which assumes no lateral expansion of the foam under compression, as mentioned previously. Consequently, the same condition is employed in this scenario (i.e. $d_{\perp_1} = d_{\perp_2} = d_{\perp_o}$). Due to it being foamlike media under consideration, the three-strut CARUC model is, once again, utilized for comparison with the data sets obtained from Dukhan [9]. As in the case of Boomsma and Poulikakos [2], it is not clear from Dukhan [9] whether a hard or soft model should be utilized. Therefore, both these model scenarios are also implemented in this section. For the application of the hard model, $d_{s_{\parallel}} = d_{s_{\perp_1}} = d_{s_{\perp_2}} = d_s$ once again. Due to the decrease in porosity combined with the assumption of constant solid volume during compression, as well as the condition of no lateral expansion, d_s increases with compression in this case. The values of d_s can therefore be determined from equation (4.96). For the application of the soft model, $d_{s_{\parallel}} = f_{\parallel}(e_{\parallel})d_{s_o} = \left(1 + e_{\parallel}\right)/2d_{s_o}$ and $d_{s_{\perp_1}} = d_{s_{\perp_2}} = d_{s_{\perp}}$ where $d_{s_{\perp}}$ is determined by implementing the required conditions of a soft and streamwise compressed model in equation (4.54), leading to an equation similar to equation (4.123) (but for streamwise compression conditions). Streamwise compression also implies that equation (4.89) is applicable in this scenario. Once again, due to the absence of information that makes the determination of $d_{\parallel_o}$ possible, it is assumed that the metal foams are isotropic in the uncompressed state and consequently, d_{p_o} provided in Table 4.3 can be used to obtain d_o and d_{s_o} using equations (2.75) and (2.74), respectively.

Model validation

In Figures 4.16 to 4.18 the predictions and experimental data of the Darcy permeability coefficient, Forchheimer permeability coefficient and specific surface area are shown, respectively. Empirical expressions for the Darcy permeability and form drag coefficients were furthermore provided by Dukhan et al. [34] and Dukhan [9], from which the expression for the form drag coefficient can be utilized to obtain the prediction for the Forchheimer permeability coefficient. The predictions acquired from these expressions are included for comparison purposes in Figures 4.16 and 4.17.

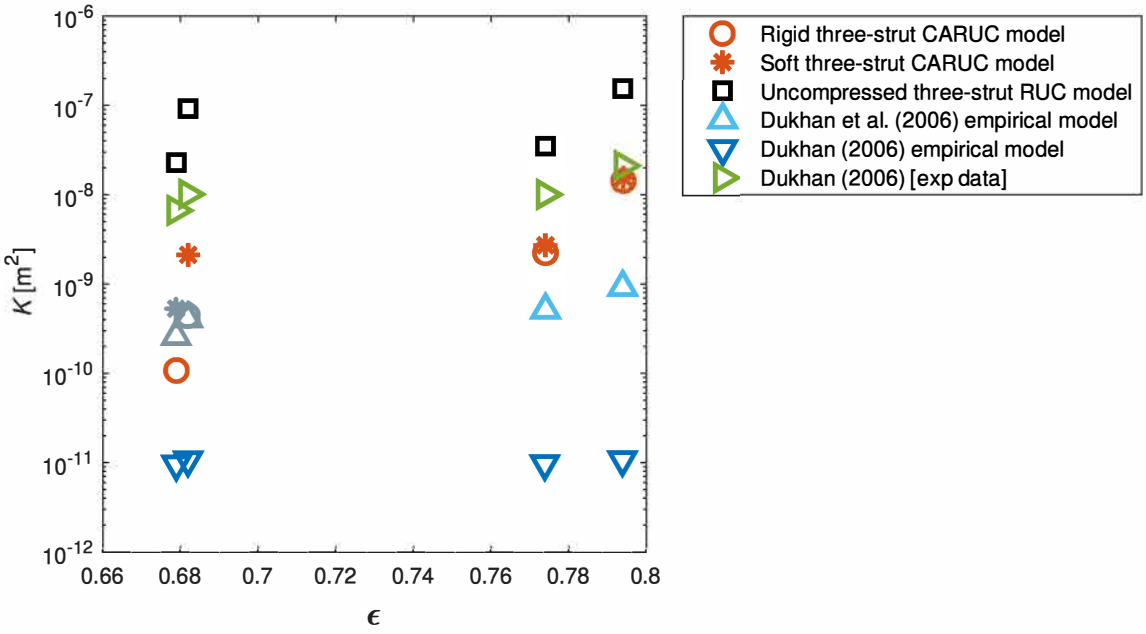

FIGURE 4.16: *Darcy permeability prediction versus porosity of CARUC models and metal foam experimental data under compression from Dukhan [9]*

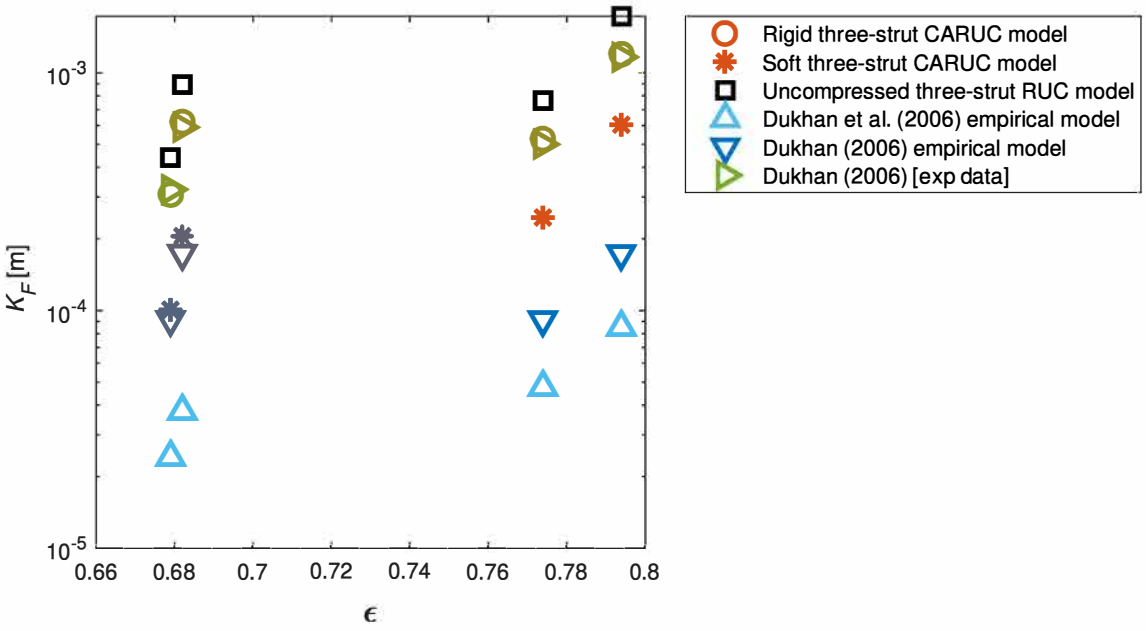

FIGURE 4.17: *Forchheimer permeability prediction versus porosity of CARUC models and metal foam experimental data under compression from Dukhan [9]*

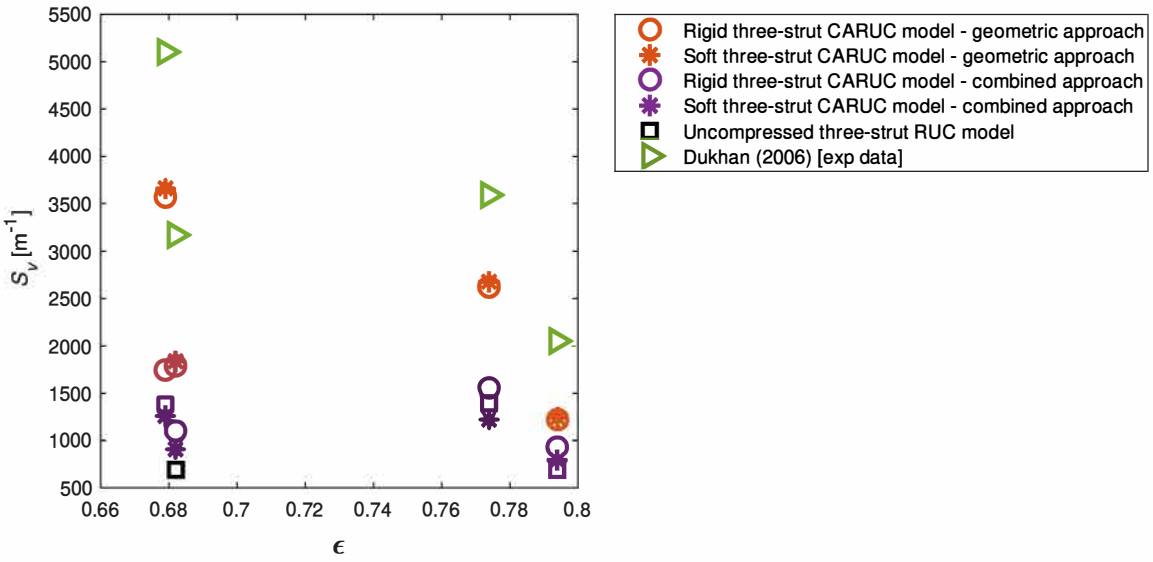

FIGURE 4.18: *Specific surface area prediction versus porosity of CARUC models and metal foam experimental data under compression from Dukhan [9]*

In Figure 4.16 both the three-strut CARUC model predictions provide closer correspondence to the experimental data than the uncompressed model predictions with the soft model providing slightly more accurate predictions than that of the hard model. (It should be noted that a semilog plot was used to illustrate the permeability predictions in Figures 4.16 and 4.17 in order to distinguish between the predicted values. Consequently, the CARUC model predictions are even closer to the experimental data than they might appear.) In Figure 4.17 it can be seen that the hard CARUC model corresponds satisfactorily to the experimental data and outperforms the uncompressed, soft compressed and empirical models considered. The experimental data values are lower than that of the uncompressed model for both permeability coefficients, as expected, with the three-strut CARUC model predictions also being lower than that of the uncompressed model predictions. The under-prediction of the soft CARUC model may be due to the chosen ratio function $f_{\parallel}(e_{\parallel})$ representing the compression of the strut diameter. It is also noted that the three-strut CARUC models also provide closer predictions to the experimental data than that of the empirical models of Dukhan et al. [34] and Dukhan [9], which lends favor to the foam CARUC model presented in this study.

In Figure 4.18 both the predictions for the specific surface area obtained using a geometric approach and a combined approach are shown. The results obtained using a combined approach were acquired by substituting the streamwise face diameter with the Darcy permeability coefficient, as was done throughout this chapter. It can be seen that the three-strut CARUC models resulting from the predictions obtained using a geometric approach correspond closer to the experimental data. The hard and soft CARUC models provide similar predictions in this case. The specific surface area predictions of the CARUC models acquired using a combined approach, however, corresponds closer to the predictions of the uncompressed model, which significantly underpredicts the data. This may be due to the uncertainty already incorporated into the permeability prediction which is used as input to the combined approach. The combined approach can however be used to obtain S_v values of the correct order of magnitude, should specific surface area data

be required but is unavailable. Taking all the results into consideration, the three-strut CARUC model exhibits a more favourable predictive capability for the permeability and specific surface area of the compressed metal foam samples in this section compared to that of the uncompressed model. This outcome aligns with the intended objective of the study.

In the following section, a data set acquired from Jaganathan et al. [10] is considered.

4.4.4 Jaganathan et al. [10]:

Jaganathan et al. [10] studied the change in pore sizes of fibre-type media due to compression. Their data was obtained by performing Digital Volumetric Imaging (DVI) on polyester fibres. The average fibre diameter of the fibers was $b = 15\,\mu$m. Flow through the fibres did not form part of their study and consequently, the streamwise flow direction and the direction of compression of the polyester fibres were not specified. The compression factor in this section will therefore merely be denoted by e_x.

TABLE 4.4: *Experimental data obtained from Jaganathan et al. [10] for polyester fibres*

ϵ	e_x
0.6558	0.21
0.8240	0.37
0.8805	0.54
0.9388	1

Jaganathan et al. [10] only provided the solid volume fraction percentage and the thickness of the fibre sample before and after compression. The data obtained from Jaganathan et al. [10] is listed in Table 4.4. Equations (4.86) and (4.88) are furthermore implemented in this section. In the explanation provided by Jaganathan et al. [10], it is evident that lateral expansion of the fibres under compression were prohibited by a miniature compression cell which they constructed. The use of equation (4.86) is consequently justified with $\epsilon_o = 0.9388$. The compression factor versus porosity relation acquired using this equation is furthermore shown in Figure 4.19. Alternatively, the average value for C in equation (4.88) can be acquired from the compression factor and porosity data set provided in Table 4.4. In this case, $C = 0.0658$. The predictions obtained from equation (4.88) with this value for C is also shown in Figure 4.19.

In comparison to the data provided by Jaganathan et al. [10], both equations (4.86) and (4.88) perform satisfactorily, as is evident in Figure 4.19. The predictions provided by equation (4.88) correspond slightly better with the data than the predictions provided by equation (4.86).

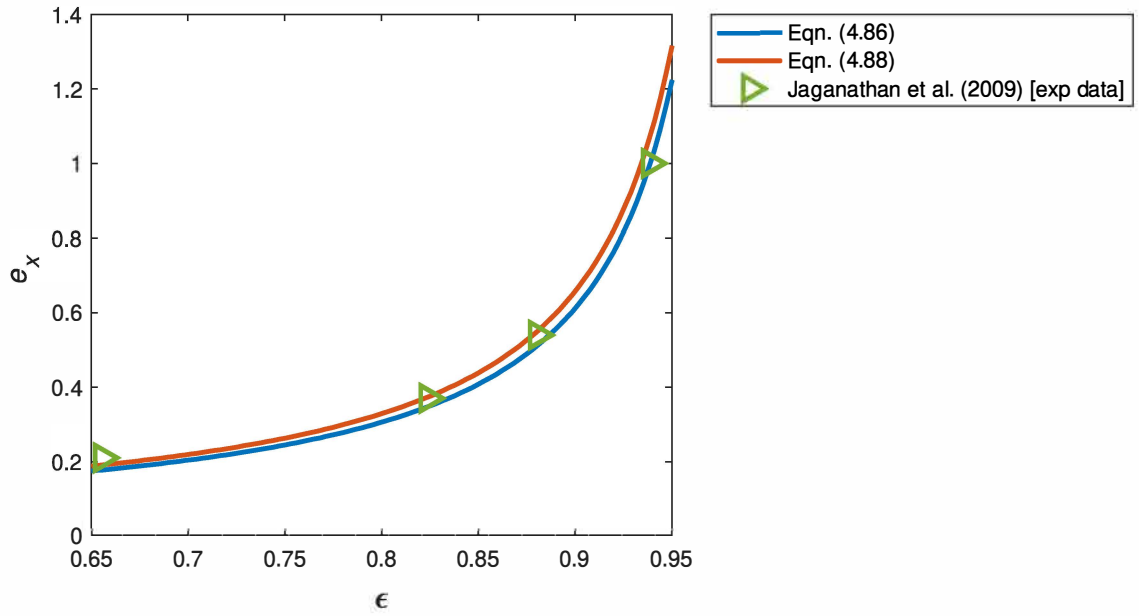

FIGURE 4.19: *Compression factor versus porosity compared to porous media data from Jaganathan et al. [10] without lateral expansion*

The data obtained from the study of Akaydin et al. [11] will be investigated in the next section and used for the evaluation and comparison of the CARUC models.

4.4.5 Akaydin et al. [11]:

Akaydin et al. [11] measured and investigated the permeability of a soft fibre-type material, i.e. a regular polyester pillow material (that they acquired from local retail stores) consisting of 95% polyester and 5% silk with an average fibre radius of $a = 5\,\mu$m, at different levels of compression. They determined the permeability experimentally by measuring the pressure for different ratios of compression. They noted that the permeability changed significantly at different compression ratios of the polyester fibre material, but the porosity remained almost constant. Akaydin et al. [11] obtained the experimental porosity values by measuring the solid volume which was performed by immersing the material in a solution of a dishwashing liquid in water and measuring the displaced volume of fluid, calculated using the density and weight. They provided values for the compaction (or compression ratio) which is equivalent to $1 - e_x$, along with the porosity and Darcy permeability measurements. Akaydin et al. [11] furthermore provided experimental values for what they termed the Forchheimer constant (defined as the inertia coefficient in this study).

The data relevant to this study, provided by Akaydin et al. [11], is presented in Table 4.5. The fibres were oriented randomly and therefore present a 3D-type fibre arrangement. The compression of the fibres was performed in the streamwise direction and therefore equation (4.89) can once again be used. Due to the 3D-type fibre arrangement of the fibres utilized by Akaydin et al. [11], the three-strut CARUC model is used in this section. Initial isotropy is furthermore assumed since Akaydin et al. [11] did not provide any other information regarding the uncompressed state of the fibre media sample (i.e.

TABLE 4.5: *Experimental data obtained from Akaydin et al. [11] for soft polyester fibre media with* $b_o = 10\,\mu m$

ϵ	$e_{\parallel}$	$K \times 10^9$ [m^2]	$K_F \times 10^3$ [m]
0.9780	0.15	0.66	0.039
0.9883	0.27	1.36	0.417
0.9914	0.37	2.15	0.526
0.9930	0.45	2.88	0.625
0.9941	0.55	3.86	0.476
0.9959	0.78	6.44	0.667
0.9968	1	9.53	1.25

equations (2.72) and (2.77) are used to obtain the value for d_o using b_o). The polyester material is considered as a soft material and consequently the soft model is utilized in order to portray the compression of the polyester fibres. The fibre samples were prohibited from expanding by the wall of the cylinder in which it was placed and therefore the scenario of no lateral expansion of the model is assumed. These conditions imply that $d_{s_{\parallel}} = f_{\parallel}(e_{\parallel})d_{s_o}$ (where $f_{\parallel}(e_{\parallel}) = (1+e_{\parallel})/2$ is once again assumed for illustration purposes), $d_{s_{\perp_1}} = d_{s_{\perp_2}} = d_{s_{\perp}}$ and $d_{\perp_1} = d_{\perp_2} = d_{\perp_o}$. $d_{s_{\perp}}$ can then be determined, as explained in Section 4.4.3 for the comparison with the data acquired from Dukhan [9], by implementing the conditions of a soft model with no lateral expansion for streamwise compression in equation (4.54). The parameter $d_{\perp_o}$ can similarly be determined by substituting the values for the uncompressed dimensions in equation (4.54). Since both the data for the porosity and compression factor were provided by Akaydin et al. [11], equation (4.88) will be utilized. In this case, $C = 0.0032$. Finally, the Darcy and Forchheimer permeability are determined using equations (4.77) and (4.78), respectively.

Model validation

The predictions of the Darcy permeability of the three-strut CARUC and uncompressed three-strut RUC models, along with the corresponding experimental data, are shown in Figure 4.20. The predictions and data of the Forchheimer permeability are similarly shown in Figure 4.21.

In both Figures 4.20 and 4.21 it is evident that the three-strut CARUC model once again provides the best correspondence with the experimental data. Both the CARUC models for the Darcy permeability and Forchheimer permeability, however, still overpredict the experimental data at the higher porosity values. This observation can be attributed to the conditions made regarding the uncompressed state of the fibrous porous medium of Akaydin et al. [11] resembling isotropy.

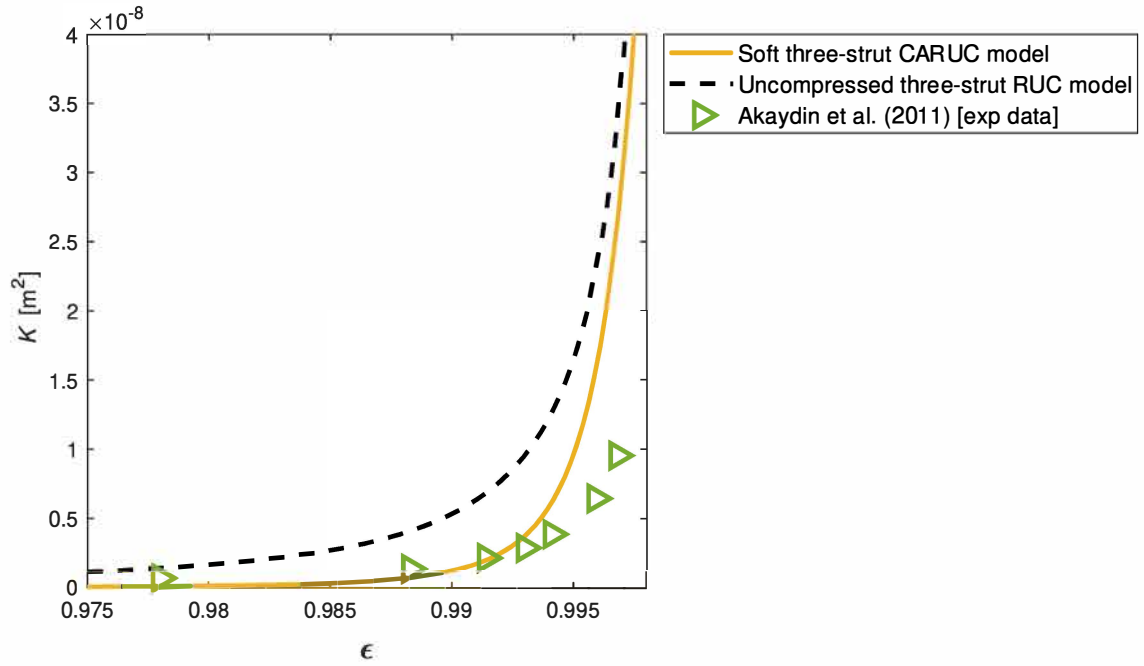

FIGURE 4.20: *Darcy permeability prediction versus porosity of CARUC models and metal foam experimental data under compression from Akaydin et al. [11]*

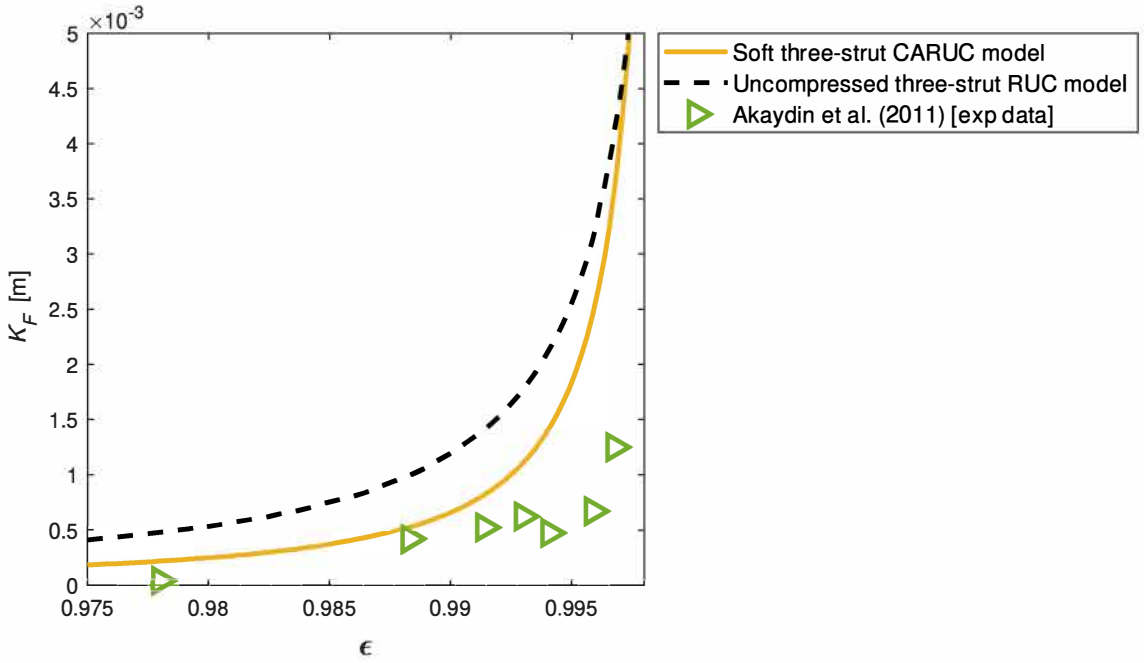

FIGURE 4.21: *Forchheimer permeability prediction versus porosity of CARUC models and metal foam experimental data under compression from Akaydin et al. [11]*

Finally, the data sets acquired from De Jaeger et al. [12] are discussed and utilized for evaluation purposes.

4.4.6 De Jaeger et al. [12]

In the study of De Jaeger et al. [12] the typical occurrence of unidirectional cell elongation in foams was considered. They provided experimental data for nine foam samples with two different face diameters. In Table 4.6 the data provided by De Jaeger et al. [12] is shown.

De Jaeger et al. [12] provided the cross-sectional area of the struts of the samples from which the strut diameter was determined. The data provided by De Jaeger et al. [12] is consequently applicable to the application of the CARUC models to rectangular geometry in the uncompressed state and constant strut diameter (i.e. the application of the rectangular CARUC models). Due to metal foams being the medium under consideration, the rectangular three-strut CARUC model is required. In accordance with information provided by De Jaeger et al. [12], d_1 in Table 4.6 is the face diameter of two of the cell dimensions, and d_2 is applied to one of the dimensions, e.g. $d_{\perp_1} = d_{\perp_2} = d_1$ and $d_{\parallel} = d_2$. Since no permeability data is provided and only the evaluation of the specific surface area is included for this data set, the assignment of the face diameters, i.e. which face diameters are equal to d_1 and which one is equal to d_2 (referring to the streamwise or transverse orientation thereof), is not important.

TABLE 4.6: *Experimental data obtained from De Jaeger et al. [12] for anisotropic metal foams*

ϵ	d_s [μm]	d_1 [μm]	d_2 [μm]	S_v [m^{-1}]
0.913	215.17	2520	3780	860
0.917	266.46	3260	4640	624
0.918	413.28	5200	6540	431
0.918	348.14	4100	6580	478
0.923	214.48	2780	3940	700
0.932	315.91	4220	6230	440
0.937	194.16	2770	4150	720
0.951	247.99	4280	6420	380
0.967	112.25	2600	3670	580

The strut diameter as given in Table 4.6 is furthermore assumed to be applicable to the strut diameters in all directions, that is $d_{s_{\parallel}} = d_{s_{\perp_1}} = d_{s_{\perp_2}} = d_s$. The values assigned to the pore-scale parameters can consequently be substituted into equation (4.80) in order to predict the specific surface area of the rectangular three-strut CARUC model.

Model validation

The predictions acquired from the rectangular three-strut CARUC model and isotropic RUC model, respectively, and the experimental data given in Table 4.6 for the specific surface area are shown in Figure 4.22. The cubic (or isotropic) three-strut RUC model predictions are shown for comparison purposes and are determined using equation (2.86), where d_p is determined from equations (2.72) and (2.74) of which the values used for d_s and ϵ are those given by De Jaeger et al. [12] in Table 4.6.

Figure 4.22 shows that the isotropic RUC model overpredicts the experimental data, as expected, whilst the rectangular CARUC model underpredicts the data. In general,

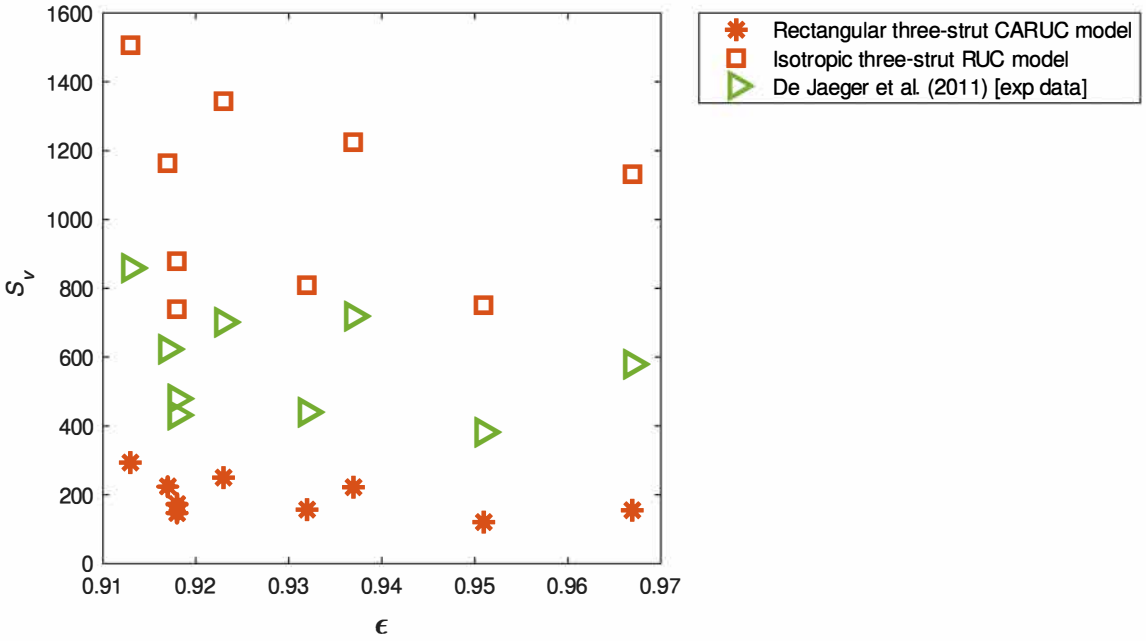

FIGURE 4.22: *Specific surface area prediction versus porosity of CARUC models and experimental data representing anisotopic metal foams from De Jaeger et al. [12]*

however, the rectangular model provides more accurate predictions in comparison to the experimental data than that of the cubic model. While the rectangular model presented in this scenario represents an improvement over the isotropic model, additional experimental data is required for a more comprehensive evaluation. Such data will enable further assessment of the rectangular model's predictive capabilities and potential areas for improvement.

In the following section a summary of the equations and results obtained in this chapter are presented.

4.5 Chapter summary

In this chapter equations were obtained for the two-strut and three-strut RUC models as provided in Chapter 2, that have been adjusted to accommodate changes to the dimensions of the fibrous medium induced by compression or for fibrous media identified as anisotropic rather than isotropic. More information is needed in order to utilize the equations proposed for the compression adjusted RUC (CARUC) models than for the cubic models. Different scenarios were discussed in this chapter in order to illustrate how the models can be applied subject to the available model input parameters provided by experimental data sets. The main scenarios addressed were the compression of hard media, the compression of soft media and the case where anisotropic geometry can be accounted for by employing the rectangular model (i.e. a special case of the CARUC model in the uncompressed state). The implementation of the special case of the streamwise compressed two-strut CARUC model for through plane flow was furthermore provided in greater detail in Section 4.3.2, of which the results were published in Woudberg et al. [77]. Different data sets were acquired in order to evaluate the performance of the

CARUC models utilizing the accompanying conditions. The results obtained proved to be an improvement when compared to the corresponding uncompressed cubic models, and were therefore satisfactory. The three-strut CARUC model presented in this chapter and the implementation of and comparison to the experimental data acquired from Dukhan [9] was furthermore presented at the 12th International Conference on Porous Metals and Metallic Foams in Dresden, Germany, from 5 - 7 July 2023. A peer reviewed paper is yet to be published in the conference proceedings with reference Maré and Woudberg [80].

Unlike the previous chapter summaries, a table providing the key equations obtained in this chapter is not provided due to the length of the equations obtained and that it would, consequently, not fit into a table. Table 4.7 is provided where the parameters to be obtained using the equations in this chapter, what the equations are in terms of and lastly the equation numbers are listed so that the relevant equations can be easily accessed in the chapter. The equations necessary for attaining the permeability or specific surface area of fibrous media under compression or with identified anisotropic geometry without compression (for which the rectangular CARUC model is used) can consequently be acquired by utilizing the equation reference numbers provided in Table 4.7.

TABLE 4.7: *Summary of specifications and numbers of the porosity, permeability coefficient and specific surface area equations acquired based on the various CARUC models presented in Chapter 4*

CARUC model	Eqn. for	Eqn. i.t.o.	Eqn. no.
Two-strut in-plane flow (Section 4.1)	ϵ	$(d_{s_\parallel}, d_{s_{\perp_1}}, d_{s_{\perp_2}}, d_\parallel, d_{\perp_1}, d_{\perp_2})$	(4.3)
	K	$(d_{s_\parallel}, d_{s_{\perp_1}}, d_{s_{\perp_2}}, d_\parallel, d_{\perp_1}, d_{\perp_2})$	(4.22)
	K_F	$(d_{s_{\perp_1}}, d_{s_{\perp_2}}, d_\parallel, d_{\perp_1}, d_{\perp_2}, \epsilon)$	(4.23)
	S_v	$(d_{s_\parallel}, d_{s_{\perp_1}}, d_{s_{\perp_2}}, d_\parallel, d_{\perp_1}, d_{\perp_2})$	(4.45)
		$(d_{s_\parallel}, d_{s_{\perp_1}}, d_{s_{\perp_2}}, d_{\perp_1}, d_{\perp_2}, K)$	(4.49) & (4.50)
Two-strut through plane flow (Section 4.1)	ϵ	$(d_{s_\parallel}, d_{s_{\perp_1}}, d_{s_{\perp_2}}, d_\parallel, d_{\perp_1}, d_{\perp_2})$	(4.5)
	K	$(d_{s_\parallel}, d_{s_{\perp_1}}, d_{s_{\perp_2}}, d_\parallel, d_{\perp_1}, d_{\perp_2})$	(4.42)
	K_F	$(d_{s_{\perp_1}}, d_{s_{\perp_2}}, d_\parallel, d_{\perp_1}, d_{\perp_2}, \epsilon)$	(4.43)
	S_v	$(d_{s_\parallel}, d_{s_{\perp_1}}, d_{s_{\perp_2}}, d_\parallel, d_{\perp_1}, d_{\perp_2})$	(4.47)
		$(d_{s_\parallel}, d_{s_{\perp_1}}, d_{s_{\perp_2}}, d_{\perp_1}, d_{\perp_2}, K)$	(4.49) & (4.52)
Three-strut (Section 4.2)	ϵ	$(d_{s_\parallel}, d_{s_{\perp_1}}, d_{s_{\perp_2}}, d_\parallel, d_{\perp_1}, d_{\perp_2})$	(4.54)
	K	$(d_{s_\parallel}, d_{s_{\perp_1}}, d_{s_{\perp_2}}, d_\parallel, d_{\perp_1}, d_{\perp_2})$	(4.77)
	K_F	$(d_{s_{\perp_1}}, d_{s_{\perp_2}}, d_\parallel, d_{\perp_1}, d_{\perp_2}, \epsilon)$	(4.78)
	S_v	$(d_{s_\parallel}, d_{s_{\perp_1}}, d_{s_{\perp_2}}, d_\parallel, d_{\perp_1}, d_{\perp_2})$	(4.80)
		$(d_{s_\parallel}, d_{s_{\perp_1}}, d_{s_{\perp_2}}, d_{\perp_1}, d_{\perp_2}, K)$	(4.49) & (4.82)

Additionally, the equations determined in order to predict the permeability and specific surface area of the two-strut CARUC model for through plane flow and three-strut CARUC model (published by Woudberg et al. [77], of which the author of this dissertation is a co-author) are listed in Table 4.8. Note that in Table 4.8, $m = (d_\perp - d_s)^2$.

Furthermore, an overview of which conditions should be applied to the different scenarios of compression or rectangular adjustment without compression of the CARUC models in this chapter are shown in Figure 4.23.

TABLE 4.8: *Summary of equations acquired based on the hard CARUC models compressed in the streamwise direction in Section 4.3.2*

CARUC model	Eqn. for	Eqn. i.t.o.	Eqn. no.	Eqn.
Two-strut through plane flow	ϵ	$(d_s, d_\parallel, d_\perp)$	(4.98)	$\dfrac{d_\parallel d_\perp^2 - 2d_s^2 d_\perp + d_s^3}{d_\parallel d_\perp^2}$
	$d_\perp$	$(\epsilon, d_s, d_\parallel)$	(4.99)	$\dfrac{d_s\left(d_s + \sqrt{d_s^2 + d_s d_\parallel(\epsilon - 1)}\right)}{d_\parallel(1-\epsilon)}$
	K	$(d_s, d_\parallel, d_\perp)$	(4.108)	$\dfrac{d_\parallel(d_\perp - d_s)^2}{24 d_s d_\perp^2}\left[\dfrac{1}{(d_\perp - d_s)^2} + \dfrac{2d_\perp - d_s}{2d_\perp(d_\parallel - d_s)^2}\right]^{-1}$
	S_v	$(d_s, d_\parallel, d_\perp)$	(4.111)	$\dfrac{2d_s(4d_\perp - 3d_s)}{d_\parallel d_\perp^2}$
	S_v	$(d_s, d_\perp, K)$	(4.115)	$a' S_v^3 + b' S_v^2 + c' S_v + g' = 0$ with $a' = 48K d_s^3 d_\perp^9 + 24K d_s d_\perp^8 (2d_\perp - d_s) m$ $b' = -192K d_s^3 d_\perp^7 (4d_\perp - 3d_s) - 4d_s^3 d_\perp^5 m^2 (4d_\perp - 3d_s)$ $c' = 192K d_s^3 d_\perp^5 (4d_\perp - 3d_s)^2 + 16 d_s^3 d_\perp^3 m^2 (4d_\perp - 3d_s)^2$ $g' = -16 d_s^3 d_\perp m^2 (4d_\perp - 3d_s)^3$
Three-strut	ϵ	$(d_s, d_\parallel, d_\perp)$	(4.90)	$1 - \dfrac{2d_s^2}{d_\parallel d_\perp} - \dfrac{d_s^2}{d_\perp^2} + \dfrac{2d_s^3}{d_\parallel d_\perp^2}$
	$d_\perp$	$(\epsilon, d_s, d_\parallel)$	(4.91)	$\dfrac{d_s\left[d_s + \sqrt{d_s^2 + d_\parallel(d_\parallel - 2d_s)(1-\epsilon)}\right]}{d_\parallel(1-\epsilon)}$
	K	$(d_s, d_\parallel, d_\perp)$	(4.92)	$\dfrac{d_\parallel(d_\perp - d_s)^2}{24 d_s d_\perp^2}\left[\dfrac{2}{(d_\perp - d_s)^2} + \dfrac{1}{(d_\parallel - d_s)^2}\right]^{-1}$
	S_v	$(d_s, d_\parallel, d_\perp)$	(4.94)	$\dfrac{4d_s}{d_\parallel d_\perp^2}\left[(d_\parallel - d_s) + 2(d_\perp - d_s)\right]$

CARUC model	Eqn. for	Eqn. i.t.o.	Eqn. no.	Eqn.
	S_v	$(d_s, d_\perp, K)$	(4.49) & (4.95)	$a'S_v^3 + b'S_v^2 + c'S_v + g' = 0$
				with
				$a' = 48d_s^3 d_\perp^8 K + 24 d_s d_\perp^8 Km$
				$b' = -768 d_s^3 d_\perp^7 K + 576 d_s^4 d_\perp^6 K - 8 d_s^3 d_\perp^5 m^2 + 12 d_s^4 d_\perp^4 m^2$
Three-strut (continued)				$\quad -288 d_s^2 d_\perp^6 Km$
				$c' = 3072 d_s^3 d_\perp^6 K - 3072 d_s^4 d_\perp^5 K + 128 d_s^3 d_\perp^4 m^2 - 320 d_s^4 d_\perp^3 m^2$
				$\quad +192 d_s^5 d_\perp^2 m^2 + 1152 d_s^3 d_\perp^4 Km$
				$g' = -512 d_s^3 d_\perp^3 m^2 + 1792 d_s^4 d_\perp^2 m^2 - 2048 d_s^5 d_\perp m^2 + 768 d_s^6 m^2$
				$\quad -12288 d_s^4 d_\perp^4 K + 24576 d_s^5 d_\perp^3 K - 12288 d_s^6 d_\perp^2 K - 1536 d_s^4 d_\perp^2 Km$

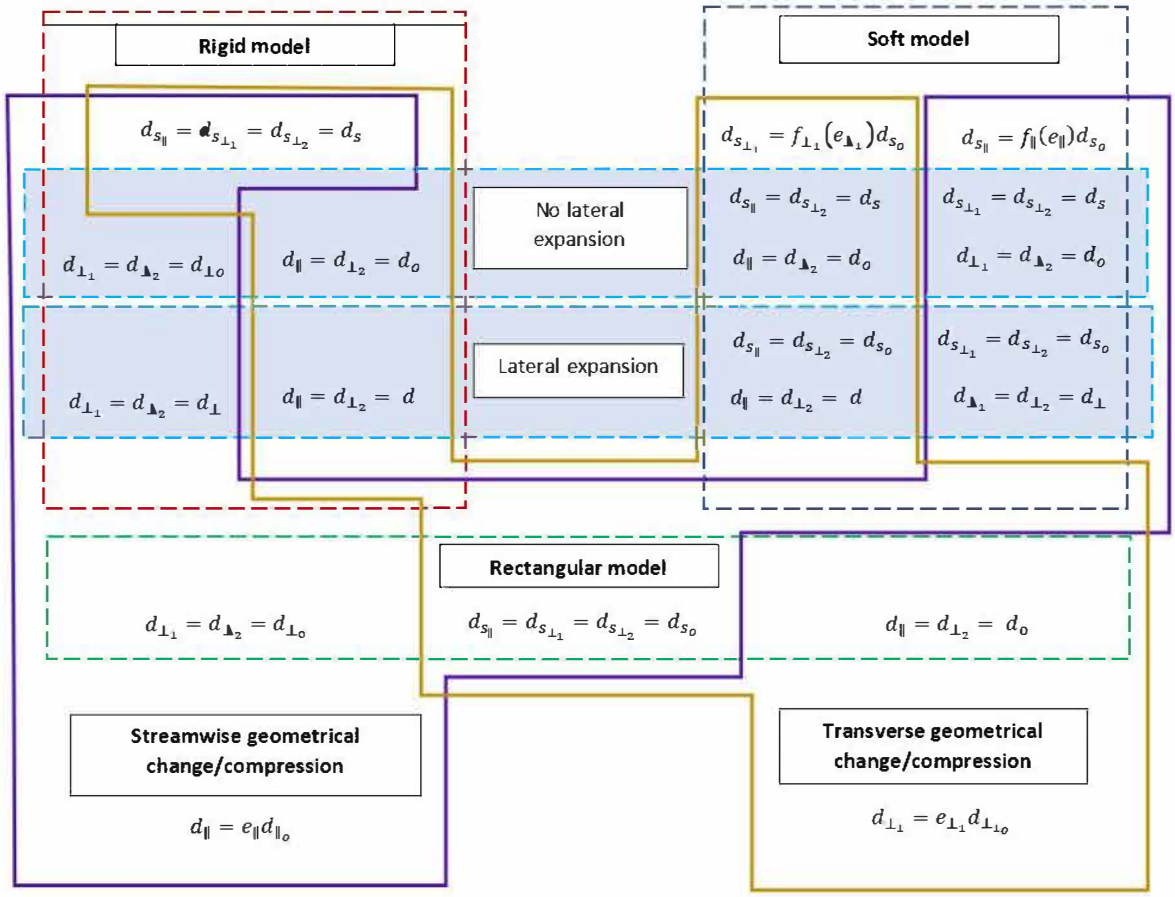

FIGURE 4.23: *Overview of conditions associated with different scenarios of CARUC model adjustments*

For example, in the case where the CARUC model is adjusted for hard struts, with no lateral expansion and streamwise compression, the conditions that should be applied (as determined using Figure 4.23) are $d_{s_\parallel} = d_{s_{\perp_1}} = d_{s_{\perp_2}} = d_s$, $d_{\perp_1} = d_{\perp_2} = d_{\perp_o}$ and $d_\parallel = e_\parallel d_{\parallel_o}$. Another example where the CARUC model is adjusted for soft struts, with lateral expansion and transverse compression, constitutes the following conditions: $d_{s_{\perp_1}} = f_{\perp_1}(e_{\perp_1}) d_{s_o}$, $d_{s_\parallel} = d_{s_{\perp_2}} = d_{s_o}$, $d_\parallel = d_{\perp_2} = d_\perp$ and $d_{\perp_1} = e_{\perp_1} d_{\perp_{1_o}}$. A final example is where the rectangular CARUC model is changed to accommodate a different streamwise dimension in comparison to the transverse dimensions, i.e. a streamwise change. In this scenario, the conditions that should be applied are $d_{s_\parallel} = d_{s_{\perp_1}} = d_{s_{\perp_2}} = d_{s_o}$, $d_{\perp_1} = d_{\perp_2} = d_{\perp_o}$ and $d_\parallel = e_\parallel d_{\parallel_o}$.

CHAPTER 5

Klinkenberg effect on RUC models

It has been noted in numerous studies in the literature that the permeability of gas and the permeability of liquid through a porous medium tend to differ (e.g. Carman [90], Wu et al. [91], Innocentini and Pandolfelli [92], Tanikawa and Shimamoto [93]). One of the factors that contributes to this difference between permeability values is a slippage effect of gas on the pore walls of the porous medium, known as the Klinkenberg effect. The purpose of this chapter is to extend the study of Woudberg and Du Plessis [94], Van Heiningen [57] and Maré [65], who incorporated the Klinkenberg effect into the two-strut and three-strut RUC models, by incorporating the effect into all the RUC models presented in Chapters 2 to 4. The method of incorporation is furthermore done in a similar manner as in the studies of the aforementioned authors.

5.1 Conditions of the Klinkenberg effect

The Klinkenberg effect accounts for the increase in gas permeability, as opposed to liquid permeability, when the molecular mean free path is comparable to the pore dimension (Miguel and Serrenho [95]). The slip effect occurs at low or near atmospheric pressure and happens when the gas molecules collide with the pore wall rather than with other molecules. Consequently, a deviation from Darcy's law occurs by implementing a slip-boundary condition. Due to the flow conditions mentioned, the Klinkenberg effect is only applicable to the Darcy permeability and will be incorporated as such into the RUC models. In order to distinguish between different states of gas flow, a ratio known as the Knudsen number Kn was introduced, and is defined as (Barber and Emerson [96], Hooman et al. [97])

$$Kn = \frac{\lambda}{D_h}, \tag{5.1}$$

where λ denotes the molecular mean free path. The molecular mean free path can be calculated using the following equation (Skjetne and Auriault [98], Chastanet et al. [99]):

$$\lambda = \frac{\mu\sqrt{\pi R_g T/2M}}{p}, \tag{5.2}$$

where R_g is the universal gas constant, T is the absolute temperature and M is the molecular weight. For $10^{-3} < Kn < 10^{-1}$ the Navier-Stokes equation is still valid, but a slip boundary condition has to be incorporated. For $Kn \leq 10^{-3}$ the Klinkenberg effect is

negligible, i.e. the no slip-boundary condition is applicable, and for $Kn \geq 10^{-1}$ the continuum assumption breaks down (Barber and Emerson [100], Hosseini and Tafreshi [101]). The gas flow state in which the Klinkenberg effect is therefore taken into consideration is for $10^{-3} < Kn < 10^{-1}$.

5.2 Incorporation into RUC models

The liquid and gas permeabilities can be related using the Klinkenberg equation, as proposed by Klinkenberg [102], and is given by

$$K_g = K_l \left(1 + \frac{b_K}{p_{\text{avg}}}\right), \tag{5.3}$$

where K_g and K_l denotes the gas and liquid permeabilities, respectively, b_K is the Klinkenberg factor, or the gas dependent constant, and p_{avg} is the average of the inlet and outlet pressures. A similar type of Klinkenberg equation was proposed by Woudberg and Du Plessis [94], i.e.

$$K_g = K_l \left[1 + 12\frac{(2-\sigma)}{\sigma} Kn\right], \tag{5.4}$$

where σ is the fraction of molecules that undergo diffuse reflection at the pore wall and is referred to as the tangential momentum accommodation coefficient (TMAC) . The TMAC is dependent on multiple factors related to the gas, the conditions under which the flow of gas takes place, as well as the condition of the pore surfaces. It was, however, shown that the dependence of the TMAC on the smoothness of the surface is strong and that for a rough surface, σ tends towards a value of 1 and for an idealized or smooth surface, σ tends towards 0 (Barber and Emerson [100]). Equation (5.4) was deduced by incorporating the slip boundary condition into flow between parallel plates and consequently by adjusting the expression for the average wall shear stress (given by equation (1.12)). Maré [65] applied an equation similar to equation (5.4) to the two-strut RUC model for through plane flow and adjusted it to accommodate the hard two-strut RUC model for through plane flow and three-strut RUC model under compression. The derivation of the adjusted expression for the average wall shear stress is shown by the aforementioned authors (i.e. Woudberg and Du Plessis [94] and Maré [65]) and will not be repeated in this study. However, in order to accommodate the different assumptions applied to the calculation of the distance between the parallel plates of the different RUC models (as explained in Chapter 1), both equations (1.11) and (1.12) are adjusted with the incorporation of a slip boundary condition. Equations (1.11) and (1.12) then become

$$\tau_w = \frac{12\mu v_{\text{avg}}}{D_h} \frac{1}{\left[1 + 12\frac{(2-\sigma)}{\sigma} Kn\right]}, \tag{5.5}$$

and

$$\tau_w = \frac{6\mu v_{\text{avg}}}{B} \frac{1}{\left[1 + 12\frac{(2-\sigma)}{\sigma} Kn\right]}, \tag{5.6}$$

respectively. Consequently, the Darcy permeability expressions of all the RUC models presented can be adjusted using the Klinkenberg-type equation, given by equation (5.4), provided that the Knudsen number is assumed to be constant for the porous medium and

flow conditions presented. In the case where a constant Knudsen number is not provided (i.e. experimental data for the Knudsen number is not provided), the application of equation (5.1) requires that the same assumptions in the derivation of the average wall shear stress and permeability expressions of the RUC models need to be implemented, i.e. the hydraulic diameter in equation (5.1) is then equal to the respective expressions for the hydraulic diameter in each average wall shear stress expression obtained in the process of determining the permeability expression for each RUC model. The expressions for the Darcy permeability in the case where the Knudsen number needs to be determined using equation (5.1) will be given next for each of the RUC models under consideration. The equations for predicting the Darcy permeability of the RUC models given in Chapter 1, i.e. the RUC models without any other adjustments, are adapted first.

5.2.1 1D RUC model

The hydraulic diameter for the 1D RUC model for transverse flow differs from the hydraulic diameter for the 1D RUC model for parallel flow. Consequently, the Knudsen numbers differ and the respective Klinkenberg-type equations are thus also different. Due to the presence of only one strut in each of the respective models, the Klinkenberg-type equations for predicting the gas permeability can be presented as a function of the liquid permeability.

1D RUC model: Transverse flow

In the case of the 1D RUC model for transverse flow, the hydraulic diameter is equal to twice the pore diameter, i.e. $D_h = 2d_p$. In terms of b, the gas permeability therefore becomes:

$$K_g = b^2 \frac{\pi \left(1-\sqrt{1-\epsilon}\right)^3}{54\left(1-\epsilon\right)^{3/2}} \left[1 + \frac{12\lambda\left(2-\sigma\right)\sqrt{1-\epsilon}}{\sqrt{\pi}\, b\, \sigma \left(1-\sqrt{1-\epsilon}\right)}\right], \tag{5.7}$$

which, in turn, is given by

$$K_g = K_l \left[1 + \frac{12\lambda\left(2-\sigma\right)\sqrt{1-\epsilon}}{\sqrt{\pi}\, b\, \sigma \left(1-\sqrt{1-\epsilon}\right)}\right], \tag{5.8}$$

in terms of the liquid permeability, K_l (where K_l is given by equation (2.16)).

1D RUC model: Parallel flow

The hydraulic diameter of the 1D RUC model for parallel flow is given by equation (2.20) and consequently yields the following Klinkenberg-type equation:

$$K_g = K_l \left[1 + \frac{24\lambda\left(2-\sigma\right)\left(1-\epsilon\right)}{\sqrt{\pi}\, b\, \epsilon\, \sigma}\right], \tag{5.9}$$

where K_l is given by equation (2.23).

5.2.2 2D RUC model

The "mixing rule", as discussed in Chapter 2, Section 2.2.2, is once again applicable in order to determine the expressions for the 2D RUC models, for in-plane and through plane flow, respectively. The weights assigned to the respective model orientations remain the same as those provided in Chapter 2.

2D RUC model: In-plane flow

Since the 2D RUC model for in-plane flow is orientated in such a way that one strut is perpendicular to the streamwise flow direction and the other is parallel to the streamwise flow direction, a combination of both the permeability expressions of the 1D RUC model for transverse flow and the 1D RUC model for parallel flow is required. Consequently, the permeability equation for the 2D RUC model for in-plane flow cannot be adjusted in order to incorporate the Klinkenberg effect in such a way that the gas permeability can be written in terms of the liquid permeability. The gas permeability equation is therefore given by

$$K_g = b^2 \frac{\pi}{4} \left[\frac{1}{2} \left[\frac{48\left(1-\epsilon\right)^2}{\epsilon^3} \left[1 + \frac{24\lambda\left(2-\sigma\right)\left(1-\epsilon\right)}{\sqrt{\pi}\, b\, \epsilon\, \sigma} \right]^{-1} \right] + \frac{1}{2} \left[\frac{13.5\left(1-\epsilon\right)^{3/2}}{\left(1-\sqrt{1-\epsilon}\right)^3} \left[1 + \frac{12\lambda\left(2-\sigma\right)\sqrt{1-\epsilon}}{\sqrt{\pi}\, b\, \sigma\left(1-\sqrt{1-\epsilon}\right)} \right]^{-1} \right] \right]^{-1}, \tag{5.10}$$

In the case where the Knudsen number indicates that the Klinkenberg effect is not negligible, equation (5.10) is thus used rather than equation (2.52).

2D RUC model: Through plane flow

The 2D RUC model for through plane flow, however, only has struts orientated perpendicular to the streamwise flow direction and therefore only requires the use of equation (5.7). The equation for the Darcy permeability for gas flow can therefore be expressed in terms of the liquid permeability, i.e.

$$K_g = K_l \left[1 + \frac{12\lambda\left(2-\sigma\right)\sqrt{1-\epsilon}}{\sqrt{\pi}\, b\, \sigma\left(1-\sqrt{1-\epsilon}\right)} \right], \tag{5.11}$$

where K_l is determined using equation (2.55).

5.2.3 3D RUC model

Similar to the 2D RUC model for in-plane flow, the 3D RUC model is a combination of struts orientated perpendicular and parallel to the streamwise flow direction. The gas permeability can consequently not be expressed as a function of the liquid permeability, given by equation (2.78). Equations (5.8) and (5.9) can therefore be substituted into

equation (2.49) as $K_\perp$ and $K_\parallel$, respectively, along with the corresponding weights provided in Section 2.3.2 (Chapter 2), in order to determine the following expression:

$$K_g = b^2 \frac{\pi}{4} \left[\frac{1}{3} \left[\frac{48\,(1-\epsilon)^2}{\epsilon^3} \left[1 + \frac{24\lambda\,(2-\sigma)\,(1-\epsilon)}{\sqrt{\pi}\,b\,\epsilon\,\sigma} \right]^{-1} \right] + \frac{2}{3} \left[\frac{13.5\,(1-\epsilon)^{3/2}}{\left(1-\sqrt{1-\epsilon}\right)^3} \left[1 + \frac{12\lambda\,(2-\sigma)\,\sqrt{1-\epsilon}}{\sqrt{\pi}\,b\,\sigma\,\left(1-\sqrt{1-\epsilon}\right)} \right]^{-1} \right] \right]^{-1} . \tag{5.12}$$

Equation (5.12) can therefore be utilized in the case of gas flow through a fibrous porous medium where the Klinkenberg effect is not negligible.

5.2.4 Two-strut RUC model

The hydraulic diameter for the two-strut RUC model is $D_h = 2d_p$, whether for in-plane flow or through plane flow. All the flow channel dimensions within the two-strut RUC models also remain the same. The gas permeability of the two-strut RUC models can therefore be expressed in terms of the liquid permeability.

Two-strut RUC model: In-plane flow

The expression for the gas permeability of the two-strut RUC model for in-plane flow, where the Klinkenberg effect is incorporated, is given by

$$K_g = K_l \left[1 + \frac{12\lambda\,(2-\sigma)\,(\psi-\epsilon)}{\sqrt{\pi}\,b\,\epsilon\,\sigma} \right] , \tag{5.13}$$

where K_l is given by equation (2.99).

Two-strut RUC model: Through plane flow

Similarly, the gas permeability for the two-strut RUC model for through plane flow can also be obtained using equation (5.13). The expression for K_l in this case is, however, given by equation (2.110).

5.2.5 Three-strut RUC model

The hydraulic diameter of the three-strut RUC model is also given by $D_h = 2d_p$. However, due to different model dimension relations, the Klinkenberg-type equation of the three-strut RUC model is different to equation (5.13). The gas permeability equation for the three-strut RUC model in terms of the fibre diameter yields

$$K_g = K_l \left[1 + \frac{6\lambda\,(2-\sigma)\,(\psi-1)}{b\,\sigma\,(3-\psi)} \right] , \tag{5.14}$$

where K_l can be determined from equation (2.125). In terms of the pore diameter, the gas permeability becomes

$$K_g = K_l \left[1 + \frac{6\lambda\,(2-\sigma)}{d_p\,\sigma} \right] , \tag{5.15}$$

where K_l is given in this case by equation (2.127).

All the relations between the pore dimensions of the 1D, 2D, 3D, two-strut and three-strut RUC models remain the same, as explained in Chapter 2. The method of incorporation of the Klinkenberg effect into the Darcy permeability equations of the NARUC models, of which the liquid permeability equations are provided in Chapter 3, are discussed in the next section.

5.2.6 NARUC models

In Chapter 3, the three-strut RUC model was adapted to account for accumulation of solid present at the nodes of a foam. The adjusted Darcy permeability equation of the NARUC model is given by equation (3.87), which represents the liquid permeability in the context of this chapter. The hydraulic diameter in this case is $D_h = 2d_p^*$, since the parameter adjustment (as discussed in Chapter 3, Section 3.2) also needs to be incorporated in this section. Consequently, in terms of d_p, the hydraulic diameter can be deduced from equation (3.76), and is given by

$$D_h = \frac{2\left(1 - 2r_1 R\right)}{1 - 2r_1 R} d_p \,, \tag{5.16}$$

where the different methods of calculating r_1 and R are discussed in detail in Chapter 3, Sections 3.2.1 and 3.2.2. The resulting Klinkenberg-type equation for the NARUC model results in

$$K_g = K_l \left[1 + \frac{6\lambda\left(2 - \sigma\right)\left(1 - 2r_1\right)}{d_p\,\sigma\left(1 - 2r_1 R\right)}\right] \,, \tag{5.17}$$

where K_l is given by equation (3.87), as noted previously.

In the following sections, the CARUC models, adjusted to accommodate compression and the anisotropic geometry of fibrous porous media in the uncompressed state, are adapted by incorporating the Klinkenberg effect.

5.2.7 Two-strut CARUC model

In the case of the two-strut CARUC models, the hydraulic diameter is dependent on the orientation of the struts due to the distinction between the dimensions (based on orientation with respect to the streamwise direction) in these models, i.e. there is a distinction between the different distances of the parallel plates formed by the different struts. The gas permeability equations can therefore also not be presented in terms of the liquid permeability.

Two-strut CARUC model: In-plane flow

Incorporating the Klinkenberg effect into the Darcy permeability for the two-strut RUC model for in-plane flow leads to the following equation for the gas permeability:

$$K_g = \frac{d_{\parallel} d_{\perp_1} \left(d_{\perp_2} - d_{s_{\perp_2}}\right)}{12 d_{\perp_2}} \left[\frac{d_{s_{\perp_1}} \left(d_{\parallel} - d_{s_{\parallel}}\right) + d_{s_{\parallel}} \left(d_{\perp_1} - d_{s_{\perp_1}}\right) + d_{s_{\parallel}} d_{s_{\perp_1}}}{\left(d_{\perp_2} - d_{s_{\perp_2}}\right)^2} \right.$$
$$\times \left[1 + \frac{6\lambda\,(2-\sigma)}{\sigma \left(d_{\perp_2} - d_{s_{\perp_2}}\right)}\right]^{-1} + \frac{d_{s_{\perp_2}} d_{\perp_1}}{\left(d_{\parallel} - d_{s_{\parallel}}\right)^2} \left[1 + \frac{6\lambda\,(2-\sigma)}{\sigma \left(d_{\parallel} - d_{s_{\parallel}}\right)}\right]^{-1}$$
$$\left. + \frac{d_{s_{\perp_2}} d_{\perp_1}}{\left(d_{\perp_1} - d_{s_{\perp_1}}\right)^2} \left[1 + \frac{6\lambda\,(2-\sigma)}{\sigma \left(d_{\perp_1} - d_{s_{\perp_1}}\right)}\right]^{-1} \right]^{-1} . \tag{5.18}$$

The three different pore diameters yield three different hydraulic diameters associated with the three expressions for the average wall shear stress used to acquire the permeability. Consequently, it is noticed that there are three different Klinkenberg-type terms present in equation (5.18). Just for reference, the liquid permeability of the two-strut RUC model for in-plane flow is given by equation (4.22).

Two-strut CARUC model: Through plane flow

In the case of the two-strut RUC model for through plane flow, determined similarly as in the case of the two-strut model for in-plane flow, the gas permeability equation is given by

$$K_g = \frac{d_{\parallel} \left(d_{\perp_1} - d_{s_{\perp_1}}\right) \left(d_{\perp_2} - d_{s_{\perp_2}}\right)}{12} \left[\frac{d_{s_{\parallel}} d_{\perp_1} d_{\perp_2}}{\left(d_{\perp_2} - d_{s_{\perp_2}}\right)^2} \left[1 + \frac{6\lambda\,(2-\sigma)}{\sigma \left(d_{\perp_2} - d_{s_{\perp_2}}\right)}\right]^{-1} \right.$$
$$+ \frac{d_{s_{\parallel}} d_{\perp_1} d_{\perp_2}}{\left(d_{\perp_1} - d_{s_{\perp_1}}\right)^2} \left[1 + \frac{6\lambda\,(2-\sigma)}{\sigma \left(d_{\perp_1} - d_{s_{\perp_1}}\right)}\right]^{-1}$$
$$+ \frac{d_{s_{\perp_1}} d_{\perp_1} \left[\left(d_{\perp_2} - d_{s_{\perp_2}}\right) + \frac{1}{2} d_{s_{\perp_2}}\right] + d_{s_{\perp_2}} d_{\perp_2} \left[\left(d_{\perp_1} - d_{s_{\perp_1}}\right) + \frac{1}{2} d_{s_{\perp_1}}\right]}{\left(d_{\parallel} - d_{s_{\parallel}}\right)^2}$$
$$\left. \times \left[1 + \frac{6\lambda\,(2-\sigma)}{\sigma \left(d_{\parallel} - d_{s_{\parallel}}\right)}\right]^{-1} \right]^{-1} , \tag{5.19}$$

where the liquid permeability is again for the sake of reference given by equation (4.42).

5.2.8 Three-strut CARUC model

The liquid permeability of the three-strut CARUC model is given by equation (4.77). The Klinkenberg effect is incorporated into the Darcy permeability similarly as in the case of the two-strut CARUC models which leads to the following expression for the gas permeability of the three-strut CARUC model

$$K_g = \frac{d_{\parallel}\left(d_{\perp_1} - d_{s_{\perp_1}}\right)\left(d_{\perp_2} - d_{s_{\perp_2}}\right)}{12 d_{\perp_1} d_{\perp_2}} \left[\frac{d_{s_{\parallel}} + d_{s_{\perp_1}}}{\left(d_{\perp_2} - d_{s_{\perp_2}}\right)^2} \left[1 + \frac{6\lambda\,(2-\sigma)}{\sigma\left(d_{\perp_2} - d_{s_{\perp_2}}\right)}\right]^{-1} \right.$$
$$+ \frac{d_{s_{\parallel}} + d_{s_{\perp_2}}}{\left(d_{\perp_1} - d_{s_{\perp_1}}\right)^2} \left[1 + \frac{6\lambda\,(2-\sigma)}{\sigma\left(d_{\perp_1} - d_{s_{\perp_1}}\right)}\right]^{-1}$$
$$\left. + \frac{d_{s_{\perp_1}} + d_{s_{\perp_2}}}{\left(d_{\parallel} - d_{s_{\parallel}}\right)^2} \left[1 + \frac{6\lambda\,(2-\sigma)}{\sigma\left(d_{\parallel} - d_{s_{\parallel}}\right)}\right]^{-1} \right]^{-1}. \tag{5.20}$$

It is important to note that the equations for the specific surface area determined using a combined approach and the Darcy permeability in Chapters 2 to 4 can also be adapted to incorporate the Klinkenberg effect by replacing K in these equations with K_g, acquired in the current section for each of the RUC models, respectively. For example, in order to determine S_v in terms of K_g for the 2D RUC model for in-plane flow, equations (2.61) and (5.10) are combined instead of equations (2.52) and (2.61), in the case where the Klinkenberg effect is not negligible in obtaining the Darcy permeability data.

In order to illustrate the application of the two- and three-strut CARUC models with the incorporated Klinkenberg effect, examples of a hard streamwise compressed two-strut CARUC model for through plane flow and three-strut CARUC model and the incorporation of the Klinkenberg effect is considered in the following section.

5.2.9 Hard streamwise compressed CARUC models

Similar to Chapter 4, these CARUC model examples, where the two-strut CARUC model for through plane flow and three-strut CARUC model is considered to be hard and undergoes streamwise compression (provided in Section 4.3.2), will further be specifically adjusted in this section to incorporate the Klinkenberg effect. The resulting expressions are also included in Woudberg et al. [77]. In this section, the case where a constant Knudsen number is provided is considered. The adjustments made to account for the Klinkenberg effect is consequently the implementation of equation (5.4).

Two-strut CARUC model: Through plane flow

Incorporating the liquid permeability predictions of the hard two-strut CARUC model for through plane flow subject to streamwise compression, given by equation (4.108), into

equation (5.4) leads to

$$K_g = \frac{d_{\parallel}\left(d_{\perp}-d_s\right)^2\left[1+12\left(\left(2-\sigma\right)/\sigma\right)Kn\right]}{24d_s d_{\perp}^2}\left[\frac{1}{\left(d_{\perp}-d_s\right)^2}+\frac{2d_{\perp}-d_s}{2d_{\perp}\left(d_{\parallel}-d_s\right)^2}\right]^{-1}. \quad (5.21)$$

Equation (5.21) can furthermore be utilized to determine the specific surface area using a combined approach. A third-degree polynomial in terms of S_v is obtained similarly as the polynomial obtained in Section 4.3.2, given by equation (4.115), with the following coefficients:

$$\begin{aligned}
a' &= 48d_s^3 d_{\perp}^9 K_g + 24d_s d_{\perp}^8 K_g m\left(2d_{\perp}-d_s\right)\\
b' &= -192d_s^3 d_{\perp}^7 K_g\left(4d_{\perp}-3d_s\right) - 4d_s^3 d_{\perp}^5 m^2 l\left(4d_{\perp}-3d_s\right)\\
c' &= 192d_s^3 d_{\perp}^5 K_g\left(4d_{\perp}-3d_s\right)^2 + 16d_s^3 d_{\perp}^3 m^2 l\left(4d_{\perp}-3d_s\right)^2\\
g' &= -16d_s^3 d_{\perp} m^2 l\left(4d_{\perp}-3d_s\right)^3 ,
\end{aligned} \quad (5.22)$$

where $m = \left(d_{\perp}-d_s\right)^2$ once again, and $l = \left[1+12\left(\left(2-\sigma\right)/\sigma\right)Kn\right]$.

Three-strut CARUC model

Similar to the two-strut CARUC model for through plane flow, the gas permeability equation of the the hard three-strut CARUC model subject to compression in the streamwise direction can be determined by incorporating equation (4.92) into equation (5.4), i.e. the equation for the liquid permeability, yielding

$$K_g = \frac{d_{\parallel}\left(d_{\perp}-d_s\right)^2\left[1+12\left(\left(2-\sigma\right)/\sigma\right)Kn\right]}{24d_s d_{\perp}^2}\left[\frac{2}{\left(d_{\perp}-d_s\right)^2}+\frac{1}{\left(d_{\parallel}-d_s\right)^2}\right]^{-1}. \quad (5.23)$$

Utilizing equation (5.23) to obtain the specific surface area then leads to the following polynomial coefficients, as opposed to the coefficients given in equation (4.95):

$$\begin{aligned}
a' &= 48d_s^3 d_{\perp}^8 K_g + 24d_s d_{\perp}^8 K_g m\\
b' &= -768d_s^3 d_{\perp}^7 K_g + 576d_s^4 d_{\perp}^6 K_g - 8d_s^3 d_{\perp}^5 m^2 l + 12d_s^4 d_{\perp}^4 m^2 l - 288d_s^2 d_{\perp}^6 K_g m\\
c' &= 3072d_s^3 d_{\perp}^6 K_g - 3072d_s^4 d_{\perp}^5 K_g + 128d_s^3 d_{\perp}^4 m^2 l - 320d_s^4 d_{\perp}^3 m^2 l + 192d_s^5 d_{\perp}^2 m^2 l\\
&\quad + 1152d_s^3 d_{\perp}^4 K_g m\\
g' &= -512d_s^3 d_{\perp}^3 m^2 l + 1792d_s^4 d_{\perp}^2 m^2 l - 2048d_s^5 d_{\perp} m^2 l + 768d_s^6 m^2 l\\
&\quad - 12288d_s^4 d_{\perp}^4 K_g + 24576d_s^5 d_{\perp}^3 K_g - 12288d_s^6 d_{\perp}^2 K_g - 1536d_s^4 d_{\perp}^2 K_g m ,
\end{aligned} \quad (5.24)$$

which can be used to solve the third-degree polynomial for the specific surface area (i.e. $a'S_v^3 + b'S_v^2 + c'S_v + g' = 0$). The expressions for m and l are the same as provided in the case of the two-strut CARUC model for through plane flow, that is, $m = \left(d_{\perp}-d_s\right)^2$ once again, and $l = \left[1+12\left(\left(2-\sigma\right)/\sigma\right)Kn\right]$.

In the following section, some of the RUC models with and without the Klinkenberg effect will be compared to one another as well as against available experimental data obtained from the literature.

5.3 Comparison of RUC models

Similar to the comparison of the CARUC models in Chapter 4, the data sets utilized in the comparison of the RUC models with the Klinkenberg effect are provided in this section and not in Chapter 1. With regards to the information required to take the slippage effect into account (i.e. the Knudsen number or a manner in which to obtain the Knudsen number, the TMAC and the conditions which makes the slippage affect non-negligible in the prediction of the Darcy permeability), there is a scarcity of data sets available in the literature for comparison purposes. Consequently, only two data sets are included in this chapter. The first data set comprises of experimental data acquired from Jackson and James [8].

5.3.1 Jackson and James [8]:

As mentioned in Chapter 4, Jackson and James [8] provided experimental permeability data for a wide variety of fibrous media from the literature. In order to ensure that the data they considered did not require the inclusion of adjustments for slippage effects of the fluids at the fibre surfaces, they required that $Kn < 0.01$. In our study, however, it is required that $0.001 < Kn < 0.1$ for the Klinkenberg effect to be taken into consideration and consequently some of the data considered by Jackson and James can be utilized in this section to study the Klinkenberg effect incorporation in some of the fibre RUC models. The data they acquired from Sullivan [63] and Wheat [103] for goat wool and glass fibres will be utilized in this study and is listed in Table 5.1. The data furthermore includes the Knudsen numbers associated with the different fibrous media, as provided by Jackson and James [8].

In the work of Sullivan [63] the goat and glass wool samples were packed in a tube in such a way that it was aligned with the flow. The data regarding the sample of glass fibres, as provided in Table 5.1, was acquired by Jackson and James [8] from Wheat [103], who provided data on filter mats. A constant Knudsen number for flow through the different samples of fibrous porous media was provided by Jackson and James [8] and consequently equation (5.4) is utilized in order to take the Klinkenberg effect into account in the relevant RUC models. It is assumed that the goat wool, glass wool and glass fibres have smooth surfaces and therefore that the value for the TMAC is $\sigma = 0.2$. In the case of the goat and glass wool a 2D fibre arrangement corresponding to in-plane flow is considered due to the alignment of the samples with the streamwise flow direction. Consequently, equations (2.52) and (2.99) are used to determine K_l for the 2D and two-strut RUC models, respectively, which is then substituted into equation (5.4) to obtain the values for K_g. A 2D arrangement for through plane flow is assumed in the sample of glass fibres due to the confirmation that the data was obtained for the permeability of filter mats. Equations (2.55) and (2.110) are utilized in this case to obtain the values for K_l for the 2D and two-strut RUC models for through plane flow, respectively.

Model validation

In Figure 5.1 the predictions of the Darcy permeability for the 2D and two-strut RUC models for in-plane flow, with and without the Klinkenberg effect taken into account, and the experimental data provided in Table 5.1 for the goat wool are shown. Due to the

TABLE 5.1: *Experimental data obtained from Jackson and James [8] for goat wool and glass fibre-type media*

Fibre type	ϵ	$b\,[\mu\text{m}]$	Kn	$K \times 10^9\,[\text{m}^2]$
Goat wool	0.638	0.000039	0.002	0.121
	0.64			0.125
	0.805			0.612
	0.844			0.947
	0.861			1.12
	0.883			1.56
	0.888			1.92
	0.902			2.29
	0.9065			2.32
	0.9221			3.12
	0.9405			5.21
	0.9532			7.41
	0.961			9.73
	0.9666			11.8
	0.9708			13.9
	0.9766			18.7
	0.9787			21.5
	0.9805			24.5
	0.982			27.5
	0.9833			30.7
	0.9844			34.3
Glass wool	0.866	0.000076	0.01	4.32
Glass fibres	0.747	78	0.008	0.00000072
	0.769	144		0.00000214

low number of data provided for the glass wool and glass fibres, the predictions regarding these samples are listed in Table 5.2.

Figure 5.1 shows that the incorporation of the Klinkenberg effect leads to a slight increase in the permeability predictions of the 2D and two-strut RUC models, as expected. It is furthermore evident that the RUC model predictions correspond more accurately to the experimental data for porosities higher than 0.9, where-as for lower porosity values it progressively underpredicts the data. It should be noted, however, that Figure 5.1 displays a semilog plot and therefore the models also correspond closely to the experimental data situated at low porosities. The average relative percentage errors between the liquid and gas permeability predictions of the RUC models when compared to the experimental data are furthermore provided in Table 5.2.

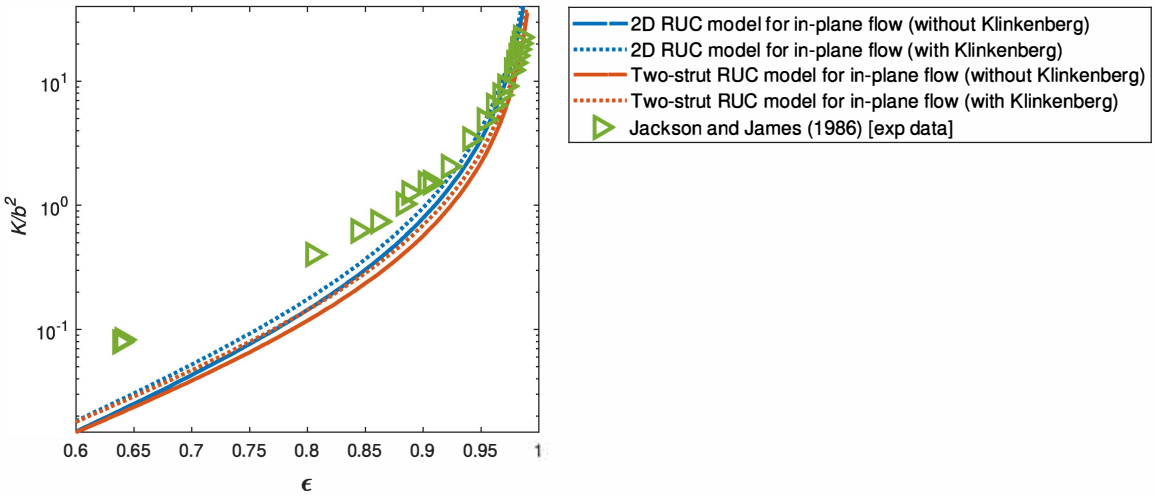

FIGURE 5.1: *Darcy permeability prediction versus porosity of 2D and two-strut RUC models for in-plane flow and goat wool experimental data of Jackson and James [8] with incorporated Klinkenberg effect*

TABLE 5.2: *Predictions of the Darcy permeability of RUC models with and without incorporated Klinkenberg effect and relative percentage error compared to the experimental data obtained from Jackson and James [8]*

Fibre type	ϵ	**RUC model**	K_l	K_g
			$K \times 10^9$ [m^2]	
Glass wool	0.866	2D: in-plane flow	2.31	4.81
		Two-strut: in-plane flow	1.75	3.64
Glass fibres	0.747	2D: through plane flow	0.34×10^{-6}	0.64×10^{-6}
		Two-strut: through plane flow	0.23×10^{-6}	0.43×10^{-6}
	0.769	2D: through plane flow	1.52×10^{-6}	2.84×10^{-6}
		Two-strut: through plane flow	1.05×10^{-6}	1.95×10^{-6}
Average relative percentage error:				
Goat wool		2D: in-plane flow	37%	40%
		Two-strut: in-plane flow	49%	38%
Glass wool		2D: in-plane flow	47%	11%
		Two-strut: in-plane flow	59%	16%
Glass fibres		2D: through plane flow	41%	22%
		Two-strut: through plane flow	59%	24%

Table 5.2 (together with Figure 5.1) show that the 2D and two-strut RUC models that take the Klinkenberg effect into account provide closer correspondence to the experimental data acquired from Jackson and James [8] with the exception being the 2D RUC model for in-plane flow in comparison with the goat wool data. This is observed even though the Knudsen numbers provided were closer to the boundary of where no-slip flow is expected to occur. Furthermore, in cases where the Knudsen number is higher, i.e. for the glass wool sample, the improvement in permeability prediction due to the incorporation of the Klinkenberg effect is rather significant, i.e. by performing more than 40% accurate in the case of both models. Consequently, the boundary condition of implementing the Klinkenberg effect for which $Kn > 10^{-3}$ is justified.

Next, experimental data acquired from Le Coq [13] is considered.

5.3.2 Le Coq [13]:

Le Coq [13] studied experimentally the flow of air through compressed non-woven glass fibre media with a mean fibre diameter of $b = 2.7\mu$m. The permeability values were obtained from mercury porosimetry and permeametry, with compression examined only in the streamwise direction. Four states of compression were considered, including the non-compressed state, where the four values for the experimentally measured compression ratio $e_{\parallel}$ are given in Table 5.3, together with the corresponding measured porosity and hydraulic pore diameter values at the different states of compression. The pore size distribution forms a log-normal distribution of which the standard deviation in the D_h-values, denoted by s_{D_h}, are also indicated in Table 5.3. Miguel and Serrenho [95] estimated the mean free path of air to be $\lambda = 70$ nm. This value for λ, along with the hydraulic diameter values provided by Le Coq [13] and equation (5.1), were used to calculate the Knudsen numbers for airflow and are also given in Table 5.3. Since all the Knudsen numbers fall within the range $10^{-3} < Kn < 10^{-1}$, although just above the lower boundary value, the effect thereof on the permeability prediction is, however, still investigated.

TABLE 5.3: *Experimental data obtained from Le Coq [13] for glass fibre blends with $b = 2.7\,\mu$m*

Experimental procedure	ϵ	$e_{\parallel}$	D_h [μm]	s_{D_h} [μm]	$Kn \times 10^3$	$K \times 10^9$ [m^2]
mercury porosimetry	0.86	0.55	16	3.6	4.4	0.00017
	0.89	0.75	16.5	3.4	4.2	0.0014
	0.92	0.85	17	3.5	4.1	0.0020
	0.94	1	28	2.4	2.5	0.0082
permeametry	0.92	0.85	17	3.5	4.1	0.0021
	0.94	1	28	2.4	2.5	0.0100

A horizontal view of a portion of the non-woven glass fibre media shown in Figure 2(b) of Woudberg et al. [83] leads to the consideration that the two-strut CARUC model provides a more realistic representation of the average pore-scale geometry than that of the three-strut RUC model, even though Woudberg et al. [83] used the same media to validate the three-strut RUC model. The fibrous media was furthermore produced by randomly depositing fibres in a horizontal plane in order to form a stacking of layered sheets. The glass fibre material can therefore be regarded as isotropic in the plane of each sheet but anisotropic in the thickness. The layered sheets were orientated perpendicular to the streamwise flow direction. The data will consequently be used in this section to validate the two-strut RUC models for through plane flow. Since the fibres under consideration are made from glass, the surfaces are expected to be smooth and consequently a value of 0.2 is used for σ. Since the fibres are made of glass the material is considered to be hard and therefore the condition $d_{s_{\parallel}} = d_{s_{\perp_1}} = d_{s_{\perp_2}} = d_{s_o}$ is implemented. Due to the fibre arrangement being regarded as isotropic planes, it is furthermore assumed that $d_{\perp_1} = d_{\perp_2} = d_{\perp}$. In order to determine the state of the uncompressed media, i.e. where $e_{\parallel} = 1$, the hydraulic diameter data is utilized by assuming that $D_h = d_{\perp} - d_s$ (representing the pore diameter of the planes transverse to the streamwise direction). Two methods of incorporating the Klinkenberg effect are therefore considered in this section: one in which

$D_h = d_\perp - d_s$ is utilized along with the data for D_h provided in Table 5.3 and equation (5.19), and one in which equation (5.4) is utilized, where K_l is determined from equation (4.108) and Kn is as provided in Table 5.3. Combining the assumed expression for the hydraulic diameter with equation (4.98) for the two-strut CARUC model for through plane flow, the following expression is obtained for the streamwise face diameter:

$$d_\parallel = \frac{d_s^2 \left(2D_h + d_s\right)}{\left(D_h + d_s\right)^2 \left(1 - \epsilon\right)}. \tag{5.25}$$

Substituting equation (5.25) into the expression on the left-hand side of equation (4.84), and utilizing the values of $e_\parallel$ and D_h provided in Table 5.3, an average value for $d_{\parallel_o}$ can be determined for the two-strut CARUC model for through plane flow, yielding 7.2 μm. The transverse dimension $d_\perp$ can then be calculated using equation (4.99) and the streamwise dimension $d_\parallel$ can be determined using equation (4.89). In order to provide a continuous prediction of the permeability, equation (4.88) can furthermore be utilized, where C is determined to be 0.079. In the case where a constant Kn is utilized, however, a continuous prediction cannot be provided and therefore the ϵ- and e-values are acquired from Table 5.3.

Model validation

The predictions of the Darcy permeability as a function of porosity obtained for the two-strut RUC model for through plane flow of the uncompressed case, the compressed case without the Klinkenberg effect and the compressed case in which the Klinkenberg effect is taken into consideration, are shown in Figure 5.2. The experimental data provided by Le Coq [13] as presented in Table 5.3 are also indicated.

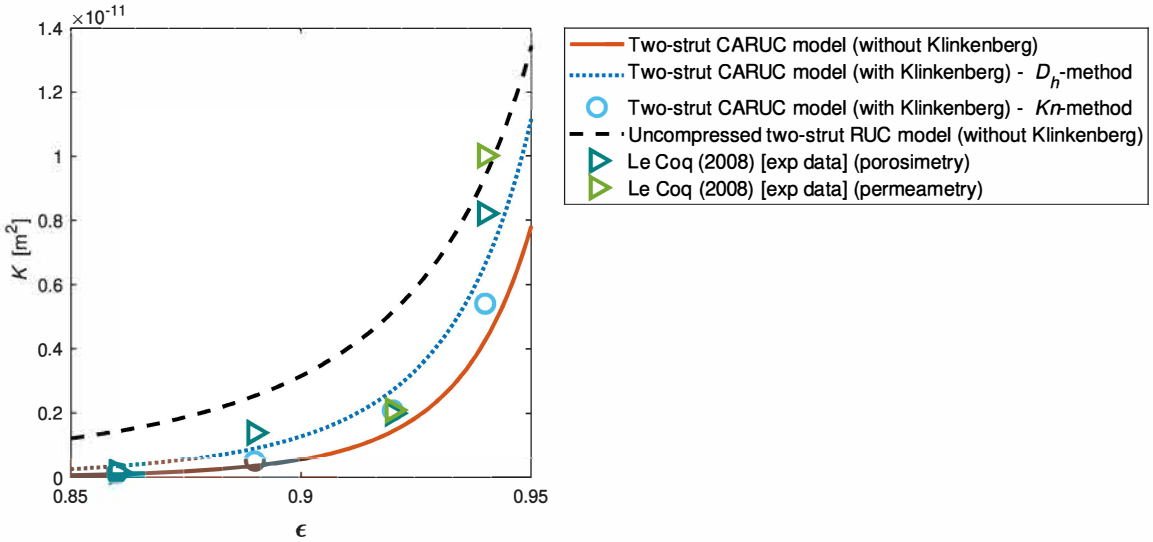

FIGURE 5.2: *Darcy permeability prediction versus porosity of two-strut RUC models for through plane flow and glass fibre experimental data of Le Coq [13] subject to compression with incorporated Klinkenberg effect*

The model predictions acquired using equation (5.19) and the D_h-data provided in Table 5.3 is indicated in Figure 5.2 as the 'D_h-method' and the predictions acquired using equation (5.4) and the Kn-data is described as the 'Kn-method'. It can be seen in Figure 5.2

that the two-strut CARUC model excluding the Klinkenberg effect, provides lower predictions than that of the uncompressed model, as expected. The increase in permeability as a result of the Klinkenberg effect for gas flow observed in the two-strut model predictions is justified from a physical point of view and provides confidence in the mathematical modelling procedure. Furthermore, the two-strut RUC models for through plane flow where both compression and the Klinkenberg effect is taken into consideration, for both the D_h- and Kn-method, provide the best agreement (in general) amongst the models and cases considered in this section. The average relative percentage error between the measured permeability values and the two-strut CARUC model prediction including the Klinkenberg effect of the D_h-method is 48% and of the Kn-method is 32%, which is lower than the average relative percentage error of 50% and 249% of the compressed and uncompressed two-strut RUC model predictions without the Klinkenberg effect, respectively. Figure 5.2 indicates that the model with the Klinkenberg effect and acquired using the D_h-method, however, corresponds considerably closer to the trend of the experimental data than the other models, even though the average relative percentage error is close to the compressed model without the Klinkenberg effect incorporated. The D_h-method is furthermore preferred due to the ability to provide a continuous prediction, whereas the Kn-method in this case can only provide the specific predictions for the data points provided by Le Coq [13].

The stacking of fibrous sheets constituting the fibrous medium consists of three layers, referred to as the upstream, center and downstream layers (Le Coq [13]). The standard deviation in pore size (i.e. the hydraulic diameter) across the thickness of the three layers can be expressed in terms of percentage errors as 8.5% for the uncompressed state and about 20% for the three states of compression. The influence of the standard deviation in mean hydraulic pore diameter values on the two-strut CARUC model prediction including the Klinkenberg effect and obtained using the D_h-method is shown in Figure 5.3.

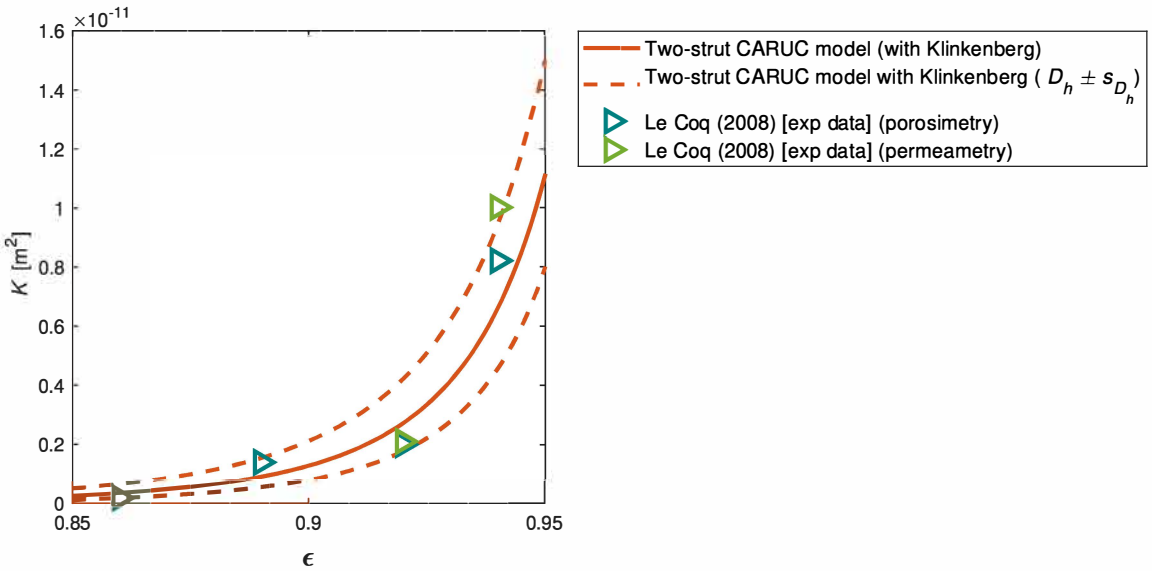

FIGURE 5.3: *Darcy permeability prediction versus porosity of two-strut CARUC model for through plane flow with incorporated Klinkenberg effect and glass fibre experimental data of Le Coq [13] under compression including the effect of standard deviation in hydraulic diameter values*

The effect of the standard deviation incorporated into the mean hydraulic pore diameter

values on the model prediction proves to be rather significant, as observed in Figure 5.3. Since the pore size distribution takes on a log-normal distribution, it is more probable that the hydraulic pore diameter increases through the different layers as a result of the heterogeneity. The average of the average relative percentage errors with the standard deviation added to the mean hydraulic pore diameter values and subtracted from the mean hydraulic pore diameter values at the different stages of compression is 67%. Table 5.3 shows that the standard deviation increases with an increase in compression which can be interpreted as an increase in heterogeneity (Woudberg et al. [77]). One can therefore not be too critical about the accuracy of the model prediction given the accompanied uncertainty in the experimental values. In Figure 5.3 it is furthermore noted that most of the experimentally obtained permeability values lie within the bounding curves provided by the model predictions in which the standard deviation of the hydraulic diameter is included. Furthermore, although the Knudsen numbers are close to the bounding value separating the no-slip and slip flow regimes, the Klinkenberg effect proved to be non-negligible and, as expected, become more significant with an increase in Knudsen numbers, albeit still in the slip flow regime.

5.4 Chapter summary

The Klinkenberg effect was discussed and incorporated into the RUC models presented in Chapters 1 to 4. The conditions under which the Klinkenberg effect should be taken into consideration were addressed and a general equation which relates the liquid and gas permeabilities of the RUC models was provided, i.e. equation (5.4). RUC models incorporating the Klinkenberg effect for which a constant Knudsen number is not provided were determined. A summary of the equation numbers of these expressions, as well as the required parameters to obtain the gas permeability of each RUC model is, furthermore, given in Table 5.4. Only the equation numbers are provided in Table 5.4, similar as in Table 4.7 in the summary of Chapter 4, due to the length of some of the equations exceeding the maximum table dimensions.

In Table 5.4, ψ_1 and ψ_2 can be determined from equations (2.44) and (2.72), respectively, and r_1 and R can be determined as explained in Sections 3.2.1 and 3.2.2 of Chapter 3.

Two data sets were utilized in order to compare and evaluate the relevant RUC models. The gas permeability predictions were higher than that of the liquid permeability predictions (as expected) and the results obtained proved to be satisfactory, i.e. the gas permeability predictions of the RUC models provided in most cases closer correspondence to the experimental data than that of the liquid permeability predictions. The availability of more experimental data sets will be useful in order to evaluate the remaining Klinkenberg effect adjusted models presented in this study.

TABLE 5.4: *Summary of specifications and numbers of the gas Darcy permeability coefficient equations acquired based on the various RUC models presented in Chapter 5*

RUC model	Eqn. i.t.o.	Eqn. no.
1D Perpendicular flow (Section 5.2.1)	$(b,\ \epsilon,\ \lambda,\ \sigma)$	(5.8)
1D Parallel flow (Section 5.2.1)	$(b,\ \epsilon,\ \lambda,\ \sigma)$	(5.9)
2D In-plane flow (Section 5.2.2)	$(b,\ \epsilon,\ \lambda,\ \sigma)$	(5.10)
2D Through plane flow (Section 5.2.2)	$(b,\ \epsilon,\ \lambda,\ \sigma)$	(5.11)
3D (Section 5.2.3)	$(b,\ \epsilon,\ \lambda,\ \sigma)$	(5.12)
Two-strut In-plane flow (Section 5.2.4)	$(b,\ \epsilon,\ \psi_1,\ \lambda,\ \sigma)$	(5.13)
Two-strut Through plane flow (Section 5.2.4)	$(b,\ \epsilon,\ \psi_1,\ \lambda,\ \sigma)$	(5.13)
Three-strut (Section 5.2.5)	$(b,\ \epsilon,\ \psi_2,\ \lambda,\ \sigma)$	(5.14)
	$(d_p,\ \epsilon,\ \psi_2,\ \lambda,\ \sigma)$	(5.15)
NARUC model (Section 5.2.6)	$(d_p,\ \epsilon,\ \psi_2,\ \lambda,\ \sigma,\ r_1,\ R)$	(5.17)
CARUC models		
Two-strut In-plane flow (Section 5.2.7)	$(d_{s_\parallel},\ d_{s_{\perp_1}},\ d_{s_{\perp_2}},\ d_\parallel,\ d_{\perp_1},\ d_{\perp_2},\ \lambda,\ \sigma)$	(5.18)
Two-strut Through plane flow (Section 5.2.7)	$(d_{s_\parallel},\ d_{s_{\perp_1}},\ d_{s_{\perp_2}},\ d_\parallel,\ d_{\perp_1},\ d_{\perp_2},\ \lambda,\ \sigma)$	(5.19)
Three-strut (Section 5.2.8)	$(d_{s_\parallel},\ d_{s_{\perp_1}},\ d_{s_{\perp_2}},\ d_\parallel,\ d_{\perp_1},d_{\perp_2},\ \lambda,\ \sigma)$	(5.20)

CHAPTER 6

Conclusions

In this study expressions for the permeability, of both the Darcy and Forchheimer regimes, and the specific surface area were provided for fibre-type and foamlike media by continuing the study of fibre and foam RUC models. A comparative study was conducted of the existing expressions based on the 2D, 3D, two-strut and three-strut RUC models. Additionally, the newly proposed expressions for the Forchheimer permeability based on the 2D and 3D models and the two-strut RUC model for in-plane flow (and for all the expressions associated with this model) were included, that have not been presented elsewhere in the literature besides the publications of which the author of this dissertation is a co-author. The comparison between the RUC models to existing geometric and empirical models and to experimental and numerical data obtained from the literature revealed that the RUC models provided satisfactory results and that the two-strut and three-strut RUC models generally performed better than the 2D and 3D RUC models. The two-strut and three-strut RUC models furthermore provided more accurate average correspondence to the available data than the other models in the literature. Two methods of incorporating solid accumulation that occur at strut intersections into the foam (or three-strut) RUC model were presented and was also compared to existing models with similar adjustments and to relevant experimental data from the literature. The expressions for the permeability and specific surface area of the Node Adjusted RUC (NARUC) model, obtained by using cubic nodes and combined with the dodecahedron model, as well as the NARUC model with curved wedge nodes, are novel and provided satisfactory results. These expressions are an overall improvement when compared to the three-strut RUC model for foams with solid accumulation present at the nodes. The two-strut and three-strut RUC models were furthermore adjusted to accommodate changes to the dimensions of a fibrous medium induced by compression or for fibrous media identified as anisotropic (rectangular in terms of the RUC) rather than isotropic (or cubic in terms of the RUC). The newly proposed compression changes include scenarios where the fibre or foam sample is compressed in a streamwise or transverse direction, whether the fibres or struts are soft and compress with the medium or hard and do not compress with the medium and whether the medium is allowed to expand with compression or not. Comparison of the three-strut Compression Adjusted RUC (CARUC) model to available experimental data in the literature revealed that the CARUC model provides more accurate predictions than that of the isotropic model, which is the desired outcome. Lastly, the Klinkenberg effect was incorporated into all the RUC models presented in the study as well as the NARUC and CARUC models.

The available and relevant experimental data revealed further improvement when taking the effect into account in conditions where slip-flow of gas molecules is expected to occur. The equations presented in this study for the permeability coefficients and specific surface area are available for other authors to use in their experimental and/or numerical studies for further validation and analysis due to its user friendliness in terms of simplicity and it being functions of measurable macroscopic parameters. Further studies could include attaining more reliable and suitable experimental data for the conditions described in this study in order to refine the model validation and rely less on assumptions to determine unknown model input parameters. Furthermore, a more in-depth study on the changes/deformation of fibres/struts of fibrous media under compression could contribute towards the implementation of the CARUC models presented in this study, especially where the dependence of the compression function on the compression ratio is concerned.

References

[1] V V Calmidi and R L Mahajan. The effective thermal conductivity of high porosity fibrous metal foams. *Journal of Heat Transfer*, 121:466–471, 1999.

[2] K Boomsma and D Poulikakos. On the effective thermal conductivity of a three-dimensionally structured fluid-saturated metal foam. *International Journal of Heat and Mass Transfer*, 44:827–836, 2001.

[3] A Bhattacharya, V V Calmidi, and R L Mahajan. Thermophysical properties of high porosity metal foams. *International Journal of Heat and Mass Transfer*, 45:1017–1031, 2002.

[4] J G Fourie and J P Du Plessis. Pressure drop modelling in cellular metallic foams. *Chemical Engineering Science*, 57:2781–2789, 2002.

[5] T T Huu, M Lacroix, C P Huu, D Schweich, and D Edouard. Towards a more realistic modeling of solid foam: Use of the pentagonal dodecahedron geometry. *Chemical Engineering Science*, 64:5131–5142, 2009.

[6] D Edouard. The effective thermal conductivity for "slim" and "fat" foams. *American Institute of Chemical Engineers Journal*, 57(6):1646–1651, 2011.

[7] J Ahmed, C Pham-Huu, and D Edouard. A predictive model based on tortuosity for pressure drop estimation in "slim" and "fat" foams. *Chemical Engineering Science*, 66:4771–4779, 2011.

[8] G W Jackson and D F James. The permeability of fibrous porous media. *The Canadian Journal of Chemical Engineering*, 64:364–374, 1986.

[9] N Dukhan. Correlations for the pressure drop for flow through metal foam. *Experiments in Fluids*, 41:665–672, 2006.

[10] S Jaganathan, H V Tafreshi, E Shim, and B Pourdeyhimi. A study on compression-induced morphological changes of nonwoven fibrous materials. *Colloids and Surfaces A: Physicochemical and Engineering Aspects*, 337:173–179, 2009.

[11] H D Akaydin, A Pierides, S Weinbaum, and Y Andreopoulos. Permeability of soft porous media under one-dimensional compaction. *Chemical Engineering Science*, 66:1–14, 2011.

[12] P De Jaeger, C T Joen, H Huisseune, B Ameel, and M De Paepe. An experimentally validated and parameterized periodic unit-cell reconstruction of open-cell foams. *Journal of Applied Physics*, 109(10):103519:1–103601:10, 2011.

[13] L Le Coq. Influence on permeability of the structural parameters of heterogeneous porous media. *Environmental Technology*, 29:141–149, 2008.

[14] S Woudberg and J P Du Plessis. An analytical Ergun-type equation for porous foams. *Chemical Engineering Science*, 148:44–54, 2016.

[15] D Edouard, M Lacroix, C P Huu, and F Luck. Pressure drop modeling on SOLID foam: State-of-the art correlation. *Chemical Engineering Journal*, 144:299–311, 2008.

[16] S Y Kim, J W Paek, and B H Kang. Flow and heat transfer correlations for porous fin in a plate-fin heat exchanger. *Journal of Heat Transfer*, 122(3):572–578, 2000.

[17] J T Gostick, M W Fowler, M D Pritzker, M A Ioannidis, and L M Behra. In-plane and through-plane permeability of carbon fiber electrode backing layers. *Journal of Power Sources*, 162:228–238, 2006.

[18] F Topin, J Bonnet, B Madani, and L Tadrist. Experimental analysis of multiphase flow in metallic foam: Flow laws, heat transfer and convective boiling. *Advanced Engineering Materials*, 8(9):890–899, 2006.

[19] G I Garrido, F C Patcas, S Lang, and B Kraushaar-Czarnetzki. Mass transfer and pressure drop in ceramic foams: A description for different pore sizes and porosities. *Chemical Engineering Science*, 63:5202–5217, 2008.

[20] B Dietrich, W Schabel, M Kind, and H Martin. Pressure drop measurements of ceramic sponges - Determining the hydraulic diameter. *Chemical Engineering Science*, 64:3633–3640, 2009.

[21] S Mancin, C Zilio, A Cavallini, and L Rossetto. Heat transfer during air flow in aluminum foams. *International Journal of Heat and Mass Transfer*, 53:4976–4984, 2010.

[22] S Mancin, C Zilio, A Diani, and L Rossetto. Experimental air heat transfer and pressure drop through copper foams. *Experimental Thermal and Fluid Science*, 36:224–232, 2012.

[23] G M Manzo, Y Wu, G G Chase, and A Goux. Comparison of nonwoven glass and stainless steel microfiber media in aerosol coalescence filtration. *Separation and Purification Technology*, 162:14–19, 2016.

[24] F Theron, E Lys, A Joubert, F Bertrand, and L Le Coq. Characterization of the porous structure of a non-woven fibrous medium for air filtration at local and global scales using porosimetry and X-ray micro-tomography. *Powder Technology*, 320:295–303, 2017.

[25] J J L Higdon and G D Ford. Permeability of three-dimensional models of fibrous porous media. *Journal of Fluid Mechanics*, 308:341–361, 1996.

[26] S Fotovati, S A Hosseini, H Vahedi Tafreshi, and B Pourdeyhimi. Modeling instantaneous pressure drop of pleated thin filter media during dust loading. *Chemical Engineering Science*, 66:4036–4046, 2011.

[27] L Tadrist, M Miscevic, O Rahli, and F Topin. About the use of fibrous materials in compact heat exchangers. *Experimental thermal and fluid science*, 28:193–199, 2004.

[28] P Soltani, M S Johari, and M Zarrebini. Effect of 3D fiber orientation on permeability of realistic fibrous porous networks. *Powder Technology*, 254:44–56, 2014.

[29] T Stylianopoulos, A Yeckel, J J Derby, X Luo, M S Shephard, E A Sander, and V H Barocas. Permeability calculations in three-dimensional isotropic and oriented fiber networks. *Physics of Fluids*, 20:123601:1–123601:10, 2008.

[30] M A Tahir and H V Tafreshi. Influence of fiber orientation on the transverse permeability of fibrous media. *Physics of Fluids*, 21:083601:1–083604:5, 2009.

[31] A Tamayol and M Bahrami. Parallel flow through ordered fibers: An analysis approach. *Journal of Fluids Engineering*, 132:114502:1–114502:7, 2010.

[32] A Inayat, H Freund, T Zeiser, and W Schwieger. Determining the specific surface area of ceramic foams: The tetrakaidecahedra model revisited. *Chemical Engineering Science*, 66:1179–1188, 2011.

[33] J G Speight. *Rules of Thumb for Petroleum Engineers*. John Wiley & Sons, 2017.

[34] N Dukhan, R Picón-Feliciano, and Á R Álvarez Hernández. Air flow through compressed and uncompressed aluminum foam: Measurements and correlations. *Journal of Fluids Engineering*, 128:1004–1012, 2006.

[35] O Gerbaux, T Vercueil, A Memponteil, and B Bador. Experimental characterization of single and two-phase flow through nickel foams. *Chemical Engineering Science*, 63:5202–5217, 2008.

[36] S Woudberg. *Comparative analysis of predictive equations for transfer process in different porous structures*. PhD thesis, Stellenbosch University, Stellenbosch, 2012.

[37] S Ergun. Flow through packed columns. *Chemical Engineering Progress*, 48(2):89, 1952.

[38] E A Moreira and J R Coury. The influence of structural parameters on the permeability of ceramic foams. *Brazilian Journal of Chemical Engineering*, 21(1):23–33, 2004.

[39] M L Hunt and C L Tien. Effects of thermal dispersion on forced convection in fibrous media. *International Journal of Heat and Mass Transfer*, 31(2):301–309, 1988.

[40] B V Antohe, J L Lage, D C Price, and R M Weber. Experimental determination of permeability and inertia coefficients of mechanically compressed aluminum porous matrices. *Journal of Fluids Engineering*, 119:404–412, 1997.

[41] C Schaschke. *A dictionary of Chemical Engineering*. Oxford University Press, 2014.

[42] J Grosse, B Dietrich, G I Garrido, P Habisreuther, N Zarzalis, H Martin, M Kind, and B Kraushaar-Czarnetzki. Morphological characterization of ceramic sponges for applications in chemical engineering. *Industrial and Engineering Chemistry Research*, 48:10395–10401, 2009.

[43] R Bird, W Stewart, and E Lightfoot. *Transport Phenomena*. John Wiley & Sons, New York (NY), 2nd edition, 2007.

[44] F C Buciuman and B Kraushaar-Czarnetzki. Ceramic foam monoliths as catalyst carriers. 1. Adjustment and description of the morphology. *Industrial and Engineering Chemistry Research*, 42:1863–1869, 2003.

[45] J T Richardson, Y Peng, and D Remue. Properties of ceramic foam catalyst supports: pressure drop. *Applied Catalysis A: General*, 204:19–32, 2000.

[46] S Mancin, C Zilio, A Cavallini, and L Rossetto. Pressure drop during air flow in aluminum foams. *International Journal of Heat and Mass Transfer*, 53:3121–3130, 2010.

[47] W Mickel, S Münster, L M Jawerth, D A Vader, D A Weitz, A P Sheppard, K Mecke, B Fabry, and G E Schröder-Turk. Robust pore size analysis of filamentous networks from three-dimensional confocal microscopy. *Biophysical Journal*, 95:6072–6080, 2008.

[48] X Huang, Q Wang, W Zhou, D Deng, Y Zhao, D Wen, and J Li. Morphology and transport properties of fibrous porous media. *Powder Technology*, 283:618–626, 2015.

[49] J P Du Plessis and J H Masliyah. Mathematical modelling of flow through consolidated isotropic porous media. *Transport in Porous Media*, 3(2):145–161, 1988.

[50] J P Du Plessis and J H Masliyah. Flow through isotropic granular porous media. *Transport in Porous Media*, 6(3):207–221, 1991.

[51] J P Du Plessis. Saturated crossflow through a two-dimensional porous medium. *Advances in Water Resources*, 14(3):131–137, 1991.

[52] J P Du Plessis and J Van der Westhuizen. Laminar crossflow through prismatic porous domains. *R&D Journal*, 9(2):18–24, 1993.

[53] J P Du Plessis. Analytical quantification of coefficients in the Ergun equation for fluid friction in a packed bed. *Transport in Porous Media*, 16(2):189–207, 1994.

[54] A Tamayol and M Bahrami. Transverse permeability of fibrous media. *Physical Review E*, 83(4):046314:1–046314:9, 2011.

[55] S Woudberg. Permeability prediction of an analytical pore-scale model for layered and isotropic fibrous porous media. *Chemical Engineering Science*, 164:232–245, 2017.

[56] S Crosnier, J P Du Plesses, R Riva, and J Legrand. Modelling of gas flow through isotropic metallic foams. *Journal of Porous Media*, 9(1):35–54, 2006.

[57] M C van Heyningen. *Investigating the effect of compression on the permeability of fibrous porous media*. MSc thesis, Stellenbosch University, South Africa, 2014.

[58] A Tamayol and M Bahrami. Analytical determination of viscous permeability of fibrous porous media. *International Journal of Heat Mass Transfer*, 52:2407–2414, 2009.

[59] Y Zhang, J Liu, T Luan, Y Gao, and J Mostaghimi. Predicting of flow characteristics in fibrous porous medium using a novel modeling algorithm and lattice Boltzmann method. *Chemical Engineering Science*, 221:115647:1–115647:18, 2020.

[60] M M Tomadakis and T J Robertson. Viscous permeability of random fiber structures: Comparison of electrical and diffusional estimates with experimental and analytical results. *Journal of Composite Materials*, 39(2):163–188, 2005.

[61] M A Van Doormal and J G Pharoah. Determination of permeability in fibrous porous media using the lattice Boltzmann method with application to PEM fuel cells. *International Journal for Numerical Methods in Fluids*, 59:75–89, 2009.

[62] A. Tamayol, K. W. Wong, and M. Bahrami. Effects of microstructure on flow properties of fibrous porous media at moderate Reynolds number. *Physical Review E*, 85:026318:1–026318:7, 2012.

[63] R R Sullivan. Specific surface measurements on compact bundles of parallel fibers. *Journal of Applied Physics*, 13:725–730, 1942.

[64] L Giani, G Groppi, and E Tronconi. Mass-transfer characterization of metallic foams as supports for structured catalysts. *Industrial and Engineering Chemistry Research*, 44:4186–4195, 2005.

[65] E Maré. *Investigating correlation among geometrical parameters of isotropic and anisotropic fibrous porous media.* MSc thesis, Stellenbosch University, South Africa, 2020.

[66] L L Gibson and M F Ashby. *Cellular solids.* Pergamon Press, Oxford, 1988.

[67] T J Lu, H A Stone, and M F Ashby. Heat transfer in open-cell metal foams. *Acta matererialia*, 46(10):3619–3635, 1998.

[68] M Lacroix, P Nguyen, D Schweich, C P Huu, S Savin-Poncet, and D Edouard. Pressure drop measurements and modeling on SiC foams. *Chemical Engineering Science*, 62:3259–3267, 2007.

[69] W Thomas. On the division of space with minimum partitional area. *Acta mathematica*, 11(1–4):121–134, 1887.

[70] R Phelan, D Weaire, and K Brakke. Computation of equilibrium foam structures using the surface evolver. *Experimental Mathematics*, 4(3):181–192, 1995.

[71] P Kumar, F Topin, and J Vicente. Determination of effective thermal conductivity from geometrical properties: Application to open cell foams. *International Journal of Thermal Sciences*, 81:13–28, 2014.

[72] S Woudberg, F Theron, E Lys, and L Le Coq. Investigating the influence of local porosity variations and anisotropy effects on the permeability of fibrous media for air filtration. *Chemical Engineering Science*, 180:70–78, 2018.

[73] L Spielman and S L Goren. Model for predicting pressure drop and filtration efficiency in fibrous media. *Environmental Science & Technology*, 2(4):279–287, 1968.

[74] J L Nava, MT Oropeza, C Ponce de Léon, J González-García, and A J Frías-Ferrer. Determination of the effective thickness of a porous electrode in a flow-through reactor; effect of the specific surface area of stainless steel fibres, used as a porous cathode, during the deposition of Ag(I) ions. *Hydrometallurgy*, 91:98–103, 2008.

[75] L Zeng, J Sun, T S Zhao, Y X Ren, and L Wei. Balancing the specific surface area and mass diffusion property of electrospun carbon fibers to enhance the cell performance of vanadium redox flow battery. *International Journal of Hydrogen Energy*, 45:12565–12576, 2020.

[76] E Maré and S Woudberg. A geometric versus kinetic modelling approach for characterizing porous media foams. *10th International Conference on Computational and Experimental Methods in Multiphase and Complex Flow*, Lisbon, Portugal, 191-202, 21-23 May 2019.

[77] S Woudberg, E Maré, M C Van Heyningen, F Theron, and L Le Coq. Predicting the permeability and specific surface area of compressed and uncompressed fibrous media including the Klinkenberg effect. *Powder Thechnology*, 377:488–505, 2021.

[78] E Maré and S Woudberg. A comparative study of geometric models for predicting permeability coefficients and specific surface area of fibrous porous media. *Transport in Porous Media*, 1-34, 2023.

[79] E Maré and S Woudberg. Geometric models for incorporating solid accumulation at the nodes of open-celled foams. 2023 (submitted to international journal).

[80] E Maré and S Woudberg. Analytical determination of the geometrical properties of metal foams under compression. *12th International Conference on Porous Metals and Metallic foams*, Dresden Radebeul, Germany, 5-7 July 2023 (submitted/under publication).

[81] K J Mattern and W M Deen. "Mixing rules" for estimating the hydraulic permeability of fiber mixtures. *American Institute of Chemical Engineers Journal*, 54(1):32–41, 2008.

[82] P Du Plessis, A Montillet, J Comiti, and J Legrand. Pressure drop for flow through high porosity metallic foams. *Chemical Engineering Science*, 49(21):3545–3553, 1994.

[83] S Woudberg, M C Van Heyningen, L Le Coq, J Legrand, and J P Du Plessis. Analytical determination of the effect of compression on the permeability of fibrous porous media. *Chemical Engineering Science*, 112:108–115, 2014.

[84] P Ouagne and J Bréard. Continuous transverse permeability of fibrous media. *Composites: Part A*, 41:22–28, 2010.

[85] S Hong, Y Jung, R Yen, H F Chan, Leong K W, Truskey G A, and Zhao X. Magnetoactive sponges for dynamic control of microfluidic flow patters in microphysiological systems. *Lab on a Chip*, 14:514–521, 2014.

[86] C Perrot, R Panneton, and X Olny. Periodic unit cell reconstruction of porous media: Application to open-cell aluminum foams. *Journal of Applied Physics*, 101(11):113538:1–113538:11, 2007.

[87] P Magnico. Analysis of permeability and effective viscosity by CFD on isotropic and anisotropic metallic foams. *Chemical Engineering Science*, 64:3564–3575, 2009.

[88] S Woudberg. Investigation of the effect of compression on a soft fibrous porous medium. *7th International Conference on Computational and Experimental Methods in Multiphase and Complex Flow*, A Coruña, Spain, 351-361, 3-5 July 2013.

[89] W L Ingmanson, B D Andrews, and R C Johnson. Internal pressure distribution in compressible mats under fluid stress. *TAPP1*, 42:840–849, 1959.

[90] P C Carman. Diffusion and flow of gases and vapours through micropores I. Slip flow and molecular streaming. *Proceedings of the Royal Society of London. Series A. Mathematical and Physical Sciences*, 203(1072):55–74, 1950.

[91] Y S Wu, K Preuss, and P Persoff. Gas flow in porous media with Klinkenberg effects. *Transport in Porous Media*, 32:117–137, 1998.

[92] M D M Innocentini, V R Salvini, A Macedo, and V C Pandolfelli. Prediction of ceramic foams permeability using Ergun's equation. *Journal of the American Ceramic Society*, 85(5):941–944, 2001.

[93] W Tanikwa and T Shimamoto. Klinkenberg effect for gas permeability and its comparison to water permeability for porous sedimentary rocks. *Hydrology and Earth System Sciences Discussions*, 3(4):1315–1338, 2006.

[94] S Woudberg and J P Du Plessis. Predicting the permeability of very low porosity sandstones. *Transport in Porous Media*, 73(1):39–55, 2008.

[95] A F Miguel and A Serrenho. On the experimental evaluation of permeability in porous media using a gas flow method. *Journal of Physics D: Applied Physics*, 40:6824–6828, 2007.

[96] R W Barber and D R Emerson. The influence of Knudsen number on the hydrodynamic development length within parallel plate micro-channels. *Advances in Fluid Mechanics IV*, 36:207–216, 2002.

[97] K Hooman, A Tamayol, M Dahari, M R Safaei, H Togun, and R Sadri. A theoretical model to predict gas permeability for slip flow through a porous medium. *Applied Thermal Engineering*, 70:71–76, 2014.

[98] E Skjetne and J L Auriault. Homogenization of wall-slip gas flow through porous media. *Transport in Porous Media*, 36:293–306, 1999.

[99] J Chastanet, P Royer, and J L Auriault. Does Klinkenberg's law survive upscaling? *Transport in Porous Media*, 56:171–198, 2004.

[100] R W Barber and D R Emerson. Challenges in modeling gas-phase flow in microchannels: from slip to transition. *Heat Transfer Engineering*, 27(4):3–12, 2006.

[101] S A Hosseini and H V Tafreshi. Modeling permeability of 3-D nanofiber media in slip flow regime. *Chemical Engineering Science*, 65:2249–2254, 2010.

[102] L J Klinkenberg. The permeability of porous media to liquids and gases. *American Petroleum Institute*, Drilling and Production Practice, 2:200-213, 1941.

[103] J A Wheat. The air flow resistance of glass fibre filter paper. *The Canadian Journal of Chemical Engineering*, 41(2):67–72, 1963.

[104] J M Wilms. *On the hydrodynamic permeability of foamlike media.* MSc thesis, Stellenbosch University, South Africa, 2006.

APPENDIX A

Cardanic method of solving a cubic polynomial

Wilms [104] presented a method for solving a cubic polynomial, such that

$$x^3 + a_1\,x^2 + a_2\,x + a_3 = 0\,, \tag{A.1}$$

where a_1, a_2 and a_3 are constants. The method is known as the Cardanic method and the solutions to the cubic polynomial are given by

$$x_1 = 2\sqrt{-Q}\,\cos\left(\frac{1}{3}\,\Theta\right) - \frac{1}{3}\,a_1\,,$$
$$x_2 = 2\sqrt{-Q}\,\cos\left(\frac{1}{3}\,\Theta + \frac{2}{3}\,\pi\right) - \frac{1}{3}\,a_1$$

and

$$x_3 = 2\sqrt{-Q}\,\cos\left(\frac{1}{3}\,\Theta + \frac{4}{3}\,\pi\right) - \frac{1}{3}\,a_1\,,$$

where

$$Q = \frac{3\,a_2 - a_1^2}{9}\,;\;\; P = \frac{9\,a_1\,a_2 - 27\,a_3 - 2\,a_1^3}{54}\,;\;\; \cos\Theta = \frac{P}{\sqrt{-Q^3}} \text{ and } D = Q^3 + P^2\,,$$

if $D < 0$ and a_1, a_2 and a_3 are real. The roots of equation (A.1) are then real and unequal.

Geometric factor of the 2D (or two-strut) RUC model

In order to solve for the geometric factor ψ of the two-strut RUC model in terms of ϵ, equation (2.43) is used, i.e.

$$\psi^3 - \psi^2 - \epsilon\,\psi + \epsilon^2 = 0\,. \tag{A.2}$$

From the comparison of equation (A.2) to the cubic polynomial in equation (A.1), it is deduced that

$$a_1 = -1 \;\;;\;\; a_2 = -\epsilon \;\text{ and }\; a_3 = \epsilon^2\,,$$

from which it follows that

$$Q = \frac{3(-\epsilon) - (-1)^2}{9} = -\frac{3\epsilon + 1}{9},$$
$$P = \frac{9(-1)(-\epsilon) - 27(\epsilon^2) - 2(-1)^3}{54} = \frac{9\epsilon - 27\epsilon^2 + 2}{54},$$

and

$$D = \left(-\frac{3\epsilon + 1}{9}\right)^3 + \left(\frac{9\epsilon - 27\epsilon^2 + 2}{54}\right)^2 = \frac{1}{4}\epsilon^4 - \frac{11}{54}\epsilon^3 - \frac{5}{108}\epsilon^2.$$

Since $0 < \epsilon < 1$, it follows that $\epsilon^4 < \epsilon^3 < \epsilon^2$. Also, $\frac{1}{4} < \frac{11}{15} + \frac{5}{108}$, which implies that $D < 0$. All the conditions are therefore satisfied and it can be determined that

$$\cos\Theta = \frac{(9\epsilon - 27\epsilon^2 + 2)/54}{\sqrt{-\left(-\frac{3\epsilon+1}{9}\right)^3}} = \frac{9\epsilon - 27\epsilon^2 + 2}{2\sqrt{27\epsilon^3 + 27\epsilon^2 + 9\epsilon + 1}}.$$

The solutions of equation (A.2) can consequently be expressed as

$$x_1 = \frac{2}{3}\sqrt{3\epsilon + 1}\cos\left[\frac{1}{3}\cos^{-1}\left(\frac{9\epsilon - 27\epsilon^2 + 2}{2\sqrt{27\epsilon^3 + 27\epsilon^2 + 9\epsilon + 1}}\right)\right] + \frac{1}{3},$$
$$x_2 = \frac{2}{3}\sqrt{3\epsilon + 1}\cos\left[\frac{1}{3}\cos^{-1}\left(\frac{9\epsilon - 27\epsilon^2 + 2}{2\sqrt{27\epsilon^3 + 27\epsilon^2 + 9\epsilon + 1}}\right) + \frac{2}{3}\pi\right] + \frac{1}{3},$$

and

$$x_3 = \frac{2}{3}\sqrt{3\epsilon + 1}\cos\left[\frac{1}{3}\cos^{-1}\left(\frac{9\epsilon - 27\epsilon^2 + 2}{2\sqrt{27\epsilon^3 + 27\epsilon^2 + 9\epsilon + 1}}\right) + \frac{4}{3}\pi\right] + \frac{1}{3}.$$

In Figure A.1 the solutions of the polynomial obtained for the geometric factor of the 2D (or two-strut) RUC model are displayed.

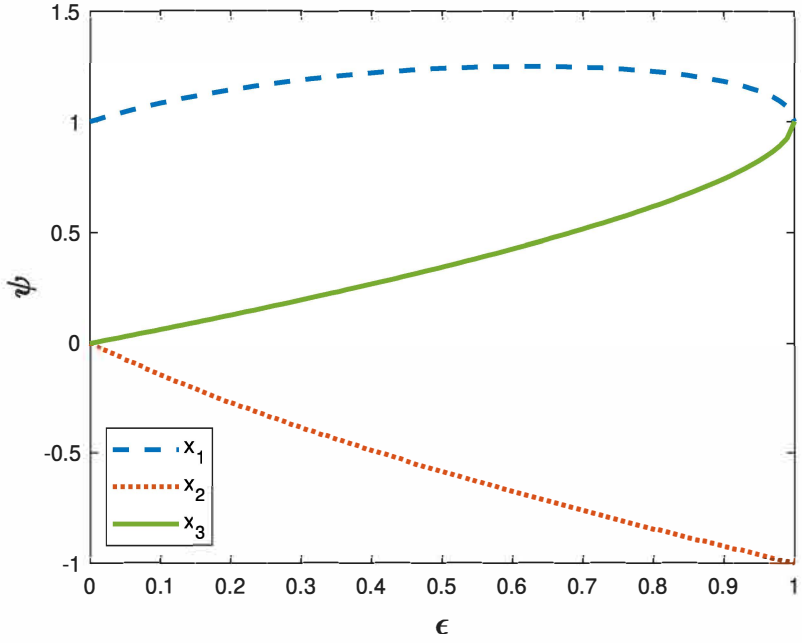

FIGURE A.1: *Solutions for the geometric factor versus porosity for the 2D (or two-strut) RUC model*

If there are no stagnant zones, the geometric factor, ψ, is equal to the tortuosity which would usually range between values of 1 and 2. It can therefore be concluded from Figure A.1 that the solution of equation (A.2) that is physically relevant, is the solution x_1, i.e.

$$\psi = \frac{2}{3}\sqrt{3\epsilon + 1}\cos\left[\frac{1}{3}\cos^{-1}\left(\frac{9\epsilon - 27\epsilon^2 + 2}{2\sqrt{27\epsilon^3 + 27\epsilon^2 + 9\epsilon + 1}}\right)\right] + \frac{1}{3}, \tag{A.3}$$

which is the desired geometric factor expression in terms of the porosity for the 2D (or two-strut) RUC model.

Geometric factor of the 3D (or three-strut) RUC model

The geometric factor, ψ, of the 3D (or three-strut) RUC model is solved similarly by using equation (2.71) in this case, that is the following polynomial equation:

$$\psi^3 - 6\,\psi^2 + 9\,\psi - 4\,\epsilon = 0\,. \tag{A.4}$$

Comparing equation (A.4) to the general cubic polynomial equation (A.1), leads to

$$a_1 = -6 \;\;;\;\; a_2 = 9 \;\text{ and }\; a_3 = -4\,\epsilon\,,$$

and thus

$$Q = \frac{3\,(9) - (-6)^2}{9} = -1\,,$$
$$P = \frac{9\,(-6)\,(9) - 27\,(-4\epsilon) - 2\,(-6)^3}{54} = 2\,\epsilon - 1\,,$$

and

$$D = (-1)^3 + (2\,\epsilon - 1)^2 = 4\,(\epsilon^2 - \epsilon)\,.$$

Since $0 < \epsilon < 1$, it follows that $\epsilon^2 < \epsilon$ which implies that $D < 0$. With the conditions being satisfied, the following expression can therefore be determined:

$$\cos\Theta = \frac{2\,\epsilon - 1}{\sqrt{-(-1)^3}} = 2\,\epsilon - 1\,.$$

The solutions of equation (A.4) is then furthermore found to be

$$x_1 = 2\,\sqrt{-(-1)}\,\cos\left(\frac{1}{3}\,\Theta\right) - \frac{1}{3}\,(-6) = 2\,\cos\left[\frac{1}{3}\,\cos^{-1}(2\,\epsilon - 1)\right] + 2\,,$$
$$x_2 = 2\,\sqrt{-(-1)}\,\cos\left(\frac{1}{3}\,\Theta + \frac{2}{3}\,\pi\right) - \frac{1}{3}\,(-6) = 2\,\cos\left[\frac{1}{3}\,\cos^{-1}(2\,\epsilon - 1) + \frac{2}{3}\,\pi\right] + 2$$

and

$$x_3 = 2\,\sqrt{-(-1)}\,\cos\left(\frac{1}{3}\,\Theta + \frac{4}{3}\,\pi\right) - \frac{1}{3}\,(-6) = 2\,\cos\left[\frac{1}{3}\,\cos^{-1}(2\,\epsilon - 1) + \frac{4}{3}\,\pi\right] + 2\,.$$

In Figure A.2 the solutions are plotted against the porosity.

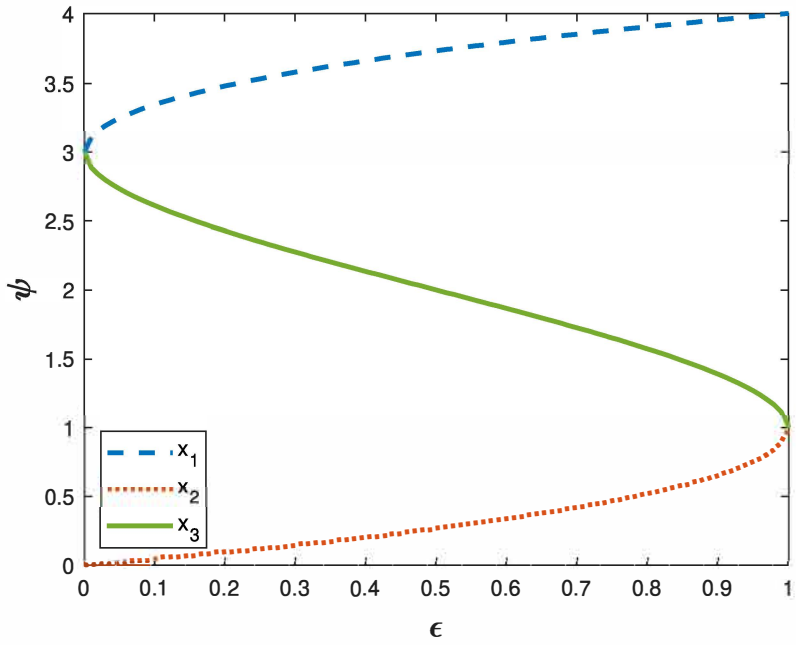

FIGURE A.2: *Solutions for the geometric factor versus porosity for the 3D (or three-strut) RUC model*

The geometric factor will range between values of 1 and 2 and it can therefore be concluded from Figure A.2 that the solution for equation (A.4) that is physically relevant is the solution given by x_3, i.e.

$$\psi = 2 + 2\,\cos\left[\frac{4\,\pi}{3} + \frac{1}{3}\,\cos^{-1}(2\,\epsilon - 1)\right]\,, \tag{A.5}$$

which is the desired geometric factor in terms of porosity for the 3D (or three-strut) model.

Strut diameter ratio of the NARUC model with cubic nodes

The polynomial equation to be solved in this case is given by

$$\left[16r_1^3\right]\,R^3 + \left[-12r_1^2\right]\,R^2 + \left[12r_1^2 - 16r_1^3 + 8kr_1^3\left(r_2^3 - 2r_2 + 1\right)\right] = 0\,. \tag{A.6}$$

Using the Cardanic method, the values for R can be determined from equation (A.6). The comparison of equation (A.6) to equation (A.1), and therefore also the division of equation (A.6) by $16r_1^3$, then leads to

$$a_1 = -\frac{12r_1^2}{16r_1^3} = -\frac{3}{4r_1}\,,$$
$$a_2 = 0\,,$$

and

$$a_3 = \frac{12r_1^2 - 16r_1^3 + 8kr_1^3\left(r_2^3 - 2r_2 + 1\right)}{16r_1^3} = \frac{3}{4r_1} - 1 + \frac{k}{2}\left(r_2^3 - 2r_2 + 1\right)\,.$$

Consequently,

$$Q = -\frac{1}{16r_1},$$

and

$$P = -\frac{a_3}{2} + \frac{1}{64r_1^3} = -\frac{3}{8r_1} + \frac{1}{2} - \frac{k}{4}\left(r_2^3 - 2r_2 + 1\right) + \frac{1}{64r_1}.$$

The following expression can therefore be determined:

$$\begin{aligned}\cos\Theta &= \frac{\frac{1}{2}\left(\frac{1}{32r_1^3} - a_3\right)}{\sqrt{\frac{1}{16^3 r_1^6}}} \\ &= 1 - 32a_3r_1^3 \\ &= 1 + 8r_1^2\left(4r_1 - 3\right) - 16kr_1^3\left(r_2^3 - 2r_2 + 1\right).\end{aligned}$$

Equation (A.6) then provides the following solutions:

$$x_1 = \frac{1}{2\sqrt{r_1}}\cos\left[\frac{1}{3}\cos^{-1}\left[1 + 8r_1^2\left(4r_1 - 3\right) - 16kr_1^3\left(r_2^3 - 2r_2 + 1\right)\right]\right] + \frac{1}{4r_1},$$

$$x_2 = \frac{1}{2\sqrt{r_1}}\cos\left[\frac{1}{3}\cos^{-1}\left[1 + 8r_1^2\left(4r_1 - 3\right) - 16kr_1^3\left(r_2^3 - 2r_2 + 1\right)\right] + \frac{2}{3}\pi\right] + \frac{1}{4r_1},$$

and

$$x_3 = \frac{1}{2\sqrt{r_1}}\cos\left[\frac{1}{3}\cos^{-1}\left[1 + 8r_1^2\left(4r_1 - 3\right) - 16kr_1^3\left(r_2^3 - 2r_2 + 1\right)\right] + \frac{4}{3}\pi\right] + \frac{1}{4r_1}.$$

The r_1- and r_2-ratios are determined as explained in Section 3.2.1, by combining the NARUC model (adjusted using cubic nodes) with the "fat" dodecahedron model, MCL model or modified tetrakaidecahedron model, respectively. The solutions of the strut diameter ratio of the NARUC model with cubic nodes combined with each of the aforementioned models are shown in Figures A.3, A.4 and A.5, respectively. The number of nodes is furthermore chosen as 3, i.e. $k = 3$. The choice of k, however, does not influence the results obtained for R when the NARUC model is combined with the "fat" dodecahedron model or the modified tetrakaidecahedron model. It does influence the results obtained for R for the NARUC model combined with MCL model, but not significantly. The results for the "fat" dodecahedron model with cylindrical struts are shown for $0 < \epsilon < 0.9$ and the results for the "fat" dodecahedron model with triangular struts are shown for $0.9 < \epsilon < 1$ in Figure A.3.

In Figure A.3 a slight difference is noted at the porosity equal to 0.9, i.e. where the prediction of the model combination with the "fat" dodecahedron model with cylindrical struts ends and the prediction of the model combination with the "fat" dodecahedron model with triangular struts begin. Although the difference is not ideal, it is similar to other observations where the dodecahedron model was evaluated in this study.

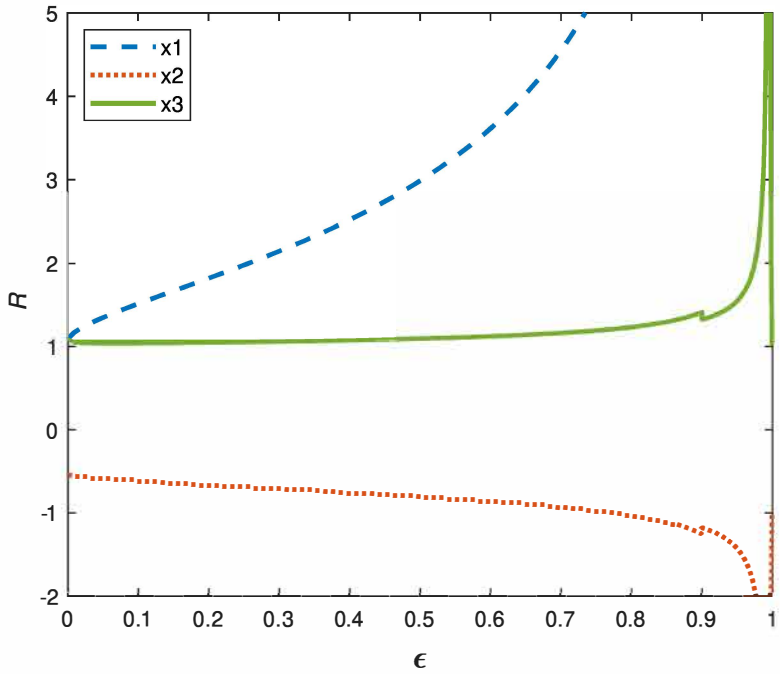

FIGURE A.3: *Solutions for R versus porosity for the NARUC model with cubic nodes combined with the "fat" dodecahedron model*

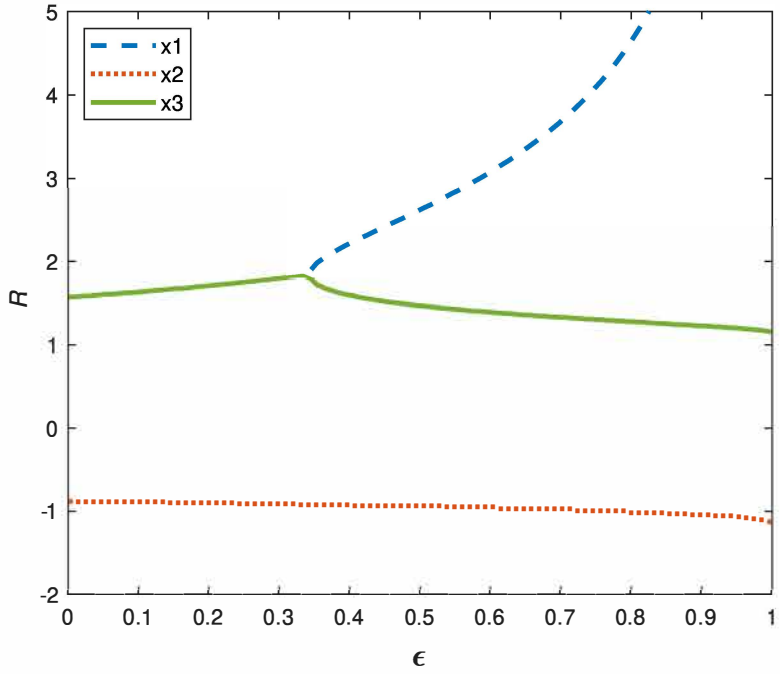

FIGURE A.4: *Solutions for R versus porosity for the NARUC model with cubic nodes combined with the MCL model*

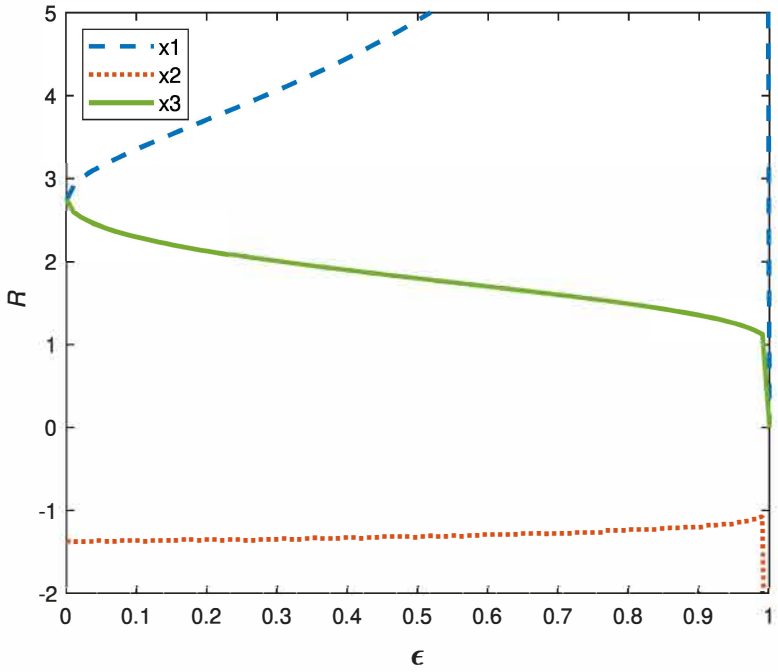

FIGURE A.5: *Solutions for R versus porosity for the NARUC model with cubic nodes combined with the modified tetrakaidecahedron model*

Figures A.3 to A.5 reveal that the different model combinations affect the results obtained for R. The expectation for the value of R is to be greater than 1, since the strut diameter is expected to increase when solid accumulation occurs. It is, however, not expected of R to increase as drastically as the results obtained from the solutions provided by x_1 for all the model combinations. Since R cannot be negative, it is concluded that the solution given by x_3 is therefore the most plausible solution for R, as seen from Figures A.3 to A.5. R is consequently given by the following expression:

$$R = \frac{1}{2\sqrt{r_1}} \cos\left[\frac{1}{3}\cos^{-1}\left[1 + 8r_1^2\left(4r_1 - 3\right) - 16kr_1^3\left(r_2^3 - 2r_2 + 1\right)\right] + \frac{4}{3}\pi\right] + \frac{1}{4r_1}.$$

In Figure A.3 a more or less constant prediction for R for $\epsilon < 0.9$ is observed. R increases and decreases significantly where $0.9 < \epsilon < 1$, i.e. the predictions for R spikes between the aforementioned porosity values. These predictions could confirm the observations of Kumar et al. [71], who noted that solid accumulation at the nodes occur at high porosity values due to the change of strut shapes at these porosity values (as discussed in Section 3.1.1). Alternatively, the strut ratio could decrease with an increase in porosity, as predicted by the model combination with the modified tetrakaidecahedron model and shown in Figure A.5. The latter trend would make sense if it is assumed that low porosity foams have large nodes in comparison to the strut diameters and that the nodes decreases in size as the porosity increases. The significant decrease of R where $\epsilon > 0.99$ also corresponds to the observations of Ahmed et al. [7], i.e. that solid accumulation at the nodes of foams with high porosities are less likely to occur due to weak solid precursor deposited onto the foam. The trend given by the combination with the MCL model for x_3, as shown in Figure A.4, predicts an unexpected increase and decrease where $3 < \epsilon < 4$ and therefore does not appear to be a viable solution for all the porosity values. For high porosity

values (which is the focus area of this study), the predictions provided by this model combination, however, resembles that of the NARUC model combination with the modified tetrakaidecahedron model (i.e. the predictions decreases with increasing porosity). It is finally noted that R is expected therefore to either follow the trend given by the combination with the "fat" dodecahedron model or the modified tetrakaidecahedron model and not necessarily the trend given by the combination with the MCL model (specifically for lower porosities). The "fat" dodecahedron model combination and modified tetrakaidecahedron model combination have contrary predictions in that the former predicts an increase of R as the porosity increases and the latter predicts a decrease of R as the porosity increases. Further studies investigating the solid accumulation at strut intersections for different porosity values can be conducted experimentally in order to determine which trend would be most likely to occur.

Strut diameter ratio of the NARUC model with curved wedge nodes

The polynomial equation in terms of the strut diameter ratio of the NARUC model with curved wedge nodes is given by

$$\left[16r_1^3\right] R^3 + \left[-12r_1^2\right] R^2 + \left[12r_1^2 - 16r_1^3 + k\left(1-\frac{\pi}{4}\right)\left(2r_1^3 - 2r_1^2 + \frac{r_1}{2}\right)\right] = 0\,. \qquad \text{(A.7)}$$

When comparing equation (A.7) to equation (A.1) it is deduced that a_1 and a_2 are the same as in the case of the NARUC model with cubic nodes. a_3 is, however, determined to be

$$a_3 = \frac{3}{4r_1} - 1 + \frac{k}{8}\left(1-\frac{\pi}{4}\right)\left(1 - \frac{1}{r_1} + \frac{1}{4r_1^2}\right)\,.$$

Q is also the same as in the case of the NARUC model with cubic nodes and P for this case is given by

$$P = -\frac{a_3}{2} + \frac{1}{64r_1^3} = -\frac{3}{8r_1} + 1 - \frac{k}{16}\left(1-\frac{\pi}{4}\right)\left(1 - \frac{1}{r_1} + \frac{1}{4r_1^2}\right) + \frac{1}{64r_1^3}\,,$$

and hence

$$\cos\Theta = 1 - 32a_3r_1^3 = 1 + 8r_1^2\left(4r_1 - 3\right) - k\left(1-\frac{\pi}{4}\right)\left(4r_1^3 - 4r_1^2 + r_1\right)\,.$$

Equation (A.7) then provides the following solutions:

$$x_1 = \frac{1}{2\sqrt{r_1}}\cos\left[\frac{1}{3}\cos^{-1}\left[1 + 8r_1^2\left(4r_1 - 3\right) - k\left(1-\frac{\pi}{4}\right)\left(4r_1^3 - 4r_1^2 + r_1\right)\right]\right] + \frac{1}{4r_1}\,,$$

$$x_2 = \frac{1}{2\sqrt{r_1}}\cos\left[\frac{1}{3}\cos^{-1}\left[1 + 8r_1^2\left(4r_1 - 3\right) - k\left(1-\frac{\pi}{4}\right)\left(4r_1^3 - 4r_1^2 + r_1\right)\right] + \frac{2}{3}\pi\right] + \frac{1}{4r_1}\,,$$

and

$$x_3 = \frac{1}{2\sqrt{r_1}}\cos\left[\frac{1}{3}\cos^{-1}\left[1 + 8r_1^2\left(4r_1 - 3\right) - k\left(1-\frac{\pi}{4}\right)\left(4r_1^3 - 4r_1^2 + r_1\right)\right] + \frac{4}{3}\pi\right] + \frac{1}{4r_1}\,.$$

The solutions of the strut diameter ratio of the NARUC model with curved wedge nodes are shown in Figure A.6. The r_1-ratio was determined as described in Section 3.2.2 and

the number of nodes was chosen to be 12. The choice of the value of k, however, does not affect the trend of the results provided in Figure A.6.

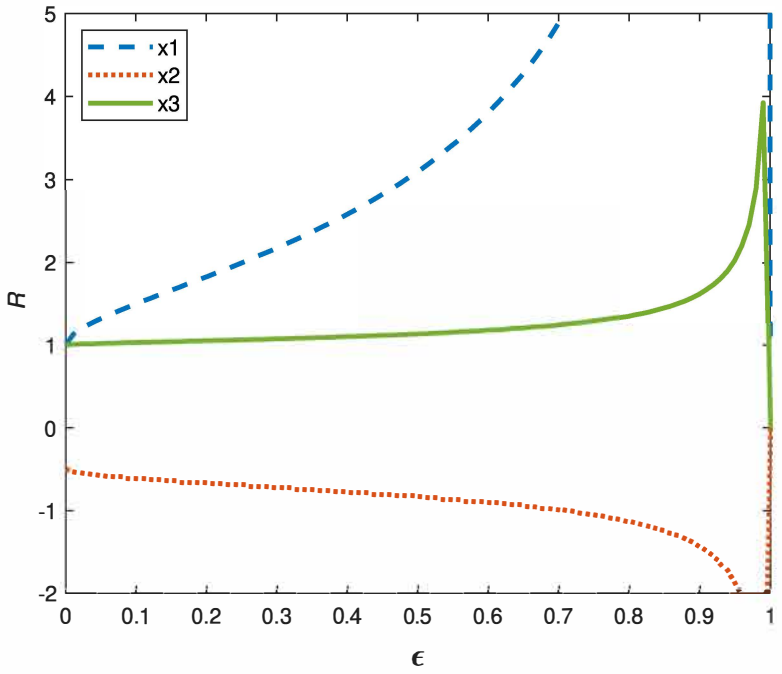

FIGURE A.6: *Solutions for R versus porosity for the NARUC model with curved wedge nodes*

The solution given by x_3 is once again the most plausible solution for R, as seen from Figure A.6. R is consequently given by the following expression:

$$R = \frac{1}{2\sqrt{r_1}} \cos\left[\frac{1}{3}\cos^{-1}\left[1 + 8r_1^2\left(4r_1 - 3\right) - k\left(1 - \frac{\pi}{4}\right)\left(4r_1^3 - 4r_1^2 + r_1\right)\right] + \frac{4}{3}\pi\right] + \frac{1}{4r_1}\,.$$

It is noted that the trend observed by the solutions for R for the NARUC model with curved wedge nodes is similar to the trend observed for R for the NARUC model with cubic nodes combined with the "fat" dodecahedron model. A similar reasoning to explain the validity of the predictions for R for the NARUC model with curved wedge nodes is therefore followed as in the case of the R determined using the NARUC model (with cubic nodes) combined with the "fat" dodecahedron model.